INVESTIGATING IMPACTS OF NATURAL AND HUMAN-INDUCED ENVIRONMENTAL CHANGES ON HYDROLOGICAL PROCESSES AND FLOOD HAZARDS USING A GIS-BASED HYDROLOGICAL/HYDRAULIC MODEL AND REMOTE SENSING DATA

A Dissertation

by

LEI WANG

Submitted to the Office of Graduate Studies of
Texas A&M University
in partial fulfillment of the requirements for the degree of

DOCTOR OF PHILOSOPHY

August 2006

Major Subject: Geography

INVESTIGATING IMPACTS OF NATURAL AND HUMAN-INDUCED ENVIRONMENTAL CHANGES ON HYDROLOGICAL PROCESSES AND FLOOD HAZARDS USING A GIS-BASED HYDROLOGICAL/HYDRAULIC MODEL AND REMOTE SENSING DATA

A Dissertation

by

LEI WANG

Submitted to the Office of Graduate Studies of
Texas A&M University
in partial fulfillment of the requirements for the degree of

DOCTOR OF PHILOSOPHY

Approved by:

Chair of Committee,	Hongxing Liu
Committee Members,	Andrew G. Klein
	Daniel D. Sui
	Francisco Olivera
Head of Department,	Douglas Sherman

August 2006

Major Subject: Geography

ABSTRACT

Investigating Impacts of Natural and Human-induced Environmental Changes on Hydrological Processes and Flood Hazards Using a GIS-based Hydrological/Hydraulic Model and Remote Sensing Data, (August 2006)

Lei Wang, B.S., Peking University;

M.S., Institute of Remote Sensing Applications, Chinese Academy of Sciences

Chair of Advisory Committee: Dr. Hongxing Liu

Natural and human-induced environmental changes have been altering the earth's surface and hydrological processes, and thus directly contribute to the severity of flood hazards. To understand these changes and their impacts, this research developed a GIS-based hydrological and hydraulic modeling system, which incorporates state-of-the-art remote sensing data to simulate flood under various scenarios. The conceptual framework and technical issues of incorporating multi-scale remote sensing data have been addressed.

This research develops an object-oriented hydrological modeling framework. Compared with traditional lumped or cell-based distributed hydrological modeling frameworks, the object-oriented framework allows basic spatial hydrologic units to have various size and irregular shape. This framework is capable of assimilating various GIS and remotely-sensed data with different spatial resolutions. It ensures the computational efficiency, while preserving sufficient spatial details of input data and model outputs.

Sensitivity analysis and comparison of high resolution LIDAR DEM with traditional USGS 30m resolution DEM suggests that the use of LIDAR DEMs can greatly reduce uncertainty in calibration of flow parameters in the hydrologic model and hence increase the reliability of modeling results. In addition, subtle topographic features and hydrologic objects like surface depressions and detention basins can be extracted from the high resolution LiDAR DEMs. An innovative algorithm has been developed to efficiently delineate surface depressions and detention basins from LiDAR DEMs.

Using a time series of Landsat images, a retrospective analysis of surface imperviousness has been conducted to assess the hydrologic impact of urbanization. The analysis reveals that with rapid urbanization the impervious surface has been increased from 10.1% to 38.4% for the case study area during 1974 - 2002. As a result, the peak flow for a 100-year flood event has increased by 20% and the floodplain extent has expanded by about 21.6%. The quantitative analysis suggests that the large regional detentions basins have effectively offset the adverse effect of increased impervious surface during the urbanization process. Based on the simulation and scenario analyses of land subsidence and potential climate changes, some planning measures and policy implications have been derived for guiding smart urban growth and sustainable resource development and management to minimize flood hazards.

DEDICATION

I want to dedicate this dissertation to my wife, Yang He. She devoted all her time to support my work during my study at Texas A&M University. There is no doubt that without her endless love and continued support, I could not have completed this work.

ACKNOWLEDGMENTS

I would like to acknowledge the inspirational instruction and guidance from my advisor, Dr. Hongxing Liu. His insightful understanding of the research was always the source of power that initiated and expanded my research work. He is so knowledgeable in so many fields that I obtained a tremendous amount of know-how just by working with him on all these projects. He is strict about the quality of the research, but encouraged me to explore. With his guidance, support, and encouragement, I was able to push my way through numerous obstacles along the way.

I also wish to express my sincere gratitude to my committee members. Dr. Francisco Olivera directed me in revising the hydrological modeling. With his support, I made significant progress towards model parameterization and calibration. His background and expertise in hydrological and hydraulic modeling supplied solid support for me. Dr. Daniel Sui helped me to establish links from GIS to the hydrological modeling in this research. His perception in GIScience inspired many thoughts in my dissertation during our discussions. Dr. Andrew Klein provided enormously valuable comments and input to this dissertation. He carefully reviewed my dissertation and gave lots of valuable comments and suggestions.

I would also like to thank the people in the Knowledge Engineering Lab. Dr. Robert Coulson presented me a new vision of the applications of GIS and remote sensing in many other areas. Dr. Maria Tchakerian is a nice supervisor and friend with whom I always felt comfortable. Dr. Andrew Birt provided his help to review and

correct several chapters of my dissertation. I also improved my programming skills by working with him.

I want to thank my friends in the Geography Department: Jaehyung Yu, Jose Gavinha, Zengwang Xu, Songgang Gu, Wimmy Lin, and Matthew Clemonds, current or former students. We shared happiness, success, and all kinds of feelings during our studies together. Having them as friends has made life much more joyful and easier.

I also want to thank my family in China, my mom, sisters, and the in-laws. They are always there supporting us. Their love and trust are important for me to finish my study.

Finally, I would like to acknowledge that this research has been funded by the NASA Earth System Science Fellowship Grant NG5-30467.

TABLE OF CONTENTS

Page

LIST OF FIGURES

FIGURE Page

FIGURE Page

FIGURE Page

FIGURE Page

LIST OF TABLES

CHAPTER I

INTRODUCTION

1.1. Research background

Flooding is considered the most influential natural disaster in the United States. Among the top ten natural disasters ranked in terms of FEMA's relief costs, eight of them are hurricane or flood related (FEMA, 2003). Inland flooding is responsible for more than half of the casualties and property damages associated with hurricanes and tropical storms. Floods are the number one natural disaster in the United States in terms of the number of lives lost and property damage (Perry, 2000). Between 1940 and 1982, flooding caused an average of 102 casualties and about 1.5 billion loss of property each year (NWS 1985). Although tremendous efforts have been made to control and relieve the severity and damage caused by floods, there remains a statistically significant increasing trend of flood damage at about 2.92% per year (Pielke and Downton, 2000). As a result, annual flood losses have risen from about $1 billion in the 1940s to about $4 -5 billion in the 1990s (Pielke and Downton, 2000; NWF, 1998).

The National Flood Insurance Program (NFIP) was founded in the late 1960s as a result of the Southeast Hurricane Disaster Relief Act passed by the Congress. NFIP requires that any new development larger than 50 lots or 5 acres should include base-flood elevation (BFE). Those communities with flood insurance studies and BFE are

---

This dissertation follows the style of the Journal of Hydrology.

qualified for up to 45% discount in annual flood insurance premiums. Depending on the different types of flood risk data provided by FEMA, communities must adopt minimum floodplain management as regulated by NFIP. The FEMA Flood Insurance Rate Maps (FIRMs) quantify flood risk of communities that are vulnerable to flood hazards. NFIP requires that a detailed analytical method should be used for the floodplain mapping process.

In general, the analytical method refers to a two-step approach that is widely recognized by the research community to determine base flood elevation. The first step models and simulates the channel water profiles at the peak flow. The second step transfers water surface elevation into maps. Automated approaches to the floodplain boundary mapping and flooding risk assessment have been widely adopted by researchers and scientists because of an increased availability of computation facilities, software packages, and digital databases. Additionally, the increasing awareness of the importance of Geographic Information Systems (GIS) in hydrological/hydraulic modeling motivated numerous efforts and attempts to integrate GIS into the modeling process.

A variety of hydrological models has been widely proposed in literature. The floodplain mapping process can be summarized into four phases: GIS data preparation; hydrological modeling; hydraulic modeling; and floodplain mapping and damage assessment (Sui and Maggio, 1999). Of these phases, the hydrological modeling process is the least standardized. According to Chow et al. (1988), hydrological models can be classified in terms of how following three components are addressed: space, randomness,

and temporal dimension. Hydrologic models can be classified as lumped or spatially distributed according to the scale of basic spatial units in the model. A typical lump model divides the watersheds into a limited number of sub-basins. The lumped model assumes the spatial homogeneity of the sub-watersheds. Lack of knowledge about spatial distribution of hydrological parameters within sub-watersheds is usually the reason why lumped models are chosen in the early years. However, the homogeneous assumption for large watershed divisions is often invalid. Recent development of geospatial data acquisition technologies, including GPS, Remote Sensing, and GIS, have led to the increasing availability of enormous spatial datasets, detailing the earth's physical environment, including land cover, topography, soil, and climate. In turn, the availability of data and computing resources has driven the development of hydrologic models with explicit spatial components. Most of the spatially distributed hydrologic models follow the Freeze and Harlan (1969) blue-print, which defines a set of equations and boundary conditions for a physically-based hydrologic simulation model (Beven, 2002). Singh et al. (2002) made a thorough review of the proliferation of the distributed watershed hydrologic models. They cited the most popular models, including HEC-HMS (USACE, 2000), SHE (Abbott et al., 1986), TOPMODEL (Beven and Kirkby, 1979), ANSWERS (Beasley and Huggins, 1978), WATFLOOD (Kouwen et al., 1993), CASC2D (Julien et al., 1995), and SWAT (Arnold et al., 1998). An important driving force for the development of distributed hydrologic models has been the innovation of technologies to acquire detailed spatial information of earth surface and the lower bound of the atmosphere.

Satellite imagery, airborne photographs, LIDAR topographic data, and NEXRAD radar rainfall data are mostly influential to environment monitoring and hydrological modeling. Airborne LIDAR (LIght Detection And Ranging) technology has emerged as a cost-effective means for the acquisition of highly accurate topographic data. A LIDAR DEM offers greatly improved vertical and horizontal accuracy compared to the conventional 30m USGS DEM. Current LIDAR technology can provide DEMs at about 1-5 m spatial resolution with a vertical accuracy of better than 15 ~ 25cm. The elevation model is critical to all the hydrological models because of the need for accurate definition of the flow patterns and drainage courses in overland flow simulations (Garbrecht and Martz, 2000). In areas of low-lying and moderate relief, the LIDAR DEMs provides the detailed topographical information required to define the hydrological responses, where the USGS DEMs are inadequate. The improvement of vertical accuracy and horizontal resolution of topographic data will greatly expand our capability in modeling the overland and channel flows. It also renders the capability in extracting and quantifying micro-scale hydrologic features like detention basins.

Next Generation Radar (NEXRAD) is a Doppler radar system which is also know as the Weather Surveillance Radar-1988 Doppler (WSR-88D)) (Crum and Alberty, 1993). This device sends out active radar beams and receives reflected signals of clouds from various elevations. The average density of water particles in the air can be measured as a function of the radar reflectance. The radar system acquires and updates rainfall estimates every six minutes in severe weather conditions. Measurements for precipitation can be acquired at a spatial resolution of 1 km. The maximum detectable

range may extend to 230 kilometers from the radar station. Compared to the traditional gage station records, NEXRAD has many advantages in terms of spatial and temporal resolutions, reliability, and control of data uncertainties. The case study area is covered by the Galveston WSR-88D station, and the continuous NEXRAD data for a number of hurricanes and tropical storm events are available.

Satellite remote sensing technologies provide means to survey large areas efficiently and repeatedly. Multispectral spaceborne satellite images with a frequent repeat cycle and moderate spatial resolution, including Landsat, SPOT, ASTER, and MODIS data, provide fundamental information about land cover and vegetation conditions, which influences the rainfall interception, evapotranspiration, and infiltration (Ragan and Jackson 1980). Airborne Digital Orthographic Quadrangle (DOQ) images and the high resolution IKONOS and QuickBird Satellite images make it possible to accurately quantify the impervious surface and classify urban land uses. The benefits of using the remote sensing imagery in the hydrological models and floodplain mapping have been widely recognized (Mimikou and Baltas, 1996; Moglen and Hartman, 2002; Zhang and Montgomery, 1994; Arnaud et al., 2002; Bjerkelie et al., 2003; Andersen et al., 2002; Lakshmi and Susskind, 2001; and Droogers and Kite, 2002). In short, the recent advance of remote sensing technologies has brought a new era for hydrological models.

However, difficulties and problems associated with modeling spatially enriched information remain, which have not been adequately addressed in the literature. An immediate difficulty associated with high-resolution spatial data is the intensive computation and large memory requirement. For instance, the file size for a 5 m

resolution LIDAR DEM will be 36 times as large as that of a 30 m resolution USGS DEM for the same study area. In the numerical computations of distributed hydrologic models, the scale is indicated by the cell size of basic spatial units (Singh and Woolhiser, 2002). The scale and resolution issue has been addressed by various authors in the hydrological modeling literature (e.g. Braun et al., 1997; Haddeland et al., 2002; Hardy et al., 1999). Zhang and Montgomery (1994) suggest that the runoff process should be simulated using neither the finest resolution nor the coarsest resolution. For their case study, they observe that resolution higher than 10 m would not provide additional advantages to the model simulation. They conclude that in order to correctly model the hydrologic processes, the scale should be smaller than the topographically divergent hill slope length (Zhang and Montgomery 1994). Despite these empirical studies, it remains no clear guidelines for selecting an appropriate scale for the distributed hydrological models. The distributed hydrologic models operate on a raster data structure of constant scale (namely grid cells of same size). Given multi-scale input data, the common practice is to interpolate (resample) all input data into grids with a uniform cell size. If all the input data layers are resampled into grids with the same cell size as the input data layer with the finest resolution (scale), all the spatial information will be preserved but the input data volume will be increased dramatically. This often makes the distributed hydrological model crash because the computation and memory requirements are too high. If all the input data layers are resampled into coarser grids, the distributed hydrological models may be operational but the spatial details in the original input data layers will be lost. A new modeling framework other than lumped and distributed

frameworks is needed to solve the dilemma, namely, achieving high computational efficiency without loss of detailed spatial information.

Retrospective analysis and monitoring of the environment changes using multi-temporal remote sensing imagery have been conducted by many research workers such as Hill et al. (1995) and Gordon (1980). In hydrological modeling, one of the most important parameters is the land use and land cover. Urbanization of watersheds has caused the expansion of man-made structures and impervious surfaces, and removal of vegetation covers. Previously, the effects of land use change and urbanization on hydrological processes have been investigated by numerous researchers (e.g. Cheng and Wang, 2002; Bultot et al., 1990; and Kang et al. 1998). However, detailed studies for Houston metropolitan area have not been conducted. Houston is one of the largest cities in US, and lacks zoning regulations. Although urbanization tends to have adverse effects on flooding, many human activities like construction of detention basins and channelization may have positive effect in mitigating and reducing potential flood damage. Regional and local flood water detention facilities have been widely built to temporally store the flood water for the purpose of attenuating flood water peak elevations. Due to the lack of spatially detailed measurements, little research has been conducted to provide a quantitative assessment for the impacts of environmental changes and human activities on the hydrological processes and flood magnitude.

1.2. Research objectives

The goal of this research is to develop algorithms and a modeling framework for incorporating multi-sensor remote sensing data in a GIS-based hydrological modeling

and evaluate the impacts of natural and human-induced environmental changes on hydrological processes and flooding hazards in low-lying coastal floodplains. The specific objectives of the research are:

1) Compare the simulated hydrograph created by using the traditional USGS DEM and the newly developed LIDAR DEM. Evaluate and quantify the increased model simulation accuracy, reduced uncertainties, and feasibility of the new elevation model;
2) Identify the problems related to assimilating spatial datasets with various spatial details and scales. Develop and implement a model framework and data structure which allows variable scales;
3) Perform retrospective analysis based on multi-temporal remote sensing imagery. Evaluate the impacts of urban expansions on increasing flood hazards.
4) Perform "what-if" scenarios based on current and projected natural and human-induced environmental changes. The scenarios include construction of floodwater detention basins, land subsidence, and climate changes.
5) By comparing retrospective analysis and different scenario, derive planning and policy implications for urban smart growth and for mitigating the flood risk and damage.

1.3. Methodology

1.3.1. Study area

The case area for this research is the highly urbanized White Oak Bayou watershed (Fig. 1.1) in Houston City and Harris County, Texas. The main streams in the case study watershed include White Oak Bayou, Little White Oak Bayou, and Cole Creak. White Oak Bayou adjoins Buffalo Bayou in downtown Houston. The total population in the watershed is estimated to be about 416,000 (HCFCD, 2004). It covers the northwest part of Houston Metropolitan area. Houston is the fourth largest city in the United States and it is currently the only major city in the US without a zoning ordinance. The market forces are free to drive commercial location decisions (McDonald, 1995). Since many residential areas were built prior to the detailed floodplain mapping and regulations, the flood damage caused by tropical storms were devastating. Because of intense rainfalls and clay soils (SCS 1976), Houston is very susceptible to localized flooding (Bedient et al., 2000). According to FEMA (2003), Harris County and Houston are among the top 10 communities with the highest number of repetitive flood losses in the country. White Oak Bayou is one of the watersheds in Harris County receiving the most severe rainfall and associated flooding. In 2001, Tropical Storm Allison caused severe flooding in southeast Texas and southern Louisiana, resulting in 24 fatalities and more than $5 billion in damage, most of which occurred in Houston, Texas (NWS, 2001). This was the costliest tropical storm in U.S. history (HCFCD and FEMA, 2002). In White Oak Bayou watershed, over 11,000 residences were devastated by the tropical storm. Among the 73,000 applicants for residential flood damage assistance received in Harris County,

17 percent are in White Oak Bayou watershed (HCFCD and FEMA 2002). Because of excessive ground-water withdrawal and oil and gas extraction, this region has been experiencing extensive land subsidence (Gallow et al. 1999). Some areas have subsided up to 4.5 feet during the past 25 years.

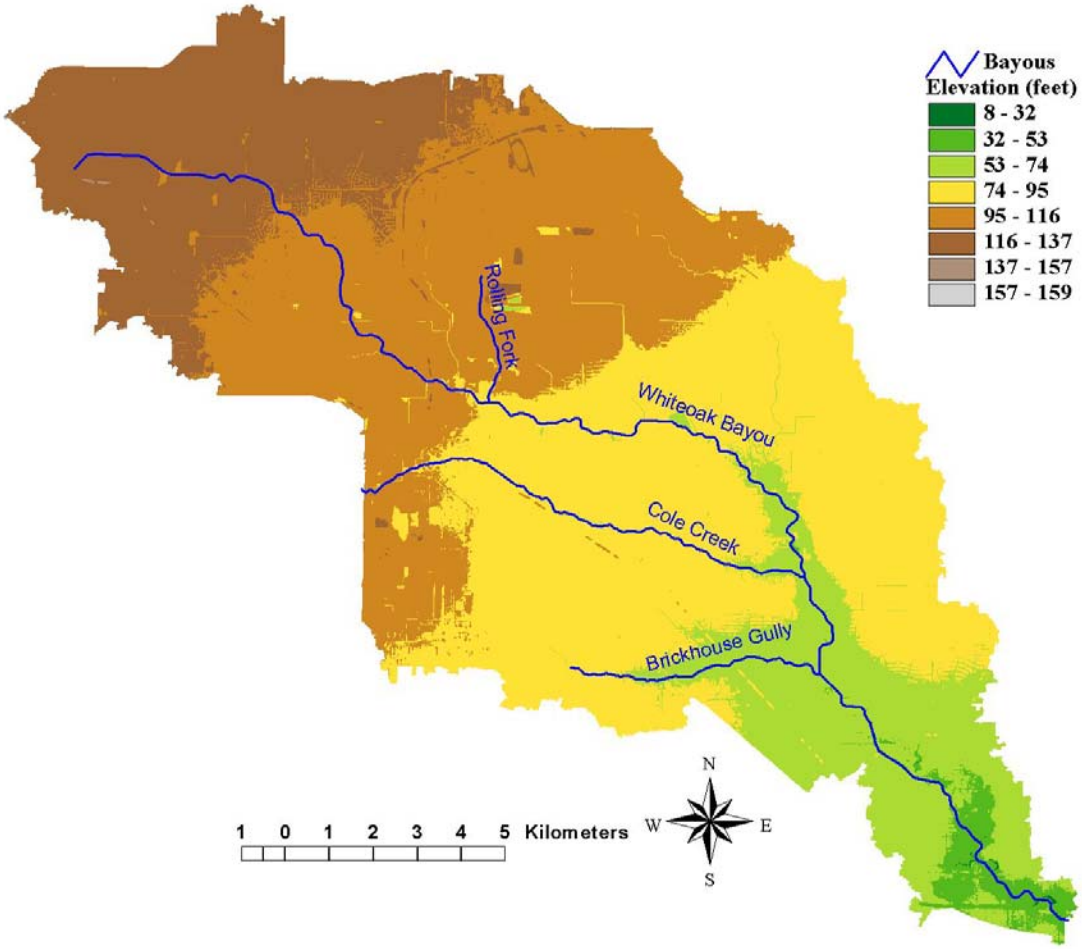

Fig. 1.1 Study area: White Oak Bayou watershed in Harris County, Texas

The White Oak Bayou watershed is chosen as the study area based on following reasons. First, the watershed is ideal for addressing the impacts of natural and human-induced environmental changes on flood hazards. Second, multiple remote sensing data

and ground based observation are available for supporting a detailed hydrologic investigation of flood events. A long history (66 years) of stream gage data, collected by the USGS and the Harris County Office of Emergency Management (HCOEM) stream gaging stations, are available. Particularly, Harris County is one of a few counties in the nation where highly accurate LIDAR data are becoming publicly available. Thirdly, Harris County Flood Control District (HCFCD) has constructed six regional floodwater detention basins along White Oak Bayou, along with numerous smaller basins constructed to offset the impact of new development (HCFCD and FEMA 2002). This provides great opportunities to model human-induced changes and their impacts on flood hazards.

1.3.2 Methodology and data flows

By incorporating spatially detailed topographical and land cover information derived from LIDAR and high-resolution satellite imagery, this research will develop a hydrologic modeling system for the White Oak Bayou watershed. It will allowing for simulating stream discharges, predicting the extent and depth of potential floods, analyzing the possible hydrological responses to the climate change, land subsidence, and assessing the impacts of human-induced changes on the magnitude and frequency of flood hazards.

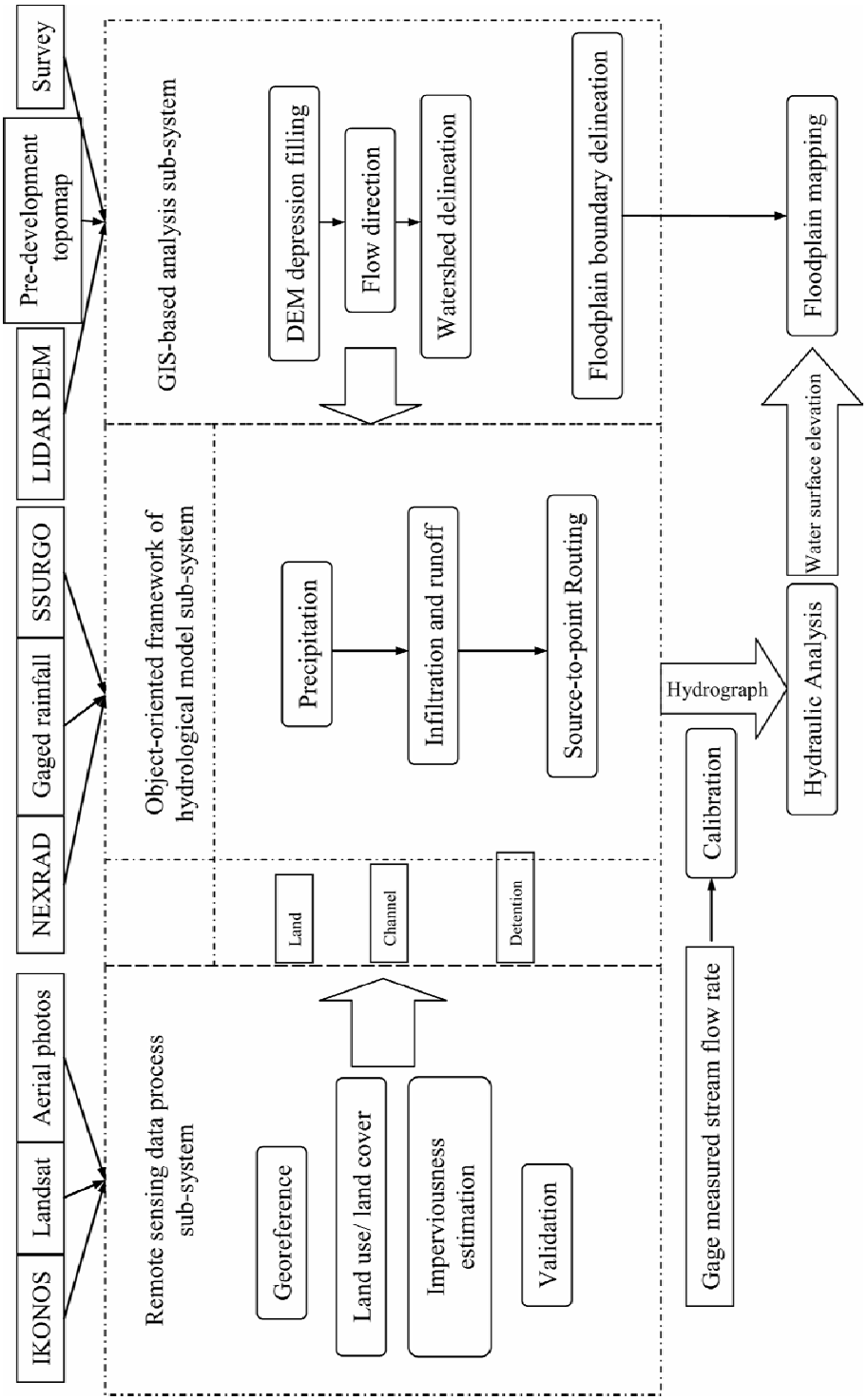

Fig. 1.2 Model framework and data flows

As shown in Fig. 1.2, the hydrological model will incorporate high resolution NEXRAD precipitation data, SSURGO soil data, subpixel estimation of surface imperviousness from Landsat imagery, and LIDAR DEM for stream extraction, watershed delineation, and surface water routing. Infiltration is the major component of rainfall abstraction. Other components such as interception, depression storage, and evapo-transpiration are neglected in the model because they are insignificant for short term flash floods. Infiltration is calculated using the infiltration model proposed by Green and Ampt (1911) and modified by Li et al (1976). Soil information is acquired from Soil Survey Geographic (SSURGO) database. The parameters include soil porosity, hydraulic conductivity, and wet front suction. Subpixel surface imperviousness is derived from Landsat imagery using a spectral mixture model and validated using aerial photos and high resolution IKONOS images. Existence of impervious surfaces prevents water from infiltrating down into soil layers and therefore increases the amount of runoff water. Precipitation is determined NEXRAD measurements with a spatial resolution of 2km at a 15-minute interval. Runoff water is routed overland and in the channels using the approach proposed by Olivera and Maidment (1999). This approach transfers routing problems to linear combination of flow path response functions. Further decomposition of flow paths enables GIS implementation of this computation method. The hydrograph at the outlet can be calculated by adding all the flow responses from upland sources convoluted with the runoff amount. Spatial hydrological units (SHU) are generated by segmenting and combining different data layers including soil, surface imperviousness, and LIDAR DEM. Once SHUs are created, computation of infiltration and water routing

are performed based on them. The upstream and downstream Floodwater detention basins are identified and measured from LIDAR DEM and high resolution remote sensing images. They are incorporate into the model as special SHUs which receive input from upland units. In this way, the capability to attenuate peak discharge can be measured and simulated.

Hydraulic analysis is performed in HEC-RAS software with the support of GIS. Cross-sections surveyed along main channels and floodplain are input to the model and analyzed using the channel discharge hydrograph simulated in the hydrological model. The data is available from the HCFCD (Doan 2000). Using HEC-RAS, flood water elevation of each cross-section can be determined. The results will be calibrated and validated using the high water marks. By interpolating the flood water elevations in the floodplain and comparing to LIDAR DEM, the flood extent and depth can be calculated.

After calibration and validation with stream flow observations, the integrated hydrological/hydraulic modeling system will be used to perform simulation and scenario analysis. The scenarios include climate changes, land subsidence, land use and land cover changes, and human construction activities. By comparing different scenarios, planning and policies implications about urban smart growth, flood hazard mitigation, and flood insurance studies are derived and inferred.

1.4. Significance of this research

1. This research is a case study of implementation of conceptual GIS theories about spatial scale, data model and data structure, and object-oriented approach in a distributed hydrologic model. It provides a solution and guideline to create object-

oriented model through converting raster data models to spatial objects and to perform hydrological simulations with spatial objects. This research is also the evidence of the superiority of object-oriented model over traditional simply lumped models or raster models with constant spatial scale.

2. Increases and demonstrate our capability to model and predict flood hazards in flat, low-lying coastal plains using state-of-the-art remote sensing data in the hydrologic model simulations.
3. Provide a practice to infer planning and decision-making implications for urban smart growth and flood hazards mitigations via retrospective and scenario studies. This will not only benefit the case study area, but also be able to generalized and expanded to other areas.

Information products derived from this research include:

1. A system that integrates GIS, hydrological, hydraulic model, and relevant image processing algorithm and is coded in C++ programming language under the object-oriented framework.
2. Floodplain maps with 5, 20, 50, and 100-year return frequency provided for the study area.
3. An algorithm and tool to quantify regional floodwater detention basin from LIDAR elevation model.
4. A series of programs to derive subpixel level of surface imperviousness from remote sensing images.

1.5. Organization of this dissertation

The entire dissertation consists of seven chapters. After this introduction chapter, Chapter II will present the basis elements of the hydrological modeling theory, including infiltration and runoff water routing. Methods and procedures of acquiring data, selection of parameters, and calibrations are described. Chapter III introduces the object-oriented model hydrological modeling framework. This chapter first compared the LIDAR DEM with the USGS DEM to address the problems with low quality DEM data and the need for high quality DEM for hydrological modeling in low-lying coastal floodplain. To overcome the problems of conventional lumped and distributed models, the object-oriented model framework is introduced and described. Chapter IV presents the method and procedures to delineate detention basins from LIDAR DEM and algorithms to model the detention basins. Chapter V examines the procedures and methods to perform hydraulic analysis and floodplain mapping. In this chapter, I introduced a new method to calculate flood depth and extent based on a GIS. Compared with traditional TIN based methods, this method is able to examine hydraulic connectivity when expanding the flood water elevation into the floodplain. Chapter VI investigates the impacts of human-induced and natural environmental changes on hydrological processes and flood hazards. Chapter VII gives a general summary of all the previous chapters and generalizes conclusions from previous chapters. Inferences for urban growing and polity-making are discussed.

CHAPTER II

HYDROLOGICAL RAINFALL RUNOFF ANALYSIS

2.1. Rainfall modeling using NEXRAD and rain gage data

2.1.1. Overview

Precipitation drives the entire hydrological modeling process. The importance of precipitation to the hydrological modeling has been widely recognized. For example, Ball and Luk (1998) considered the rainfall model as the "generation component" in the entire hydrological modeling system. The accurate representation of spatial variation in rainfall is of great importance for accurate simulation of stream flows. There are four major sources of rainfall measurement: (1) rain gages, (2) radar, (3) remote sensing imagery and (4) synthetic rainfall. The first three sources are from field and remote measurements. Synthetic rain fall is mostly used for design purpose and floodplain management and sometimes to evaluate the reliability of the models, for example, in Ball and Luk (1998).

Traditionally, installation of rain gages has been the most cost-efficient and effective way to record rainfall for easily accessible locations. Depending on the history and development of meteorological studies, different regions may have different types, quality and quantities of gage stations. Automatic stations have been increasingly employed due to the improvement of the instrument and computer-based hardware and software. For example, the Automated Local Evaluation in Real Time (ALERT) was initially set up and operated by the National Weather Service (NWS). It imposes a set of

standards for sensing and transmitting data. The ALERT system has remotely installed sensors and a center computer to collect real time measurements via radio-based telecommunication devices. The ALERT systems have been widely used in many countries because of its low-lost, accurate, reliable, and interchangeable design. The remote sensors are typically tipping bucket devices that send a tipping signal for each 1mm rainfall collected. The center computer listens to these signals, distinguishes the device IDs, and records them. Since the ALERT system design is simple, installation of new sensors is convenient and does not significantly increase the complexity of the system. The Harris County Office of Emergency Management (HCOEM) maintains the ALERT system that has 164 rain gage stations distributed over Harris County of Texas. For the White Oak Bayou study area, there are 46 rain gauge stations, equivalent to approximately 12 square kilometers or 5 square miles per station.

There are some limitations of rain gauge records of precipitation. Most applications rely on spatially interpolating point-based gage measurements to surface precipitation. However, the storm may pass through the gauge network without being correctly described by the gages. Furthermore, the ALERT system has its technical difficulties. For an example, automatic station records may have missing or inconsistent values due to malfunctioning of the sensor or overlapping of signals (DIAD, 2000).

2.1.2. Distributed rainfall measurement from NEXRAD

Radar is the acronym for “radio detection and ranging”. NEXRAD which stands for “next generation radar” is technically called as WSR-88D or weather surveillance radar prototyped in 1988 (Bedient and Hubber, 2002). It is a Doppler radar using S-band (10

cm wavelength). Doppler radar can detect the velocity of the objects that are moving towards to or away from the radar device due to the Doppler Effect. The movement of tropical storms, strong winds, or the tornados can be measured using Doppler radars. Rainfall intensity can be measured through the magnitude of reflected radar signals. The relationship between the rainfall intensity and the radar reflectivity can be approximated using the Z-R equation (Fulton et al., 1998):

$$Z = aR^b \tag{2.1}$$

where Z is the radar reflectivity; R is the rainfall rate; a and b are estimated parameters which are designed to be adjustable for local conditions (Fulton et al., 1998). The Z-R relationship is estimated from the physical drop size distribution (DSD). Experiments may result in different a and b values. The most recognized equations are the standard equation adopted by the National Weather Service (NWS):

$$Z = 300R^{1.4} \tag{2.2}$$

and the tropical equation:

$$Z = 250R^{1.2} \tag{2.3}$$

The tropical equation creates better results for warm rain processes, as found by Vieux and Bedient (1998). While the equations directly produce the rainfall rate, as shown by Smith et al. (1996), many difficulties and biases are related to the estimation of rainfall from radar. The gauge-radar adjustment or so called radar to gauge calibration is always necessary for each study area. An adjustment methodology has been developed by Wilson and Brandes (1979) which removes the Mean Field Bias (MFB) from the radar estimations. The general adjustment procedure can be described as:

(1) Quality checking of the rain gage measurements

(2) Estimating multiplicative factor F

(3) Applying the multiplicative factor to each radar cell

The NEXRAD data used in this research was processed by the OneRain Company located in Colorado. They employed the procedures described above to generate a calibrated rainfall rate from radar measurement for Tropic Storm Allison at a sample rate of 15min and grid spacing of 1km. Although this data is readily available, rain gage data is still useful for researchers, not only because that the radar system may not exist in some circumstances, but also because in some areas the rain gages are so densely distributed that they provide better or equivalent measurement of rainfalls than radar. Especially for extreme rainfall events like the Tropical Storm Allison, radar tends to underestimate the rainfall due to the "reflectivity cap" effect (Hoblit et al., 2002). For such events, without rain gage data, the real time monitoring system using radar data may not work as well as expected. In these circumstances, the real time flood monitoring system built on the dense rain gage network (for example, ALERT) may be preferred.

2.1.3. Cross-validation of the NEXRAD data with the rain gage measurements

The NEXRAD data from OneRain is provided in a cell based format covering the entire Harris County for the event of Tropical Storm Allison. Each cell has its ID and geo-registered in an ArcGIS Shape file. Each cell can be linked to a table that records the precipitation rate at any specific 15min interval during the storm in inch/hr. To ensure the data quality, a gage-radar-pair comparison was undertaken. There are a total of 46 gage stations in the study area (a bounding rectangle of about 600 square kilometers). 10

stations were selected to construct gage-radar pairs. The correlation coefficient of the radar and gage pair at each station is listed in table 2.1. The overall agreement of these two datasets is very high. Fig. 2.1 illustrates the scatter plots of four selected stations. Linear regression analysis was also performed on these radar-gage pairs. Most of the regressions have slopes less than one. This can also be observed from the four sample

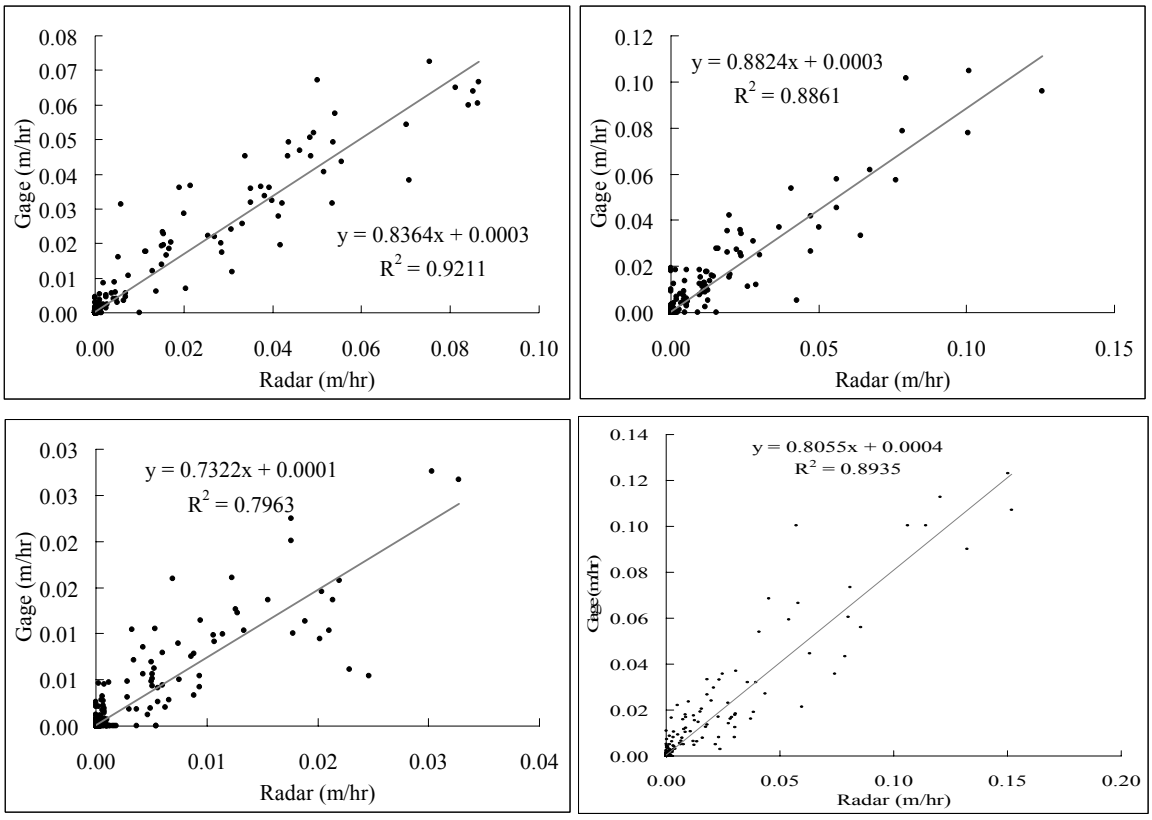

Fig. 2.1 Scatter-plot of selected four radar-gage pairs

stations in Fig. 2.1. This might be because of the "reflectivity cap" effect mentioned previously. The existence of reflectivity cap causes radar to underestimate rainfall intensity. This validation procedure is one of the important steps to ensure the

correctness of input data. It also suggested that at circumstances when one of the sources is not available, the other one can be alternative.

Table 2.1

Correlation coefficients of radar-gage pairs

Gage ID	Gage Name	Correlation Coefficient
1660	P100 Greens Bayou @ Knobcrest	0.868
1690	P118 Halls Bayou @ Airline	0.960
2120	U100 Langham Creek @ W. Little Yo	0.869
0545	E100 White Oak Bayou @ Fairbanks	0.945
0560	E101 Little White Oak Bayou @ Tri	0.716
3610	IH 45 @ N Main	0.945
2270	W100 Buffalo Bayou @ West Belt	0.892
2110	Addicks Dam	0.920
0575	E100 White Oak Bayou @ Tidwell	0.941
1000	Houston Transtar	0.836

2.2. Rainfall infiltration modeling

2.2.1. Overview

Infiltration is the process surface water diffuses into soil layers. It is considered as the most important loss factors of precipitation. Other loss factors may include interception, evaportranspiration, depression storage, and channel bed loss. For short-term flash floods applications, the other factors are insignificant compared to the infiltration loss. The infiltration capacity of the soil is related to soil physical and chemical properties and

the initial soil moisture condition. Urban sprawl leads to concrete or asphalt surfaces that are impermeable to water, such as pavement, parking lots, buildings and foundations. In many cases, the simple infiltration model called an initial-constant rate model introduced by Goldman (1988) works well enough. This model assumes the land surface has some initial capacity due to the depression storages (water detained by micro topographic features). When the precipitation exceeds the depression storage, a constant loss rate is estimated and compared to the precipitation rate to obtain a runoff value. It is most applicable to studies at large spatial and temporal scales where the infiltration rate can be approximated as constant. However, since it does not address the spatial and temporal variations of the infiltration process, this method is not appropriate when the spatial structure of soil and land use information are important. Another widely used approach is the Soil Conservation Service (SCS) Curve Number method (SCS, 1986). This method calculates the precipitation loss as a function of soil curve number and initial soil moisture conditions. The SCS report on TR-55 Urban Hydrology for Small Watersheds (SCS, 1986) provides a look-up table for estimating CN of different land use/cover types and soil textures. This method is able to describe spatial variability in soil and land use. Another advantage of this method is that the calibration is easier than other physical models because there is only one parameter to be calibrated. However, a lack of direct, physical interpretation of the parameters hinders it from modeling variability through time. For storm-related precipitation events, because the temporal change of the rainfall is fast, this method may not be applicable.

2.2.2. Green-Ampt model description

Darcy's law states that the flow rate through porous media is proportional to the head loss and the inverse of the flow path length. The Richard's equation that governs the flow in the media can be written as:

$$\frac{\partial \theta}{\partial t} = -\frac{\partial}{\partial F}\left[k(\theta)\frac{\partial \psi(\theta)}{\partial F}\right] - \frac{\partial k(\theta)}{\partial F} \tag{2.4}$$

where θ = volumetric water content, F = depth (m), ψ(θ) = capillary suction at the front (m) of water, and k(θ) is the unsaturated hydraulic conductivity (m/s). The volumetric water content is the ratio of the content water volume to the total volume of the porous media. Green and Ampt (1911) solved this equation by relating the Darcy velocity (depth / time) to the unsaturated conductivity K(θ) and the depth below surface. An original form of Green-Ampt equation can be written as:

$$f = K_s(1 - \theta_d \psi / F) \tag{2.5}$$

where K_s is the saturated conductivity, θ_d is the difference of moisture content from initial status to saturated status, f is the infiltration rate, and F is the depth below the surface. From the equation, we can see that the infiltration flow rate is positively related to the saturated conductivity, the moisture content difference, and the suction at the wet front of the soil, and is inversely related to the depth of the water front. Laboratory experiments show that the normal range of the production of θ_d and ψ is from -0.13m to -0.01m. When the infiltration depth is above 10m, the ratio of $\theta_d \cdot \psi$ to F is very small and even negligible. Therefore the infiltration rate is almost linearly related to the saturated

conductivity. This indicates that the model is very likely to be influenced by saturated conductivity as the infiltration depth reaches a certain level.

Before surface ponding occurs, the infiltration rate is equal to the amount of in-flow water. But when the infiltration capacity becomes less than the rainfall intensity, the infiltration depth is governed by the Green-Ampt model (Bedient and Huble, 2002). Within the time increment of interest, we have:

$$\int_{t_0}^{t_0+\Delta t} K_s dt = \int_{t_0}^{t_0+\Delta t} \frac{F(t) f(t)}{F(t) - \psi\theta_d} dt \tag{2.6}$$

and because

$$\int f(t)dt = F(t) \tag{2.7}$$

we obtain

$$\int_{t_0}^{t_0+\Delta t} K_s dt = \int_{F_0}^{F_0+\Delta F} \frac{F(t)}{F(t) - \psi\theta_d} dF \tag{2.8}$$

By solving the integrals and take the finite difference format of the equation, we have

$$F(t) - F(t-\Delta t) = -\xi \ln(\frac{F(t)+\xi}{F(t-\Delta t)+\xi}) - K_s \Delta t \tag{2.9}$$

where $\xi = \theta_d \cdot \psi$.

This equation can be solved by the Newton's bisector or secant method.

Li et al (1976) proposed a two step method to obtain the ΔF directly. The first step is to calculate the initial estimation of infiltration depth in the increment time Δt, which can be written as

$$\Delta F_0 = \frac{1}{2}\left[K_s \Delta t - 2F + \sqrt{K_s \Lambda t (K_s \Delta t + 4F + 8\xi) + 4F^2}\right] \tag{2.10}$$

And then, the ΔF can be calculated by the following equation

$$\Delta F = -F - \frac{(F+\Delta F_0)^2}{\xi} + \frac{F+\xi+\Delta F_0}{\xi}\sqrt{(F+\Delta F_0)^2 + 2\xi(\xi\ln(1+\frac{\Delta F_0}{F+\xi}) + K_s\Delta t - \Delta F_0)} \quad (2.11)$$

This approximation causes less than 0.03% error (Li et al., 1976).

2.2.3. Data input and parameter estimation

2.2.3.1. Estimating imperviousness

Imperviousness is estimated from Landsat TM and ETM+ images. Impervious surfaces mainly refer to those in developed areas, such as parking lots, roofs of buildings, sidewalks, and roads. The spectral signature or reflectivity are used to differentiate them from the permeable surfaces such as grassland, forest areas, bare soils, sands, water, and so on. To approach the imperviousness estimation, a conceptual vegetation-impervious surface-soil (VIS) model was proposed by Ridd (1995). This model provides a solid framework for the remote sensing of urban development studies. However, because of difficulties in accurately acquiring the VIS distribution, only few successful applications are found in the literature (Wu and Murray, 2003). Before this, methods used for imperviousness estimation can be literately divided into two groups: physically-based models and empirical models. The physical models employ the spectral mixing approaches, such as Ji and Jensen (1999), Ward et al. (2000), and Wu and Murray (2003). Wu and Murray (2003) applied the Spectral Mixture Analysis (SMA) method to estimate the imperviousness using Landsat 7 data. They achieved an RMS error of 10.6% for the sample data. They also noticed that impervious estimation would be adversely affected

by high and low albedo features. However, even though they made efforts to mask those influential materials such as sand and water, the effect of the sand still remains the main cause of the outliers (Wu and Murray, 2003). Other approaches include the Artificial Neural Network method (Wang et al., 2000), Classification Tree (Smith and Goetz, 2000), and Regression Tree method (Yang et al., 2003). Yang et al. tested the regression tree method at various sites. The results are comparable to the method used by Wu and Murray (2003) and this method is consistent and "cost-effective and suitable for large-area imperviousness mapping" (Yang et al., 2003). Regression tree is an ideal tool to deal with non-linear problems through constructing a binary tree. The regression can be written as (Tamminen et al., 1999):

$$y_i = f(x_i, \theta) + \varepsilon_i \tag{2.12}$$

where i = 1,..,n and $\theta = (\theta_1 \ldots \theta_k)$ is the vector of parameter to be estimated, ε is the error term. For any node t, the averaged deviation is summed to (Tamminen et al. 1999):

$$r(t) = \frac{1}{N}\sum_i (y_i - \bar{y}(t))^2 \tag{2.13}$$

The construction of the regression tree is to iteratively find the minimized R(T) which is the sum of all the nodes. Each node on this regression is a decision rule and the tree can be easily visualized. This is one of the advantages of the regression tree method because it helps to understand the process and the divisions of the variables. Although the Artificial Neural Network method may generate better results, the regression tree method is still valuable because it is intuitive, visual and easy-to-use (Tamminen et al.,

1999). Chapter VI will detail the methods and procedures in compiling the surface imperviousness.

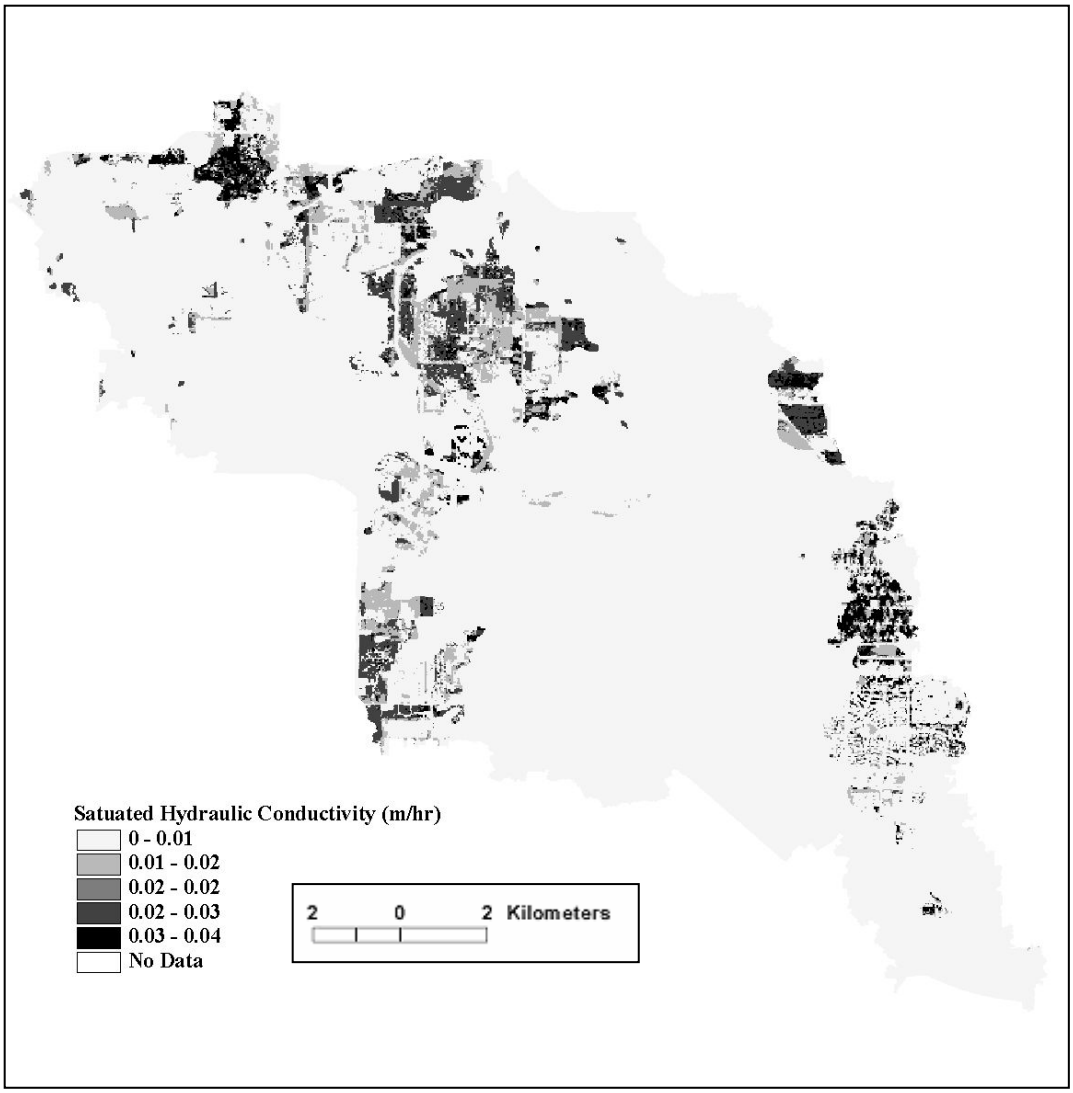

Fig. 2.2 Distribution of saturated hydraulic conductivity extracted from SSURGO

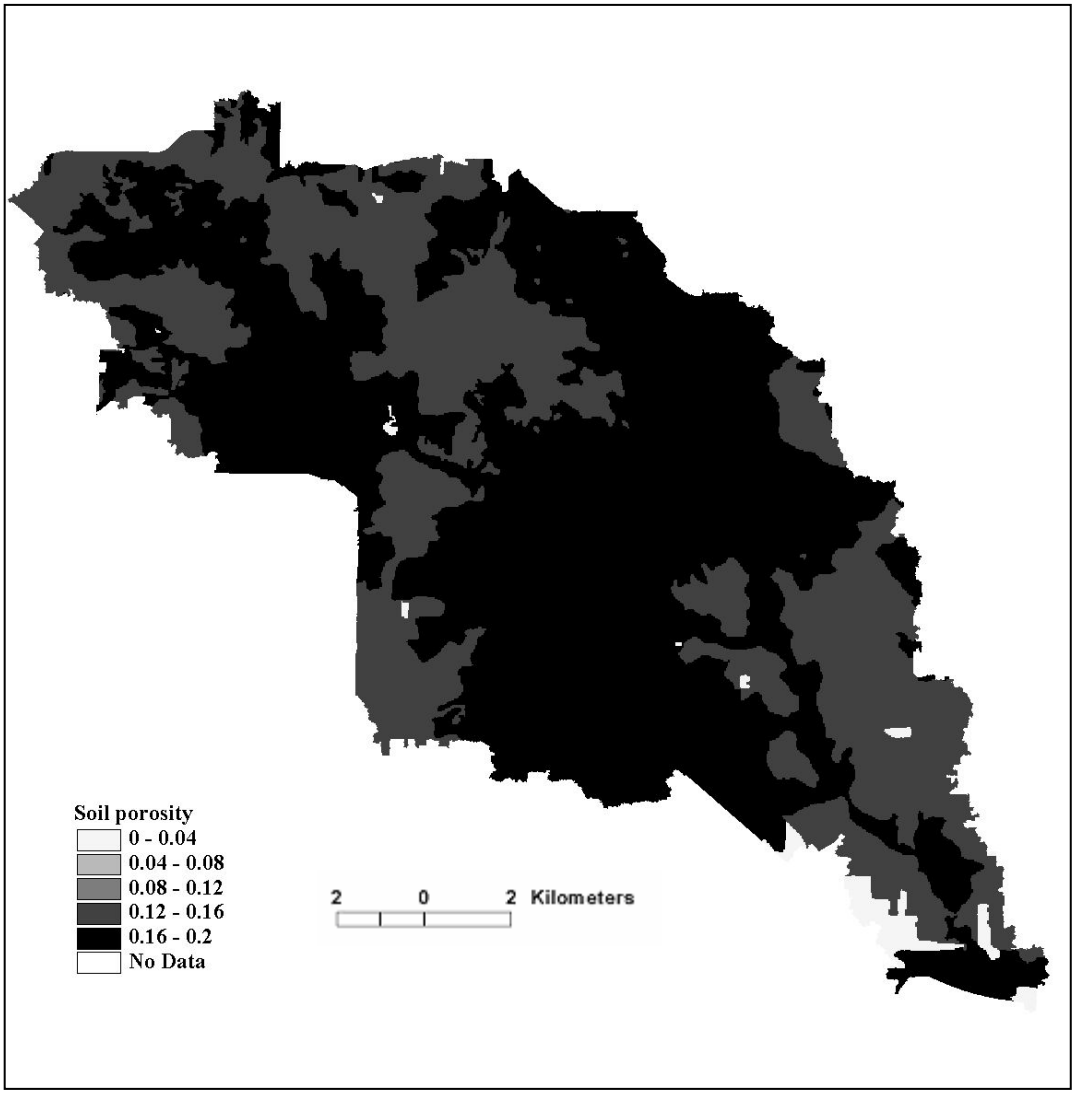

Fig. 2.3 Distribution of soil porosity (blank areas are ponds) extracted from SSURGO

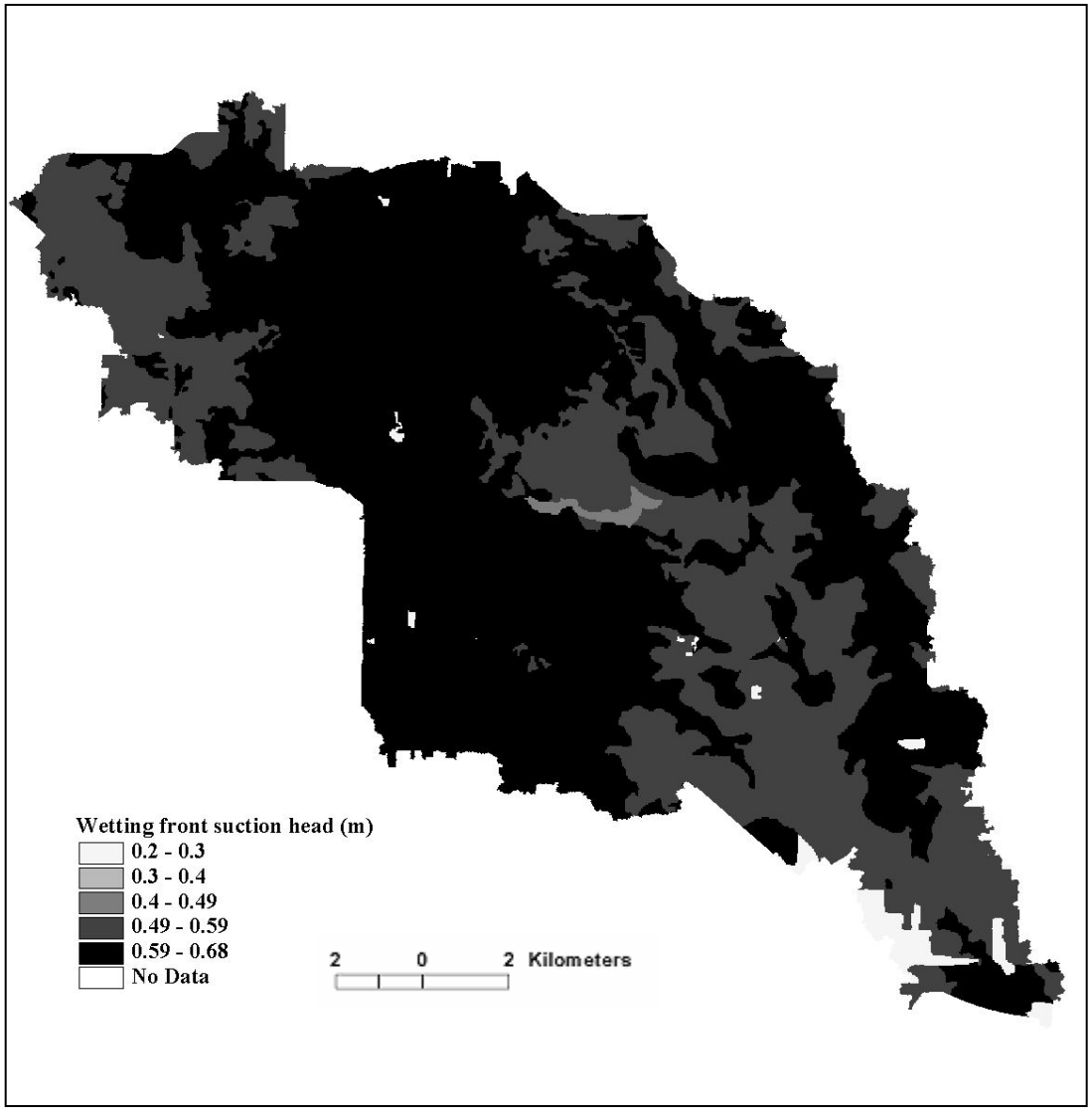

Fig. 2.4 Distribution of wetting front suction head values extracted from SSURGO

2.2.3.2. Green-Ampt model parameters estimated from the SSURGO data

As discussed before, there are three parameters used in the Green-Ampt equations. They are the porosity parameter θ_d, Saturated Hydraulic Conductivity K_s (cm/hr), and the wetting front suction head ψ (cm). For consistency, the units of these parameters have been converted into meters. So K_s will be measured as meters per hour and ψ will be measured as meters. The Soil Survey Geographic (SSURGO) dataset developed by the United States Department of Agriculture (USDA) provides detailed soil data for the entire states. The typical scale of this dataset is 1:24,000 which satisfies most of the applications. The spatial distribution of K_s, ψ, and θ_d is shown in Figs. 2.2, 2.3, and 2.4. The literature shows that the saturated hydraulic conductivity K_s has to be adjusted to the effective hydraulic conductivity because according to Bouwer (1969), the effective hydraulic conductivity parameter for the Green-Ampt model is about half of the saturated hydraulic conductivity of the soil. An empirical equation to estimate the effective hydraulic conductivity was introduced by Nearing et al. (1996) which also takes into account the curve number (CN). This equation related the land use and land cover information to the effective hydraulic conductivity. This equation is written as:

$$K_{eff} = \frac{56.82 \times K_{sat}^{0.286}}{1 + 0.051 e^{0.062 CN}} - 2 \qquad (2.14)$$

The curve number is obtained from the SCS Curve Number look-up table (SCS 1986). For the directly retrieved K_s values, equation (1.17) is applied using the curve number estimated from remote sensing data and the lookup table.

2.2.4. Infiltration Model Calibration

Table 2.2

Discharge and rainfall for the two rainfall events during June 4 to 10, 2001

	June 4 - June 6	June 6 - June 10
Rainfall (cubic m)	21151.35	77794.89
Runoff (cubic m)	9896	47443
Ratio	0.468	0.6098

To calibrate the simulated runoff to the measured total discharge volume at the outlet, two parameters need to be adjusted: the saturated hydraulic conductivity and the initial moisture content. Soil moisture is the water content in a volume of soil. It has an important role in modeling infiltration. Water is absorbed by soil much more efficiently before soil is saturated. As such, for moderate rainfall, initial soil moisture content is more important relative to severe precipitation events. In this study, a continuous simulation is performed starting from June 4 to Jun 10 of 2001. However, we can see in table 2.2 and Fig. 2.5 that there are clearly two separate rainfall events during the period of modeling, one was from June 5 to June 6, and the other started at June 8 and ended at June 9. The soil moisture is initialized for the first precipitation event from June 4 to June 6. The decay of soil moisture due to evaporation or ground water recharge is not counted because there is not enough information to model it. The initial soil moisture is not investigated but set with an arbitrary estimation: 10%, 15%, 20%, 25%, etc. Spatial variation is also not included in the model. The results are shown in table 2.3. It can be seen that the soil moisture of 10% produces the best approximation to measured runoff,

(with only a 1.5% difference). To validate the results, the two rainfall events are summarized separately. As can be seen in table 2.3, both events are within 10% error range. Therefore, the calibration is successful. The determined parameter values are 10% for initial soil moisture and the effective saturated hydraulic conductivity calculated from last section.

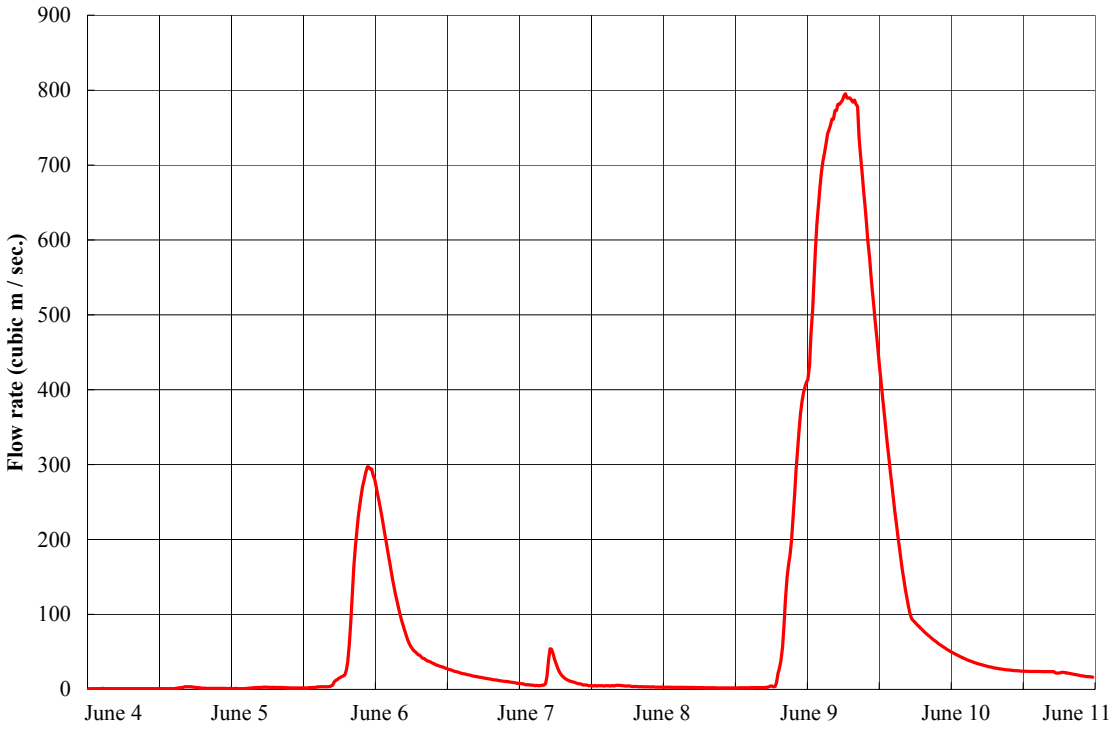

Fig. 2.5 Measured discharges at the outlet for Tropical Storm Allison (June 4 to 10, 2001)

Table 2.3

Sensitivity analysis of initial soil moisture content

Initial Soil Moisture	Total Runoff (cubic m)	Event 1	Event 2	Error (%)
5%	54790	8031	46759	4.4
10%	58011	8598	49413	1.2
15%	70104	11419	58685	22.2

2.3. Watershed terrain modeling using high resolution LIDAR data

2.3.1. Introduction

Topography is of fundamental importance to the analysis of the hydrologic behavior of a stream system. In recent decades, Digital Elevation Models (DEMs) have been widely used in the automated hydrologic analysis of surface topography (Moore et al., 1993; Band, 1999; Garbrecht and Martz, 2000). A DEM is a digital representation of a continuous terrain surface and consists of a two-dimensional array of elevations at regularly spaced ground positions. A variety of hydrologic parameters can be efficiently derived from the raster (grid) based DEMs, such as surface slope, aspect (Srinivasan and Engel, 1991), surface curvature (Moore et al., 1991), and terrain wetness index (Chirico et al., 2003). DEMs can be also utilized to extract flow direction, upslope contributing areas, drainage divides, channel networks, and the hierarchical structure of nested catchments (Band, 1986; 1999). These are the primary inputs to surface hydrologic models. The hydrologic models can be used for various purposes, such as predicting stream discharges, estimating flood extent and timing, locating areas contributing

pollutants to a stream, and simulating the effects of altering the landscape on surface water runoff.

Distributed hydrologic models have become increasingly common and convenient for environmental studies. This is very much due to the availability of spatially detailed information and the support of GIS and remote sensing. Most of the distributed hydrologic models are scale dependent and data driven. In other words, the selection of the scale that the model works on is determined by the quality and spatial resolution of the data. The Digital Elevation Model (DEM) is one of the most active components of the model, not only because that the terrain variation is much higher than other environmental variables, but also that the base flow pattern is digitally defined by the DEM. The vertical accuracy and horizontal spacing have large impacts on the estimation of hydrologic parameters. In the United States, the most commonly used topographical data in hydrological analysis are the 30 m Level-1 Digital Elevation Models (DEMs) produced by the United States Geologic Survey (USGS) using photogrammetric techniques (Garbrecht and Martz, 2000). This DEM is generally applicable for environmental studies at moderate or macro scales. However, if the study area is small and the terrain is low-lying and relatively flat, the accuracy of the DEM may not satisfy the requirement to depict subtle topographic variations. In many areas, DEMs with much better vertical accuracy (less than 15 cm) and higher spatial resolution (typically 5 m) provided by the LIDAR technique are available.

2.3.2. Difficulties and problems with previous approaches

A depression is also known as a sink or pit. It is a local minimum that does not have

downslope flow path to any adjacent cells in a DEM. A surface depression may consist of one or a group spatially connected cells of the same elevation that are completely surrounded by other cells at a higher elevation. It acts as a sink to the surrounding overland flow, in which water drains towards the depression bottom located within the interior basin, rather than towards the basin perimeter as usually occurs. Closed depressions can be complex features that might contain flat areas and other smaller nested depressions. Several methods have been proposed to treat surface depressions in the literature (e.g. Mark, 1983; O'Callaghan and Mark, 1984; Band, 1986; Hutchinson 1988, 1989; Jenson and Domingue, 1988). Some methods apply preprocessing corrective operations to the entire DEM grid to reduce or eliminate depressions prior to hydrologic analysis, while others only apply corrective operations to surface depressions in a hydrologically meaningful way without changing the non-problematic parts of the DEM. A number of commonly used GIS software packages incorporate and implement the algorithm developed by Jenson and Domingue (1988), which is considered to be fast and effective for most cases. However, since the computation complexity of this method is in $\boldsymbol{O}(N^2)$ (the consumed computation time is proportional to N^2, N is the number of pixels in a DEM) (Planchon and Darboux, 2001), this method is very time consuming when processing large data volumes. For example, the implemented function in ArcInfo GIS software requires nearly 17 hours to remove the depressions in a DEM with 8000 by 8000 pixels (tested on a desktop computer with Intel® Pentium 3 797 MHz CPU and 256 MB memory). Planchon and Darboux (2001) developed a method which is in $O(N^{1.2})$, where, iterative scans of the whole DEM data with eight alternating directions.

However, as a trade-off it adversely influences the accuracy of the original algorithm. In addition, the running time of Planchon and Dardoux method (2001) is influenced by the terrain orientation relative to the order of eight alternating scans as well as the number and size of depressions in DEMs. As this algorithm is designed for analyzing depression storage capacity of the soil, no attempt is made to determine the flow directions for the cells in depressions for hydrologic applications. I developed a fast depression-filling algorithm with the computation time complexity in *O(NlogN)* which proved to perform much faster than previous methods.

2.3.3. A fast innovative depression-filling algorithm

The spill elevation is computed according to two equations:

$$S(c_0) = E(c_0) \tag{2.15}$$

$$S(c_i) = \max\{E(c_i), S(c_{i-1})\} \;\; i = 1,2,...,m \tag{2.16}$$

where $S(c_i)$ is the spill elevation of the cell c_i, and $E(c_i)$ is the original elevation value of the cell c_i. The path is defined by a series of spill elevation values $S(c_0)$, $S(c_1)$,…, $S(c_i)$ and is guaranteed to be monotonically increasing. The combination of Equation (1) and Equation (2), we get:

$$S(c_i) = \max\{E(c_0), E(c_1), \ldots, E(c_{i-1}), E(c_i)\} \tag{2.17}$$

According to Equation (3), the spill elevation $S(c_i)$ of an interior cell c_i can be interpreted as the highest elevation of all cells located in the downstream path to the outlet. It is

clear that the progressively propagation of spill elevation handles the depressions much more efficient than conventional methods. It does not involve the iterative filling process as in Marks et al. (1984) and O'Callaghan and Mark (1984) or the merging of looped depressions as in Jenson and Domingue (1988). It employs the least cost search algorithm (Hart, 1968; Dechter and Pearl, 1988) and priority queue data structure (Corman et al., 1996) to accomplish the method for identifying the correct search direction and establishing a flow path for each grid cell in a DEM. Starting with the outlets on the boundary, the algorithm progressively links these outlets to interior cells using an upstream search strategy. A path from an outlet to a specific interior cell is comprised of a sequence of grid cells in which each successive cell is adjacent (connected) to its predecessor. The optimal path is the one that result in the lowest (least) spill elevation value for the cell c_i among all candidate paths. It is referred as lowest spill elevation path. With the lowest spill elevation path, the interior cell c_i only needs to be raised to the smallest possible elevation that allows water to spill out to an outlet. The optimal path is also the least-cost path in the sense that the cost for surface water to fill up the depressions is minimal. This optimal path can be found using a search strategy called least cost search. The least cost search is also known as the best-first search or priority-first search in the field of artificial intelligence and computer science (Corman et al., 1996, Sedgewick, 2002). The general philosophy of the algorithm is to use the heuristic information to assess the cost latent in all candidate search directions exposed during the search process. Instead of using a blind try and error approach, the algorithm gives the first priority to the direction with the least cost for further search and expansion

(Dechter and Pearl, 1988). The time complexity *is O(NLogN)* (Wang and Liu, 2006) and is a significantly improvement over previous methods. A test was performed using the same dataset with 8000 by 8000 pixels on a desktop computer with a 797 MHz Intel Pentium III processor and 256MB of RAM. My algorithm took 8 minutes whilst the traditional method spends nearly 17 hours. On average, my algorithm outperformed the traditional method by over 30 times. The flow direction is also calculated during the optimal path expansion. For cells whose spill elevation values are larger than their original elevations, their flow directions are assigned by reversing the optimal path expansion directions. For other cells, their flow directions are determined by computing steepest descent direction during the optimal path expansion. The flow direction matrix produced by our method is comparable to that of Liang and Mackay (2000).

2.4. A distributed runoff water routing model based on GIS

2.4.1. Introduction

This concept and model was proposed by Olivera and Maidment (1999), as illustrated in Fig. 2.6. If a watershed is partitioned into a limit number of sub-units or elements, the discharge at the watershed outlet can be calculated as the summation of all the elements:

$$Q(t) = \sum_i Q_j(t) \tag{2.18}$$

where t = time; Q(t) = hydrograph at the outlet; $Q_i(t)$ = contribution from element i at time t. The $Q_i(t)$ can be calculated as the convolution of the rainfall excess and the response function of an instantaneous unit input. It is presented as:

$$Q_i(t) = A_i R_i(t) * u_i(t) \tag{2.19}$$

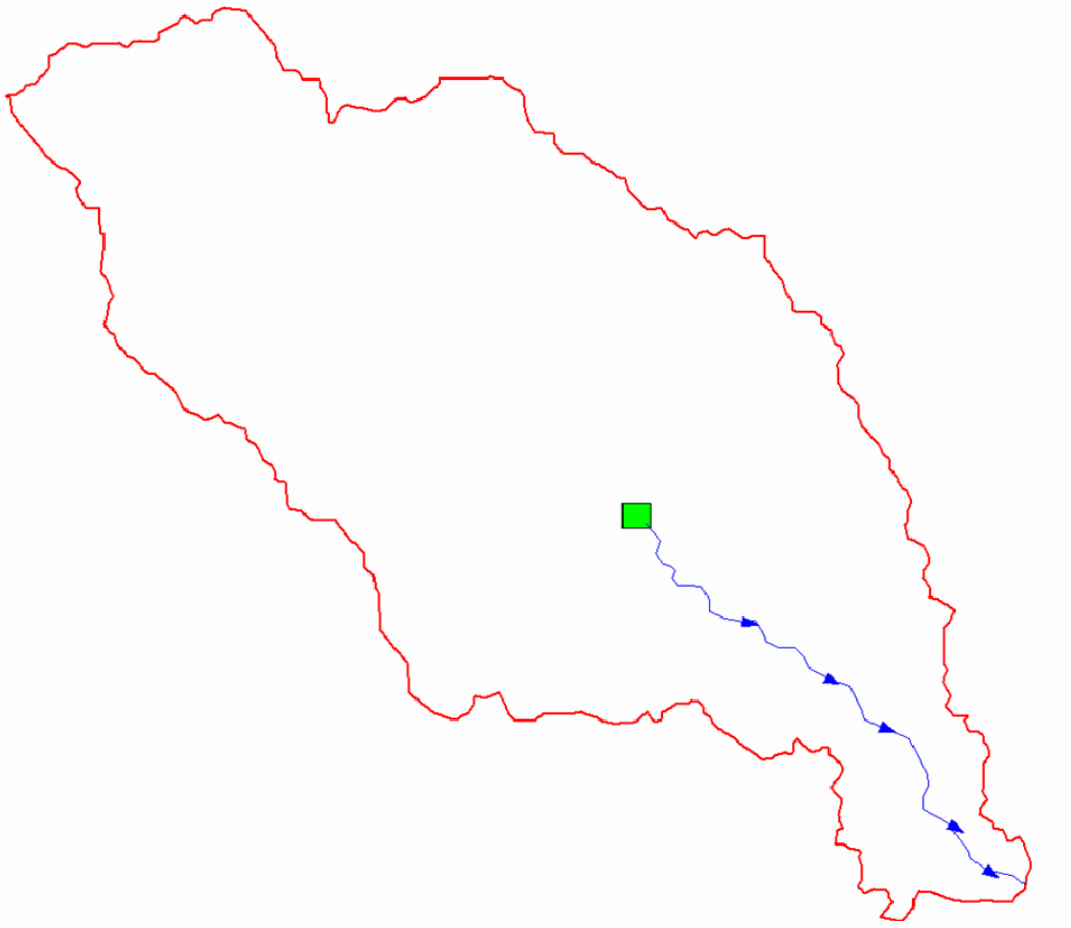

Fig. 2.6 Flow path from a location to the outlet

where A = area; R = rainfall excess; u(t) = the response function; i represents the ith element of the watershed. The $u_i(t)$ is also called the probability density function (PDF) which represents the distribution or of the time a water particle spends in the flow path from element i to the outlet. A one-dimensional diffusion flow is governed by the St. Venant equation with neglecting the inertial component. The equation can be written in the form:

$$\frac{\partial q(x,t)}{\partial t} + c\frac{\partial q(x,t)}{\partial x} - D\frac{\partial^2 q(x,t)}{\partial x^2} = 0 \tag{2.20}$$

c = the velocity of the wave head; D = the hydrodynamic dispersion coefficient.

By assuming a transmitting upstream condition and absorbing downstream condition, the solution of an instantaneous input to the first-passage-time of the system can be written as (Olivera and Koka, 2004; Nauman 1981):

$$q = \frac{1}{2t\sqrt{\pi(t/t_0)/P}}\exp\left\{-\frac{[1-(t/t_0)]^2}{4(t/t_0)/P}\right\} \tag{2.21}$$

where $t_0 = l/c$; $P = c \cdot l/D$ = Peclet number; l = distance of the system

The entire flow path can be approximated as a first-passage-time distribution owing to the central limit theorem (Olivera and Koka, 2004):

$$u(t) = \frac{1}{2t\sqrt{\pi(t/T)/\Pi}}\exp\left\{-\frac{[1-(t/T)^2}{4(t/T)/\Pi}\right\} \tag{2.22}$$

where T and Π can be calculated as (Olivera and Koka, 2004):

$$T = \sum_{i=1}^{n}\frac{l_k}{c_k} \tag{2.23}$$

$$\Pi = \frac{T^2}{\sum_{k=1}^{n}\frac{D_k l_k}{c_k^3}} \tag{2.24}$$

The flow velocity c and dispersion coefficient D can be estimated by applying the Manning's equation (Liu et al., 2003). The watershed response function is the summation of the responses in all the flow paths. To obtain discharge amount at the

outlet at the time t, we only need to sum all the watershed response function $U_i(t)$ at time t (i represents the ith element).

2.4.2. Model parameter estimation

In order to obtain the water response functions, we need to know the kinematic wave celerity c and the dispersion coefficient D values. For spatially varying parameters, *c* and *D* can be determined upon the local physical properties following the approach of Liu et al. (2003). According to Bedient and Huber (2002), *c* and *D* can be calculated respectively as

$$c = \frac{5}{3}v \tag{2.25}$$

$$D = \frac{vR}{2S} \tag{2.26}$$

where v = average velocity; R = hydraulic radius which is equal to depth; S = the bed slope. The average velocity in the open channel can be estimated using Manning's equation:

$$v = \frac{R^{\frac{2}{3}}\sqrt{S}}{n} \tag{2.27}$$

where n = roughness coefficient (Manning's n). The roughness coefficient can be obtained from the literature for different land use types (Liu et al., 2003). Combining (2.25), (2.26), and (2.27), we obtain all the parameters but one unknown R, the hydraulic radius. Reviewing the assumption of the watershed response function, the water travels though an element at a velocity that does not change with time. So the hydraulic radius R

is time invariant and only determined before the model starts running. This makes possible for R to be estimated. Liu et al. (2003) adopted the method develop by (Molnar and Ramirez, 1998) which relates the hydraulic radius to the upstream area of each cell as:

$$R = aA^b \tag{2.28}$$

where A is the drainage area at each location which can be easily obtained from the DEM using current GIS functions, *a* and *b* are coefficient that determined by the stream network and discharge frequency. By controlling the minimum and maximum hydraulic radius, for example, 0.005m for minimum value on the land surface and 1m for maximum value at the channel outlet, *a* and *b* can be determined (Liu et al.,2003). Although the estimation of *R* depends on the arbitrary selection of the minimum and maximum values, the advantage is obvious. This process makes the calibration much easier because only two numbers are to be adjusted.

2.4.3. Sensitivity analysis of the routing parameters

The first-passage-time distribution function (2.22) has two parameters, one is the mean travel time T and the other is the flow path Peclet number (II), as we can see in Fig. 2.7. The mean travel time of water particles is assumed to be 100s in this case. With a very small Peclet number, the response is an immediate peak flow with an elongated tail. When the Peclet number increases, the shape of the distribution function screws towards the center and becomes closer to a normal distribution centering at t = 100s. But when the Peclet number becomes too large, the response function will be an instant response at time T. This is because the variation of the travel time is close to 0.

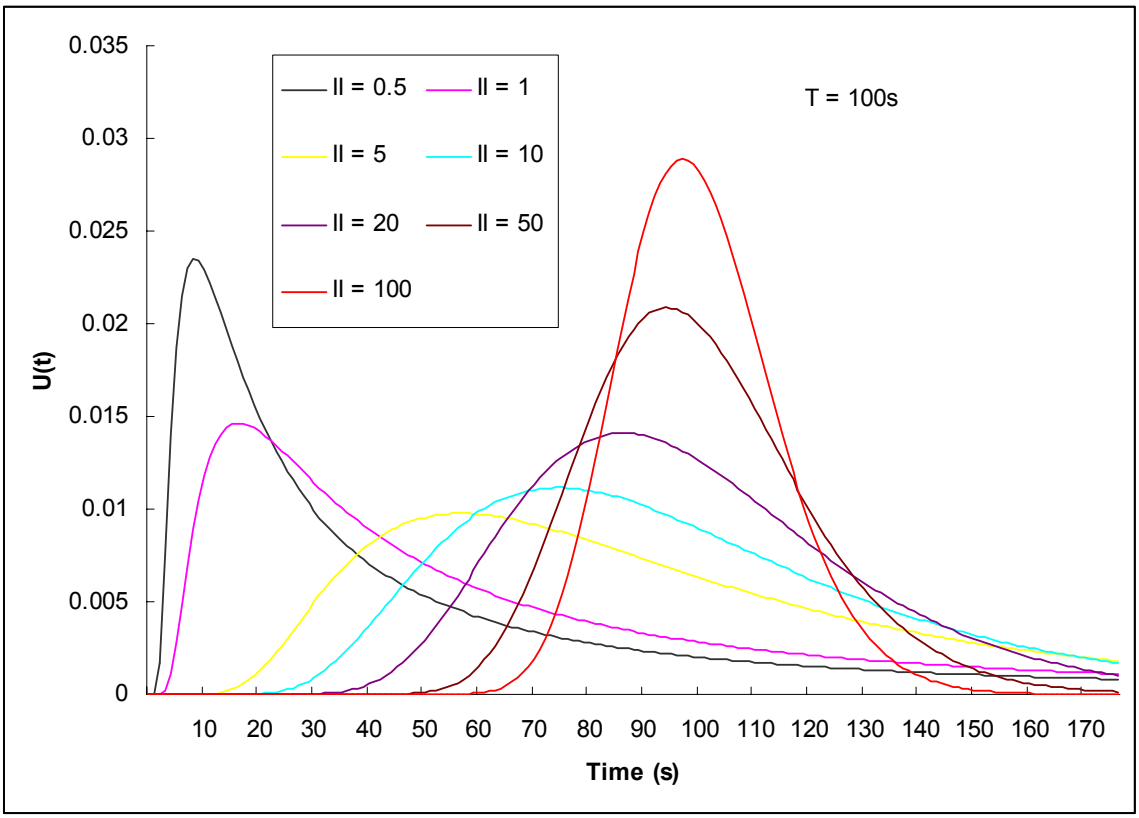

Fig. 2.7 An illustration of first-passage-time distribution with different Peclet numbers

If the locale wave celerity c and dispersion coefficient D are known, the flow path average travel time T and Peclet number II can be calculated. From equations 2.25, 2.26, and 2.27, we known that c and D can be physically determined using the values of friction resistant coefficient n, hydraulic radius R, and slope S. The Manning's roughness value is one of the most difficult variables to be estimated among the parameters. One of the common approaches is to use look-up table. The land cover types can be related to some laboratory measurements of Manning's n referring to Bedient and Huber (2002, pp. 277). The typical n value of overland flow ranges from 0.012 to 0.4.

Channels generally have less roughness value than the overland flow. The typical values are from 0.011 to 0.41. The estimate of hydraulic radius R is also rather arbitrary. The minimum overland R can vary from 0.001m to 0.005m and the maximum in channel R can be 1m to 3m. The locale slope S is the most deterministic parameter because its value can be calculated directly from the elevation model using the methods such as Burrough (1985). However, because of inaccuracy of data and natural landforms, the locale slope can only be calculated as a very small value or even zero. This imposes difficulties for equation (26) in calculating D. To avoid this problem, I reclassified those slope values which are below 0.5% to be equal to 0.5%, the same as Liu et al. (2003). In this case, there would be a minimum slope of 0.5% for the entire watershed. The previous study by Liu et al. (2003) has shown the sensitivity of the above variables used to estimate the flow path response function. Their research suggested that both the Manning's n value and the maximum hydraulic radius in channels have great impact on the hydrograph curve, while minimum slope value has the least effect. However, due to the different surface topography conditions, it is still useful to test the sensitivity of the parameters.

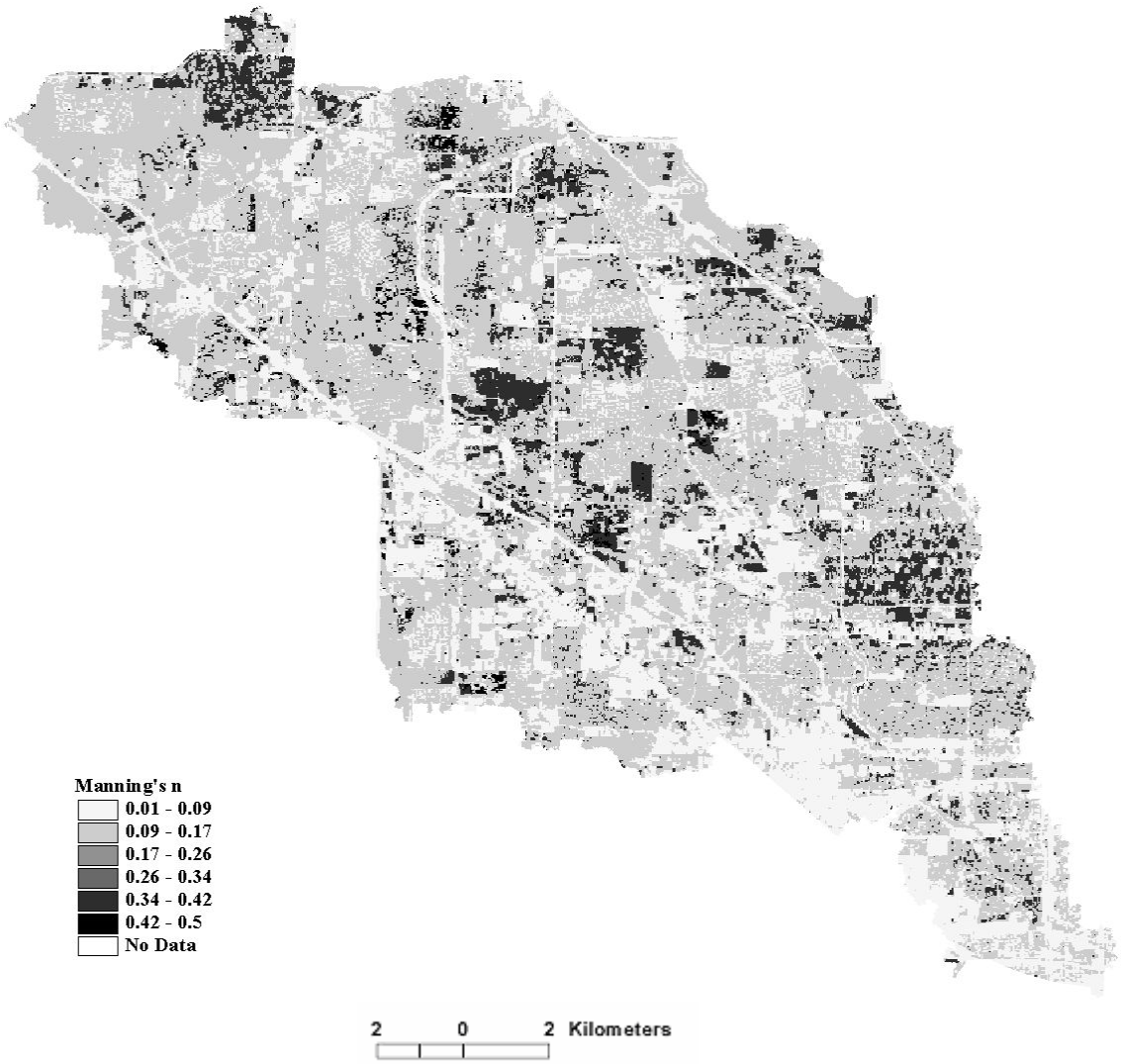

Fig. 2.8 Distribution of Manning's N value

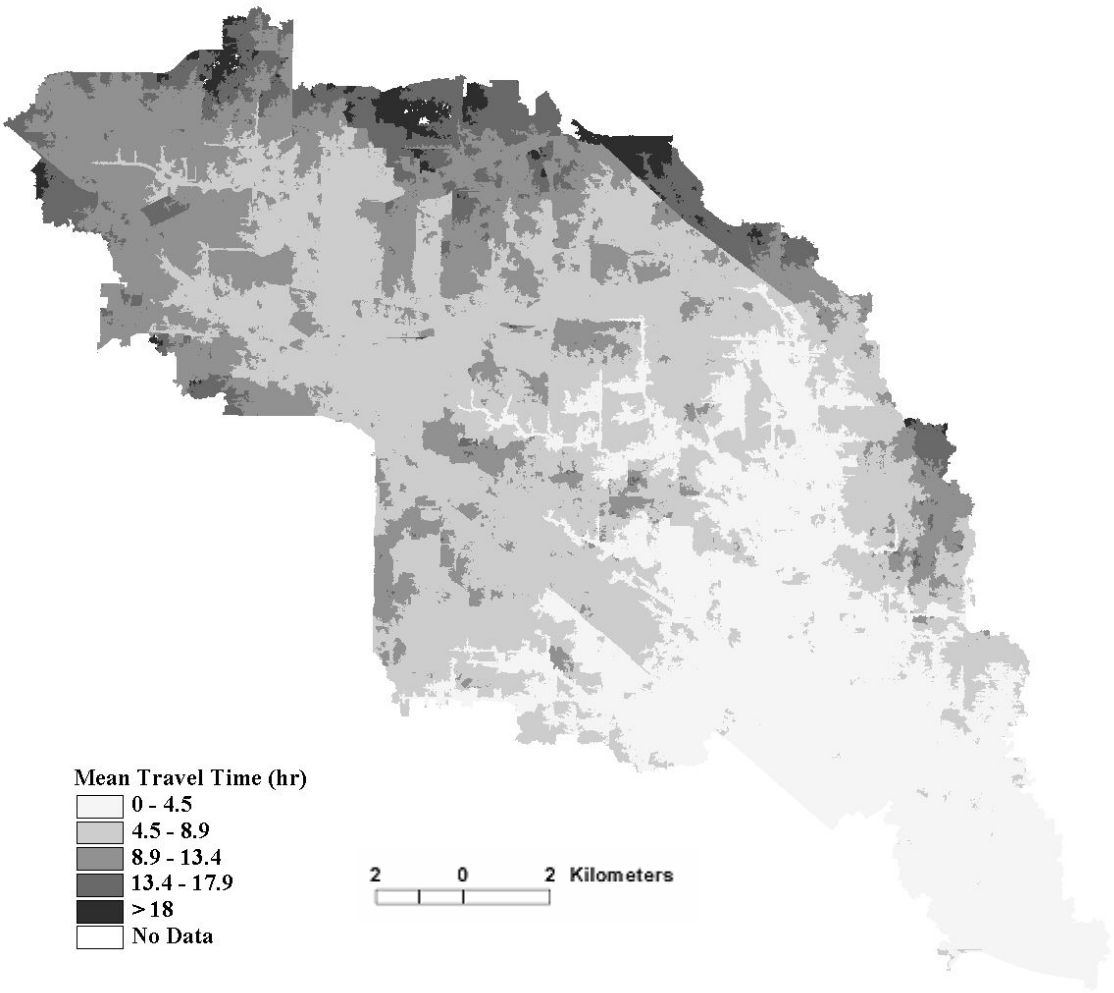

Fig. 2.9 Distribution of mean travel time (T)

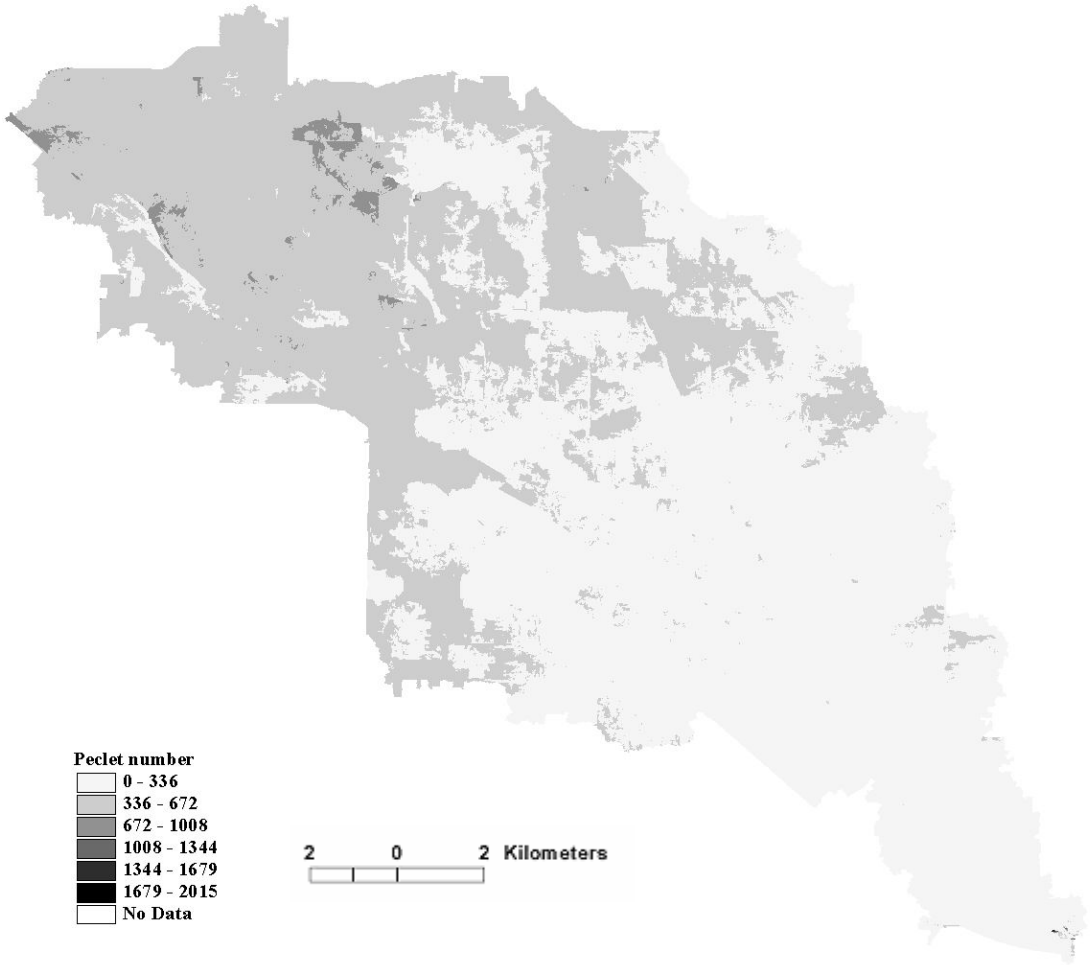

Fig. 2.10 Distribution of Peclet number (II)

Manning's n value derived from the land use land cover information is shown in Fig. 2.8. In the look-up table (Bedient and Huber 2002, pp. 277), there can be seen an adjustable range for each cover type, which is approximately +/- 10%. This range is used to calibrate the model. To test the sensitivity of the Manning's n value, the R value has been set to maximum 2m in channels and minimum 0.005m overland. Spatially distributed T and II are calculated using GIS function "flowlength" following equation (23) and (24). Figs. 2.9 and 2.10 illustrate the spatial distributions of the T and II values. Note that current Manning's n values are directly looked up from the table without any adjustment. As we can see, when the n value increases, the hydrograph curve has a lower peak and prolonged tail. This is consistent with the first-passage-time distribution and the flow path response model. The Adjustment of Manning's n value is allowed from its 80% to 120% of original value. We can see the peak moves towards right and attenuated while the Manning's n increases. Table 2.4 discloses the variation of the T and II due to different n values. Fig. 2.11 illustrates the PDF curves with different Manning's n values. We can see that the variance of the distribution barely changes. It is also interesting to see that the Peclet number II does not change with the Manning's n value. It is very important to the model calibration because we can adjust the average T value without changing the Peclet number.

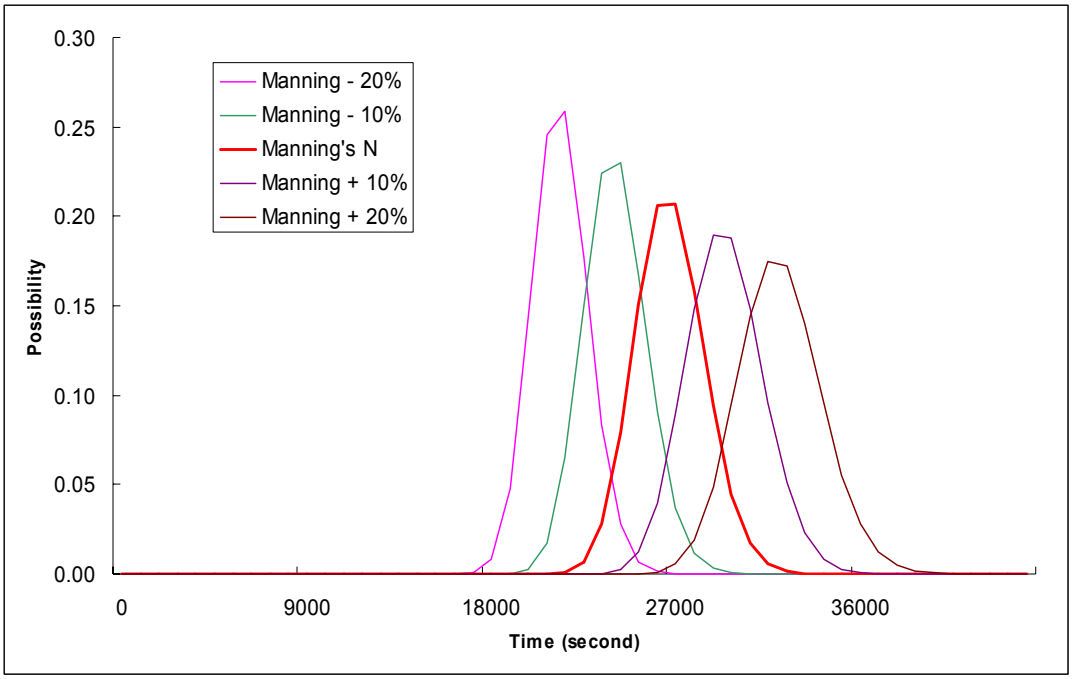

Fig. 2.11 PDF curve differences due to variation of Manning's n values

Table 2.4

Manning's n value and its corresponding mean T and Peclet number

Manning	Mean Travel Time (s)	Peclet number
N * 0.5	13361	502
N * 0.8	21377	502
N * 0.9	24050	502
N	26722	502
N * 1.1	29394	502
N * 1.2	32067	502
N * 1.5	40083	502

Following the same procedure, the sensitivity analysis of the maximum R value is shown table 2.5 and Fig. 2.12. Both the mean Pectlet number and the mean travel time are reduced while the selected maximum hydraulic radius increases. There is a larger

drop when R is changed from 1m to 2m. This means the model will be affected more significant by adjusting R between 1m and 2m. It can be seen that reducing the maximum R value causes the same trend in the hydrograph as increased Manning's n value does: the curve screws to the right with reduced peak flow.

Table 2.5

Sensitivity analysis of maximum hydraulic radius

Maximum Hydraulic Radius (m)	Mean Travel Time (s)	Mean Peclet Number
1	20538	312.09
2	14292	185.75
3	12629	160.77
4	10042	112.76

Table 2.6

Sensitivity of minimum slope value

Minimum Slope (%)	Mean Travel Time (s)	Peclet Number
0.1	23031	183.7
0.2	21669	321
0.5	20538	634.5
1	17793	1235
2	14924	2347

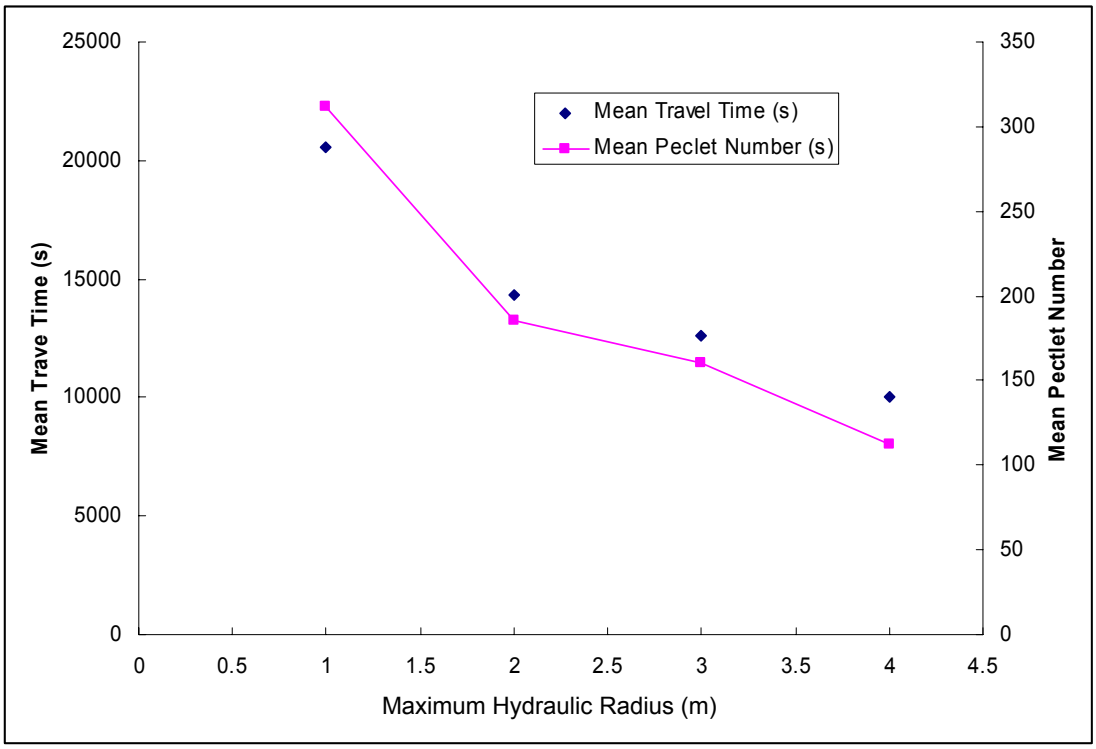

Fig. 2.12 Sensitivity of maximum hydraulic radius

Minimum slope also plays an import role in the routing model. If the area of flat surface (0 percent slope) takes up a significant portion, the minimum slope will be able to change the routing parameters effectively. Table 2.6 shows the change of mean value of T and II with different minimum slope. We can see the Peclet number (II) is strongly affected by the choice of minimum slope. It is also interesting to note that the increment of minimum slope increases the II value while decreasing the T value. This is because the dispersion coefficient (D) decreases with a higher slope value, thus variation in the water travel time along the flow path decreases.

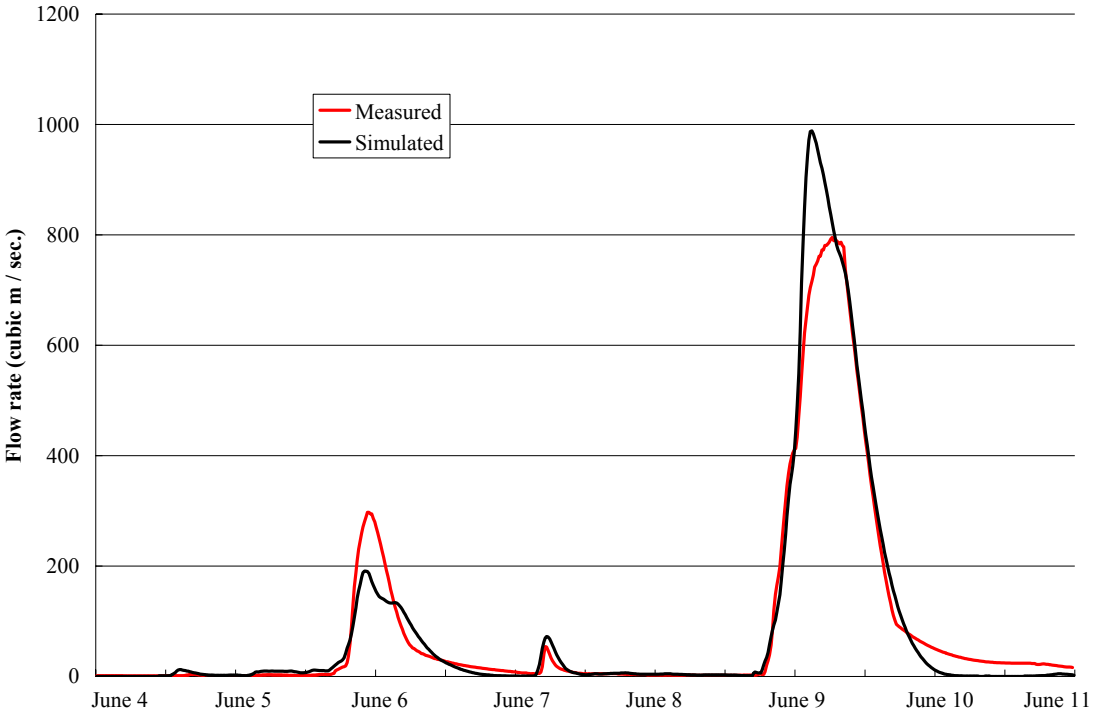

Fig. 2.13 Simulated discharge after calibration

Table 2.7

Accuracy indicators of the hydrograph

	R	PRMS
Event1	0.9464	57.083
Event2	0.9866	88.799

By trial-and-error method, combinations of parameters were tested. Both visual checking and quantitative analysis were performed to choose the optimized parameters through calibration. The indicators used to judge the goodness of fit of simulated and

measured flow are the correlation coefficient R and the Peak-weighted root mean square (PRMS) error objective function (USACE 2000). The PRMS error is calculated as:

$$Z = \left\{ \frac{1}{N} \sum_{i}^{N} (q_o(i) - q_s(i))^2 \left(\frac{q_o(i) - q_o(mean)}{2q_o(mean)} \right) \right\}^{\frac{1}{2}} \qquad (2.29)$$

where $q_o(i)$ = observed flow at time step i; $q_s(i)$ = simulated flow at i; $q_o(mean)$ = mean of observed flows. This indicator gives more weight to the time step where peak flows are located, and thus can quantify both the overall errors and the peak displacement. The correlation coefficient and the PRMS error of both the events are shown in table 2.7. The hydrographs of measured discharge and simulated discharge is shown in Fig. 2.13. It can be seen that two rainfall events do not agree with each other very well. The peak flow of the first event is too low but too high in the second one. However, the increase and recession flanks show good agreement. Further adjustment of the parameter in favor of one of the peaks is not recommended. The second event cannot be regarded as "more important" than the first one in terms of calibration. Actually, the two events work as cross-validation pairs. If the first peak is to be increased to fit for the measured curve, the second one would be even higher which is farther away from the measure peak flow value. Efforts to reduce the peak of flows would also decrease the accuracy of the first event.

CHAPTER III

AN OBJECT-ORIENTED MODELING FRAMEWORK

3.1. Resolution and accuracy issues of multi-sensor remote sensing data

The resolution and accuracy of elevation models has various impacts on hydrologic variables or simulated flows. To address the scale and DEM resolution issues on hydrological modeling, Zhang and Montgomery (1994) concluded that the appropriate scale of the DEM used in a hydrological simulation should be "somewhat smaller than the topographically divergent hill slope length". Wolock and Price (1994) studied the changes of topographic index (ln (a / tan B)) caused by different map scales and DEM resolutions. Their study shows how the resolution of the elevation models affects hydrological simulations. There were several other studies which recognized that DEM resolution will have important impacts on hydrological modeling and flow predictions, such as Walker and Willgoose (1999), Molnar and Julien (2000), Moglen and Hartman (2002), etc. The vertical resolution of the DEM is also important, especially for areas with flat terrain characteristics. As suggested by Gyasi-Agyei et al. (1995), the average elevation drop per-pixel should be greater than the elevation error; otherwise, the extracted stream network will not be satisfactory.

The USGS 7.5-minute (1:24,000) elevation model is one of most widely used elevation datasets in the US. The data is available for most of the US continental areas. The official claimed accuracy for this datasets is that for DEM generated from photogrammetry, 90% of them would have a RMSE at about 7m. For the data created from topographic maps, the accuracy is less than ½ of the contour interval. In the study

area, an inspection revealed that the DEM was created from 5-foot contour topological maps, which means the vertical accuracy of this area is less than 2.5 ft or about 0.8 m. The minimum vertical increment of the USGS elevation model in my study area is 1 foot. However, the average elevation drop per-pixel is about 0.19 m, which is less than the minimum veridical increment accuracy (1 ft or 0.3 m). According to Gyasi-Agyei et al. (1995), since the data accuracy cannot describe the average elevation drop per-pixel, this elevation data may not be appropriately applied for the hydrological analysis for my study area. As shown in Fig. 3.1, the red color represents the slopes derived from the elevation model. Contour lines that are used to interpolate the elevation values are still clearly seen in the data as artifacts. Among the contour lines are the areas with 0% slopes. This shows that the USGS 30 m DEM could not depict the local variations of the elevation values. Therefore predicted stream networks and other parameters may be contaminated by the inaccuracy of this dataset.

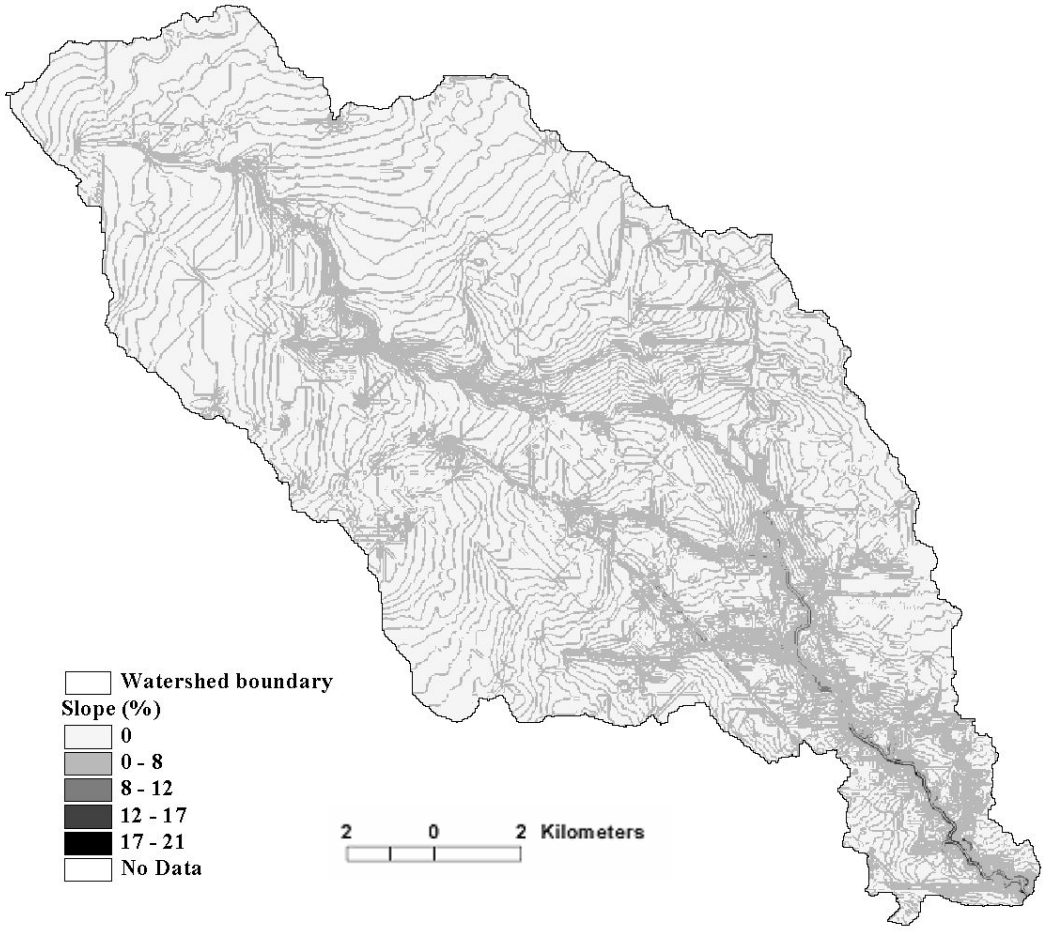

Fig. 3.1 Slope derived from USGS 7.5-minute DEM

Airborne LIDAR (LIght Detection And Ranging) technology, also known as laser altimetry, is emerging as a cost-effective alternative for the acquisition of highly accurate topographic data. A LIDAR DEM offers greatly improved vertical and horizontal accuracy compared to the most widely used 30m USGS DEM. Current LIDAR technology can provide DEMs at about 1-5 m grid spacing and vertical accuracy

less than 15 cm (Berger 2001). Unlike the traditional photogrammetric methods, LIDAR DEM does not rely on post processing or the quality of the stereo pairs of photos. The elevation of the earth surface is acquired by the laser ranger directly from the air. The acquisition of LIDAR measurement is not influenced by weather or sun illuminations. Due to the relatively high cost of the LIDAR devices and techniques, there is no wide coverage for the entire US. However, in 2002, a joint effort by FEMA and Harris County Flood Control District made LIDAR DEM available for watersheds in Harris County of Texas, including the case study area of this research.

3.2. Comparing LIDAR DEM to the USGS 30m DEM

3.2.1. General comparison

The quality of the LIDAR DEM and USGS DEM has been discussed in previous sections. It is clear that the LIDAR DEM has advantages in both horizontal and vertical resolution and accuracy. As mentioned before, the smallest vertical unit of the USGS DEM is 1 foot. After rounding errors, the USGS DEM cannot depict elevation differences below 1 foot or 0.3 m. This means if the local slope is less than 1% (0.3 m / 30 m), the slope derived from USGS DEM will be 0. This area is so flat that the USGS DEM does not reliably represent the local elevation variations. A quantitative analysis was also performed on the two datasets. Ten thousand random points were sampled to evaluate the agreement of the two datasets. Since the two datasets are in different vertical datum (LIDAR in NAVD 88; USGS DEM in NGVD 29), the shift of the two datum in this area is less than 1cm which is not significant. The regression line in Fig. 3.2 shows the linear relationship of the two datasets. The correlation coefficient is 0.988.

This indicates that the general trend of the topography is depicted similarly in both of the DEM datasets. However, the root mean square difference of these two datasets is 5.2 feet. This value is even larger than the published vertical accuracy (2.5 feet) of USGS DEM. It suggested that local variations of elevation values have large amount of disagreement between the two data. Considering the high quality of LIDAR DEM (15cm RMSE), the USGS DEM have very large uncertainty to describe local elevation variations.

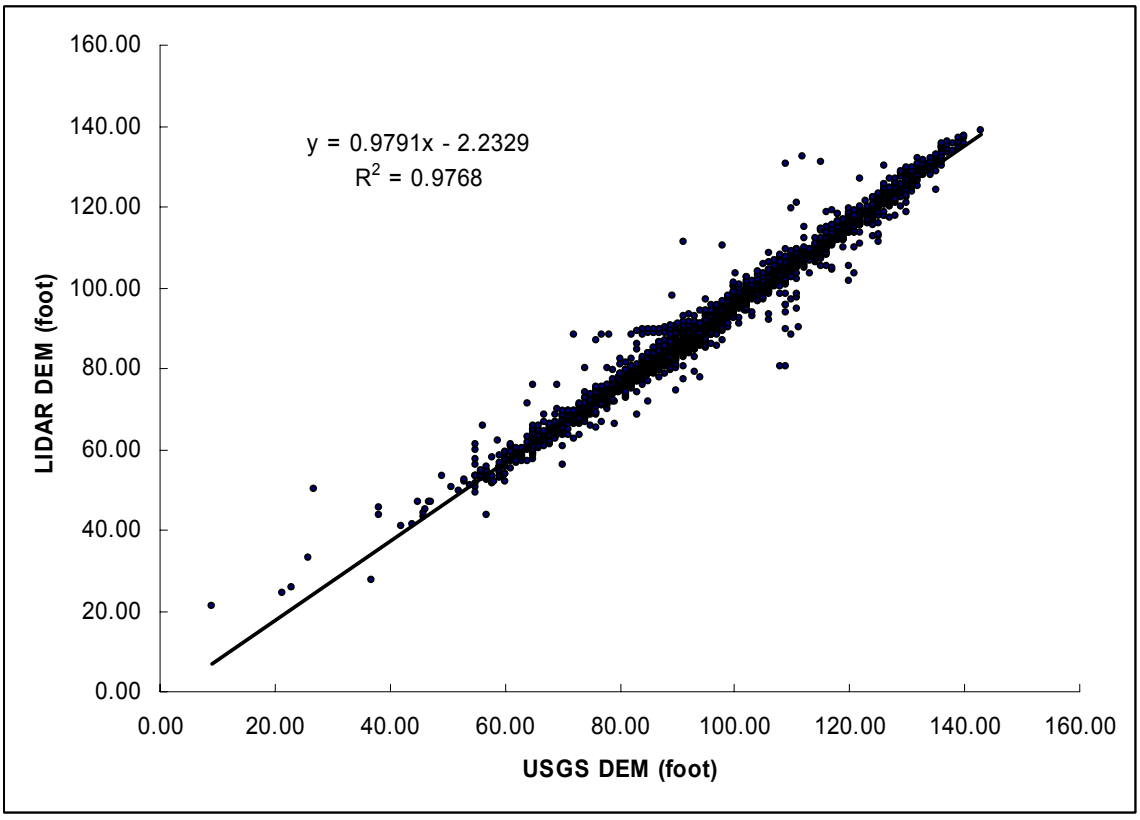

Fig. 3.2 Regression analysis of the sampled LIDAR DEM and USGS DEM elevation

3.2.2. Differences in flow direction and watershed delineation

Delineation of watershed boundaries is important to determine the upstream area that contributing runoff water. Therefore, the hydrological characteristics of upstream area are thus essential for simulating hydrologic processes. Watershed boundary can be determined from elevation models using functions built in GIS systems. The flow directions are determined follows the D8 algorithm (Jenson and Domingue, 1988). Surface depressions are removed by depression filling algorithm developed by Wang and Liu (2006). Most of the depressions are the result of data inaccuracy and noise, although man-made features and lakes could also be surface depressions. Fig. 3.3 shows the surface depressions and their depth derived from both the datasets. The area of the surface depressions in LIDAR DEM is 144,745,075 m^2, which is much larger than the USGS DEM 20,964,600 m^2. However, the average depth of the surface depression of LIDAR DEM is 0.76 feet or 0.22 m, and 2 feet for USGS DEM. We can see these are consistent with the vertical accuracy of the DEMs. Surface depressions contribute to the initial abstraction of rainfall water. The ability to quantify this information of LIDAR DEM is another advantage comparing to the USGS DEM to be used in a distributed model.

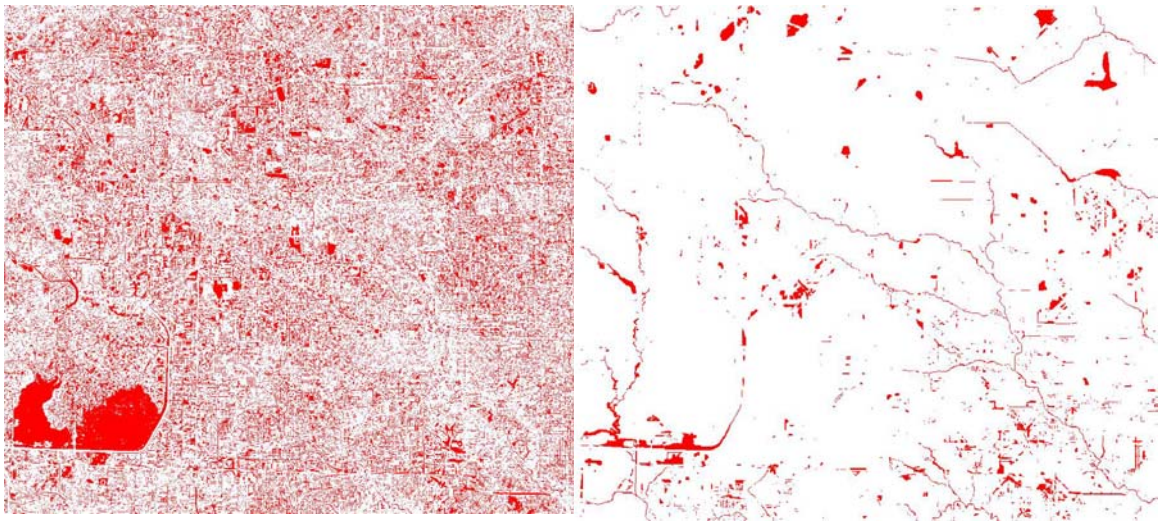

Fig. 3.3 Distribution of surface depressions. Left: from LIDAR DEM; right: from USGS DEM

Flow directions can be calculated using the approach of D8 (Jenson and Domingue, 1988). The principle of this algorithm is to find the direction that has the largest elevation drop among the eight neighbors of a center pixel. Following the flow directions, upstream and downstream searching and spanning can be implemented. Upstream spanning results in a spanning-tree which is rooted from the outlet. Watersheds can be delineated by tracing the spanning-trees. Delineation of watershed boundaries is important to determine the upstream area that contributing runoff water. Therefore, the hydrological characteristics of upstream area are thus essential for simulating hydrologic processes. The sizes of watersheds derived from the USGS DEM and LIDAR DEM are 230,292,000 m^2 and 226,408,675 m^2 respectively. The difference is as low as 1.72%, which is not significant (below 2% of the total area size). However, visual checking of the boundary of the two datasets reveals much greater differences

(Fig. 3.4). The absolute boundary difference is 37.12 km^2 which is about 16.4% of the total area. This suggests that 16.4% runoff water comes from different locations if these two DEM datasets are to be compared.

To conclude, differences exist in the watershed delineation process using these two data sources. It is suggested that up to 16.4% of the runoff water may or may not be considered to the model simulation according to these two DEM datasets. However, how much this difference contributes to the watershed modeling is still unknown.

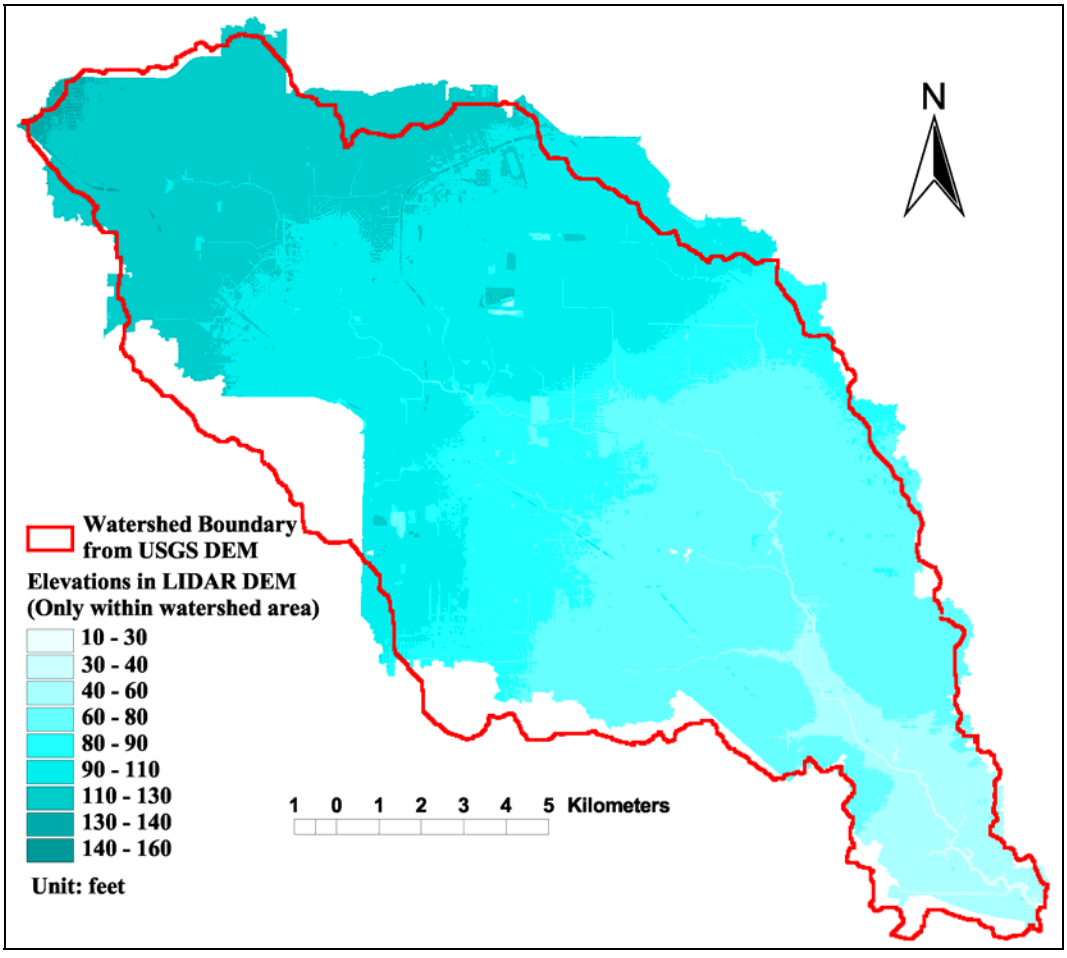

Fig. 3.4 Comparison of the derived watershed area from two DEM datasets

3.2.3. Calibrating the USGS DEM based model parameters

Using the same mathematical equations, the runoff and discharge can be calculated using the parameters derived from the USGS DEM at 30meter resolution. To calibrate the model, a sensitivity analysis of the parameters should also be conducted. The sensitivity analysis is based on changing the values of minimum slope value, hydraulic radius, and the Manning's n. Table 3.1 showed the results of sensitivity analysis. To retrieve values of T and II that are comparable to the calibrated results from last section (average T = 20538s, II = 635), the combination of Slope = 0.5, R = 1.5m, and original Manning's n is chosen which produces T = 22297s and II = 608.

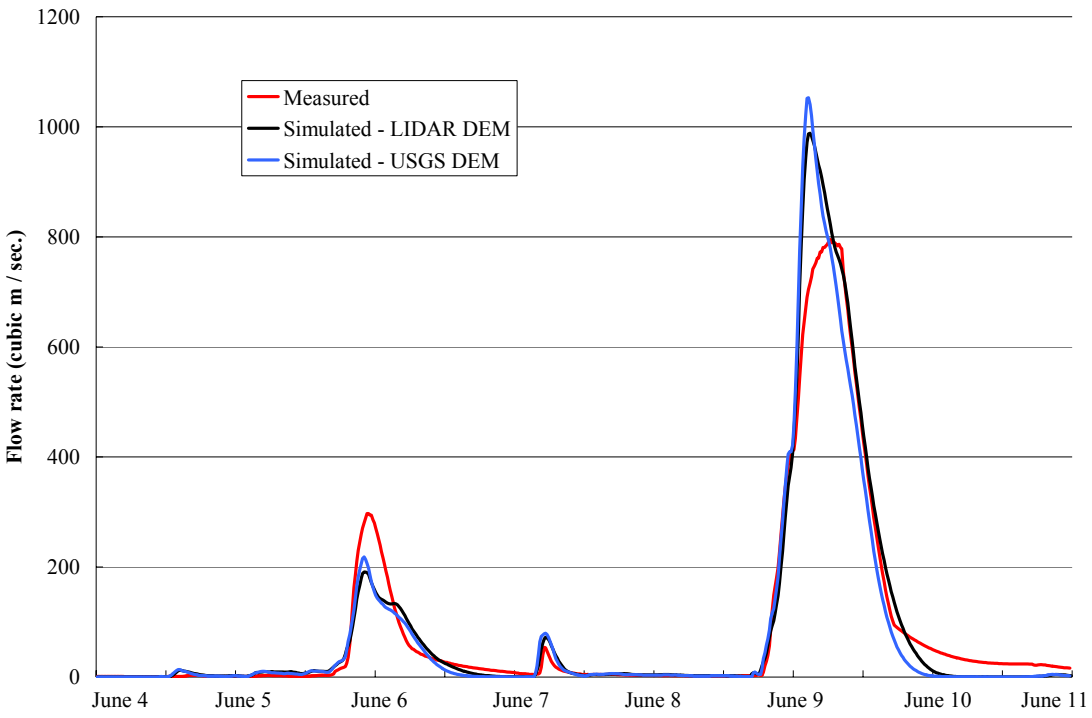

Fig. 3.5 Hydrographs of simulated results and observed discharges

Table 3.1

Goodness of fit indicators for model simulation using USGS DEM

	LIDAR		USGS	
	R	PRMS	R	PRMS
Event1	0.9464	57.083	0.959	123.549
Event2	0.9866	88.799	0.969	109.834

The comparison of hydrographs is important when evaluating two models or two datasets. However, there is no reason to expect the model has better results using LIDAR DEM than using the USGS DEM because both of the results have been through calibration. Fig. 3.5 provides a visualization of the results. We can see that through calibration, the performance of the two datasets is almost identical. However, it is interesting that differences in the PRMS are much greater than the differences in correlation coefficient R and these differences are not obvious from visual interpretation. This indicates that PRMS may not be a robust statistic for summarizing goodness of fit.

3.2.4. Sensitivity analysis

The analysis showed that both USGS DEM and LIDAR DEM can produce a reasonable simulation after calibration. Since calibration is an unavoidable procedure in most of the hydrological models, we still cannot conclude any advantages in terms of modeling the hydrograph using LIDAR DEM over the USGS DEM. Uncertainty of the model is directly related to the sensitivity of the parameters. Sensitivity of the model to each parameter can be used to guide calibration, but can also be used to evaluate uncertainties in model parameters. The more sensitive the parameter, the more influence and

uncertainty it will contribute to the model. Since the parameters are estimated to be within certain ranges, the variability of the model due to the possible change of these parameters results in the model uncertainty. If the model output is very sensitive to one parameter, the uncertainty related to this parameter will be relatively high.

3.2.4.1. Manning's N

Sensitivity of Manning's n value is shown in table 3.2. As discussed before, Manning's n does not influence the Peclet number (II). By varying it from 80 percent to 120 percent, we can see the mean T value changes from 24050s to 32067s, a delay of about 2.5 hours. Because Pectlet number is not changed, we can imagine an increment of the dispersion coefficient and therefore more attenuated flow curves. Since Manning's n value is not directly estimated from the DEM, although the resolution of the data may affect the model output, the sensitivity of this parameter should not be considered as one of the major differences of the two DEM datasets.

Table 3.2

Sensitivity analysis of USGS DEM-derived parameters

Slope	T	II	Radius	T	II	Manning's	T	II
0.1	35986	243	1m	26722	794	N * 0.8	13361	794
0.2	32019	390	1.5m	22297	608	N * 0.9	24050	794
0.5	26722	794	2m	19689	506	N	26722	794
1	22079	1421	3m	16570	394	N * 1.1	29394	794
2	17610	2562				N * 1.2	32067	794

Table 3.3

A comparison of sensitivity of R_{max} using both datasets

LIDAR			USGS		
Radius	T	II	Radius	T	II
1m	20538	634	1m	26722	794
2m	14292	368	2m	19689	506
3m	12629	308	3m	16570	394

3.2.4.2. Maximum hydraulic radius

The maximum hydraulic radius influences the both the wave celerity c and the dispersion coefficient D directly, according to equation 2-25 and 2-26. Higher hydraulic radius will result in higher wave celerity and, hence, a reduction in the average time that water particles spend in each segment of the flow paths. The Dispersion coefficient will also tend to increase when the hydraulic radius is higher. The maximum hydraulic radius R_{max} may vary from 1m to 4m according to Liu et al. (2003). By adjusting R_{max}, the mean travel time T and flow path Peclet number II are altered. From table 3.3 we can see that the T and II are less influenced by the selection of the maximum hydraulic radius of the LIDAR DEM than the USGS DEM.

3.2.4.3. Minimum slope value

Slope represents the hydraulic gradient if the flow is considered as kinematic wave. From the digital elevation model, we can calculate slope at each location by fitting a trend plane to the local elevations. The surface slope is also critical to determine the wave celerity and the dispersion coefficient. Unlike the hydraulic radius, the increment of the slope directly results in the increased wave celerity c but reduced dispersion

coefficient D. The peak of the flow path response will therefore become shorter and higher. The slope calculated from the USGS DEM is generally smaller than LIDAR DEM. Mean slope from USGS is 0.446% and 1.739% from LIDAR. If only the resolution of the DEM is considered, the USGS DEM can be viewed as a spatial resample of the LIDAR DEM. Resampling is actually a low-pass filter that removes local variations and smooths DEM. Therefore, the calculated slope will be smaller for the elevation data at coarser resolution. Beyond spatial resolution, the elevation measurement of USGS DEM is another influential factor. The minimum measurement unit of the USGS DEM is 1 ft. In another word, spatial variations of elevation values below 1 ft will not be seen. Therefore, due to the flat and low-lying terrain characteristic of my study area, large area will have zero slope values if calculated using the USGS DEM. If the elevation drop between adjacent cells is smaller than 1 ft, zero-slope will occur. And according to equation 2-25, if the slope is zero, the wave celerity will be 0 and the mean travel time from this area and all its upstream area will become infinity. Therefore, the slope values that are close to zero must be corrected before the routing can be modeled. In the article of Liu et al. (2003), a minimum slope of 0.5% is used to replace the zero-slope values. In their analysis, the sensitivity of the minimum slope is not as large as Manning's n and the maximum hydraulic radius (Liu et al. 2003). However, since their study area may not be as flat as my study area, the sensitivity of the minimum slope value should be re-investigated. As can be seen in Fig. 3.6, in the case study area, the zero-slope area occupies almost 40% of the entire watershed.

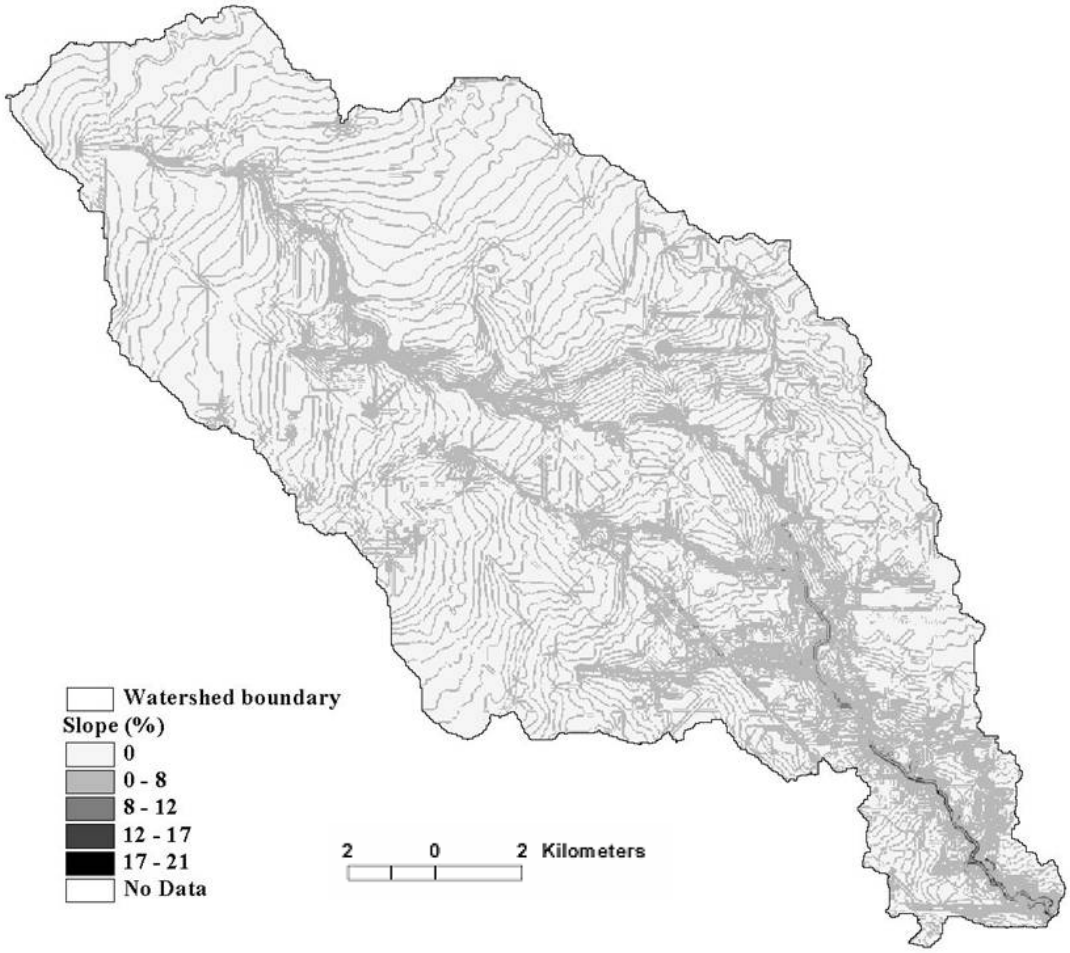

Fig. 3.6 Slope derived from USGS DEM

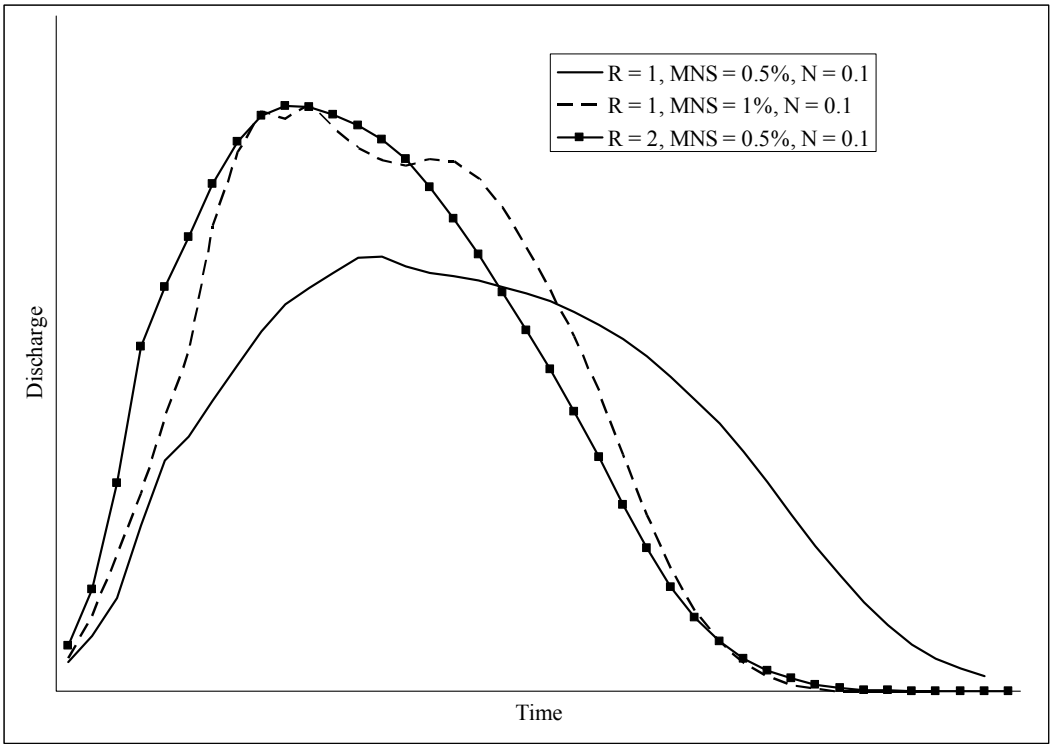

Fig. 3.7 Sensitivity analysis of USGS DEM

For the sensitivity analysis, I adjusted the minimum slope by taking the values of 0.1%, 0.2%, 0.5%, 1%, and 2%. The corresponding mean T and II values are calculated and listed in table 3.2. It can be seen that the minimum slope does have significant sensitivity. The average T value is changed from 13361s to 32067s when the minimum slope value is adjusted from 0.1% to 2%. This would give an overall delay of the flows by 18376s or 6 hrs for the USGS DEM. The LIDAR DEM has a much smaller sensitivity with a delay of only 2.3 hours. Despite the sensitivity of this parameter, more problems were identified by examining the distribution of the slope values of the two datasets. Table 3.4 shows the percent of pixels that have slope values below the given value. This percentage is extremely high for the USGS DEM. For an example, 45.2

percent area has a slope value smaller than 0.1%. So if values of 0.1% are used as the minimum slope value, 45.2 percent of the pixels would use this arbitrarily assigned slope value and it will introduce tremendous uncertainty into the model. Similarly, if we used the 0.5% value that is documented in the literature, 66.4% of the total area would have arbitrary slope values. From Fig. 3.7, we can see that the sensitivity of slope as a parameter is as much as the hydraulic radius (R) parameter if the USGS DEM is to be used. As comparison shown in Fig. 3.8, the uncertainty introduced by the slope parameter has much less contribution than the R value.

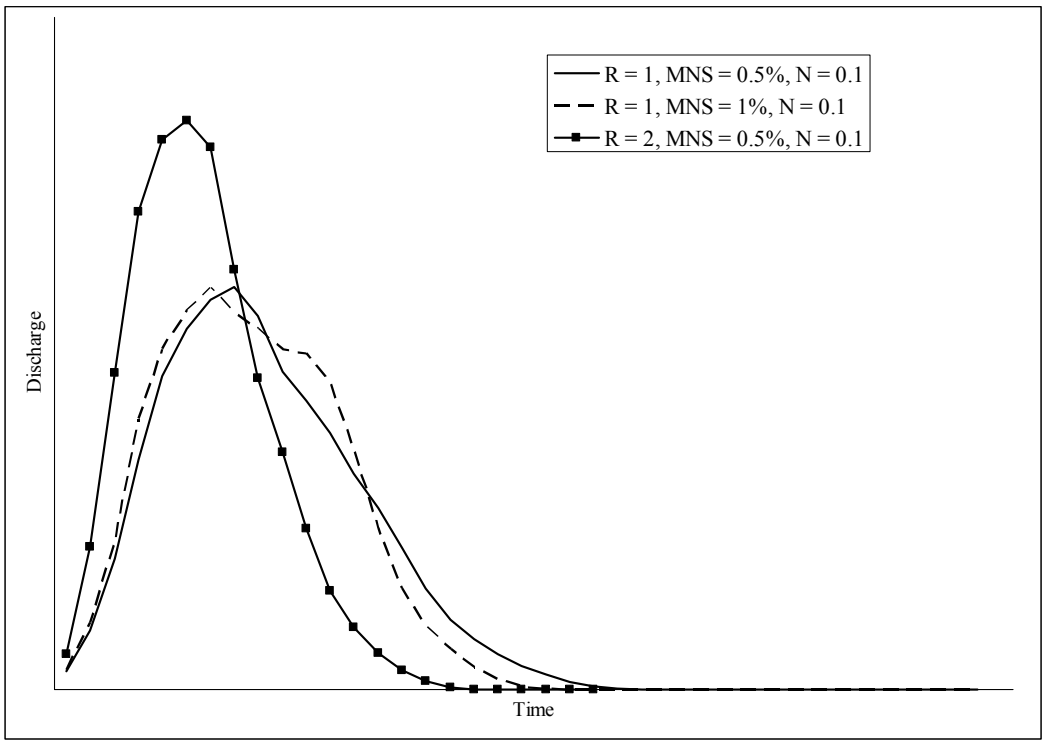

Fig. 3.8 Sensitivity analysis of LIDAR DEM

Table 3.4

Distribution of slope values

Slope	LIDAR	USGS
0.1	9.8	45.2
0.2	14.5	55
0.5	31	66.4
1	54.2	92
2	77.7	96.3

3.2.5. Spatial variations of routing parameters

Hydrologic models can be calibrated if reference data is available. By adjusting the parameters, the calibration process seeks to find the optimum "fit" for the observed data. Details on calibration methods and operations are beyond the scope of this paper. To illustrate the points to be made in this research, I choose a simple trial and error method. No observed data will be used for comparison. Instead, it is assumed that the LIDAR DEM already has a set of parameters calibrated from "truth" data and use the hydrograph derived from the LIDAR DEM and find parameters from USGS DEM to match it. Fig. 3.9 illustrates the instantaneous watershed response function derived from the LIDAR DEM using the parameters (R = 1m, MNS = 0.5%, and N = 0.1). By looking for similar response functions from the USGS DEM, we located two sets of parameters: P1{R = 3m, MNS = 1%, N = 0.1}, and P2{R=2m, MNS = 2%, N = 0.1}. From the graph, we can see both solution P1 and P2 can be used as calibrated curve for predictions by referencing to the "truth" curve determined from LIDAR DEM. The response function is the summation of all the DEM pixels' response functions. Since the calibration was not performed spatially, it is worth to see if the spatial distributions of flow pattern are

identical. Average travel time T and Pelet number II are the two momentum variables of the response function. T is the mean travel time from the source to the outlet. If we compare the spatial distribution of T and II values, we can verify if two watershed response functions are spatially identical. I randomly sampled 2000 locations of their T value from the watershed and make scatter plots (Fig. 3.10). We can see it depicts the spatial correlation of T of the parameter set P1 and P2 from USGS DEM. and the spatial correlation between P1 and LIDAR DEM. Although the discharge curves appear to be almost identical, we can observe from Fig. 3.10 that the spatial pattern of flow parameters has lot of difference between the two datasets. The USGS DEM response function curve P1 and P2 are similar both in the curve and the spatial distribution of the parameters. But they both fail to spatially match the parameter derived from LIDAR DEM which they are calibrated to. The poor spatial correlation of the calibrated parameters is one of the potential problems using the model. And this suggested that although calibration enables using USGS DEM to produce identical discharge curve to the high quality LIDAR DEM, the flow patterns are not spatially similar.

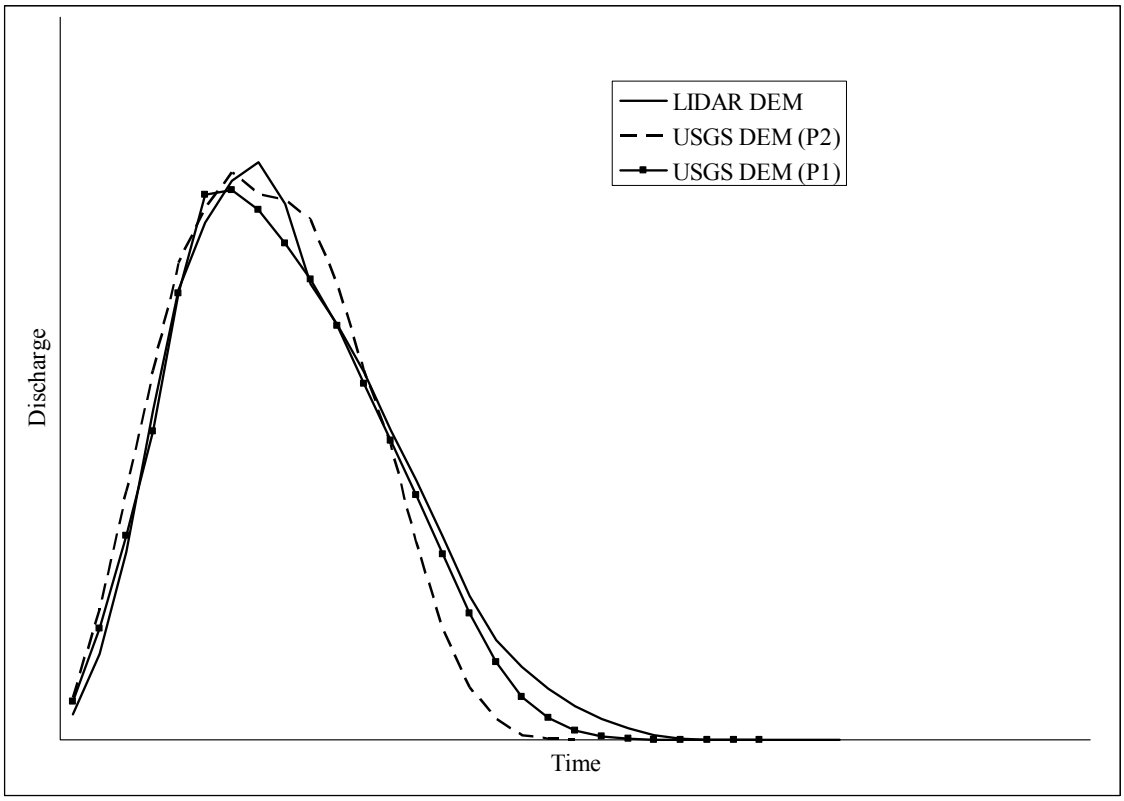

Fig. 3.9 Response functions of calibrated models using LIDAR DEM and USGS DEM

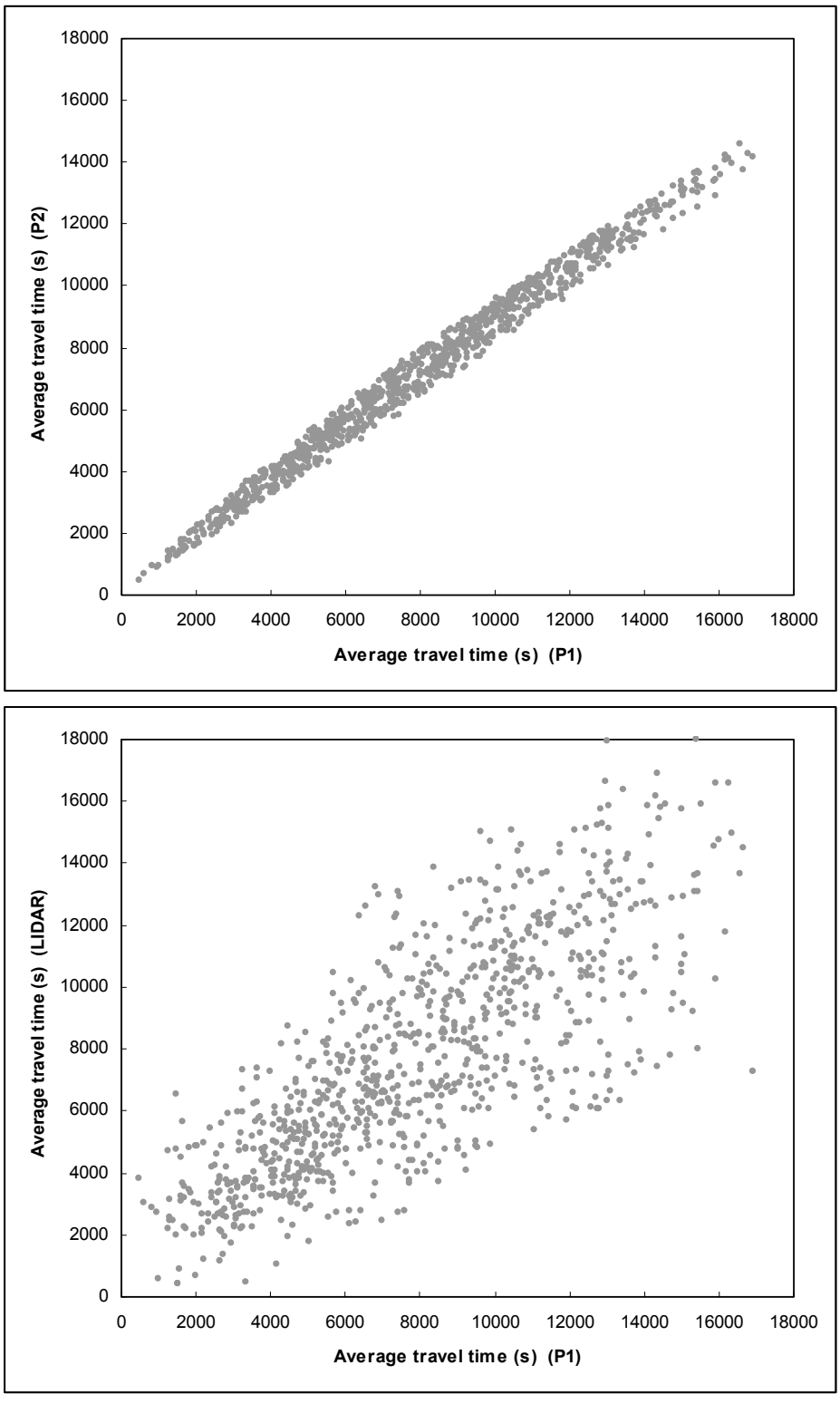

Fig. 3.10 Spatial correlations of T of calibrated models

3.2.6. Spatial distribution of the discharges

One of the important reasons that distributed models are superior than simple lumped models is that it considers the spatial variability of input data, including precipitation, land use and land cover, soil, and elevation. The impacts of using spatially varied rainfall data instead of homogenous rainfall have been revealed in Dawdy and Bergmann (1969), Julien and Moglen (1990), Singh (1997), and Singh and Woolhiser (2002). The ability of a calibrated model to predict discharges for other rainfall events relies on the spatial similarity of the calibrated model to the ground truth. This idea can also be used to illustrate the differences of calibrated models using USGS DEM and LIDAR DEM. To perform the spatial similarity analysis, a specific method is designed and presented as following:

1). Partition the entire watershed into 3 by 3 lattices (Fig. 3.11). There are totally 9 sub-areas derived from the original watershed. The 9 sub-areas can be used to perform spatial similarity comparison;

2). The response functions of the pixels located within each sub-area are summed together to represent the response function of the sub-area;

3). The response functions for the same sub-area but using different DEM are compared in Fig. 3.11.

As shown in Fig. 3.11, most sub-areas have significant differences between the two elevation data, especially for sub-area 4, 5, 8, and 9. Although the overall response functions look very alike (Fig. 3.12, P1 and LIDAR), the sub-areas have much larger differences. It suggested that if applying different rainfall data, the resultant hydrograph

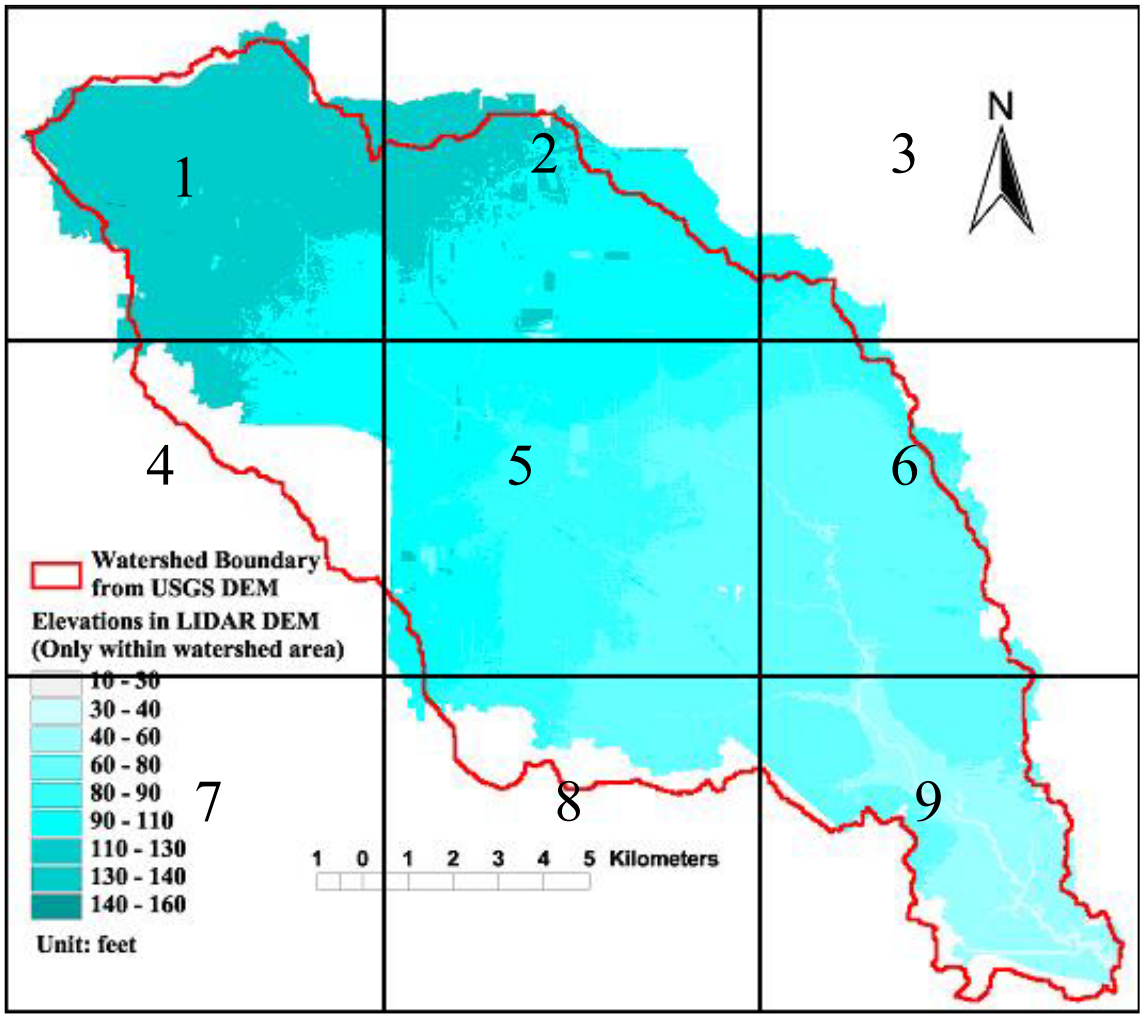

Figure 3.11 Spatial partition of the watershed for spatial similarity analysis

would be significantly different. The difference between the hydrographs of the entire watershed is less than 4% of the total discharge volume. However, the spatial difference calculated from 9 sub-areas is 32.7%, which is almost 10 times greater

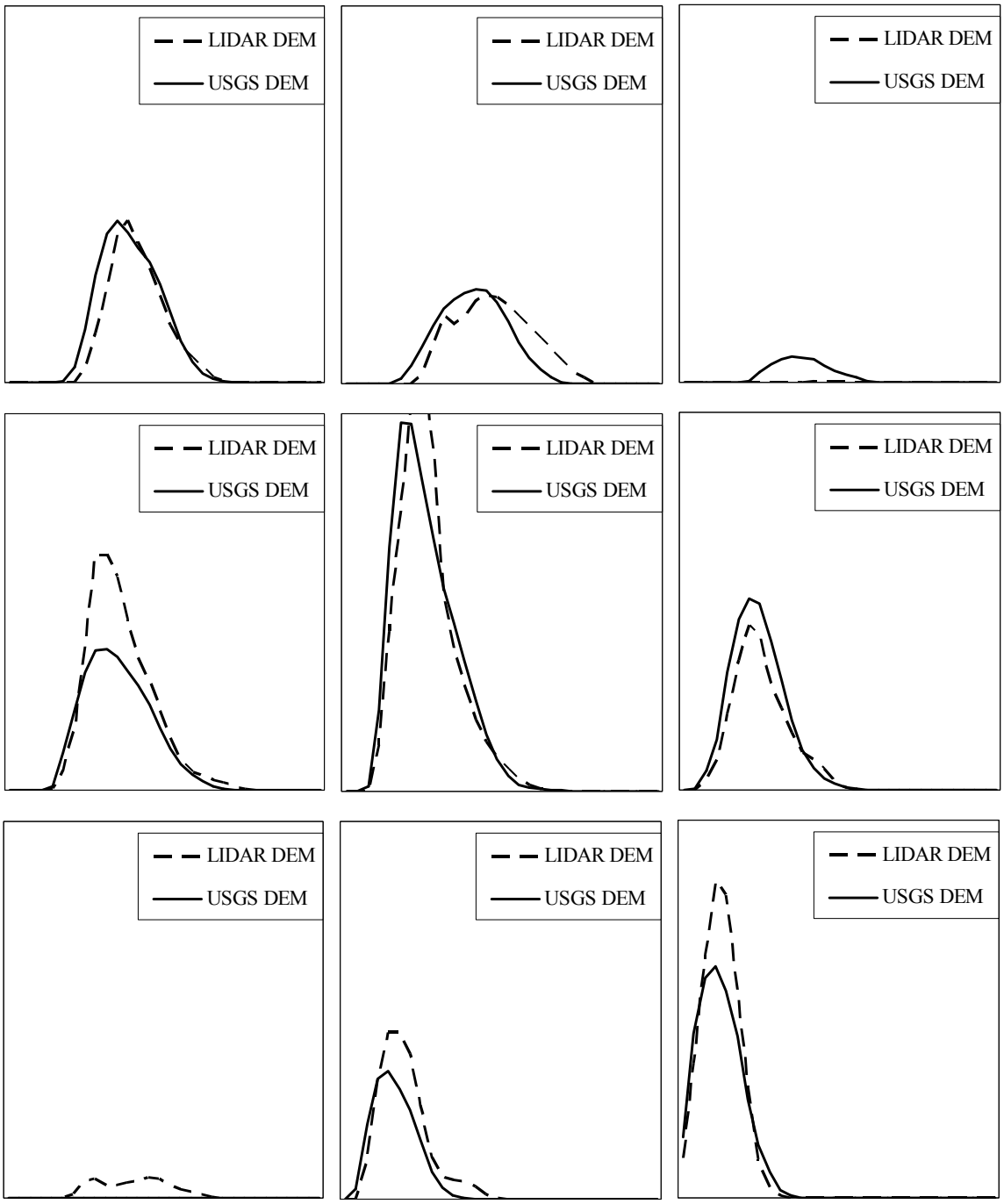

Fig. 3.12 Spatial comparison of the response functions of USGS and LIDAR DEM

3.2.7. Summary and conclusion

This research compared the traditional USGS DEM to the high resolution LIDAR DEM and their performance in a distributed hydrological routing model. The case study is selected in a low-lying and flat coastal floodplain. The delineated watersheds from these two datasets have about 16% percent absolute difference, although the size difference is very small. This suggested potential spatial discrepancy between the two datasets. It is found that USGS DEM is not adequate to describe local topographic changes due to its coarse spatial resolution and low accuracy. The slope values calculated from USGS DEM are dominated by zero-values. This is problematic because the routing model does not allow slopes to be zero. As a common practice, the zero-values are replaced using some arbitrary small values (e.g. 0.005 percent rise). However, since more than half of the areas will use arbitrarily assigned slope values, it introduces large uncertainty to the model. Sensitivity analysis results also suggested the same problems. Comparing the sensitivity of the slope threshold value of LIDAR DEM to the USGS DEM, it is found that the model becomes much more sensitive to this threshold value if USGS DEM is used. It is evident that from model calibration, the watershed response function curve from LIDAR DEM can be matched by the curve produced from USGS DEM using selected parameter sets. This suggested if carefully calibrated, both DEMs can create similar hydrographs which “fit” the observed discharges. However, spatial agreement of flow pattern determined from these two datasets is very poor although both of the models are calibrated. From all these results, it is concluded that for low-lying and flat areas, it is important to acquire high quality elevation data which is able to describe

spatial variations of topography and flow patterns. In such circumstances, if available, the high resolution DEM is recommended to be used in distributed models.

3.3. An object-oriented solution to assimilating high resolution DEM data

3.3.1. The computational difficulties in current distributed hydrological models

Distributed models compute simulation based on raster cells, while lumped models subdivides the basin into a limited number of sub-basins (Fig. 3.13). The increasing DEM resolution will consequentially cause a series of problems in the distributed model implementation and approximation. For instance, the finite difference solution of overland flow equations based on raster data structure has a restricted condition called Courant number (Courant et al., 1956), which is written:

$$T_{courant} < \frac{\Delta x}{(gh)^{1/2}} \tag{3.1}$$

where g = gravity acceleration, h = equilibrium flow depth, and Δx = grid size. If the computation time interval is longer than $T_{courant}$, the numerical solution of wave equations will be instable. It can be seen that with finer grid size Δx, $T_{courant}$ will decrease, and this demands a shorter time step for the model simulation. With shorter steps and larger data volume, the model will consume greater computational resources and in some cases causes computations to be impractical. For example, Bates and Roo (2000) developed a raster based distributed model to simulate the flooding in a 35km by 3km river floodplain which is rather smaller than the commonly defined “small watershed”. For their study area a 5m digital elevation model obtained from aerial

photogrammetry is available. However, the minimum spatial resolution they used in their analysis was 25m. They re-sampled the DEM into 25m, 100m, and 250m. Even using a 25m DEM, the simulation required a time step of less than 2s in order to obtain a stable output. According to the Courant condition, a 5m resolution DEM (as was available for their study area) would require the simulation time interval to be less than 1s.

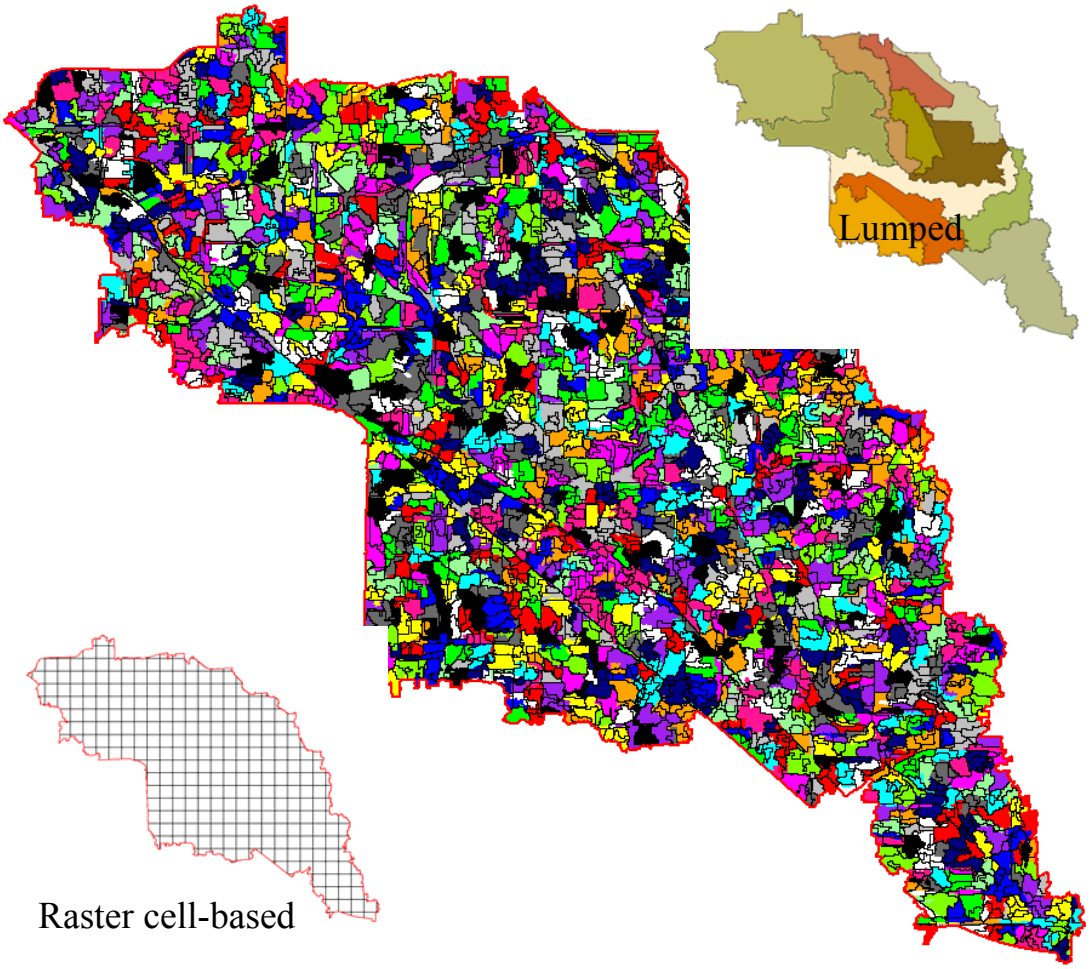

Fig. 3.13 Spatial objects from watershed segmentation

For this study, the flow path response function convolutes all the time steps. If the program simulates a 6-day event at a time step of 15 minutes, the convolution size of each flow path would be 576. A 600 km^2 watershed will have about 320,000,000 convolution computations. Since the LIDAR DEM has a typical cell size of 5m, the data volume may increase by a factor of 36 compared to the USGS DEM. Therefore the computation requirement would be massive. Experiments showed that one simulation would run more than half week. This will pose great difficulties for model implementation and calibration and makes the model very time consuming and almost impractical with current computation capabilities.

In hydrology studies, spatial scale is defined as "the sampling interval size at which hydrologic observations are made, or as the grid size used for numerical computations" (Singh and Woolhiser, 2002). In order to model the hydrologic processes, the models have to select an appropriate scale, and the scale should be "somewhat smaller than the topographically divergent hill slope length" (Zhang and Montgomery, 1994). LIDAR DEM provides much higher resolution than the traditionally used USGS 30m DEM. The grid size of LIDAR DEM could be approximately 1m to 5m. But the most important question is whether it is appropriate to use 5m as the basic unit size in our study. The selection of scale is always depending on users' experience or trial-and-error methods.

Hydrological models have various equations and theories for model processes in different land features such as overland flow, reservoirs, lakes, and in-channels flow. As pointed out by Liang and Mackay (2000) and Mackay and Band (1998), the locations of the river channels, reservoirs, and ponds are all treated as normal land area without any

differentiations. For an example, the CASC2D modeling system (Julien et al. 1995), which is a physically-based distributed model cited in many articles, solves the Saint-Vetant formula for every cell in the DEM. However, their approach treats each cell equally regardless the validity of the assumptions of the equation. As a matter of fact, for the areas of ponds, flat surfaces, detention basins, and reservoirs, the assumption of the physical equation has been violated. The linear reservoir model would be more appropriate for these areas.

Current distributed hydrologic models are constructed based on the raster or lattice data structures. Each element is treated individually using the same formulas but with spatially varying parameters. Therefore, the semantic information of the units and mutual interactions between those units are neglected. For example, each individual cell in a flat area is always forced to flow to some arbitrary locations. However, this tends to generate unrealistic flow patterns through the flat surface. Although research has been done to find solutions (for example, Martz and Garbrecht (1998)) no satisfactory solution of this flat surface problem has been discovered. Flat areas are very common in watersheds with “low-relief and flat topography” (Liang and Mackay, 2000). A flat area comprises a group of pixels with exactly the same elevation value. The hydrological models have difficulties in deciding where to drain the water because in each direction the slope is zero. A common practice to deal this problem is to force a flow through the flat area towards the outlet with the lowest elevation. Martz and Garbrecht (1998) developed a new method to improve the definition of flat area flow directions. However,

their method has defects that could not meet the requirement for large flat areas identified in the LIDAR DEM (Martz and Garbrecht, 1998; personal experiments).

3.3.2. Geographic Information Science (GIS) and object-oriented data models

Geographic Information Systems are rooted in computer cartography and digital image analysis and processing. Sui and Maggio (1999) described the GIS as "underneath its map metaphor is the implicit conceptualization of reality based on Newtonian mechanics". The problem with the data structure and concept of current GIS was identified by Goodchild (1992). The GISc community needs a solution of data structure beyond current definition of "Raster" or "Vector". Additionally, as pointed out by Maidment (1993), hydrologists are looking for comprehensive support from GIS to form an integrated GIS-Hydrologic modeling system. The current status of the relationship between GIS and hydrologic models was reviewed by Sui and Maggio (1999). They conclude that regardless of how GIS and hydrology models are coupled the models are not "fundamentally improved or put into a firmer foundation". Recognizing the limitation of the current data structure of GIS, Yuan (2001) proposed and implemented an object-oriented data model that can incorporate the concepts of objects and fields, as well as the time dimension. The research was successfully implemented in Arc/Info AML language and provided a pioneer advance to the future GIS data model. Object-oriented approaches can not only deal with object-based models but are also capable of handling field-based models. In Yuan (2001), objects were used to represent the storms, and store spatial varied precipitation rate. Although the temporal GIS has been investigated by many research works (Worboy, 1994; Peuquet, 1994; Raza and Kenz,

1999), “time is still not a dimension in GIS data models and framework” (Sui and Maggio, 1999). This is probably another factor that hinders the integration of GIS and hydrologic models.

Current hydrologic models are always self-contained, and the data structure is designed separately and therefore is not interchangeable. Recent research suggests that component-based approach is an ideal way for integration of GIS and hydrologic models because of its interoperability (Feng, 2001). Interoperability for a system or component is its portability through inter-application (Feng 2001). IEEE defines the interoperability as the “ability of two or more systems or components to exchange information and to use the information that has been exchanged” (IEEE 1990). Interoperability is established on the “layered architectures” such as JAVA, DCOM, COBRA, and RMI (Bernard 2000). If implemented in interoperable components, hydrologic models can be “plug-in” add-ons to GIS systems and replaced or renewed by alternative components for better performance or different functionalities. Although object-oriented models or data structures have no direct relationships with the component-based software architecture, the implementation of the data structure in object-oriented regime will be most suitable for the software development.

3.3.3.Object-oriented model framework design and implementation

The object-oriented concepts include the definitions of semantic meaning and inter-relationships between objects, such as topology. Objects are confined to their spatial boundary and not overlap to each other. Each object has specifically designed behavior according to their semantic definition and implementation. For instance, in hydrologic

models, reservoirs route water in a different way as a channel does. Although they share basic continuity and energy conservation concepts, the governing equations are totally different. Objects also are connected and interacted to each other. The relationship such as connectivity, proximity, and mass flow direction can be used to refine their behavior in models. In many cases, inside of the objects are regarded as black boxes or assume homogeneity once objects are defined. This simplified the model procedure because it only focuses on the output of the objects and their mutual relationships. Time dimension can be easily added to the system because it belongs to one of the natural characteristics of objects. For instance, for a hydrologic simulation, objects can easily release their output for a given time step according to the equation and behaviors predefined in the model.

Design of the object-oriented model includes generation of spatial objects and organization of the objects following their topology. In this research, spatial objects are assumed to be homogeneous inside but not black-boxed. Therefore, maintain their homogeneity is the major criterion to generate spatial objects. The principle behaviors of the spatial objects are the rainfall infiltration and runoff water routing. Therefore, the spatial objects are called hydrologic spatial units (HSU). To ensure homogeneity, segmentation techniques are employed to find the natural boundaries between HSUs. Segmentation is performed on the data of surface imperviousness, soil texture, and elevation model. A later section will detail these procedures.

Another component of the object-oriented model is the object topology. Topology is defined in this model by the flow direction. Upstream and downstream are the terms of

topology. A reservoir or detention basin receives upland flow and attenuates the flow to its downstream locations. First, the upstream area is identified and all the upstream elements are routed to the reservoir. And then, a linear reservoir routing model is applied to give an outflow. The outflow is routed again to the outlet to construct the watershed response function. Once the HSUs are constructed and their topologic relationship is set, the model is read to run. The number of elements is greatly reduced and the calculation is simplified. This will produce a hierarchic structure of the entire model as shown in Fig. 3.14. The lowermost element is the outlet. All the different types of units could possibly be routed directly to the outlet or through other units except a land object. The layered structure reveals the upstream and downstream relationship of these objects or units.

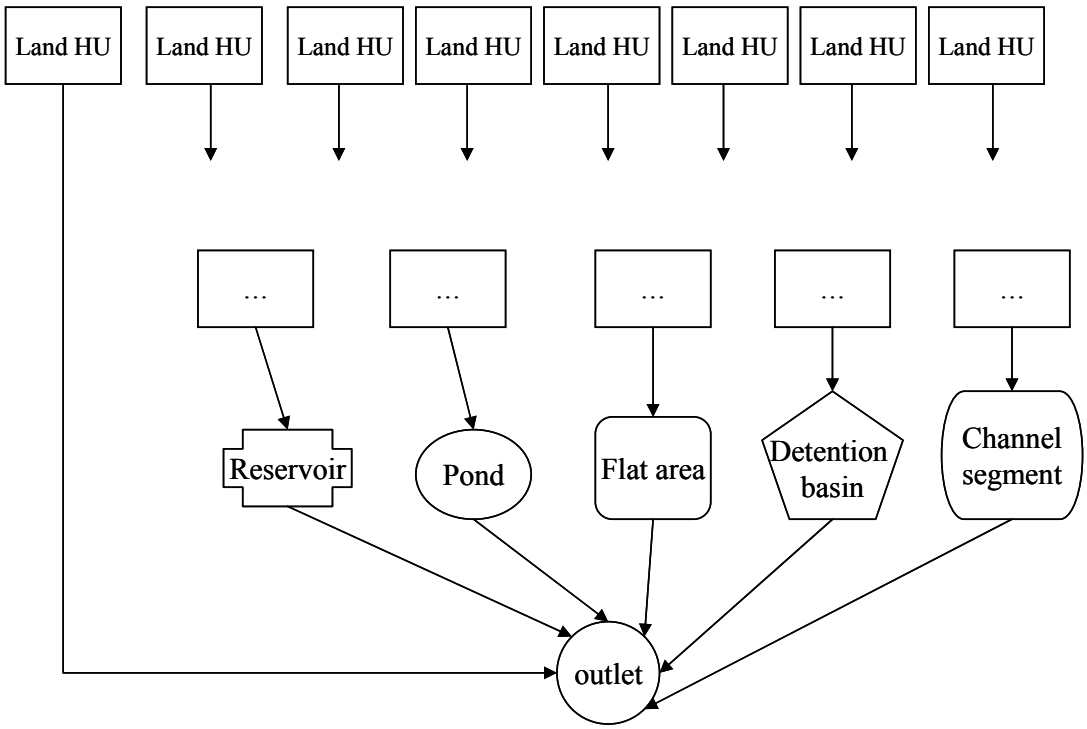

Fig. 3.14 The object oriented model framework

3.3.4. Image segmentation approach to constructing spatial objects

Constructing the objects consists of the processes of identifying the objects, assigning the attributes values, and building the relationships with other objects. Segmentation of an image is the process of partitioning it into regions that have different properties (Soille, 2002). Those regions can be treated as objects, and the relationships between these objects identified through spatial and geometric computations on the map. The general region segmentation approaches include techniques of gray level thresholding, region growing, region splitting, region merging, edge detecting, neural network method, or combination of any of these methods. The gray level thresholding method is easy to implement but only can be used for visualization purposes because of its inadequate accuracy. The region splitting or region merging itself also cannot satisfy the sensitivity and specifications of most applications. However, a combination of the region splitting, region merging, and region growing would create a powerful tool for image segmentation.

3.3.4.1. The globally optimization seeded region-growing and merging method

This algorithm is designed based on the well-known migrating means technique presented by Ball and Hall (1965). The normal region-growing method arbitrarily grows the seeds according to the sequence that the program scans the image. One seed dominates the region-growing procedure until some pre-set criteria is met. This method tends to generate regions that are aligned to the direction that the program scans the image. The results are not robust to the selection of the seeds, scanning direction, and noise in the data. The stop criteria are usually arbitrarily chosen. Sometimes it is difficult

to set feasible stop criteria because of noisy data. To avoid those problems, a modified method is designed called the globally optimized region growing algorithm. This allows the seeds to be grown with competition. In another words, only the region that has the minimum amount of increment in heterogeneity will grow. The mean and the standard deviation of a region are calculated. The heterogeneity is defined as the standard deviation. The increment of the heterogeneity is calculated as:

$$\Delta H_j = \frac{\left| Std(R_j) - Std(R_j^{'}) \right|}{N_j + 1} \tag{3.2}$$

where *Std(•)* represents the standard deviation of the region; N_j = the number of pixels in the region R_j; R_j represents the pre-growing region and $R_j^{'}$ is the post-growing region. The increment of the heterogeneity is the indicator of the likelihood of a region to grow. The process of the region growing is described by the following:

1) Initialize the seeds. The number of seeds is determined arbitrarily according to the complexity and size of the image. The number should be large enough to capture the minimum features that are to be detected. Each seed will be the core of a region. The means of the initial regions are equal to the seeds where they start growing. The standard deviation is 0 for any of the regions at the initial stage.

2) The neighbors of each region are compared to their neighboring regions. The increment of the region heterogeneity is calculated for each neighbor and the minimum value is determined. All the regions are compared and the one with the lowest value of the increment of heterogeneity is selected for the growing.

3) The region that grows will have a new mean and standard deviation. This is called "migrating means". Then the increment of heterogeneity of this region is re-evaluated and the new candidate to grow is selected until all the pixels are included to the regions.

The number of the seed points is selected to be relatively dense. It means no new region is required to be generated furthermore. Every pixel in the image will belong to one of the regions already allocated. In this case, the stop criterion is not necessary, as is for normal region growing techniques. The algorithm stops only when all the pixels are grown.

After the region growing operation, the image has been segmented into regions (Fig. 3.15). The total number of regions is pre-set. The difficulty is that, because the location and the number of the seeds are arbitrarily selected, the regions may be too small to grow. Further region merging is necessary to remove small regions and to form the final segmentations that meet the user's requirement. The merging process also follows the globally optimized rule: the region that has the smallest increment at the heterogeneity will grow first. The function of the heterogeneity change is described as:

$$\Delta H_j = \frac{\left| Std(R_j \oplus R_{ji}) - Std(R_j) \right|}{N_j + N_i} \tag{3.3}$$

where R_{ji} = the *ith* neighbor of region *j*; $\oplus$ represents the merge operation; N_j and N_i are the number of pixels in region *j* and region *i* respectively. Criteria are needed to prevent the region merging to be overdone. The shape compactness and the heterogeneity are the two stop conditions: if either the heterogeneity or the compactness is out of the range, the merging will not be performed. The entire process will stop after all the regions

cannot satisfy the two criteria. By controlling the stop criteria, a multi-resolution segmentation will result. The best representation of the objects can be selected among the multi-resolution segmentations. Fig. 3.15 shows the procedures of segmenting the surface imperviousness map.

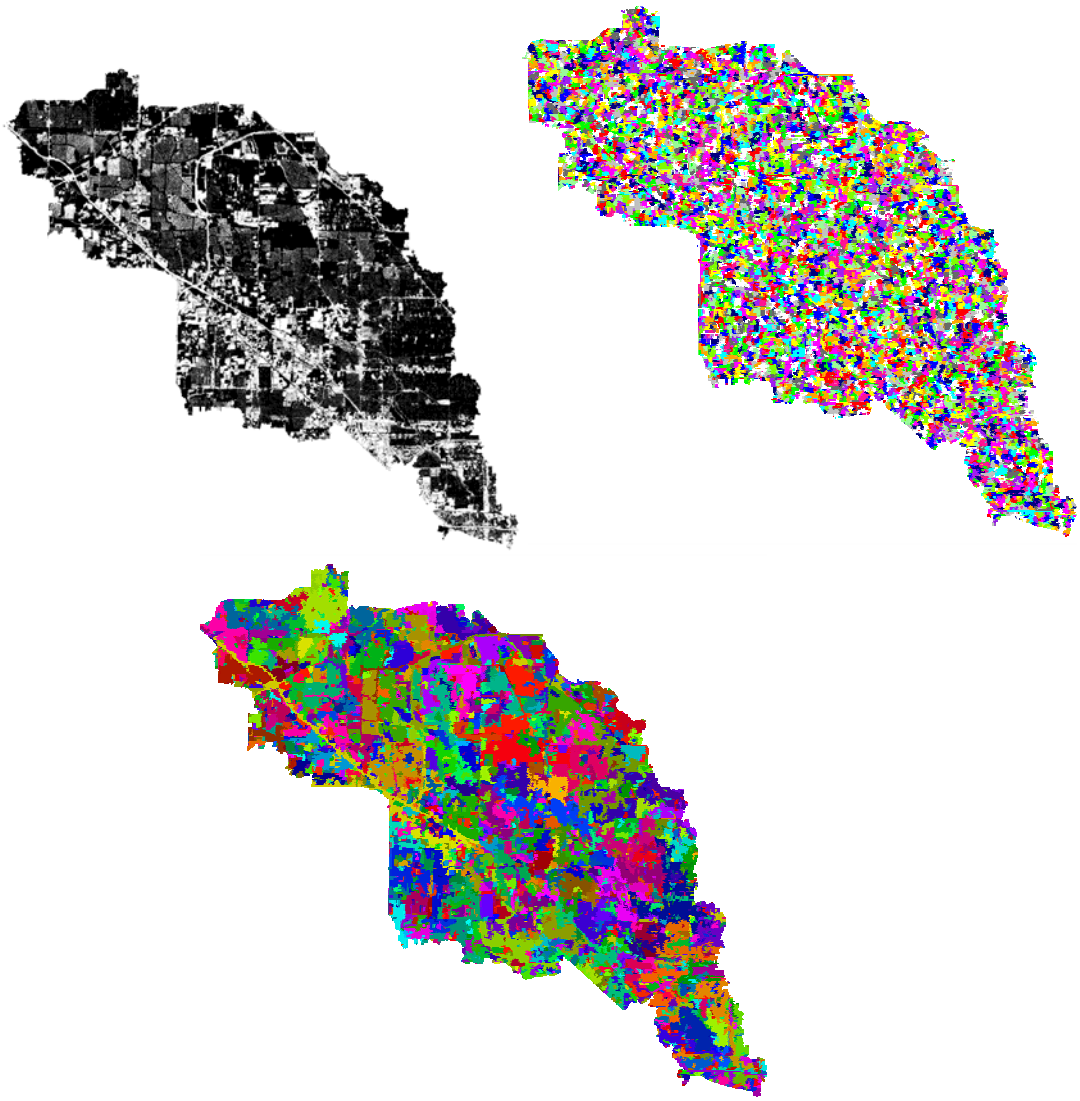

Figure 3.15 Segmentation of surface imperviousness

3.3.4.2. Sub-watershed segmentation method

The parameters for the hydrologic units include variables to calculate the Green-Ampt infiltration and those for the watershed response routing model. The most variable parameter among them is T described in section 2.3 equation (2.23) because it is estimated using the DEM. If the objects are generated through regular segmentation, they tend to be small pieces of objects. The data of images that contain T are very large because of the LIDAR DEM's massive data volume. The region-growing-and-merging algorithm is not appropriate to these datasets because it is expected to have large heterogeneity which violates the pre-assumptions of the region-growing methods. However, a clear pattern of the T values exist that they follow the flow direction determined from the LIDAR DEM. In other words, T increases when tracing it downstream. Furthermore, since the objects in the model are hydraulically connected, upstream or downstream, segmentation following the natural flow direction can preserve the topologic relationship among the objects. From these considerations, an algorithm called sub-watershed segmentation method has been developed and can be described as follows:

1) Identifying the source pixels. The sources are defined as the pixels with NO upstream neighbors. These sources are the most upstream pixels defined by the DEM. The sources are the seed-points of the sub-watersheds (regions). The initial value of the region mean is same as the value of the source, and the initial value of the region variance is set to be zero. The sources are put into a first-in-first-out (FIFO) queue waiting for processing

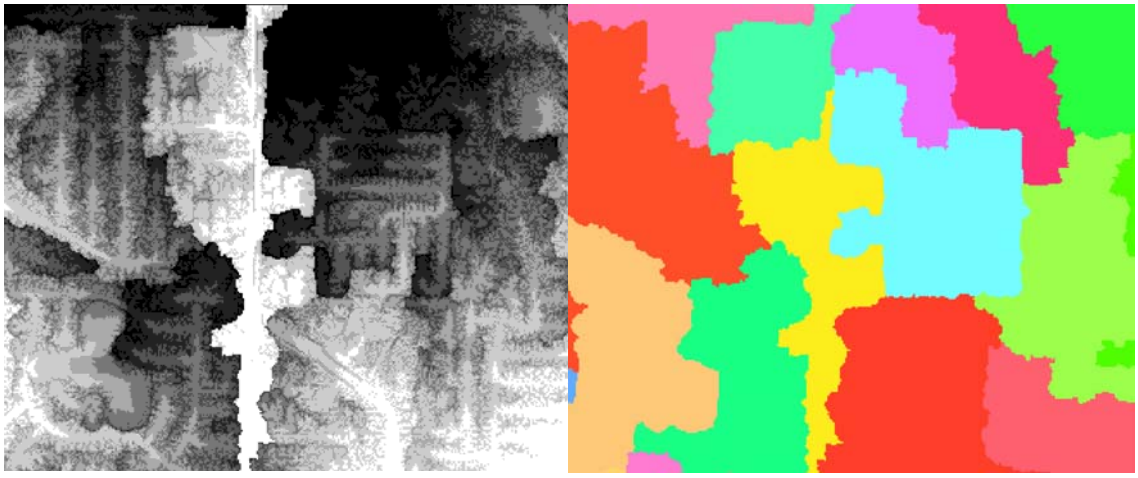

Fig. 3.16 Sub-watershed segmentation method. Left is the T value in gray scale.

Right is the segmented sub-watershed

2) Starting from each source (take them out one by one from the queue), check the variance of the sub-watershed seeded by it. If the variance exceeds a specific threshold, the segmentation of one sub-watershed is finished. And the mean and variance is set to the initial values. Otherwise the mean and variance will be inherited by the intermediate downstream neighbor.

3) Check the intermediate downstream pixel. If the downstream pixel has only one upstream pixel which is the current pixel, the downstream pixel is marked as a new source pixel and put into the FIFO queue to be processed. Otherwise, current pixel is removed from the upstream neighbor list of the downstream pixel.

4) Repeat 2) and 3) until it reaches the outlet or the FIFO queue becomes empty.

Fig. 3.16 shows an example of this algorithm. The left map shows the spatial variations of the T value. Due to the high resolution of LIDAR DEM, the streets at

community level can be seen. It will be very difficult to apply regular segmentation methods. The right picture of the Fig 3.16 is the segmented map. From this map, we can see that the result satisfies visual examination.

3.3.4.3. Object-based multiple-layers overlay

The different segmentation results in several sets of objects defined by the parameters from the soil properties, surface imperviousness, and routing parameters. However, only one partition of the area is allowed in order to assign the values to all the parameters. The overlay techniques are applied to generate smaller sub-objects of all the segmented images. "Sub-object" means the object in the final partition map is a sub-area of the object in any of the map parameters. The overlay operation, nevertheless, will generate overly narrow (sliver) or small regions that are not necessary in order to keep overall homogeneity. These sliver or small regions can be removed by checking the shape descriptors of the objects/regions. Compactness is one indicator of the shape. It is calculated as:

$$C = \frac{4\pi A}{P} \tag{3.4}$$

where C = the compactness, A = the area of the object, P = the perimeter of the object. The perimeter of the region can be estimated using chain code. The areas of the objects are also examined. Objects that can not meet the criteria will be removed and merged into the neighbor that shares the longest boundary with it.

3.3.4.4. Accuracy assessment of the object-segmentation

Since the segmentation involves generalization of the parameter values, to be specific, for the infiltration model and routing model, it is necessary to investigate how much

information has been lost due to the approximation. Generalization of the parameters is the process of replacing parameters for the entire object (segmented region) with the mean value of all the parameters. For example, if the mean travel time T is to be generalized for the object, the mean value of all the pixels enclosed in that object will be used for the routing model. As illustrated, changing the mean travel time directly modifies the PDF of the flow path, and therefore results in differences in discharges at the outlet. To assess the magnitude of potential errors, an instantaneous inflow was added to the routing model and the outlet hydrographs were compared. The simulation was run on both the original cell-based model (from LIDAR 5m DEM) and the segmented model (5051 objects were obtained through segmentation). The simulations were conducted at a 15min time step for 12 hours. The resultant hydrograph is shown in Fig. 3.17. By comparing the hydrographs, we can see that differences between the generalization and segmentation are small. The correlation coefficient R is larger than 0.999 and the average error is 1.4%. While the error is relatively small, a significant improvement of model computation performance can be seen. The number of units that need to be calculated in the model has been reduced by almost 2000 times. Before segmentation, there are a total of 9,057,358 cells. After segmentation, there are only 5051 units to be computed.

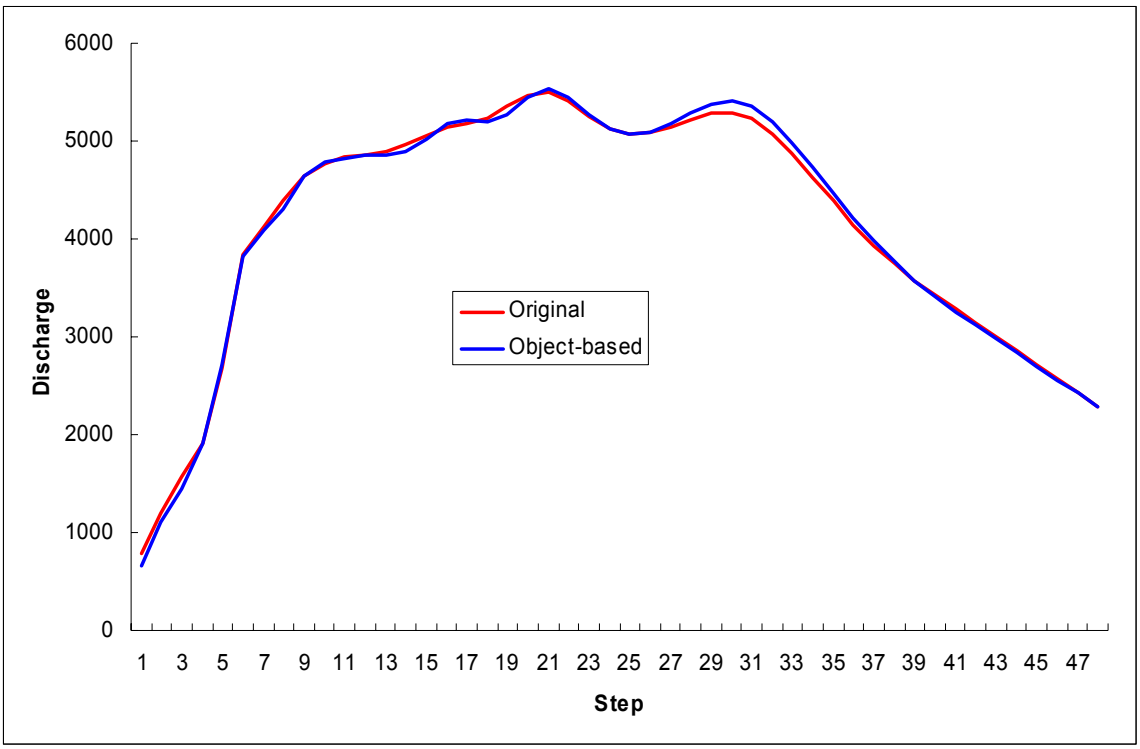

Fig. 3.17 Comparing the object-based model and raster-based model

3.3.5. Detention basins as spatial objects

It is generally accepted that detention basins are effective facilities to migrate storm-water flood risk and damages. However, only a few publications are available (e.g. Emerson, 2003; Coon, 2003) that quantify the performance of the regional flood detention basins using hydrologic models. The main purpose of building detention basins is to temporarily hold the flood water before the channel discharge reaches a certain level. Six regional detention basins were constructed in my study area during the 1970s by the Harris County Flood Control District (HCFCD). It was reported that the detention basins were filled with floodwater during the Tropical Storm Allison of 2001 (HCFCD and FEMA, 2002). The hydrograph shown in Chapter II and Fig. 3.18 is based on the model without detention basins. However, there is an obvious inconsistency in the hydrographs of the first and second rainfall event during the storm. The peak flow of the second event is too high comparing to the measured value. If we calibrate the second event so that the peak flow does not reach such high values high, we have to sacrifice some of the accuracy of the first event. The design of the detention basins requires them to work at a specific returning frequency of flood. For example, a 100-year detention basin is designed to work efficiently if flooding occurs once per 100 year. The first rainfall event is not very significant compared to the 100-year event. The detention basins may only start functioning at the second event. This could be why the simulated peak needs more attenuation. It would be a productive area of research to investigate how much the peak can be attenuated by inducing the detention basins into the model.

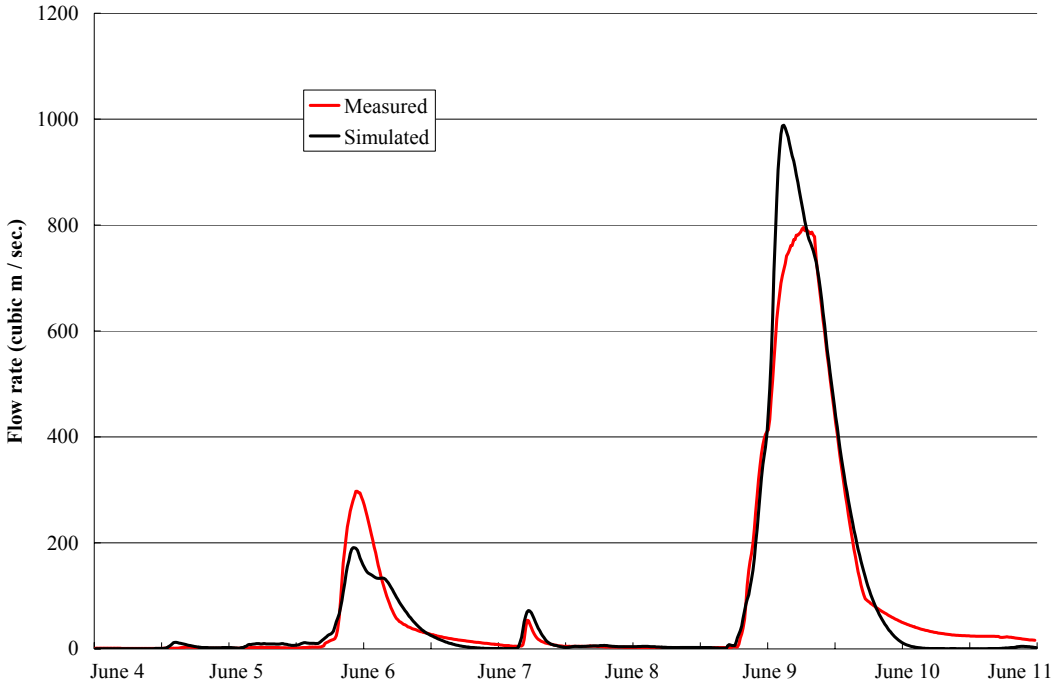

Fig. 3.18 Simulated hydrograph without detention basins

In the object-oriented model describe in 3.2. The detention basins can be incorporated into the model as one of the hydrologic units. The only difference is that the detention basins belong to "collectors" which requires knowledge the upstream areas. Once the upstream area is determined, the detention basin can be simulated using a continuity equation:

$$\frac{dS}{dt} = q_{in} - q_{out} \tag{3.5}$$

where S = volume of water stored in the detention basin or the reservoir; q_{in} = inflow rate; q_{out} = outflow rate. If the relationship between the storage volume and the outflow

rate is known, there are no unknowns in equation (6) and the outflow rate and storage volume in the detention basin can be solved. Therefore, solving equation (6) involves constructing the storage-outflow relation of the detention basin. With LIDAR technology, very detailed description of the detention basin geometry is available without costly and elaborate field surveys. The storage-level table of the detention basin is retrieved from LIDAR DEM using the procedures described in Chapter IV. A field survey of the sites also obtained information about the outlet (orifice) in the basin that is connected to the channel. Then the outflow of the detention basin can be calculated as (Bedient and Huber 2002):

$$Q_{or} = C_d A_0 \sqrt{2g(h - h_0)} \tag{3.6}$$

where Q_{or} = outflow rate generated at the orifice; C_d = the discharge coefficient which depends mainly on the geometry (Bedient and Huber, 2002); A_0 = area of the orifice; g = gravitational acceleration (9.8m^2/s); h = water surface elevation (WSE); h_0 = the elevation of the orifice center line. A_0 and h_0 are measured through field survey. According to Bedient and Huber, 2002, C_d ranges from 0.62 to about 1.0 for well-rounded entrance. Since the orifices I surveyed are very close to round shapes, the C_d chosen for the model is 0.9. Applying this equation gives the relationship between water level in the detention basin and the outflow rate in the orifice.

Once the inflow and outflow of the detention basins can be calculated and manipulated, the outflow of the detention basin can be further routed to the outlet using the same routing model in Chapter II. This is also described in the object-orient model structure in section 3.2. More detailed description and results of modeling detention basins can be find in chapter IV.

3.4. Summary and conclusions

This chapter mainly focused on the spatial resolution and accuracy issue of DEM in a distributed hydrologic model and the design and implementation of an object-oriented model framework. Traditional USGS DEM has large amount of disagreement with the high quality LIDAR DEM. It cannot depict subtle variation of topography of a low-lying and flat coastal floodplain area. The watershed boundary derived from the USGS DEM has nearly 20% difference to the LIDAR DEM. This suggested potential problem if spatially varied rainfall is applied to the model. Sensitivity analysis of model routing parameters suggested that using the traditional USGS DEM may introduce large portion

of uncertainty to the model. Using high quality DEM could introduce problems too. The direct consequence is the massive computation load that data brings. Grid cell based distributed model could not have spatially varied scale because the size of analysis must remain constant. Development of GISc theories and the blooming of GIS-based hydrological modeling prospective suggested the object-oriented model framework may represent an opportunity for GIS and for its based models. I developed an object-oriented framework and implemented the distributed model based on it. The spatial units for analysis are generated from segmentation techniques to maintain homogeneity within each unit. The validation shows that object-oriented model only introduces less than 5% error but reduces the computation requirement by nearly 2000 times. Model is also able to incorporate detention basins as spatial units for modeling. Furthermore, object-oriented models are easily to be merged or dismissed so the study area can be expandable or altered.

CHAPTER IV

DETENTION BASIN ANALYSIS

4.1. Introduction

Stormwater detention basins are built to temporarily detain high peak flow of flash floods and non-point source pollutant. According to the definition of National Resources Conservation Services (NRCS 2006), a detention basin is "an impoundment or excavated basin for the short term detention of stormwater runoff from a completed development area". From the design point of view, the detention basins are constructed so that the release rates of the floodwater can be comparable to the pre-development level. There are two types of detention basins: dry basins and wet basins. Wet basins are always having a "wet" bottom which are also called "detention pond". The existence of pool water enables physical and biological processes that help to remove pollutants. Extended wet basins allow extra capability to store storm water and elongate the time the pollutant to be settled down. Dry basins are mainly designed to mitigate storm water when flood reaches the designed level. At normal status, dry basins do not retain water until excess water from upstream fill in them. Dry detention basins are required to release temporarily retained stormwater at a certain rate, typically within 24 hours.

Detention basins are one of the Best Management Practices (BMPs) structures which include other facilities such as infiltration trenches, pits, porous pavement, rooftop storage, and Grass swales (Tsihrintzis and Hamid, 1997). Comparing to other structures, detention basins are cost-effective (Coon and Johnson, 2005) and flexible to meet a

variety of design requirements. By constructing detention basins, flood peaks are expected to be attenuated and delayed. For instance, as reported in Coon and Johnson (2005), the peak discharge was reduced by 18.1% by including detention basins into the simulation model.

Most publications and reports about stormwater detention basins were focused on planning and designing of detention basins, such as site selection (Elliot, 1998), cost (Harrell and Ranjithan, 2003), and storage-outflow curve (Guo, 2004). Efficiency and effect of existing detention basin on attenuating flood water are rarely discussed. This might be attributed to the difficulties to acquire measurement of geometric shape and storage capability of the detention basins. To obtain storage-outflow curve of detention basins, Emerson et al. (2003, 2005) measured about 100 detention basins from ground survey. The topographic properties were measured using the Incremental Storage method. This method includes "pacing off the dimensions by foot and measuring the side and bottom slopes with a lock level and surveyor's tape" (Emerson et al., 2005). Obviously, it requires intensive survey activities which are tedious and costly, and there is no validation can be performed to control the accuracy of the field measurements. The other difficulty related to hydrological modeling the detention basins is the lacking of appropriate models. Current documents and software for modeling detention basins in a hydrologic model are usually based on the modified plus model (level-pool model) for reservoir routing. This is based the assumption that the detention basins work as regular reservoirs built to attenuate upstream inflows. In the modified plus model, equations of mass conservation and flow continuity are applied to simulate inflow, outflow, and

storage volume of detention basins. This approach tends to neglect the differences between detention basins and reservoirs, such as the location, size, capacity, and the rationale how a detention basin attenuates flood water. There are several differences between a regular reservoir and a detention basin can be addressed. In term of connectivity with channels, detention basins can be “on-line” or “off-line”. An on-line detention basin works like reservoirs which attenuates water by routing water though it. The ability to reduce peak discharge relies on capability and storage-outflow curve. Off-line detention basins do not allow water to be routed through directly. They are connected to channels through pipelines and floodways. They only attenuate floods that exceed designed returning frequency. When excessive floodwater passes, detention basins receive floodwater from the emergence floodway. Obviously, this type of off-line detention basins do not work the same way as reservoirs. Therefore, a simple modified plush model is not suitable to simulate such detention basins.

Unlike reservoirs, detention basins are normally smaller and shallower since they are always built within city limits in relatively flat terrains. In another words, capacity of detention basins is one of the limitations for them to effectively reduce flood peaks. They have to be carefully designed to maximize their ability to reduce flood peaks. In most cases, multiple detention basins are constructed along the channels to meet the designed requirements of flood mitigation. Since the ability to attenuate flood peak flows is one of the main reasons to construct floodwater detention basins, it is interesting to know the actual effects of them. There were several researches focused on this issue. For example, as reported in Emerson et al. (2003; 2005), the watershed-wide peak flow was

reduced by an average of only 0.3%. However, contradictory to common knowledge and others findings, one of the peak flow was even enhanced because the peak flow of the original untenanted flow was coincided with the receding limb of the flow from the areas attenuated by the detention basins (Emerson et al., 2005). Therefore, the questions are: "what is the appropriate model to simulate a detention basin?", "Can we use other sources of data to measure the geometry of the detention basins so that they can be incorporated into hydrological simulations?", "What happened to downstream after construction of detention basin?", and "how much the flood risks have been reduced?"

4.2. Quantitative information on detention basins from LIDAR data and IKONOS imagery

4.2.1. Overview

Detention basins are the landforms of impounded earth surface. This type of landform is rare or absent in most natural terrain types (Mark, 1983). This is because fluvial erosion does not normally produce such types of features. The detention basins can be detected as surface depressions from the LIDAR DEM, because they are not hydraulically connected with outside river channels. The floodway structure and surrounding highlands form an impounded terrain which causes a detention basin to become surface depressions that are detectable from digital elevation models. Once the footprint of the detention basin is extracted, the important relationship that is used to quantify the capability of the detention basin, the storage-level relation table, can be retrieved from the LIDAR DEM.

As discussed above, detention basins can be considered as a special type of surface depressions. Therefore, they can be identified using the surface depression deification method described in chapter II. The results of surface depression identification include not only the location of the surface depressions, but also the depths to be filled. The depth information is essential for the consequential quantitative studies because it reveals the capability that a detention basin temporally retains water due to channel blocking from floodwater. The capability of detention basins to hold floodwater at designed returning frequency of rainfall events is a measure of how successful a detention basin design is. However, due the difficulties to quantify this information from field surveys or any other conventional methods, modeling the detention basins is limited by the availability of the quantitative information of them. Even their geometric parameters may be obtained from the design manuals or documentations, the data may need to be re-acquired after a certain time period because sediments and regular maintenance will gradually modify their capacity and hydraulic properties.

4.2.2. Delineating detention basins

4.2.2.1. Identifying surface depressions

Detailed topographic information is of fundamental importance to automated recognition and measurement of detention basins. Elevation model acquired by LIDAR technology has been proven to be one of the best quality data available in US. Vertical measurement of LIDAR could reach a RMSE of less than 15cm. High spatial and vertical resolutions provide opportunity to identify detention basins from elevation models. As shown in Fig.

4.1, three large detention basins are clearly depicted by the elevation data. As well other features such as river channels, streets, ponds, and other subtle topographical features are visually recognizable.

Fig. 4.1 LIDAR DEM shows the detention basins

Surface depression filling algorithm describe in chapter II is used to identify surface depressions and other topographic features. The results can be visually examined in Fig. 4.2. Fig. 4.2a illustrates the distribution of the identified surface depressions which can be visually examined against Fig. 4.2b, the hillshaded elevation model. As can be

observed from Fig. 4.2a, not only ponds and detention basins, but also some linear features such as streets and channels are present in the map. By subtracting them from the background (no depression area), these features can be recognized as spatial objects, which are comprised by connected cells with similar values (depth of depression). Therefore, they can be quantitatively measured by their shape and geometric properties. Detention basins commonly have regular geometric shapes with a smooth boundary, such as rounded rectangle, oval, or rounded trapezoid shape, and they also have relatively large depth and surface area. Although river channels may be also quite deep, they can be distinguished from detention basins by their distinctive narrow and elongated (meandering) linear shape. Depressed streets have a shallow depth, and they either appear as individual linear segments or connected cul-de-sac, gridiron, or dendritic pattern. Artifact depressions commonly have a shallow depth and an irregular and rough boundary (amorphous shape). The significant differences in geometric and shape attributes provide diagnostic clues that can aid discrimination of detention basins from depressed streets, river channels, and depression artifacts.

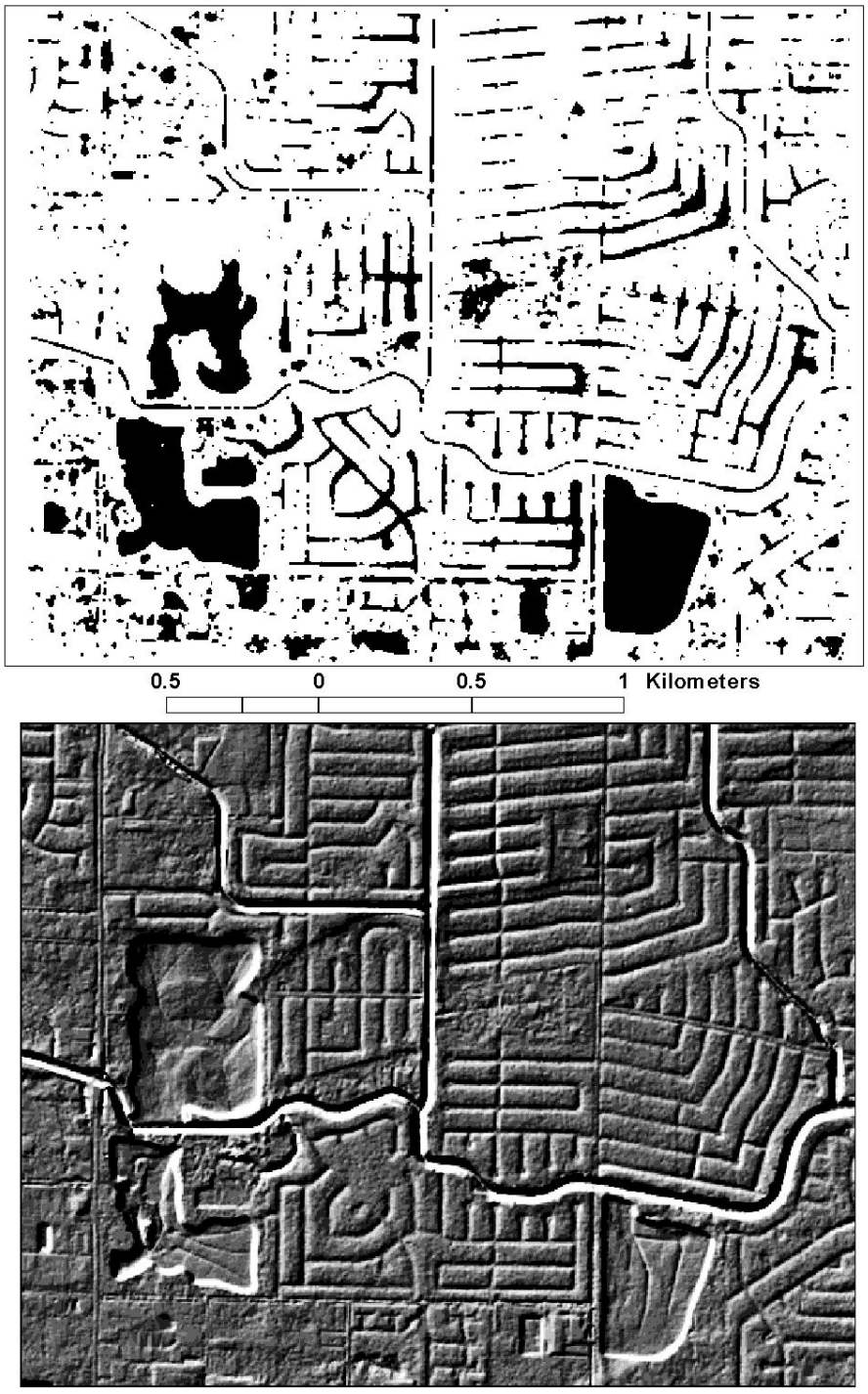

Fig. 4.2 Surface depressions derived from LIDAR DEM

4.2.2.2. Discrimination of detention basins from other types of surface depressions using a decision-tree

A two-pass blob coloring algorithm (Sonka et al. 1999) is employed to delineate discrete surface depression objects. The blob algorithm labels each spatial object incrementally with a unique ID number, starting from 1. The largest integer label gives the total number of surface depression objects. I derived three categories of spatial attributes for each depression object, including planimetric attributes, depth and volumetric attributes, and the shape attributes (table 4.1). Among planimetrtic attributes are geographical location of centroid point, perimeter (boundary length), mean distance to centroid, maximum distance to centroid, mean distance to boundary, and areal size. Depth and volumetric attributes include mean depth, maximum depth, standard deviation of depth, and storage volume of water detention capacity. Shape attributes include compact index, circularity, eccentricity, elongateness, shape complexity, length/width ratio, area perimeter ratio, and invariance moment variables. The definition of these spatial attributes and their values for some typical geometric shapes are listed in table 4.1.

Table 4.1

Geometric properties calculated for surface depression objects

Name	Equation	Description
Size (A)	$A = n \bullet w^2$ w: width of a cell in the map, n is total number of cells in the object	The area occupied by the object
Boundary length (P)	P = The number of pixels located on the boundary	Circle: 2πR (R is radius) Square: 4a (a is width)
Compact index (CI)	CI = $P / 4\sqrt{A}$ where P is boundary length, A is size of the object	Circle: $\frac{\sqrt{\pi}}{2}$ Square: 1
Mean distance to boundary (MDB)	$MDB = \frac{\sum_i^n d_i}{n}$ where d_i is the distance from point i to the nearest boundary, n is the total number of points	Circle: 2R/3 Square: a/6
Shape Complexity (SC)	SC = A/MDB^2 where A is size of the object, MDB is Mean Distance to Boundary	Circle: 9π/4 Square: 36
Length width ratio (LWR)	LWR = λ_1 / λ_2 where λ_1 and λ_2 are the eigenvalues of covariance matrix of coordinate of the image. λ_1 is the length of major axes. λ_2 is the length of minor axes.	Circle: 1 Square: 1
Area perimeter ratio (APR)	APR = A/P where P is boundary length, A is size of the object	Circle: R/4 Square: a/4)
Circularity (CI)	$P^2/4\pi A$ where P is boundary length, A is size of the object	Circle: 1 Square: 4/π
Eccentricity (EC)	EC = $\frac{(\mu_{02} - \mu_{20})^2 + 4\mu_{11}}{A}$ where $\mu_{pq} = \sum_i \sum_j (i - \bar{x})^p (j - \bar{y})^q$ i , j correspond to coordinates of cells inside the object; A is size of the object	Circle and Square: 1 Rectangle: less than 1
Maximum distance to centroid point (MDC)	MDC = $\max_i dc(i)$ where dc(i) is the distance from centroid to cell i	Circle: R (R is radius) Square: $\frac{\sqrt{2}a}{2}$
Mean distance to centroid point (MEDC)	MEDC = $\frac{\sum_i dc(i)}{n}$ where dc(i) is the distance from centroid point to cell i; n is the total number of points	Circle: R (R is radius) Square: 7a/12
Maximum depth (MAXDP)	MAXDP = $\max_i \{dp(i)\}$ Where dp(i) is the depth of cell i	
Mean depth	$\frac{\sum_i^n dp(i)}{n}$ where n is the total number of cells.	

The combination of the derived spatial attributes forms an m-dimensional attribute vector for each depression object. The attribute vector gives a comprehensive description and quantification of spatial characteristics for surface depression objects. A classification attempt is then made to discriminate detention basins from other types of surface depressions based on the attribute vector. From visual interpretation and local knowledge, four classes are determined: detention basins and ponds, streets and roads, channels, connected streets, and artifact depressions (Fig. 4.3). Then, a decision-tree method implemented in the data mining software tool C5.0 (Quinlan 1993, Quinlan 2004) to classify the surface depression objects. The decision tree method is one of the most efficient inductive machine learning techniques. Compared with traditional classification methods such as maximum likelihood and linear discriminate function classifiers, the decision-tree method has a number of advantages. As a non-parametric classifier, it makes no assumption regarding the distribution model and its parameters for input data. It is also robust with respect to nonlinear and noisy relations among input attributes and class labels. The spatial attributes for surface depressions generally do not follow the normal distribution, and certain level of linear or non-linear relation exist among these attributes and between attributes and class labels. Therefore, for the surface depression classification, the decision-tree method is a better choice than the commonly used maximum-likelihood classification method, which assumes the normal distribution of input data. In addition, explicit and intuitive classification rules derived from decision-tree method can be easily comprehended and validated.

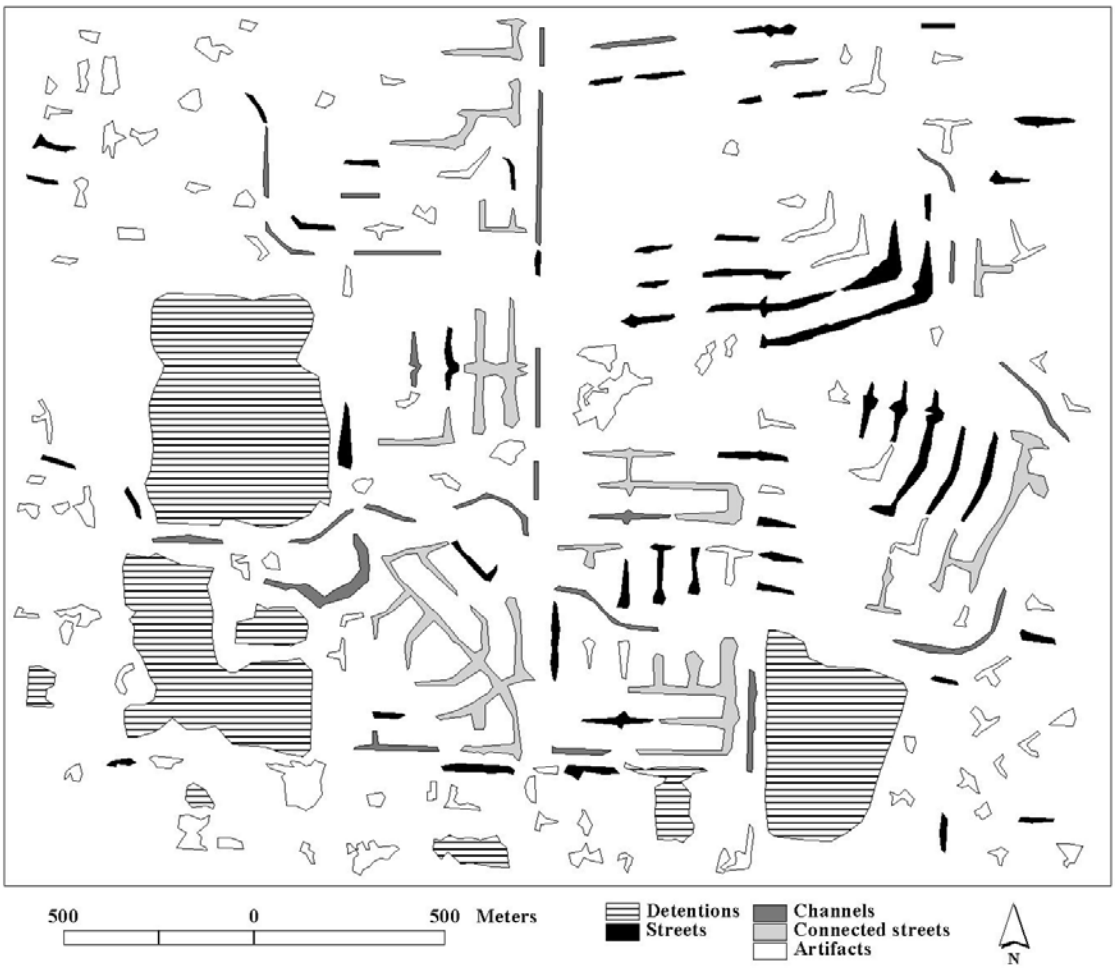

Fig. 4.3 Defined spatial objects from the surface depressions

The decision-tree based classification involves several operational steps: preparation of training data, selection of informative attributes, creation of decision tree, generation of decision rules, modification of decision rules with human knowledge, assignment of class labels to surface depression objects, and evaluation of accuracy. As an inductive machine learning technique, the decision tree method requires only a small set of good examples as training data. The decision rules that are generated by C5.0 software is

illustrated in table 4.2. The decision rules are then applied for automated recognition and inference of different type of surface depression. The resultant classification is evaluated based on a test dataset selected from my study area. A confusion matrix (table 4.3) shows the detailed breakdown of correct and incorrect classifications. The overall classification accuracy is 89.1%. The detention basins and ponds of the entire watershed are extracted using the decision-tree method, as shown in fig. 4.4.

Table 4.2

Decision rules from C5.0

Rule#	Conditions	Result
1	Asymmetry <= 0.928 and Maximum depth > 39.75cm	Detention and poinds
2	Boundary length <= 775m and Asymmetry > 0.928	Streets and roads
3	Boundary length > 775m and Asymmetry > 0.928	Channels and rivers
4	Shape complexity > 163.265 and Asymmetry <= 0.928	Connected streets
5	Shape complexity <= 163.265 and Asymmetry <= 0.928 and Maximum depth <= 39.75cm	Artifacts

Table 4.3

Classification results of testing data

	Detention	Street	Channel	Connected streets	Artifacts	Total
Detention	8		1		1	10
Street		13	2		2	17
Channel		2	4			6
Connected streets				20		20
Artifacts		1			28	29
Total	8	16	7	20	31	82

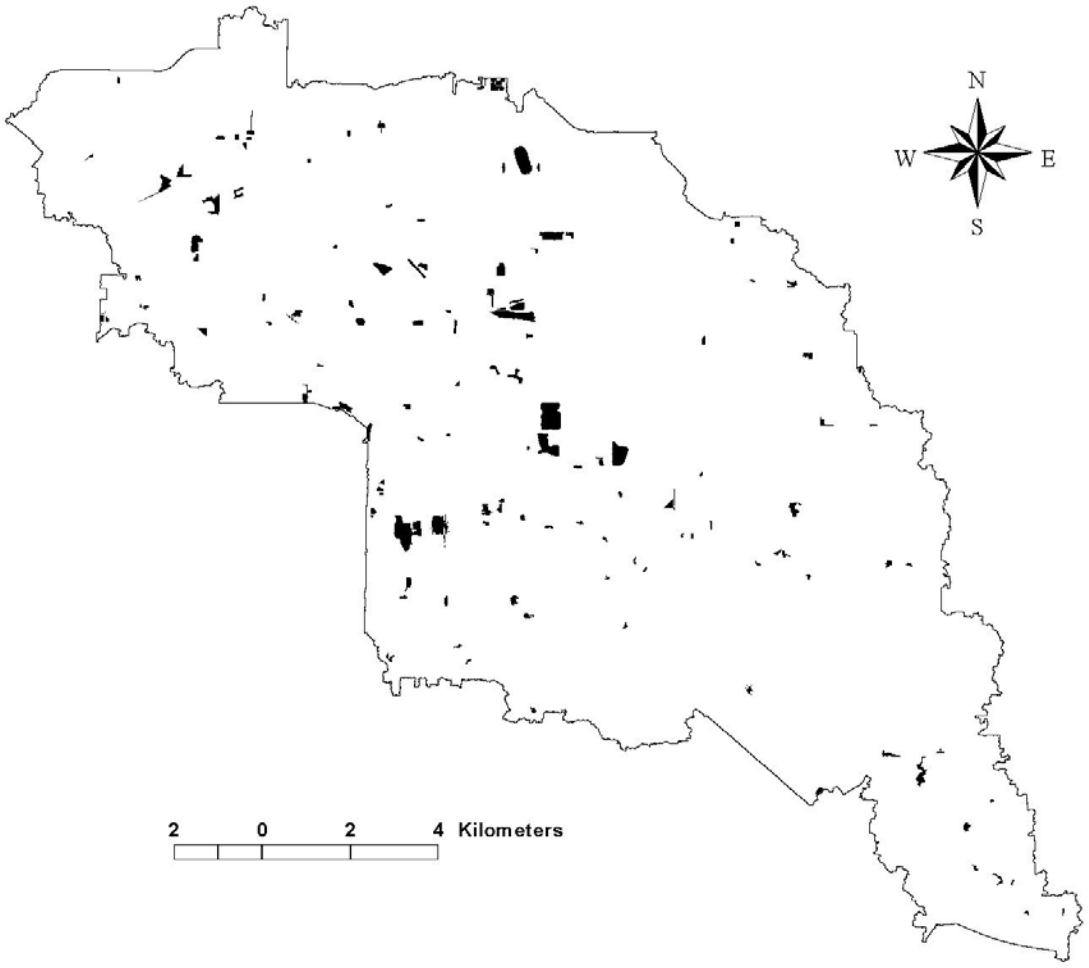

Fig. 4.4 Detention basins and ponds derived from surface depression classifications

4.3. Implementation of the flood water detention basin in the model

4.3.1. Literature review

Detention basins have been recognized as the "premier" means to attenuate peak flows (Traver and Chadderton, 1983). They are always simulated as standard reservoirs using a level-pool model. From examples, USGS (1999) employed HSPF model and a hypothetic detention basin to quantify the further development of Ninemile Creek Basin

in Onondaga County of New York. They found that by adding a detention basin, the peak discharge could be reduced to the pre-development status. In another research work, Emerson (2003) analyzed the additive effects of storm water detention basins in Valley Creek watershed in Chester County of Pennsylvania using HEC-HMS hydrological modeling software. However, his findings were contrary to the common knowledge: the network of detention basins actually increased the watershed peak flow. Basically, the difficulties presented in his work can be summarized as two points. The first one is the upstream contributing area. As we know that the detention basins are always connected to the upstream areas from pipelines, the source, parameter, the upstream area should be considered all the sources. However, these types of information are not always available and difficult to use. In the other hand, however, pipelines will not be the major contributor when there is extensive flooding because most water received in the detention basin will be that which is directly drained from the channel through the floodway. Therefore, when a detention basin functions to attenuate a flood, the water drains into the detention from upstream pipelines are actually negligible. The second difficulty has been mentioned previously. Detention basins cannot be modeled as normal reservoirs which accept inflow from upstream channels and discharge to the downstream channels.

Being aware of above differences, it is not appropriate to model a floodwater detention basin as a normal reservoir, and the upstream area of a detention basin must be delineated appropriately.

4.3.2. Deriving hydrological modeling parameters of detention basins

4.3.2.1. Determine the upstream area

In previous research work, detention basins are modeled as collectors of upstream areas, the same concept of a reservoir. Therefore, as a common practice, the upstream areas of detention basins are usually delineated from elevation models. A common approach in a GIS is to follow the natural flow direction determined from DEM. There are apparent problems using this method because the upstream area of a detention basin is not only determined by the natural terrain. As shown in Fig. 4.5, the upstream area (blue line bounded) for the detention basins delineated from LIDAR DEM is too small to contribute substantial water volume to fill the detention basin during storms. There are several reasons related to it. Firstly, detention basins may be connected to upstream area by underground pipelines which are not apparently visible. The pipeline location is not easy to be obtained and also may be too complicated to use in a hydrological model. Therefore, the contributing area of each detention basin cannot be determined from the published information (DEM, air photos, or field surveys). It is impossible to determine the flow direction by natural terrains for the flood events since water will fill up lower terrains and therefore changes the natural flow directions. Secondly, detention basins should only work when the flood is beyond a certain level of returning probability. The embankment prevents water at normal stage in the channel to be drained into the detention basin. It only allows water to fill the basin when channel water reaches a certain level (higher than the elevation of floodway). This indicates that the upstream area of the detention basin is actually the same as that of the spot where the floodway is

located which is directly connected with the channel. Therefore, it is reasonable to regard the upstream area of the location in the channel were the floodway is built as the actual contribution area of a detention basin. The method to determine the upstream area of a detention basin is to put an outlet in the channel where the floodway structure connects it and use this outlet as a source to trace upstreamly for contributing area. As shown in Fig. 4.6, the upstream area of the detention basin is now the shaded area.

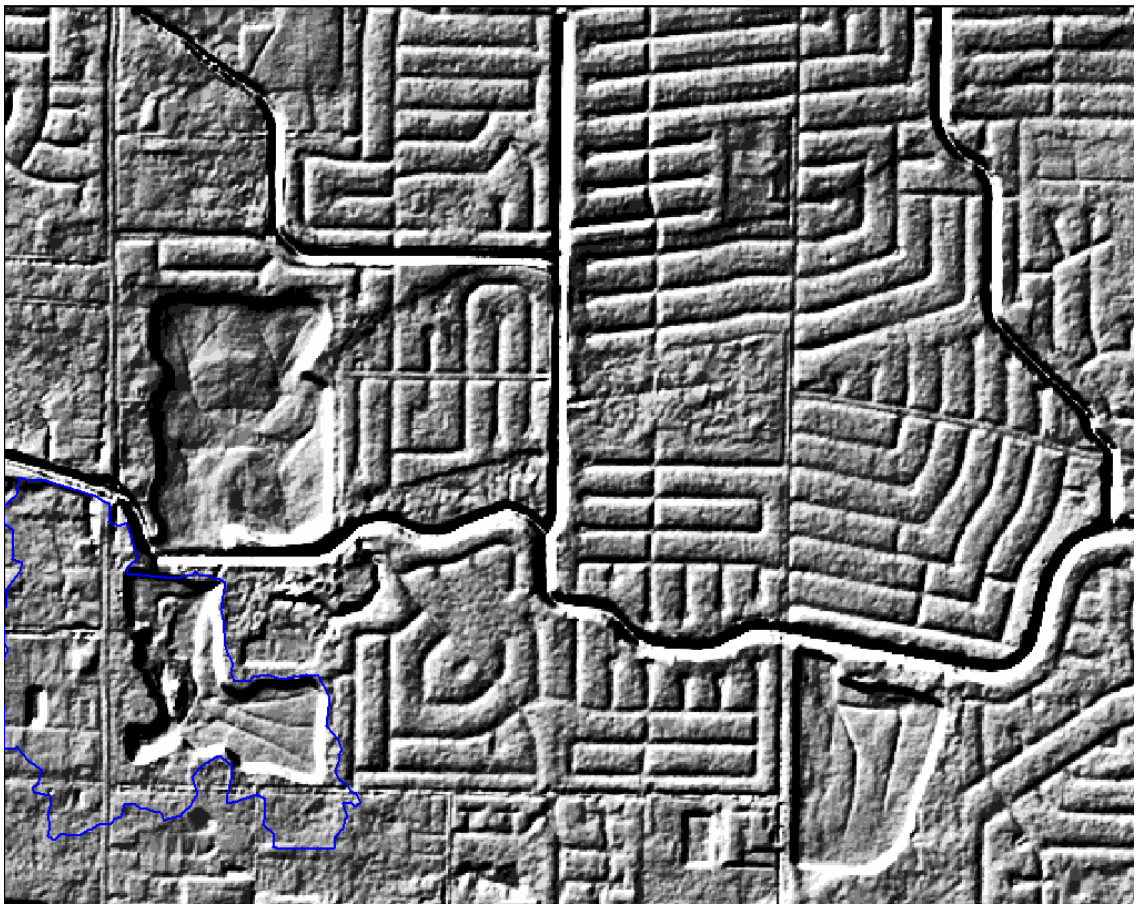

Fig. 4.5 Upstream area of a detention basin

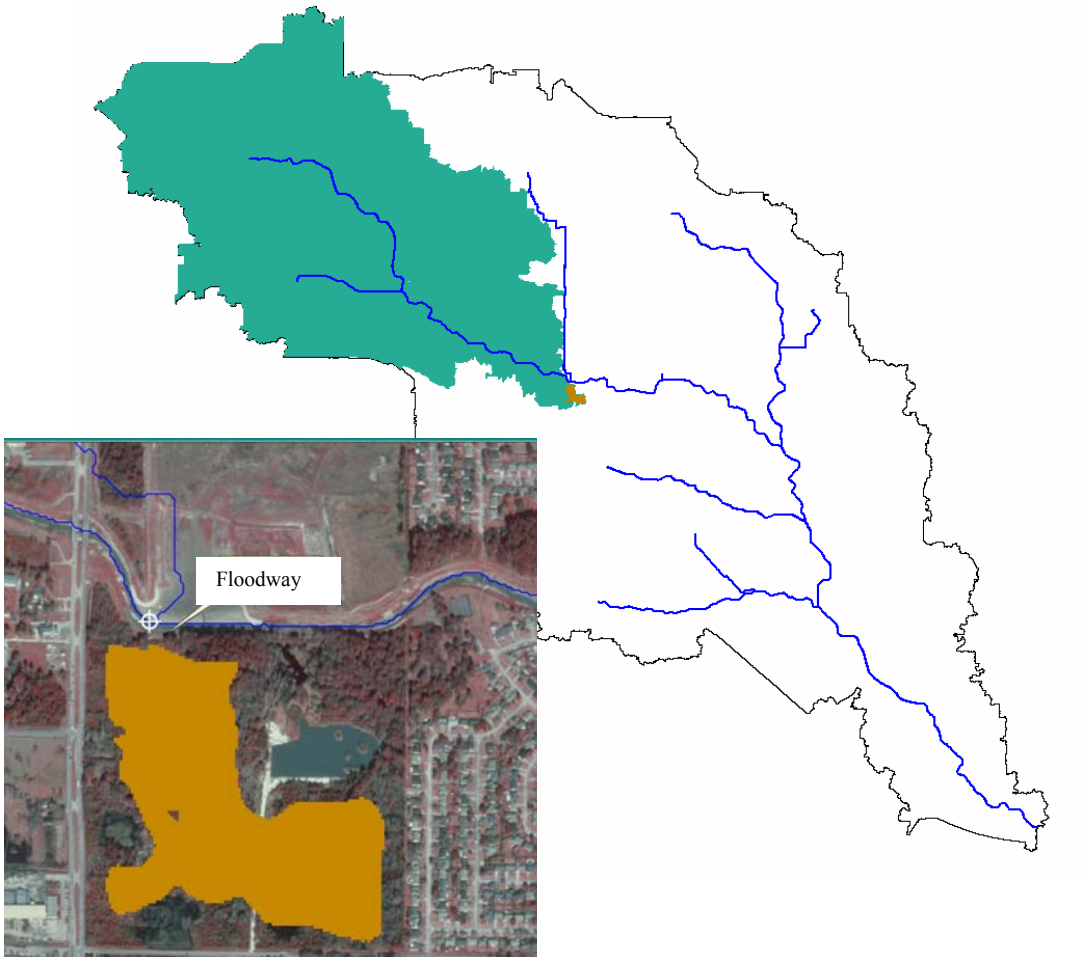

Fig. 4.6 Upstream area determined for a detention basin

4.3.2.2. Determine the storage-level curves and orifice discharge

Storage-level curve is essential to compute the inflow and outflow balance of detention basins, and it is the basis to determine the outflow rate of orifices (Bedient and Huber, 2002). By using the storage-level curve, the inflow, outflow, and storage can be calculated from continuity equations and the Manning's equation. However, it is difficult to be obtained from field survey or any other ways such as optical remote sensing. Using the LDIAR DEM and foodprint of the detention basin derived from the previous section,

it is possible to obtain this information via a multi-level slicing method. There are totally five detention basins constructed during 1970s to 1980s in my study area (Fig. 4.7). From upstream to downstream, they are labeled from 1 to 5. The storage-level curves of the detention basins are illustrated in Fig. 4.8. As we can see, detention basin 1 and 2 are especially larger than the others.

The diameter and shape of the orifice are the variables that have to be known before the model calculation. The orifices are measured in field surveys (Fig. 4.9). The major characteristics include elevation of the base, shape, diameter, and flow conditions

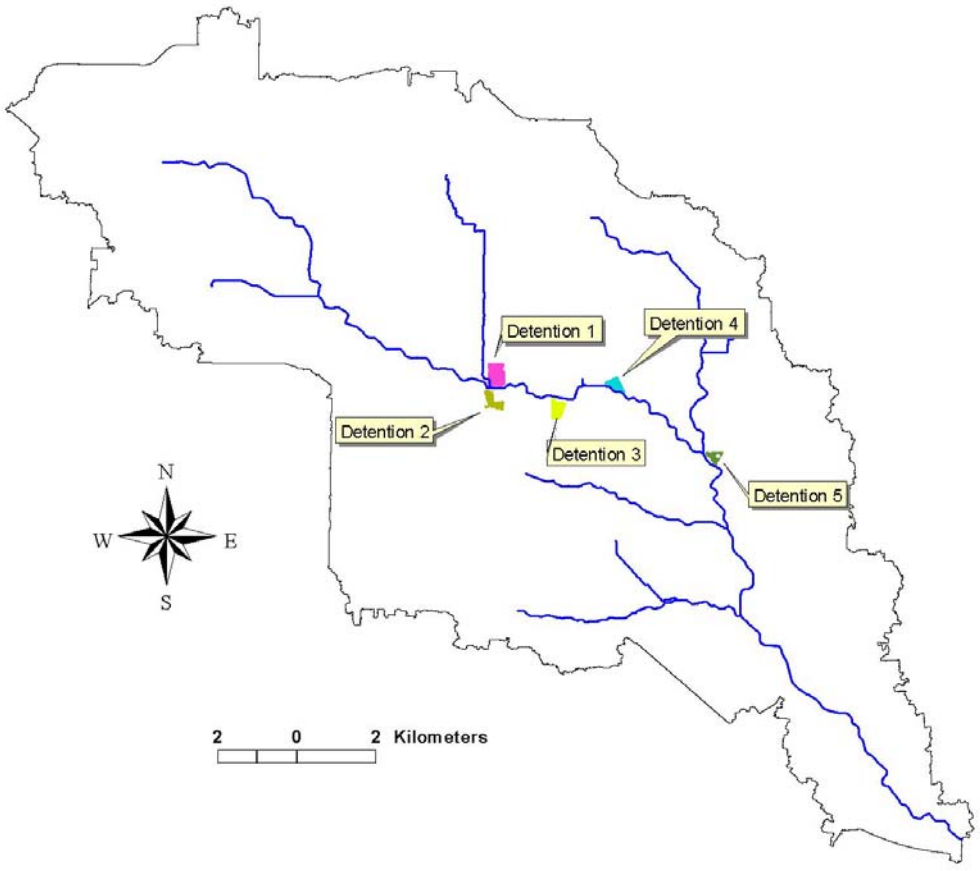

Fig. 4.7 Detention basins in the study area

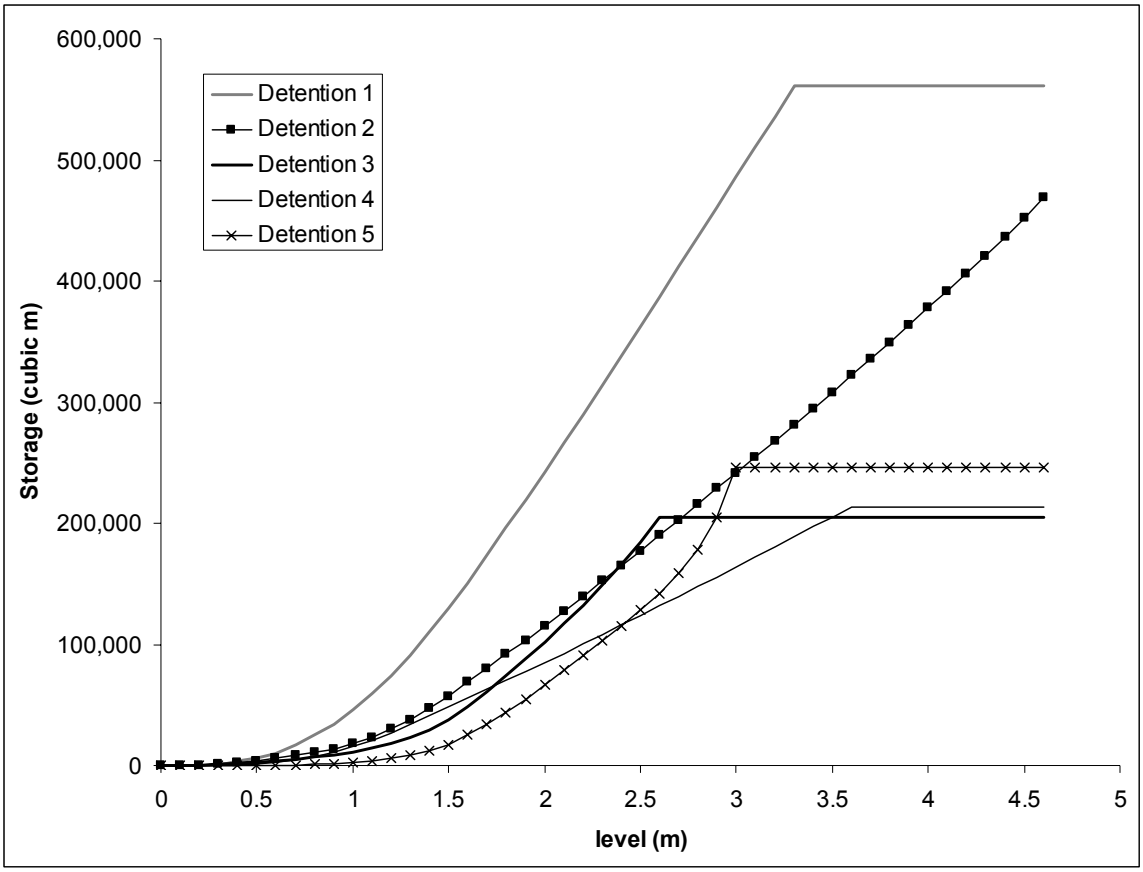

Fig. 4.8 Storage-level curves of the five detention basins

Fig. 4.9 An orifice located in the detention basin

4.3.3. Detention model implementation

The location of the floodway of the detention basin is the important spot between channel and the inner detention basin. For simplicity purposes, it is assumed that the orifices of the detention basin are also located here. The upstream area of this location in the channel is considered as the actual contributing area of the detention basin. During a flooding event, once the floodwater in the channel reaches the height of the floodway, the detention basin becomes active or “on-line”. The extra water in the river channel will drain into the basin before it goes downstream. The stage in the channel and in the basin

remains balanced until the basin reaches its maximum capability. Once the peak flow passes through the location, the floodwater level in the basin starts drop gradually by draining water back to the channel through the floodway or orifices. Before the water level goes below the floodway, the major outflow from the detention basin is via the floodway. The discharge rate is determined by the water level in the channel and in the detention basin. The orifice becomes the major source of outflow discharge from the detention basin after the water level in the channel drops below the floodway. The water continuously drains out until the basin becomes totally dry. The procedure described above can be summarized into four steps (Fig. 4.10):

1. Floodway inflow stage (channel level > basin floodway, supercritical flow)
2. Floodway outflow stage (channel level > basin floodway, subcritical flow)
3. Orifice outflow stage (channel level < basin floodway)
4. Normal stage (water totally drains out)

To implement this model, the flow stage in the channel, floodway elevation, storage-level table of the detention basin, and the orifice structure have to be known. Flow stage in channel can be calculated using Manning's equation and assumed channel geometry. The detention basin can be modeled as a level-pool which is a differentiate continuity equation:

$$\frac{dS}{dt} = q_{in} - q_{out} \tag{4.1}$$

where S = volume of water stored in the detention basin or the reservoir; q_{in} = inflow rate; q_{out} = outflow rate. If the relationship between the storage volume and the outflow rate is known, there are no unknowns in equation (4.1) and the outflow rate and storage

volume in the detention basin can be determined. Therefore, to solve equation (4.1), it relies on constructing the storage-outflow relation of the detention basin. The storage-level table of the detention basin is retrieved from LIDAR DEM using the procedures described in the previous section. A field survey to the sites obtained information about the outlet (orifice) in the basin that is connected to the channel (Fig. 4.10). The outflow of the detention basin through orifice can be calculated as (Bedient and Huber, 2002):

$$Q_{or} = C_d A_0 \sqrt{2g(h - h_0)} \tag{4.2}$$

where Q_{or} = outflow rate generated at the orifice; C_d = the discharge coefficient which depends on several factors but mainly by the geometry; A_0 = area of the orifice; g = gravitational acceleration (9.8m^2/s); h = water surface elevation (WSE); h_0 = the elevation of the orifice center line. A_0 and h_0 are measured through field survey. C_d ranges from "0.62 for sharp-edged entrance and to about 1.0 for well-rounded entrance" (Bedient and Huber, 2002). Since the orifices are close to round shapes, the C_d chosen for the model is 0.9 according to Bedient and Huber (2002). Applying this equation gives the relationship between water level in the detention basin and the outflow rate. At this stage, the detention model can determine the outflow rate at any time if the inflow rate is given.

The detention basin is connected to the river channel via a flood spillway. The spillway only works when the water surface elevation is higher than the spillway elevation. The model drains water through the detention basin without attenuations when the channel stage is lower than weir structure. The relationship of the channel stage can

be determined from Manning's equation and the geometry of the cross-section which says:

$$q = \frac{1}{n} A R^{2/3} \sqrt{S} \tag{4.3}$$

where q is the discharge rate (m^3/s), A is the wetted area (m^2), R is the hydraulic radius which can be calculated as the ratio of wetted area and wetted perimeter. If assuming triangle shapes with bank slope angle of θ, R and A can be determined by:

$$A = \frac{h^2}{tg\theta} \text{ and R = A/P, where } P = 2h\frac{1+\cos(\theta)}{\sin(\theta)} \tag{4.4}$$

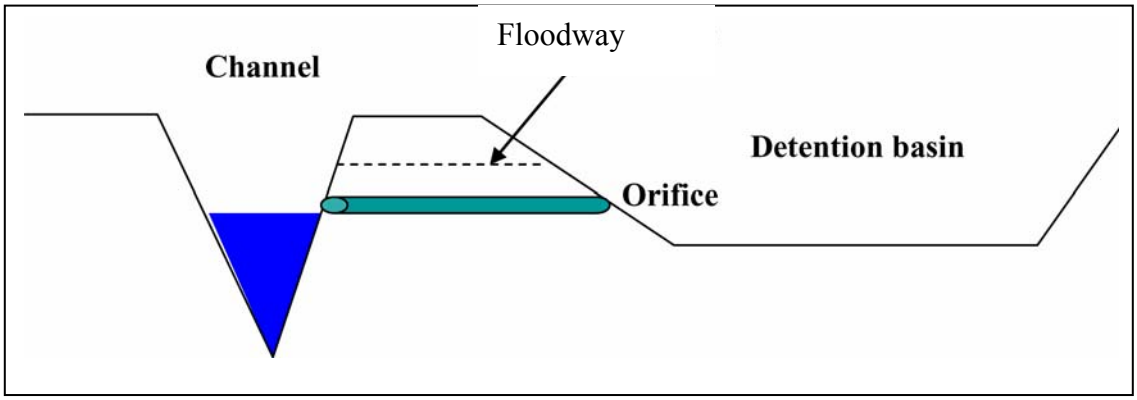

Fig. 4.10 Conceptual illustration of an off-line detention basin

The bed slope S is estimated as 0.14%. Manning's n value could vary from 0.01 to 0.4. If the stage h is larger than floodway elevation, the status of the detention basin is transferred into inflow-stage (Fig.4.11). By assuming the water flow rate on the floodway >> discharge rate in the channel, the water level in the detention basin and in the channel is assumed to be equal at each step of simulation. This brings the formula:

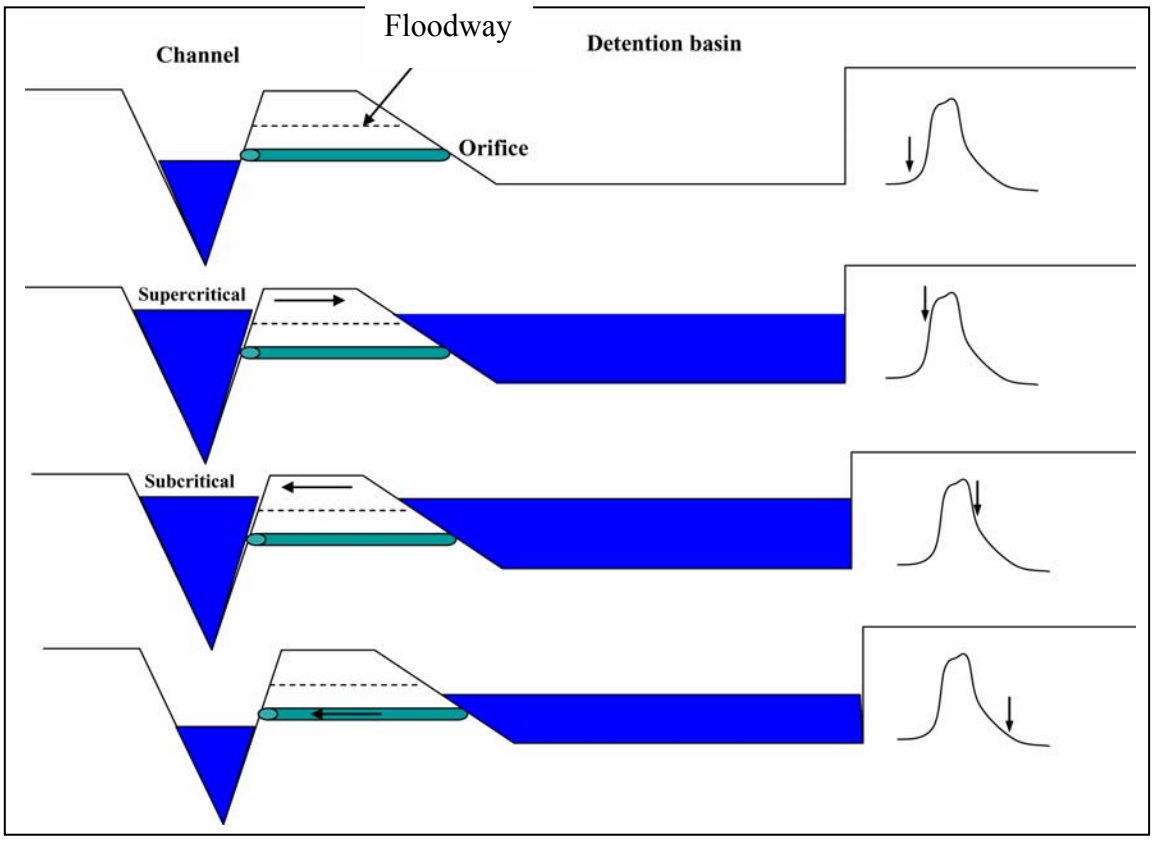

Fig. 4.11 Four-stage modeling method of detention basins

$$h_{channel} = h_{basin} \tag{4.5}$$

$$q_o - q_{channel} = \Delta s / t \tag{4.6}$$

where q_0 = inflow discharge (m^3/s), $q_{channel}$ = discharge (m^3/s) in channel through the basin, Δs = increased storage in the basin (m^3), t is the elapsed time during each step of simulation (s). The shape of the channel cross-section can be acquired from the surveyed cross-section data by the Harris County Flood Control District distributed in their release of Tropical Storm Allison Recovery Project model analysis or measured from the LIDAR DEM. The Newton's secant approximation method is used to solve the

differential equations. If the channel water level is higher than the basin level, the basin level is increased until the maximum storage is reached. At the stage of recession from basins to channels, the discharges in channels are increased due to the back-drained water from basins. As the water level in the detention basin becomes lower, the floodway orifices located in basins will gradually drain water out until basins are dry.

4.4. Calibration and results

The five major detention basins in my study area distributed along the channel are identified. The shape, structure, and capability of these detention basins are measured though the elevation model and field survey data. However, it can be seen that the first and the second detention basins have much more capability than the others. So their capacity to attenuate floodwater is much better than the others. Since most of the parameters are determined from remotely sensed or surveyed data, the only parameter to be calibrated is the channel bottom roughness or Manning's n. If n increases, the water stage in the channel will be higher. This would lead to an earlier inflow of the detention basin and an elongated time to hold the water, and vice versa. If a detention basin receives inflow too early, it will not effectively attenuate the storms as designed because it cannot receive any more water when peak flow approaches. But if it receives flooding water at a too high threshold, it would not be filled with floodwater when the peak flow passes. Therefore, the most ideal design of a floodwater detention basin is to have it exactly reach the maximum storage capacity when the designed peak flow passes. By assuming the design is perfect (reaches maximum storage when a 100-year flood passes), the goal of calibration is to maximize the capability of these detention basins of reducing

the peak flow discharge that passes through the channel. This is based on the assumption that ideally all the detention basins should be designed to attenuate the 100-year event efficiently. The calibration is done by trial and error approach one detention by another from upstream to downstream. To be noted that since detention basin 1 and 2 are located at the same spot, they are calibrated simultaneously. The result of calibrated in-flow and out-flow curve, and the storage water volume of detention 1 and 2 is shown in fig. 4.12. As we can see that they attenuate the peak flow by roughly 20% percent.

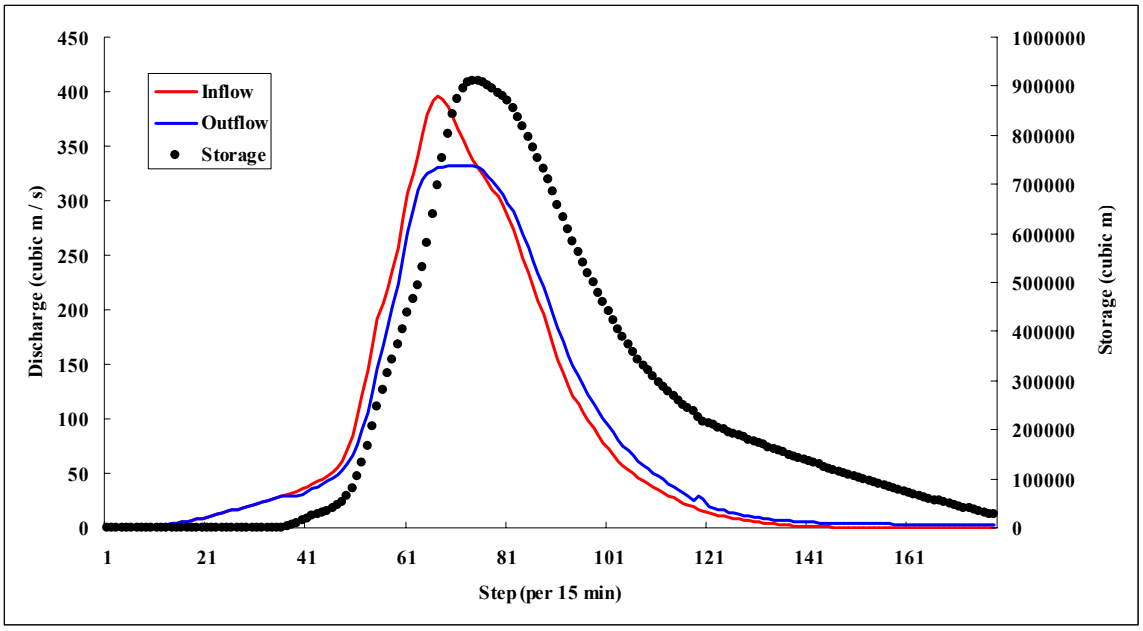

Fig. 4.12 Inflow-outflow-storage curves of detention basins

4.5. Summary

Rapid urbanization has created large portion of imperviousness area which delivered various pollutants and imposed considerable hydrological and ecological consequences in urban watersheds. Construction of storm water detention basins has been recognized as an important measure to offset and mitigate the increasing flood risk induced by urbanization. In the case study area, local government has constructed several large regional detention basins to protect downstream residential and commercial areas. Although functions of constructing detention basins are expected, little research has been done to quantify the contribution of detention basins to flood control due to lack of quantitative information for existing detention basins.

An automated method to extract spatial and geometric properties of detention basins from high quality LIDAR DEM is developed in this research. Important hydraulic parameters such as location, area, volume, and weir structure can be derived from DEM.

The level-storage curve for any specific detention basin can be obtained from analyzing terrain topography and elevation models. High resolution remote sensing images are used to validate the results.

The hydrological modeling system incorporates these detention basins as one of the major components. Properties such as location and elevation of floodway structure, orifice, and channel properties are important parameters for the model. They are acquired from various sources such as remote sensing data and field surveys. The model shows that the ability of the detention basins to attenuate floods. It is also found that the timing of water inflow is very important for designing detention basins. Manning's roughness coefficient is one of the important variables to be calibrated. The calibrated model shows that in the case study area, about 20% of peak flow can attenuated by the detention basins. More discussions of how the detention basins protect downstream area from extensive flooding through scenario analysis can be found in chapter VI.

CHAPTER V

HYDRAULIC MODELING AND FLOODPLAIN MAPPING

5.1. Introduction

Flood Insurance Rate Maps (FIRM) are published by FEMA and required by regulations from the National Flood Insurance Program (NFIP) for flood-prone areas. With detailed Flood Insurance Study (FIS), the Base Flood Elevation (BFE) is provided for flood-prone zones such as Zone AE, A1-30, AH, and VE (zones in floodplain defined by different water depth). The BFE can also be referred as the water surface elevation caused by the 100-year flood. Floodplain is the area inundated by floodwater during the flooding period. For the zones that are outside 100-year floodplain or protected by federal or regional flood control structures, the BFE is usually not given in the FIRM, and instead, only approximate methods are used in those areas. A detailed flood insurance study employs analytical methods to map the flood water elevation in the floodplain (Sui and Maggio, 1999). The analytical approach includes procesures of hydrological/ hydraulic (H&H) modeling, cross-section survey, DEM acquisition, inundation model validation with high water marks, floodplain mapping, and so on. Hydraulic modeling creates water elevation profile in the channels and the cross-sections. Using DEM and a GIS, the water elevations can be converted into flood inundation information such as floodplain extent, BFE, and flood damage assessment. One of the most widely used software for hydraulic analysis is the HEC-RAS developed by US Army Corps of Engineers (USACE, 2000).

5.2. Theoretical basis for open channel hydraulic modeling

The open channel flow is referred as the flows convoyed within defined channels with open/free surfaces. The geometric characteristics of the channels, such as the width, depth, cross-section shapes and the hydraulic roughness contribute to the conveyance capability in the channel. The water level in the channel changes with the discharge rate, or the conveyance in a unit time. According to the properties of the flows or the assumptions made for the model, the flows can be categorized into steady or non-steady, uniform or spatially varied, and subcritical or supercritical. If the flow's depth and velocity at any location does not change with time, it is called a steady flow; if water surface is parallel to the channel bottom, then the flow is called uniform flow; if the velocity and depth changes slowly with the distance downstream, this is called gradually varied flow; if the wave speed is faster than the flow speed, then the flow is in a subcritical status; and vice versa. Usually, the subcritical assumption is always used for the floodplain mapping purpose because at the peak flow status, the water is "dragged" out of the channel by the outlet where subcritical flow occurs. The wave speed can be written as: $\sqrt{gh}$, where g is the gravitational celerity, h is the hydraulic radius. To determine the status of flow, Froude number can be used::

$$Fr = \frac{v}{\sqrt{gh}} \tag{5.1}$$

If Fr > 1, it is a supercritical flow. If Fr < 1, it is subcritical. Fr = 1 gives the depth called the critical depth (Bedient and Huber 2002). Critical depth is the depth where a supercritical flow changes to a subcritical flow. If a downstream boundary condition is

unknown, it can be assumed to be the critical depth. By inserting the discharges in the cross-sections, hydraulic model can to obtain the water surface elevation for the cross-sections. For most applications, it is assumed that the flow is a gradually changed (non-uniform) steady flow.

Hydraulic analysis is based on the law of mass balance and energy conservation. The mass balance between two adjacent cross-sections can be written as:

$$v_1 A_1 = v_2 A_2 \tag{5.2}$$

where v= velocity at cross-sections; A = area of the cross-sections. And the velocity of the flow in the open channel can be related to the bed roughness and slope and the hydraulic radius (cross-section area divided by the wetted perimeter) using Manning's equation:

$$v = \frac{1}{n} R^{2/3} \sqrt{S} \tag{5.3}$$

where v is the mean velocity in ft/s, R is the hydraulic radius in ft, S is the slope of energy grade line (equal to the bed slope in assumption of kinematic wave), and n is the coefficient of roughness, known as Manning's n. The Manning's n of different types of channel bed can be obtained from McCuen (2004) (Fig. 5.1). The n value could range from 0.011 to 0.033 in my study area. This is a parameter used to be adjusted in the calibration. R is the hydraulic radius which is defined as the area of the wetted cross-section divided by the wetted perimeter. For wide rectangular shaped channels or overland flows, the hydraulic radius is approximately equal to the water depth in the channel.

	Manning's n Range
I. Unlined open channels	
A. Earth, Uniform section	
1. Clean, recently completed	0.016-0.018
2. Clean, after weathering	0.018-0.020
3. With short grass, few weeds	0.022-0.027
4. in graveled soil, uniform section, clean	0.022-0.025
B. Earth, fairly uniform section	
1. No vegation	0.022-0.025
2. Grass, some weeds	0.025-0.030
3. Dense weeds or aquatic plants in deep channels	0.030-0.305
4. Slides, clean gravel bottom	0.025-0.030
5. Slides, clean, cobble bottom	0.030-0.040
C. Dragline excavated or dredged	
1. No vegation	0.028-0.033
2. Light brush on banks	0.035-0.050
D. Rock	
1. Based on design section	0.035
2. Based on actual mean section	
a. Smooth and uniform	0.035-0.040
b. Jagged and irregular	0.040-0.045
E. Channel not maintained, weeds, and brush uncut	
1. Dense weeds, high as flow depth	0.08-0.12
2. Clean botttom, brush on sides	0.05-0.08
3. Clean bottom, brush on sides, highest stage of flow	0.07-0.11
4. Dense brush, high-stage	0.10-0.14
II. Roadside channels and swale with maintained vegetation	
(Values shown are for velocities of 2 and 6 ft/sec)	
A. Depth of flow up to 0.7 ft	
1. Bermuda grass, Kentucky bluegrass, buffalo grass	
a. Mowed to 2 in.	0.07-0.045
b. Length 4 to 6 in.	0.09-0.05
2. Good stand, any grass	
a. Length about 12 in.	0.18-0.09
b. Length about 24 in.	0.30-0.15
3. Fair stand, any grass	
a. Length about 12 in.	0.14-0.08
b. Length about 24 in.	0.25-0.13

Fig. 5.1 Manning’s roughness coefficients (McCuen 2004)

The hydraulic model also has the assumption of the balance of the energy including those carried and dispersed. The specific energy carried in the flow is calculated as (Bedient and Huber, 2002):

$$E = y + \frac{v^2}{2g} = y + \frac{Q^2}{2gA^2} \tag{5.4}$$

The head loss is the term referring the reduced energy due to the slope and the bed friction. Including the head loss into equation (5.2), we obtain the conservation of the energy between two adjacent cross-sections as (USACE, 2000):

$$E_2 = E_1 + h_e \tag{5.5}$$

$$h_e = L(S_f - S_0) \tag{5.6}$$

where h_e is the head loss; S_f is the friction slope; S_0 is the bed slope; L is the distance between the successive cross-sections; E2 and E1 is the specific energy at cross-section 1 and 2, respectively.

Combining equations (5.3), (5.4), (5.5), (5.6), and (5.7), if one cross-section has known velocity and depth, we are able to obtain the values of the second cross-section with given geometry and Manning's roughness coefficients. USACE developed the River Analysis System or known as HEC-RAS (USACE, 2002). It is based on the powerful HEC-2 software which has been recognized as the standard hydraulic analysis tool since its release in 1965. The HEC-RAS provides the easy-to-use feature of Windows GUI programs beyond the powerful HEC-2 program. HEC-RAS solve the following two equations by an iterative procedure (USACE, 2000).

$$WS_1 + \frac{\alpha_1 V_1^2}{2g} + h_e = WS_2 + \frac{\alpha_2 V_2^2}{2g} \tag{5.7}$$

$$h_e = L\overline{S_f} + C\left(\frac{\alpha_2 V_2^2}{2g} - \frac{\alpha_1 V_1^2}{2g}\right) \tag{5.8}$$

The computation procedure is:

1) Assume a water surface elevation for the cross-section 2 (WS_2), and compute the velocity, hydraulic radius, and total conveyance at cross-section
2) Calculate h_e from equation (5.8) and WS_2 from equation (5.7)
3) Repeat above steps until the disagreement between assumed water elevation and the calculated value is below some specific small number.

Given the water surface elevation and flow at one boundary of the stream, the calculation is processed from upstream to downstream (for supercritical flows) or reversely (for subcritical flows). The data requirement of HEC-RAS includes the geometry at each cross-section, flow data, and at least one boundary condition (upstream or downstream) depending on the flow regime assumed.

5.3. Cross-section data and validation

The geometry data is critical to HEC-RAS because that it is the basis to relate the in-channel velocity with the conveyances. The quality and numbers of cross-section data directly influence the computational accuracy and stableness. The cross-section data can be manually input in HEC-RAS using the graphic interface provided. A GIS tool has been developed to prepare the geometry data for HEC-RAS, called HEC-GeoRAS. GeoRAS operates as an extension of Arcview GIS software. Extensive floodplain mapping have been performed in the case study area by the Tropical Storm Allison

Recovery Project (TSARP) and HCFCD to obtain the cross-sections (Fig.5.2). A selected cross-section is plotted in Fig. 5.3 with its elevation values of survey stations annotated on the graph. The data is provided as the ArcView shape file with a unique id assigned to each of the cross-sections.

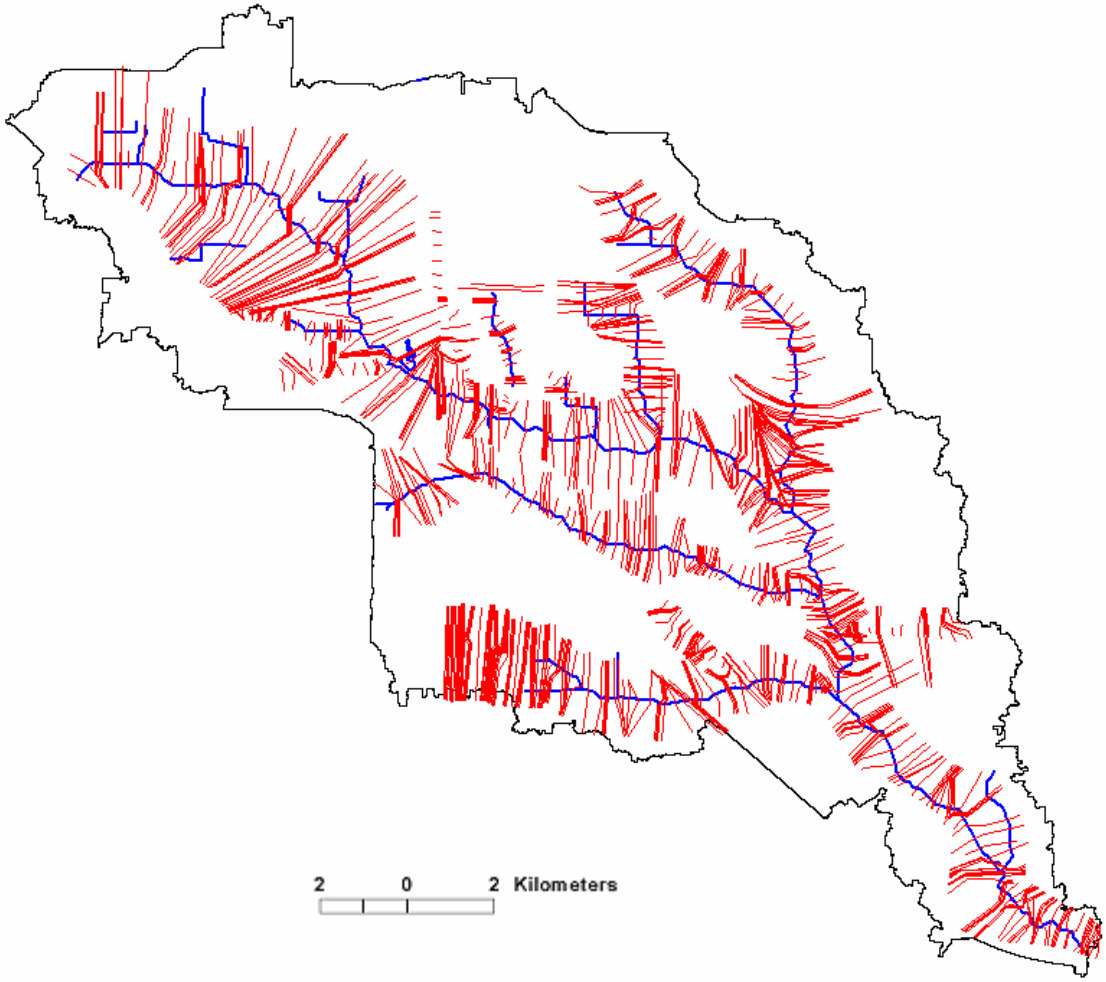

Fig. 5.2 Cross-sections in White Oak Bayou watershed

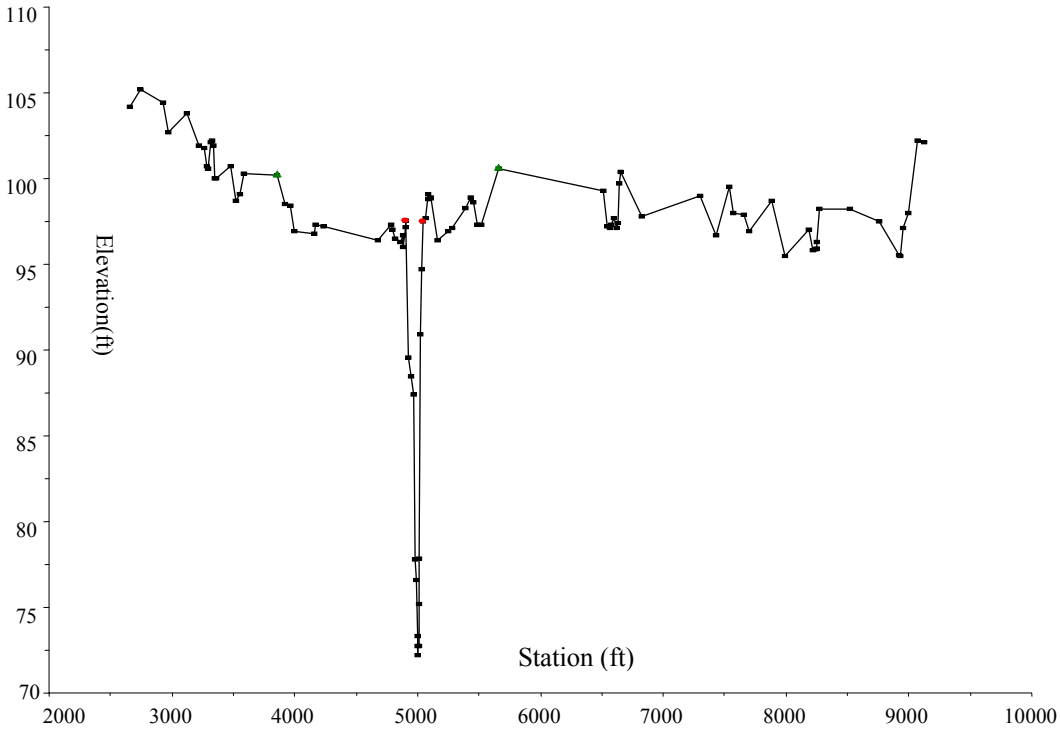

Fig. 5.3 Graphic illustration of a cross-section

5.4. Model data input, calibration, and validation

Beyond cross-section data, flow data is another critical input. Discharge rate at each cross-section must be known before the HEC-RAS could run. A gradually changing flow profile is obtained from hydrological model simulation. The flow data is required where a change in the flow data is encountered. If only one flow data is input, the flow to be simulated is a uniform flow. The cross-sections between two change locations are assumed to have the same discharge rate as the downstream end. At least one boundary condition is needed to run the model. User can select different flow regime: subcritical, supercritical, or mixed. However, as discussed in the last section, and according to

Bedient and Huber (2002, pp. 506), the subcritical flow regime with a downstream boundary condition is used for this analysis. Since the water surface elevation at the downstream boundary is unknown, the critical depth is selected to represent the downstream boundary condition.

A steady flow simulation is run by HEC-RAS after all the information was obtained. HEC-RAS generates water surface elevation (WSE) and velocity at each cross-section along the channels. The HEC-GeoRAS (USACE, 202) was used to read the simulated water elevation of each cross-section into GIS environment. Fig. 5.4 shows the water elevations of all the cross-sections. Using surface model and the water elevations at the HEC-RAS cross-sections, the floodplain boundary can be delineated.

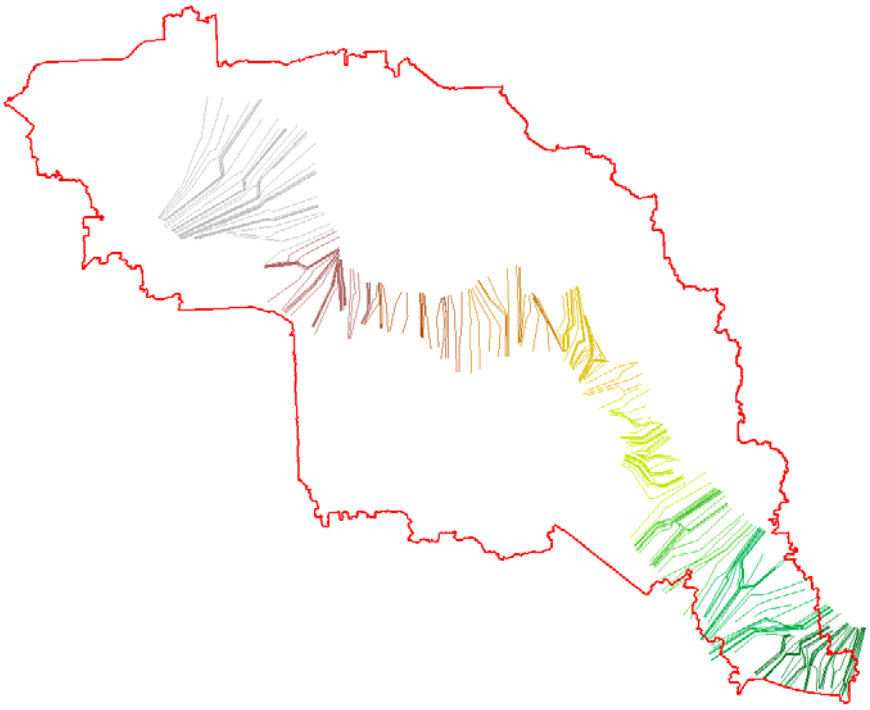

Fig. 5.4 Cross-sections and water surface elevation value along the main channel

Manning's n value in the channel bed is one of the most important factors to determine the water surface elevation (USACE, 2000). Unfortunately, this value is very hard to be obtained from other sources except direct experiments. The roughness coefficient also varies with the physical condition of the channel bed, such as the temperature, grain size, vegetation coverage, etc. The available Manning's n value from literature is always provided as a range of values. By referring to 16 high water marks (HWM) obtained from the Harris County Office of Emergency Management (HCOEM), a trial and error approach is used to calibrate the HEC-RAS model through altering Manning's n value at each cross-section. Validation and accuracy assessment can be read from table 5.1 and Fig. 5.5. The comparison of observed water elevation to the simulated values shows a RMSE at 1.27 feet and a very high correlation coefficient. It suggested that the model produced flood water surface elevation with very high accuracy after calibration.

Table 5.1

Validation of water elevation using high water marks

Street name	Observed (ft)	Simulated (	Difference
Heights	45.5	45.9	0.4
W. 11th Street	56.2	54.968	-1.232
W. 18th Street	58.8	57.3757	-1.4243
Ella Blvd.	59.8	57.8192	-1.9808
Loop 610 E. Feeder	59.8	60.8483	1.0483
W. 34th Street	62	62.98	0.98
W. 43rd Street	68.4	67.7991	-0.6009
Tidwell	72.8	73.3714	0.5714
W. Little York	77	78.0302	1.0302
Alabonson	81.9	81.5448	-0.3552
N. Houston Rosslyn	86.26	86.25	-0.01
Fairbanks N. Houston	98.1	96.7659	-1.3341
Windfern	102.6	100.2765	-2.3235
Gessner	102.6	101.3684	-1.2316
Lakeview	107.3	105.2836	-2.0164

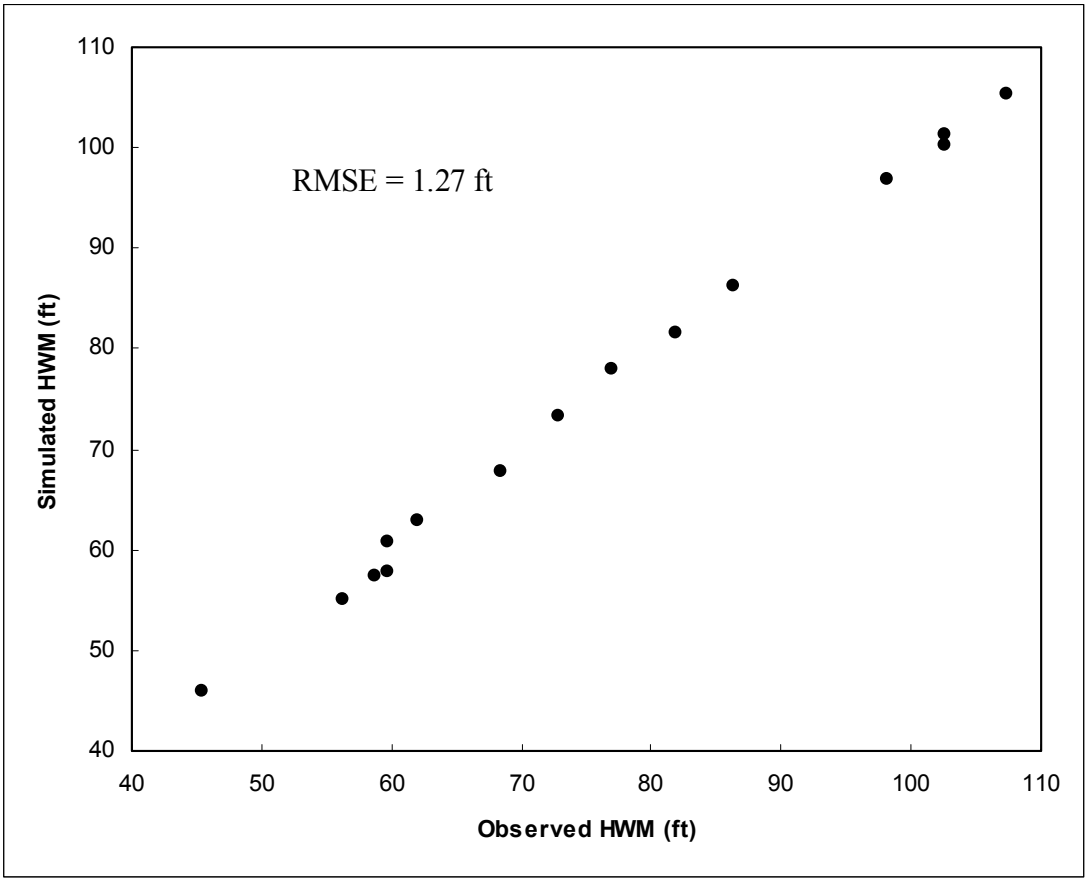

Fig. 5.5 Observed high water marks (HWM) and simulated water surface elevation

5.5. An algorithm flood inundation modeling using LIDAR DEM

5.5.1. Problems with previous methods

The general approach of the automated floodplain delineation methods are composed of two steps: 1) Extending/interpolating water surface elevation points; and 2) Subtracting the DTM from the extended water surface to obtain the water inundation depth distribution. Because in most time, the WSE is provided at the point basis, an interpolation is always performed to obtain the WSE coverage of the entire floodplain.

After the interpolation, the flood depth and extent can be retrieved by subtracting the DTM from the WSE.

The most important elements for the flood extent delineation are the choice of digital terrain model and the selection of the interpolation method. HEC-GeoRas is designed by USACE to obtain water depth values in the floodplain based on HEC-RAS model simulations. With widely applied HEC-RAS model, HEC-GeoRAS is also one of most popular software used as a GIS tool to extract flood extent and depth information. However, there are two limitations in the implementation of HEC-GeoRAS which can be summarized as below:

1) It only works with a Triangulated Irregular Network (TIN) data structure.

Currently, most software chooses to use TIN as the terrain model in flood analysis because of the "variable resolution of nodes and triangles" and the "speed of analysis is generally faster" (Noman et al., 2001). However, although it might be true that the analysis speed could be faster using TIN, the availability of TIN is much limited comparing to the DEM. A conversion from the raster format DEM to the TIN requires heavy load of computations. For an example, in the case study area, the data generated from LIDAR DEM contains 9,056,872 cells. The multi-resolution feature of TIN is not an advantage in this case because the lattice cells are regularly distributed. Although some of the operations such that finding the "VIP" points can reduce the number of points in generating TIN, the effect is very limited. From these points of view, using TIN is not superior to using a raster format DEM in determining the flood extent when raster-cell DEM is available.

TIN is used in previous methods to generate water surface elevation (WSE) by interpolating water surface elevation into the floodplain. The Delauney Triangulation method which is a standard way of triangulation has been generally adopted. The water elevation points are used to construct the water surface model by building a TIN mode. Then, the WSE values are interpolated to the floodplain that is covered by the TIN surface. Intersecting the WSE TIN model to the DTM TIN model produces the flood extent and the depths (USACE, 2002). However, there are some difficulties with these approaches. For example, TIN methods lack appropriate break lines to prevent unexpected links. The unexpected links include the links between WSE points from different reaches and links across the barriers. Although efforts have been put to solve the break line problem, it is too complicated to be solved in automated procedures (Noman, 2001).

From above analysis, it is suggested that TIN model can not provide an appropriate representation for the water elevation surface. In addition, in most cases, TIN model is not available rather than the grid based DEM. Since the algorithms that support raster based analysis do not exist, users are forced to convert the raster model to a TIN. This process would also introduce unnecessary uncertainties to the model. With a DEM with large volume, this process may be very time consuming and costly, even using optimized solutions.

2). Previous methods lack mechanism of checking hydraulic connectivity

The second problem is that the hydraulic connectivity is not considered. The lower terrain does not necessarily receive flood water unless it is hydraulically connected with

the flooded area with a higher elevation. Noman et al. (2001) illustrated this problem by the graphics shown in Fig. 5.6. Area B that is protected by flood control facilities should not be flooded even the water elevation in the adjacent area A is higher than it. If following previous methods that simply interpolate WSE to TIN and intercept with surface elevation data would produce erroneous results because it lacks consideration of hydraulic connectivity (Fig. 5.6). On the other hand, albeit efficient efforts are made to

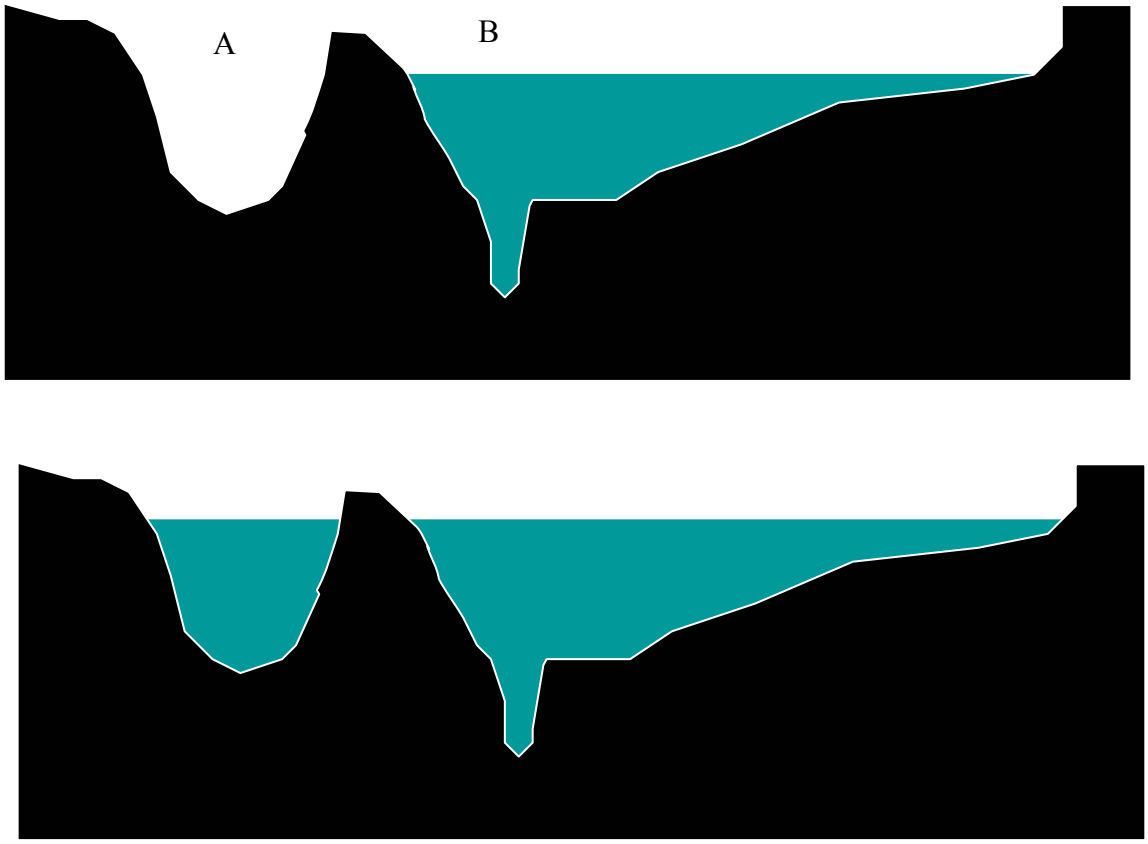

Fig. 5.6 Barrier prevents flood expansion (top) and erroneous flood extent produced by not checking hydraulic connectivity (bottom)

avoid triangulating though barriers, it still has possibility to be wrong, depending on the existence of the hydraulic connectivity.

To eliminate the limitations of current methods, a new approach is required that at least satisfies the following criteria:

1) able to utilize existing raster DEM instead of TIN models,

2) able to incorporate water levels from various resources, and

3) able to consider the hydraulic connectivity while keeping the hydraulic gradient in the floodplain.

5.5.2. The new method and its implementation

On the basis of the reviews and analysis above, I developed a new approach to delineation of the floodplain boundary with given water elevation data and a DTM in the raster format. The advantages of using the raster format include 1) simple data structure and 2) that the hydraulic connectivity can be measured.

The assumption of the flood inundation model is that the water overspills from the river bank but does not influence downstream water elevation because the hydraulic gradient is unknown. Spilling water from one point can be modeled as a sewage surging (Fig. 5.7). Surged water will go upstream and downstream, which can be called uphill connectivity and downhill connectivity respectively. The connectivity is limited by the elevation changes due to the uphill climbing. When the water elevation is lower than the terrain elevation, the upstream spilling stops, and so does the uphill connectivity. But it is possible that water could find a path linking to the areas that is behind a barrier. The downhill hydraulic connectivity is limited by the hydraulic gradient, which means when

going downhill, the water surface elevation is unknown because of existence of hydraulic gradient. The only information can be known is that the water elevation should be somehow lower than the source points. The major difficulty is that the actual hydraulic gradient on the floodplain is unknown by using the 1-D hydraulic models such as HEC-RAS. Therefore, best knowledge available about the hydraulic gradient is from the 1-D hydraulic model simulated water elevation points. Based on this, an assumption was made by this method that hydraulic gradient information is completely controlled by the given water elevation points. Fig. 5.7 illustrates this conceptual model. In Fig. 5.7 we can see that the two points A and B are the given water elevation points. A path which is defined by the digital elevation model links these two points. In the part between these two points, the hydraulic gradient from b is only valid before it reaches the hydraulically connected area from point a. A potential problem may occur that at the location that point A's hydraulic connectivity ends, there is a disrupt jump of the water surface elevation. To solve this problem, the concept of geodesic distance is introduced (Soille, 2002). The geodesic is defined as the path that links from one location to another within the feature space. The path can be defined by any information that is necessary. In this case, it is defined by the flow direction. The flow direction is determined by the single flow algorithm (D8) (Jenson and Domingue, 1988). The water elevation is then calculated by weighting the water elevation of upstream and downstream source points according to their geodesic distance to the location to be interpolated.

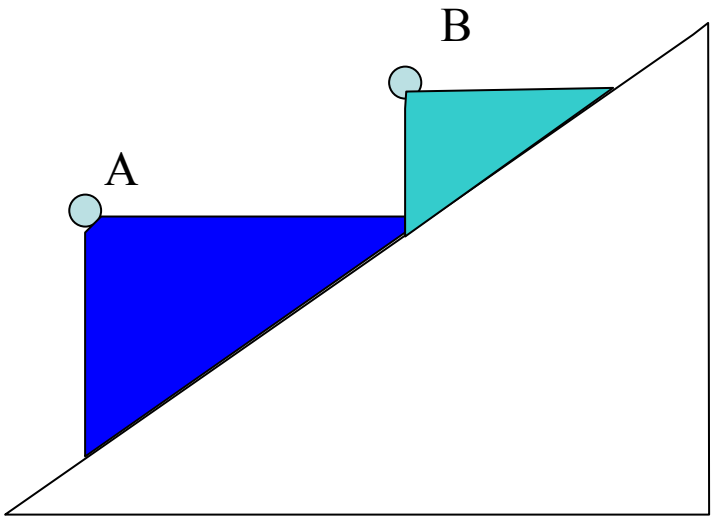

Fig. 5.7 A sewage surge model and the 1-D illustration of flood surge model

Previous methods do not have the component that validates the hydraulic connectivity. Therefore, they result in isolated flooding with no connectivity to the main channel of floodplain. Since hydraulic models simply assume homogeneity of water surface elevation along each cross-section, checking hydraulic connectivity is necessary. As shown in Fig. 5.8, traditional methods produced flood inundation map with isolated flooding area. To solve the problem, a pre-processing is applied to eliminate parts of cross-section which are not hydraulically connected to the main channel by giving a water surface elevation. This is implemented by checking along each cross-section with a certain water surface elevation value. At location a, the connectivity is blocked by a higher elevation, therefore the hydraulic connectivity is broken. The rest part of the cross-section stretching far away the main channel will be eliminated. By performing this preprocessing, the isolated inundation areas are removed, as shown in Fig. 5.8.

Hydraulic connectivity can be defined as the flow path. However, flow path defined through the standard flow direction algorithm (Jenson and Domingue, 1988) should not be adopted because the single flow direction (D8) method cannot model the hydraulic connectivity from all directions. In another word, since D8 method can only handle convergent flow but not divergent flow, it is not suitable for flood surge and inundation models. Following the floodplain delineation assumption that flood water spill over river banks, the flow path should have the same meaning as the spill path which defines a way that water spills from one to another. The uphill and downhill water-spilling is implemented using the bread-first search algorithm. From each given water elevation point (WEP), the water surface elevation (WSE) is spread to the immediate neighbors where the terrain is lower than the WSE. The spilling stops when there is a high elevation. The hydraulic connectivity is defined as the flood water spills downhill and uphill.

A C++ program has been developed for this algorithm with the support of ArcGIS developer library. The input layers include the raster format of water surface elevation points exported from HEC-RAS and the digital terrain model from LIDAR. An illustration of procedures of downstream and upstream spilling, interpolation using the geodesic distances, and determining the water depth is shown in Fig. 5.9.

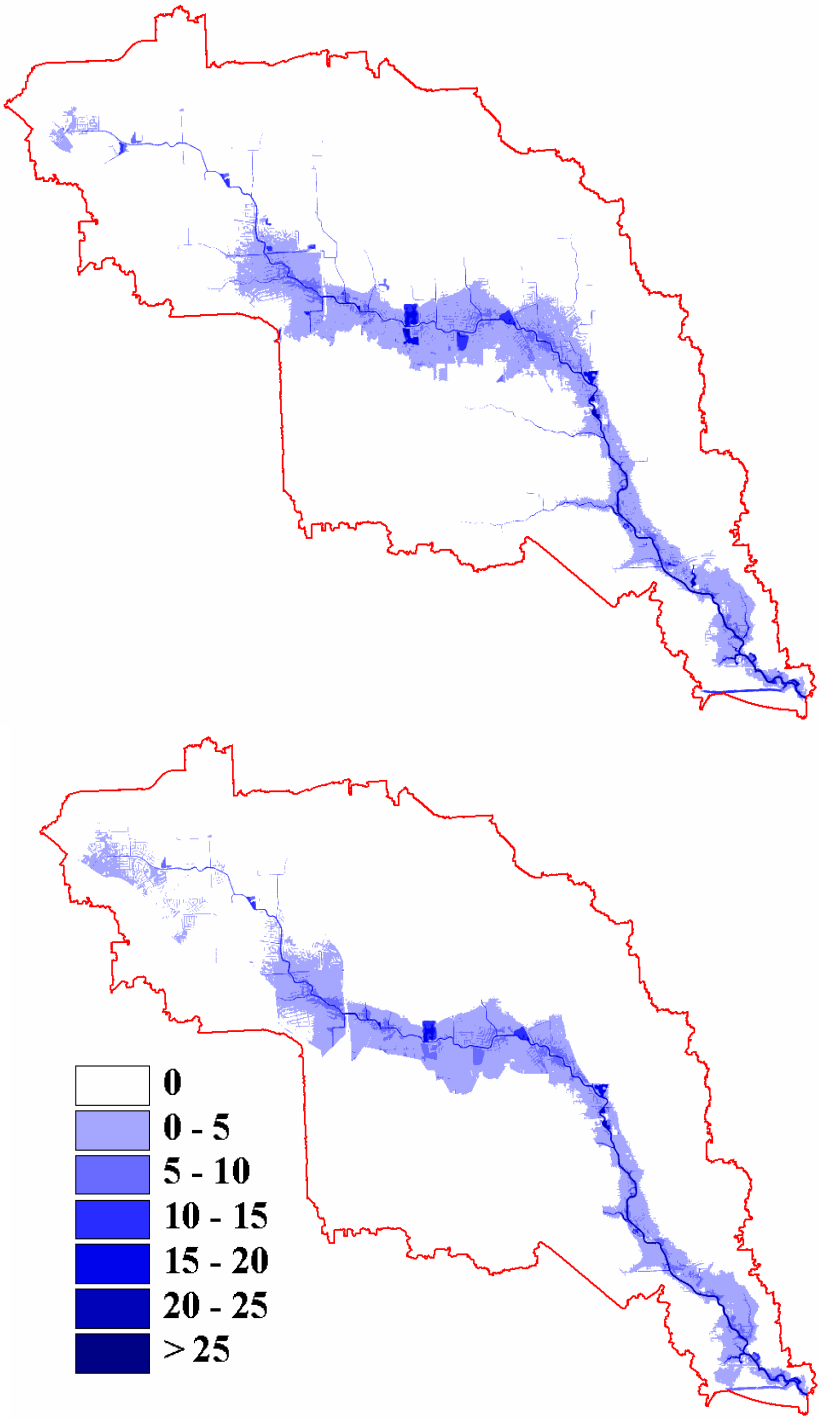

Fig. 5.8 Comparison of floodplain determined by traditional method (top) and the new method (bottom)

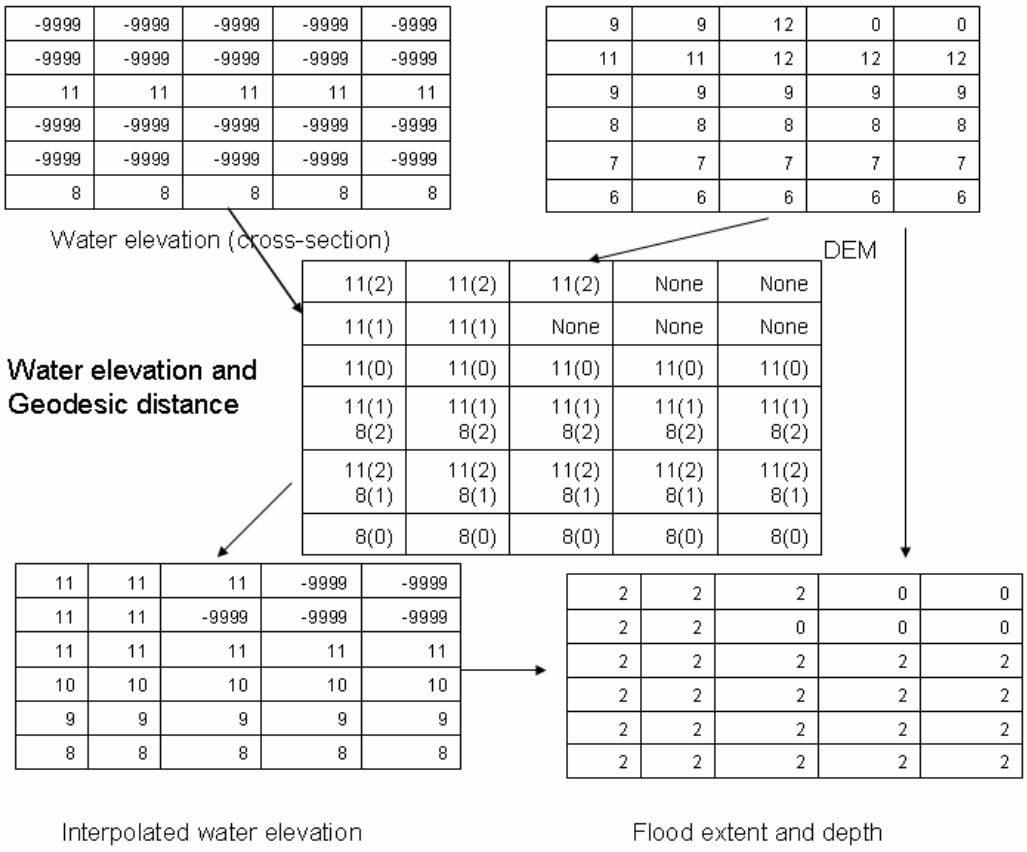

Fig. 5.9 Procedure for interpolating water elevation and derivation of flood extent and depth

5.5.3. Results and discussion

The program was tested using the HEC-RAS output data and compared to the delineated water depth determined by the HEC-GeoRAS tool. The same elevation model was used to construct a TIN mode, as required by the HEC-GeoRAS, and used for HEC-GeoRAS. The delineated flood extent and inundation depth is shown in Fig. 5.9. By comparing the results of my algorithm and the previous method, we can see such differences:

1). Previous method generated a flood inundation map that is confined to the area covered by cross-sections and their interpolations. The farthest flood extent is limited by surveyed cross-sections. However, flooding does occur in the area outside the survey boundary. It is reasonable that my algorithm map natural flood extent by its hydraulic connectivity but not confined by the survey area.

2). Previous method generates some isolated flooding areas. This is because it fails to validate hydraulic connectivity while interpolating water surface elevation across the floodplain. My method is able to eliminate those areas that are not hydraulically connected to the main channel water profile at a certain water level.

5.6. Floodplain mapping using designed rainfall events

5.6.1. Synthetic rainfall

Synthetic rainfall is always used for designing purposes or to evaluate the effectiveness of the urban drainage systems. It is usually plotted as the intensity-duration-frequency (IDF) curves. The exceedance probability is the term that defines how often a rain may exceed a certain amount. The recurrence interval is just the reverse of the exceedance

probability. A 100-year event refers to the rainfall that averagely happens once per 100 years or by the terms of exceedance probability, 1%. Unlike the historical storm rainfall, the synthetic rainfall does not represent the shape of hyetograph of any storms that actually took place. The temporal distribution of the synthetic rainfall is constructed following the published Natural Resources Conservation Services (NRCS 2005) curves for the United States. To obtain a synthetic rainfall hyetograph, one needs to specify the duration, time increment interval, and recurrence frequency of the storm. Then the intensity is calculated using following equation (TXDOT, 2004):

$$I = \frac{b}{(T_d + d)^e} \tag{5.9}$$

where I is the average intensity (mm/hr). T_d is the duration of the storm (min); b, d, and e are the coefficients determined for each county and is available from the National Weather Service (NWS) Technique Report 40 (TP 40) (TXDOT, 2004). The total rainfall depth for the synthetic event is calculated as:

$$D = I \times T_d / 60 \tag{5.10}$$

The temporal distribution of the rainfall can follow the NRCS type II or type III curves which are often used (Bedient and Huber 2002, pp 390), as shown in table 5.2 below.

Table 5.2

The NRSC type II and III 24-hour curve

time (hr)	Fraction of 24-hour rainfall	
	Type III	Type II
0	0.000	0.000
2	0.020	0.022
4	0.043	0.048
6	0.072	0.080
7	0.089	0.098
8	0.115	0.120
8.5	0.130	0.133
9	0.148	0.147
9.5	0.167	0.163
9.75	0.178	0.172
10	0.189	0.181
10.5	0.216	0.204
11	0.250	0.235
11.5	0.298	0.283
11.75	0.339	0.357
12	0.500	0.663
12.5	0.702	0.735
13	0.751	0.772
13.5	0.785	0.799
14	0.811	0.820
16	0.886	0.880
20	0.957	0.952
24	1.000	1.000

The fractions of the accumulative rainfall of the 24 hour can be interpolated into user defined intervals such as 15 minutes. By multiplying the total rainfall depth to the fractions, it will give the accumulative rainfall depth at each time interval. The incremental depth can be obtained by subtracting the accumulative values to their precursor. The coefficients e, b, d for Harris County of Texas are obtained from the document of NWS TP 40 (TXDOT, 2004). The values are shown in table 5.3.

Table 5.3

Coefficients of different returning intervals

Reoccurance interval	e	b	d
100-year	0.706	2311	7.9
50-year	0.728	2311	7.7
20-year	0.724	2057	7.7
10-year	0.753	2057	7.7
2-year	0.800	1727	7.9

To generate synthetic rainfall for this research, it is chosen to use 15-minute time increment and NRSC type III distribution. The synthetic rainfall intensity can be found in Fig. 5.10.

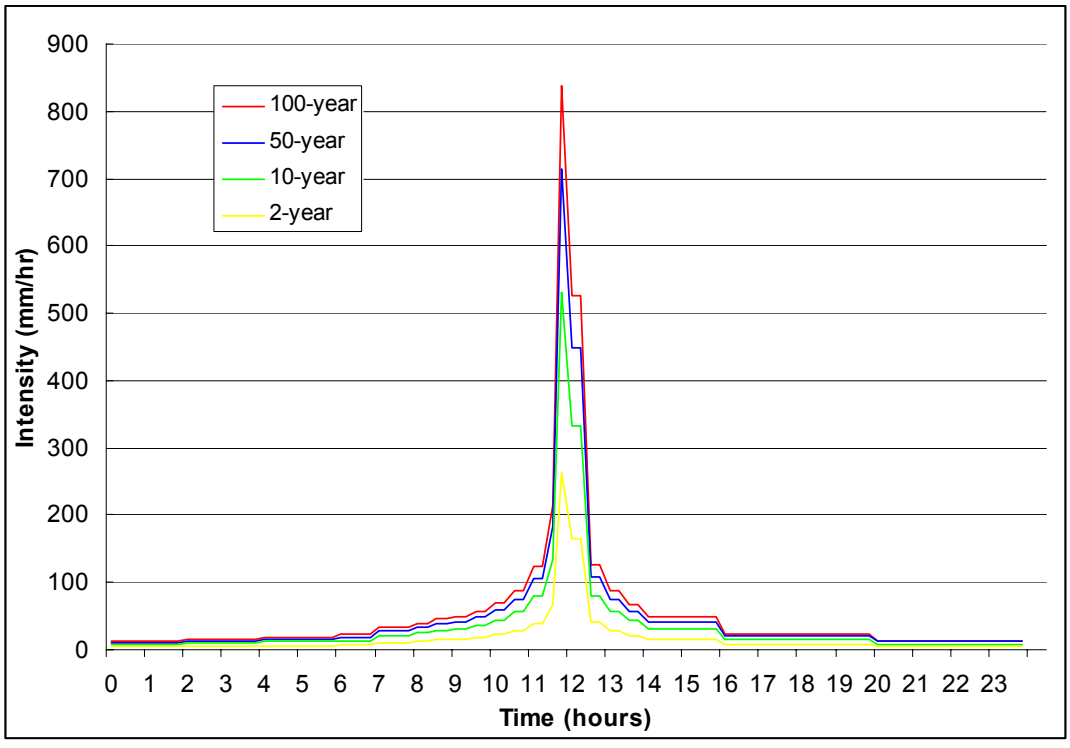

Fig. 5.10 Synthetic rainfall intensities for Harris County Texas

5.6.2. Results and discussion

The 100-year returning rainfall data is inserted into the hydrological and hydraulic modeling system to obtain flood depth and extent. Fig. 5.11 shows the discharge curve at the outlet as responses to a 24-hour 100-year rainfall event. The corresponding flood extent and depth distribution is shown in Fig. 5.12.

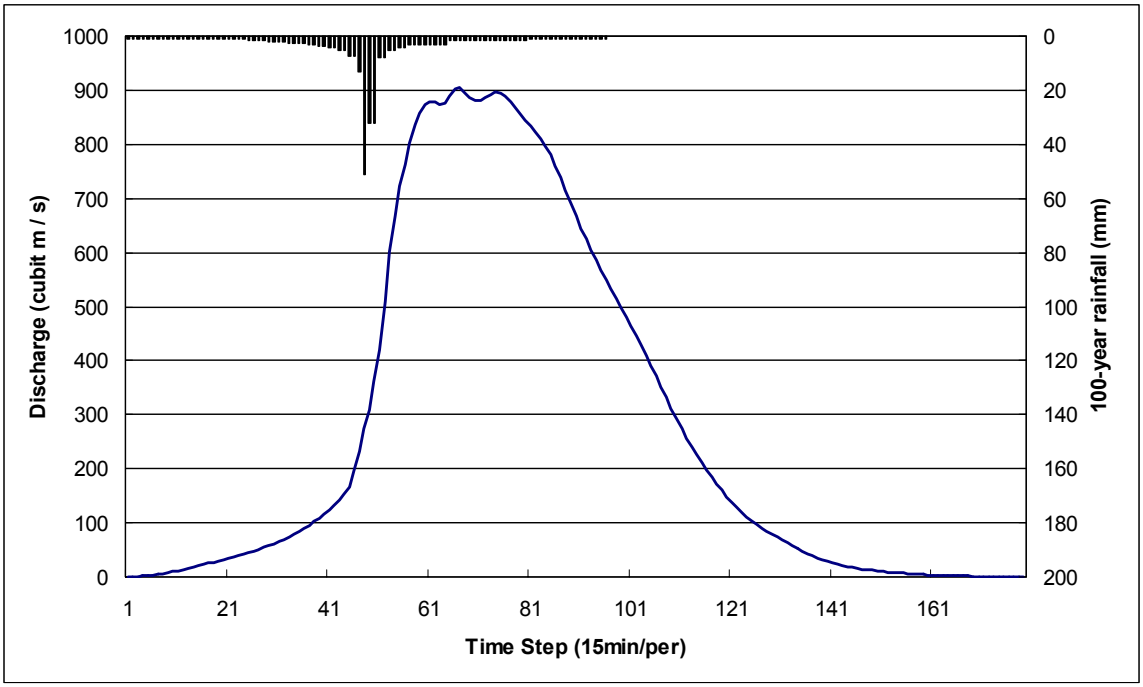

Fig. 5.11 Hyetograph and hydrograph of the 100-year event

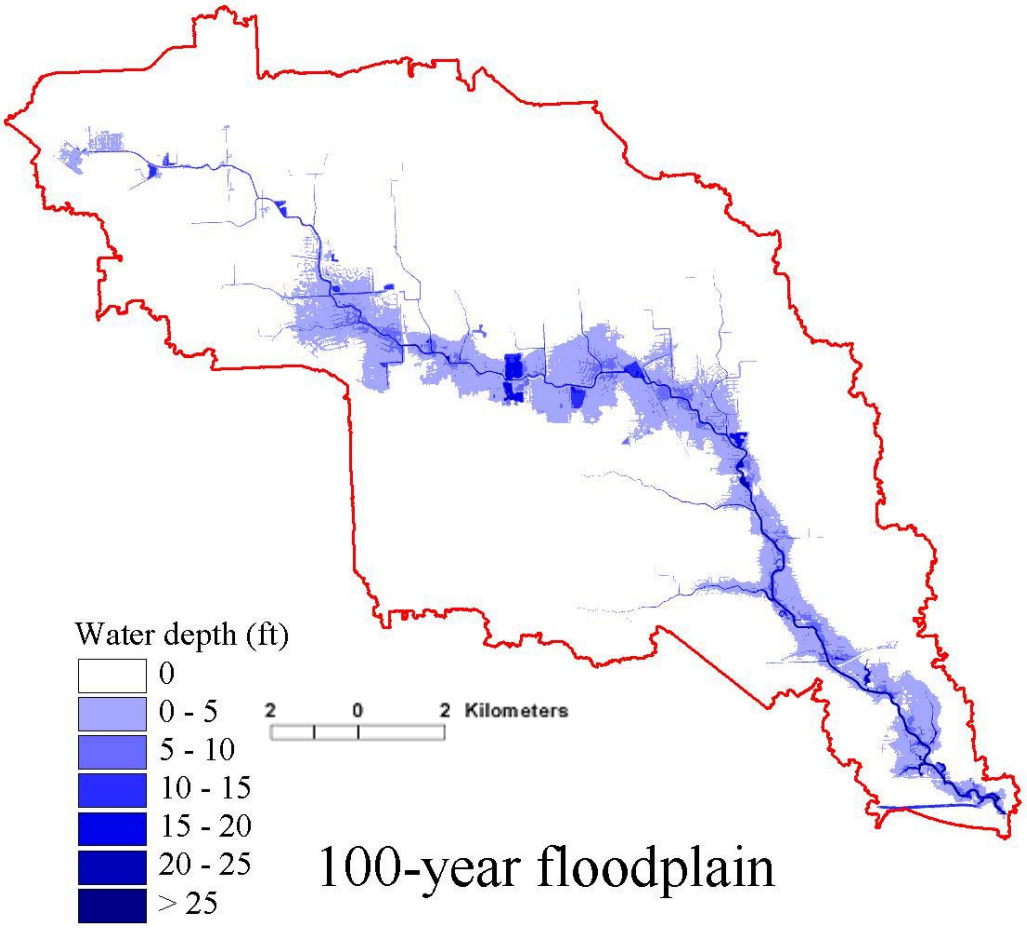

Fig. 5.12 Simulated 100-year floodplain map

5.7. Summary

A GIS supported hydraulic modeling system is adopted in this research to simulate flood extent and depth with given discharge rates in channels. The core component is HEC-RAS which is one of the most widely used professional hydraulic analysis software. The model is based on the energy and mass conservation at each cross-section with given

boundary conditions. Using HEC-RAS model, a gradually changing channel discharge profile is converted to the water surface elevation at each cross-section.

A GIS-based spatial analysis method is invented to convert the cross-section water surface into a water depth and flood extent in floodplains. The new method is able to handle raster data structure of DEM. The major advantage is that hydraulic connectivity is considered as one of the key component to extend flood water according to the given water elevation at cross-sections. The isolated flooding areas that would be generated by traditional methods are eliminated in the new method with the capability to check hydraulic connectivity. Therefore, this method is able to produce better representation of flood water depth and extent.

Flood extent and depth of the Tropical Storm Allison event is simulated and plotted in the map. Validation is done through acquiring high water mark (HWM) records during the event. The overall RMSE is 1.72 ft when comparing the observed water surface elevations to simulated results. 100-year floodplain is mapped by applying the synthetic 24-hour rainfall to the modeling system. It is essential to provide planning and policy-making implications for local urban and economic growth.

CHAPTER VI

IMPACTS OF NATURAL AND HUMAN-INDUCED CHANGES

6.1. Overview

It is widely accepted that land use changes contribute to altering the storm runoff generation and hydrology regime in the catchments. Rainfall runs off when the surface abstraction is exceeded by the amount of water received. The exposure of soil surfaces to the rainfall plays a key role for infiltration processes, and thus is crucial to the runoff reduction. The hydraulic condition in the river system is decisive for the conveyance velocity, dispersion, and convection of the flood water. Human activities change the landscape of the catchment by artificially removing and replanting vegetation, concretize the land surface, enlarging and re-formatting channels, and constructing flood control structures. It is evident that human activities in the catchment area are influential to the runoff. Engineering and management measures mainly contribute to alter of the way that water is transported above ground and under ground. Most environmental changes, although commonly mild and gradually taking place, are significant to reform current local hydrological processes. It has been evident that global warming is expediting the water cycling speed and therefore, increasing the average rainfall amount and the frequency of extreme rainfall events for certain areas. However, how these changes are functioning as a whole to affect the context of human living environment and how their relative importance for people to concern about remain unknown. This research tries to reveal the keys to the questions from a case study in the selected area by quantifying the magnitude of impacts of these environmental changes to the flooding.

Generally, there are two major driving forces for the hydrological processes: external forces from climatological factors and the internal forces from the interactions of sub-processes (Bronster, 2004). At the global scale, the extensive consumption of fossil energy has been recognized to be the major extra sources of carbon dioxide and other "green-house" gases. The hydrological cycle intensity, for example, would increase by about 10% if the atmosphere temperature is increased by 3 deg. C. (Bronstert, 2004). Although the global changes appear to be mild and gradual, the process is always considered to be invertible. Parallel to the climatological changes, local land use changes are also essential for the hydrological studies. The intensive use of land for purposes of agricultural, industrial, and residential unavoidably re-formed the landscape structure and surface conditions, which lead to the deforestation of tropical forests and urbanization of undeveloped areas. The global environmental change is very difficult to quantify not only because it occurs at continental or global scale which is beyond the capability of the monitoring devices usually operated, but also due to its long-term definition. The regional or local environmental changes and their consequential influences, however, can be quantified and evaluated through a common practice of scenario studies. Once the hydrological models have been calibrated and verified at several scenes and events, they can be utilized to quantify the environmental changes that are directly relevant to some of the parameters in the model. The impacts of the changes implicated to the hydrological processes are then to be assessed and compared historically or hypothetically.

Generally, there are two major purposes to study scenarios of environmental changes. One is to serve as the reference or guideline for the local policy makers and government to produce feasible plans for regional development. The other purpose may relate to evaluating the impacts of "real" urban development and potential trends on the altering the hydrology regime and vulnerability to the consequential flooding. For the first category of studies, a set of scenarios that covers a substantial range of alternatives should be developed and evaluated by the model. Although the regional geomorphologic and hydrological characteristics are essential to the model parameters, the scenarios are more hypothetic rather than using "real" data and prediction because the importance of this kind of study is to answer questions such like "what-if this happens" without taking much consideration of "how likely this scenario could happen", although some restrictions may apply. The scenario studies in the second category, however, have to rely on re-constructing from historical measurements of the model variables. The emphasis of this kind of study is to assess how much changes have taken place in the regional water cycle and hydrology regime during some specific periods. A comparison of the historical studies with current conditions could provide keys to the question "what the flood scene will be if the developments over the recent decades did not take place under the situation of the Tropical Storm Allison?" or "how much the difference of the floodplain boundary is, given the situation of recent urbanization?".

6.2. Effect of urbanization induced land use changes

6.2.1. Introduction

According to the purposes of the scenario studies, scenarios are constructed based on different criteria. For instance, the study of the historical scenarios requires only those that are representative for the period of time to be examined. There is no specific criterion of the numbers of the scenarios or the extremeness of each scenario. However, extreme events are important for scenarios of hypothetic studies because the scenarios have to be a reasonable coverage of the extremes that could take place. Since this research focuses on the retrospective analysis of land use and land cover changes, the scenarios are built upon historical remote sensing images. Among all the land cover changes, the surface imperviousness has the largest direct influence on flood water generation. The impervious surface is the man-made surfaces over natural soil layers that prevent water from infiltrating to the soil layers under them. The percentage of the impervious surface over a certain area is called imperviousness. The surface imperviousness is one of the most effective indicators to quantify the urbanization. This is not because other information is less important than the surface imperviousness, but that the fraction of the surface imperviousness is the most measurable value of urbanization with less subjectivity. It can be physically measured, quantified, and controlled regardless the scale that the study is carried out on (Scheuler, 1995). Rainfall water runs off if it is not intercepted by vegetation, detained by surface depressions, or absorbed by soil. All these processes contribute to the surface water abstraction. However, soil infiltration plays the most essential part of the runoff water reduction and

is determinative to the amount of water expelled into the stream network system. As the surface becomes impervious, mostly due to manmade structures and sealing, the soil losses their capacity to the water fell to the surface. Therefore, increase in the surface imperviousness directly results in higher peak discharges and more flood water. For examples, Scheduler (1995) showed that a parking lot would have a runoff coefficient 16 times larger than that of the meadow. It was also evident in Ng and Marsaletk (1989), Cheng and Wang (2002), Lee and Heaney (2003), etc. With the increasing available remote sensing data, surfaces with vegetation covers, bare soil/sands, water bodies, and manmade materials can be classified and measured.

6.2.2. Remote sensing data description

Constructing retrospective land use land cover scenarios has been identified as one of the commonly used procedures to monitoring landscape dynamics, urban expansion, and other environmental changes. The surface imperviousness can be estimated from various satellite images. Landsat mission has been collecting continuous data records of the earth surface since 1972 when it was launched as ERTS-1. Sensors used in Landsat missions were improved in terms of radiometric, spectral, and spatial resolutions, and data quality. Landsat MSS which is the earliest version of the sensor in the series is still widely used together with other sensor in multi-temporal studies such as Laba et al. (1997) and Tommervik et al. (2003). In this research, four scenes Landsat images were chosen for year 2002 (Fig. 6.1), 1990, 1984, and 1974, about 10 years apart from each other. All data are calibrated and converted to at-satellite reflectance following the methods by Markham and Barker (1987). Since the study area is limited to one small watershed, the

atmospheric condition is assumed to be homogenous. Therefore, no atmosphere correction is necessary.

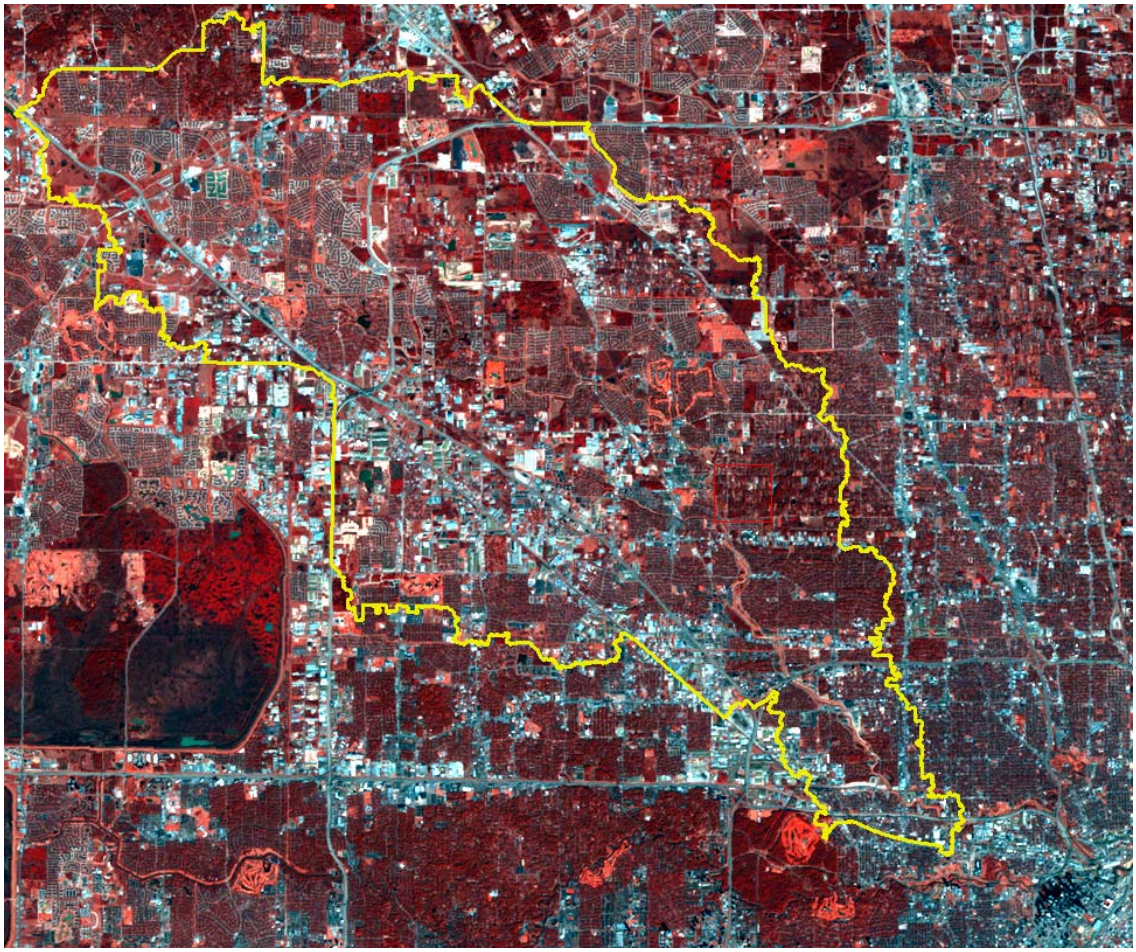

Fig. 6.1 Landsat ETM+ satellite image acquired in January 2002 for the study area

6.2.3. Methods

6.2.3.1. Literature review

To approach the subpixel imperviousness estimation, previously, a conceptual vegetation-impervious surface-soil (VIS) model was proposed by Ridd (1995). This model settled the conceptual imperviousness model for the remote sensing studies of urban development. However, due to the difficulties in accurately acquiring the VIS distribution, only few success applications are found in the literature (Wu and Murrey, 2003). The methods previously implemented for imperviousness estimation can be literately divided into two groups: physically based model and empirical models. The physical models employ the spectral mixing approaches, such as Ji and Jensen (1999), Ward et al. (2000), and Wu and Murray (2003). Wu and Murray (2003) applied the Spectral Mixture Analysis (SMA) method to estimate the imperviousness using Landsat-7 ETM+ data. They achieved an RMS error of 10.6% for all the samples. They also noticed that due to the effect of some high albedo and low albedo features, the imperviousness estimation were adversely influenced. However, even they made efforts to mask those influential materials such as sands and water, the effect of the sand still remained as the main cause of the outliers (Wu and Murray, 2003). Other approaches include the Artificial Neural Network method (Wang et al., 2000), Classification Tree (Smith and Goetz, 2000), and Regression Tree method (Yang et al., 2003). Yang et al. (2003) tested the regression tree method at various sites, and the results are comparable to the method used by Wu and Murray (2003) and this method is consistent and "cost-effective and suitable for large-area imperviousness mapping" (Yang et al., 2003).

Regression tree is an ideal tool to deal with non-linear problems through constructing a binary tree. However, since it require extensive ground truth and training datasets, it is not feasible for retrospective analysis because in many situations, there is no reference data can be obtained.

6.2.3.2. Spectral Mixture Analysis (SMA)

Ridd's conceptual V-I-S three-component mixing model attributes environmental reflectance parameters into individual endmembers. In this model, urban land cover are comprised by components of imperviousness, vegetation, and soil (VIS). Based on this conceptual model, the fraction of imperviousness can be estimated from satellite images by unmixing endmember reflectance. Endmembers are pure pixels which are assumed to be major components contributing to the reflectance of mixed pixels. In other words, any pixel can be regarded as a linear combination of the reflectance of the endmembers. Linear spectral mixture is suitable for most applications if multiply scattering can be neglected (Wu and Murray, 2003). A linear spectral mixture model is described as follows:

$$RM_b = \sum \alpha_i RE_{b,i} + \varepsilon_b \tag{6.1}$$

where RM_b = reflectance for band b of a mixture pixel; $RE_{b,i}$ = reflectance of endmember i for band b; α_i = fraction for endmember i; ε_b = residual. A linear unmixing procedure is to find out the fraction for each endmember i so that the least square error of modeled reflectance is minimized. Fully constrained least square solution (FCLS) of the linear unmixing has been discussed in Van De Meer and De Jong (2000), Chang and

Heinz (2000), and Change et al. (2004). These conditions include non-negative constrain (NC) which is:

$$\alpha_i \geq 0 \tag{6.2}$$

and the sum-to-one constrain (ASC) :

$$\sum \alpha_i = 1 \tag{6.3}$$

The goodness of the fit is measured by the RMS:

$$RMS = (\frac{1}{N}\sum \varepsilon_b^2)^{1/2} \tag{6.4}$$

The result of linear unmixing method is greatly affected by the selection of endmembers. An endmember is an "idealized pure signature" (Chang, 2006) for a clearly defined land cover. Therefore, the pixel purity index (PPI) which was developed by Boardman et al. (1993) can be used to guide users to select pure endmembers from images. The algorithm of calculating pixel purity has been implemented in ENVI software developed by Research System Inc. Detailed discussion of identifying endmembers can be found in Van Der Meer and De Jong (2000). Wu and Murray (2003) used a four-endmember method to estimate imperviousness in the metropolitan area of Columbus, Ohio. The surface imperviousness was calculated by adding low albedo and high albedo endmembers together. This is based on the fact that low albedo materials are found as asphalt, water, or shadows; and high albedo materials are mostly from concrete, sands, and clouds. It is assumed that by masking out water and sands, the rest non-impervious materials have no significant effect on determining the imperviousness from totaling low albedo and high albedo endmembers. However, in this case study area, shadows of

vegetation cannot be neglected. As shown in Fig. 6.2, the IKONOS image which was obtained on January 15, 2001, 17:10 GMT shows significant shadows in forestry area. Linear unmixing result also showed that the low albedo endmember has significant percentage which, if contributes to surface imperviousness, would cause significant inaccuracy to the resultant imperviousness. Therefore, the shadow effects have to be considered in the calculation of surface imperviousness. Shadows may be sourced from various objects: roof, building, tree crowns, and terrain. To differentiate shadows from various sources, it is assumed that the area of shadow is proportional to the area of the object.

Fig. 6.2 Shadow effects of a forested area

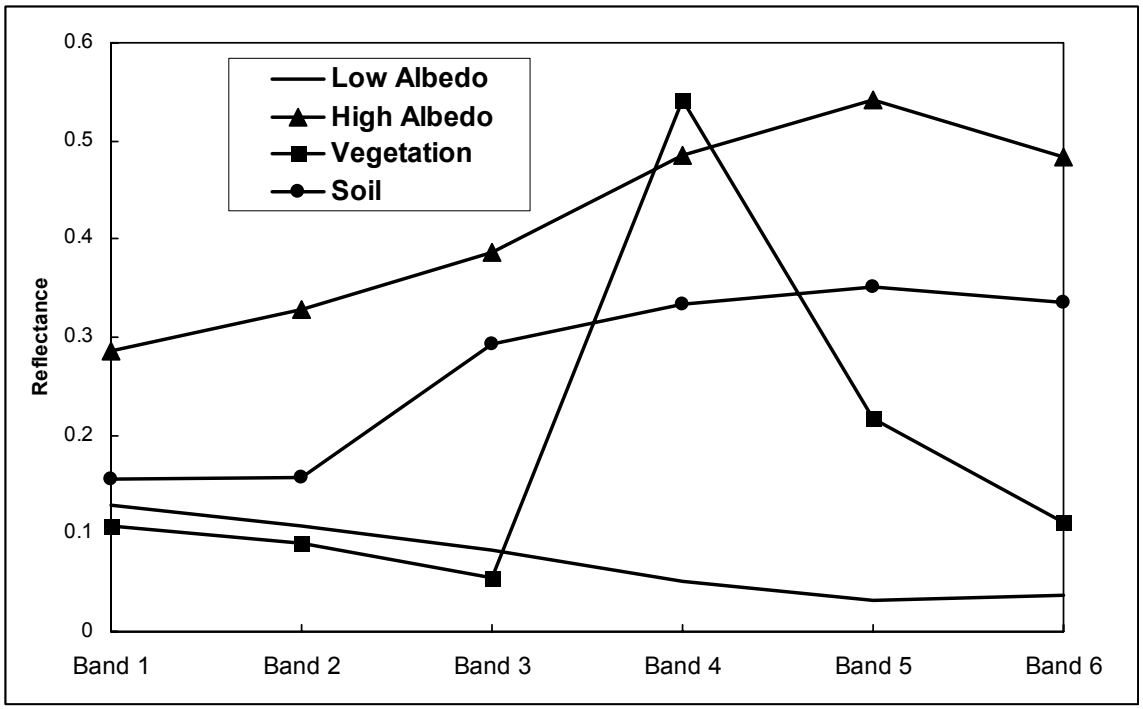

Fig. 6.3 Endmember reflectance identified from the image

6.2.3.3. Endmember selection

Endmember selection is one of the most critical steps for spectral unmixing methods. Following Wu and Murray (2003), four endmembers were identified from the 2002 Landsat image, which includes low albedo, high albedo, vegetation, and soil. Among these four endmembers, low albedo and high albedo pixels are the easiest to be found in the image because their clear reflectance signature and homogeneousness. Therefore, these two endmembers are picked manually from the image. The other two endmembers, soil and vegetation, are obtained using automated methods. A Maximum Noise Fraction (MNF) transformation was performed to separate uncorrelated signal component from correlated noise (Van Der Meer and De Jong, 2000). Then the pixel purity index (PPI)

was calculated using the method by Boardman et al. (1993). Based on the pixel purity index, those pixels that satisfy the threshold are considered as candidates of endmembers. The spectral signatures of the four endmembers are shown in Fig. 6.3.

The linear unmixing method is to find out a unique solution of the linear regression model:

$$r = M\alpha + n \tag{6.5}$$

where r = pixel vector; M = $[m_1, m_2, \ldots, m_p]$ where m is the endmember reflectance vector; $\alpha = [\alpha_1, \alpha_2, \ldots, \alpha_N]^T$; n = residue. However, the traditional approach to solving this problem will result in negative fractions for endmembers. And, according to the assumption of the linear mixture model of ground reflectance, the sum of all endmember fractions should be identical to 1, which is also not achieved. Chang and Heinz (2000) proposed a fully constrained least square unmixing method to find the optimized solution of equation (6.1) with the non-negative and sum-to-one constrains. Detailed description can be found in their articles.

As discussed before, the surface imperviousness can be estimated by adding the fractions of low albedo and high albedo endmembers (Wu and Murray, 2003). However, it should be noted that in the case study area, shadows can not be neglected but has to be considered in surface imperviousness calculations. As shown in Fig. 6.2, a residential area which mainly mixes among roof-tops, vegetation, and concrete roads. Low albedo components should attribute to both vegetation and impervious surfaces. Simply obtaining the surface imperviousness by adding the low albedo part and high albedo part will overestimate the imperviousness. In areas with soil exposures, the fraction of

impervious surface should be close to 0. But using the four-endmember model, the high albedo part is not 0, especially for areas with lower soil moisture. Therefore, soil and vegetation shadows would affect the reliability and accuracy of the SMA model estimations.

A visual inspection shows that that soil exposure areas should have large fraction of soil and small fraction of vegetation. Using a trial and error approach, it is found that if soil fraction is larger than 40% and vegetation fraction is larger than 5%, this area would be a soil exposure surface. Therefore, soil exposure mask is created by querying the resultant four-endmember fractions using above criteria. A three-endmember model without soil component is used for those areas that do not have soil exposure. For non-soil-exposure areas, by assuming the shadow contribution from vegetation is proportional to its fraction, the fraction of imperviousness can be calculated by:

$$F_{imp} = 1 - F_{veg} - F_{veg} * F_{low} \tag{6.6}$$

where F_{imp} = imperviousness; F_{veg} = vegetation fraction; F_{low} = low albedo fraction. All the fractions are obtained by using a three-endmember mixture model (Vegetation + Low albedo + High albedo). The fraction of low albedo endmember is assumed to be proportional to the fraction of vegetation and non-vegetation features. Therefore, imperviousness is calculated by subtracting vegetation and its shadows (the last component of equation 6.6).

6.2.4. Validation

The distribution of calculated surface imperviousness is illustrated in Fig. 6.4. The accuracy assessment was conducted by using the high resolution IKONOS image (1m resolution fused color image) which was acquired the same day but one year earlier that the Landsat image. A random selection of 100 points was obtained to evaluate the accuracy of the linear spectral mixing model. The IKONOS image was abstracted into unsupervised classes using the ISODATA clustering method. Then the classes are labeled as pervious or impervious according to their class spectrum signature. The imperviousness is calculated within each 90m by 90m mesh grid by dividing the number of impervious pixels within each 90m by 90m square. Manual correction was made to those that fail to match human interpretation. The purpose of using 90m squares is to avoid geo-reference errors of Landsat images. The 30m resolution imperviousness derived from linear unmixing method is then averaged within each 90m square that is same as the IKONOS test dataset.

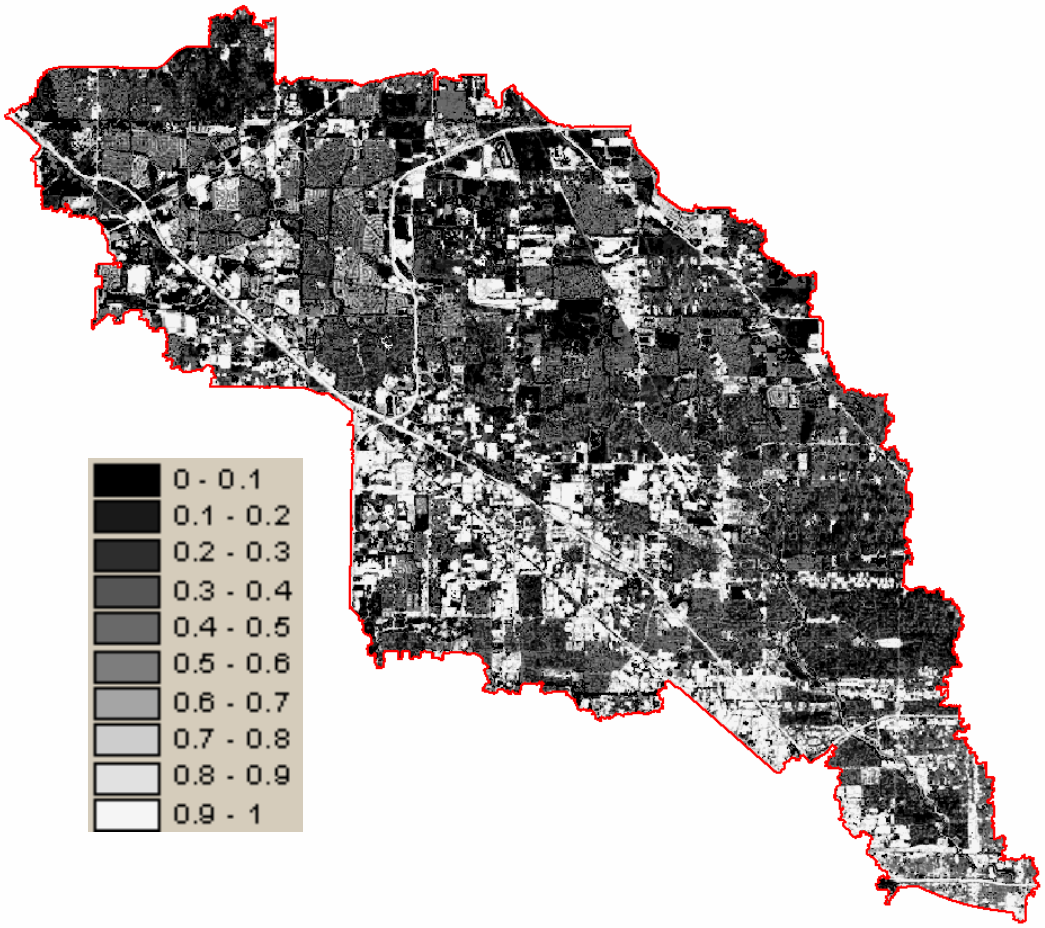

Fig. 6.4 Percentage of impervious surface derived from Landsat ETM+

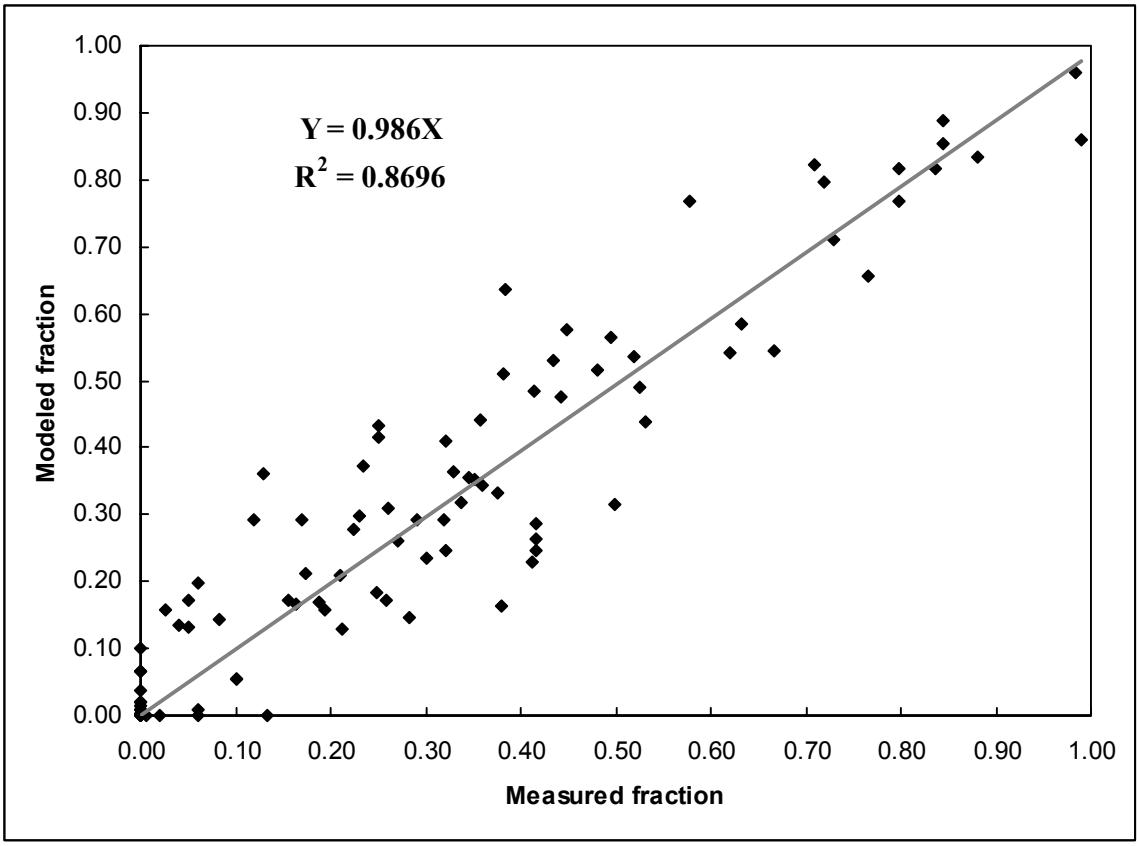

Fig. 6.5 Validation of calculated surface imperviousness using observed data

The resultant scatter plot of the modeled imperviousness and the measured imperviousness from IKONOS is shown in Fig. 6.5. The slope of the fitted trend line is close to 1. The correlation coefficient R = 0.936. This illustrates the high agreement of modeled impervious fraction to the "true" surface imperviousness. The overall RMS error is 0.094 or 9.4%. A map showing the estimated subpixel imperviousness is

illustrated in Fig. 6.4. The clear structure of urban CBD, transportation system and sub-urban residential areas are clearly represented by the surface imperviousness map. It should be noted that some high frequency noise exists in the map. It is because the identification of soil exposure mask cannot avoid noises. However, the noise does not influence the overall accuracy of the surface imperviousness estimation.

6.2.5. Imperviousness map derived from retrospective data

Surface imperviousness of 1990, 1984, and 1974 were calculated using the spectral mixture model and the procedures describe above. Endmember profiles are selected respected to the spectral bands of each year. The results are illustrated in Fig. 6.6 which shows the percentage of impervious surface for year 1974, 1984, 1990, and 2002. By fitting a regression line, as shown in Fig. 6.7, it can be seen that the imperviousness in the study area has an increment rate of about 1% per year (correlation coefficient $R > 0.99$). It also should be noted that the fastest increase of the imperviousness took place during 1984 to 1990.

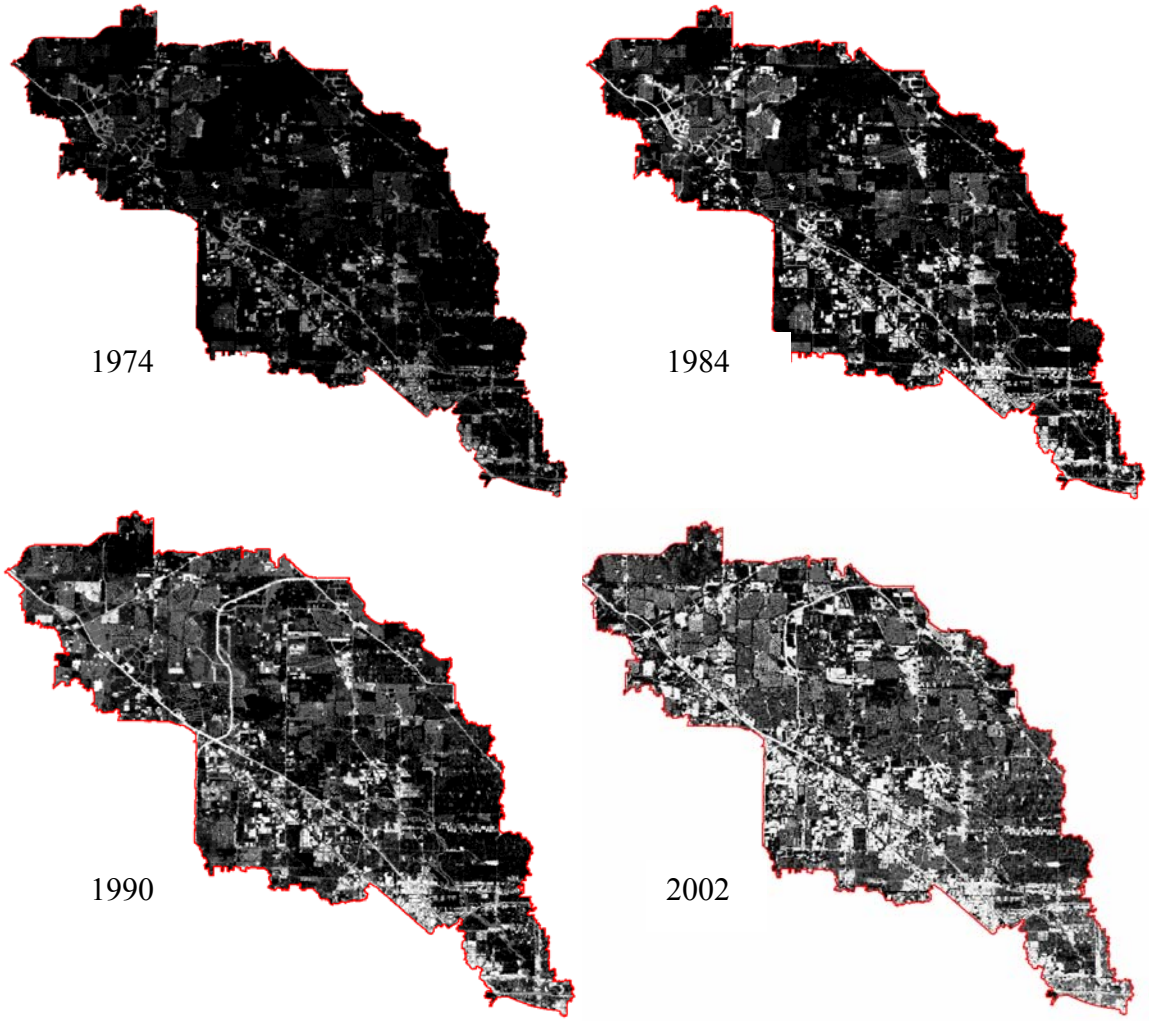

Fig. 6.6 Surface imperviousness for each year

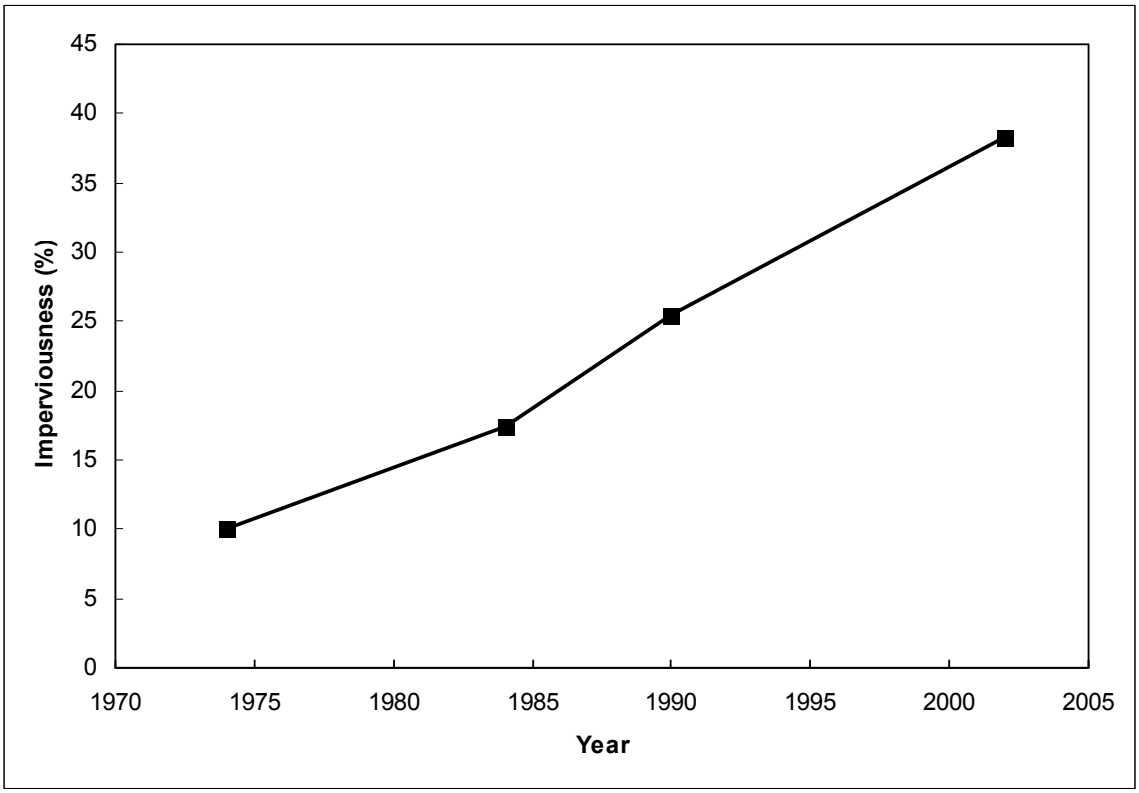

Fig. 6.7 Trend analysis of the impervious surface change from 1974 to 2002

6.2.6. Hydrologic/hydraulic model results

Surface imperviousness is the variable that controls how much proportion of water will become direct runoff without subjecting to infiltration. For examples, if the surface is 0% percent impervious, all precipitation will be subject to infiltration. On the other hand, if the surface is 100% impervious, all water will flow directly downstream. Increasing the percentage of imperviousness will result in high volume runoff for a given amount of precipitation. The imperviousness data derived from the above procedure was used as the parameters for the infiltration model described in chapter II. The total runoff volume of the 100-year rainfall event under surface imperviousness conditions of those different

years is listed in table 6.1. As can be seen, runoff amount increased about 33.43% from 1974 to 2002. Accompanied by a larger volume of runoff, peak flow rate is increased by 19.62%. The discharge hydrograph of the 100-year event is illustrated in Fig. 6.8. As can be seen, the peak time is almost the same except a little bit earlier in 2002 comparing to the year 1974.

Table 6.1

Hydrological simulation results using imperviousness data of each year

	2002	1990	1984	1974
Runoff (cubic meters)	44,325,000	38,889,630	36,066,510	33,219,270
Increased runoff (cubic meters)	11,105,730	5,670,360	2,847,240	0
Increased (%)	33.43	17.07	8.57	0
Peak flow	904.6	827.7	790.2	756.2
Increased (%)	19.62	9.46	4.50	0

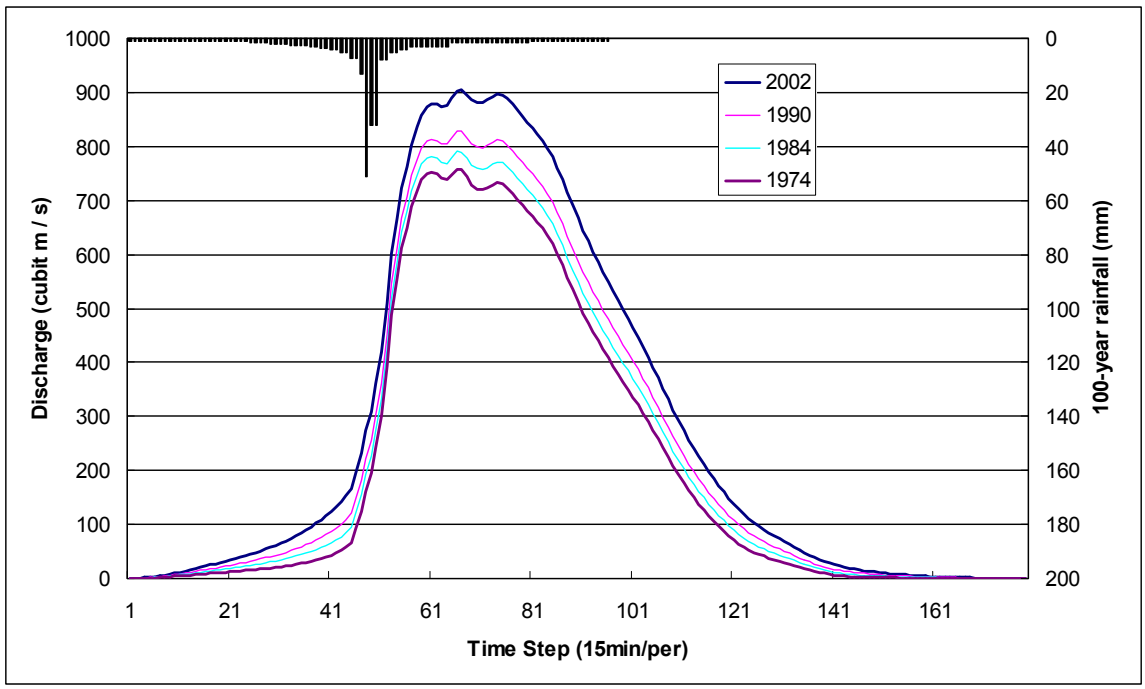

Fig. 6.8 Hydrograph of the 100-year event from model simulation

To obtain the flood extent and depth, simulated discharge data is manually input into HEC-RAS hydraulic model. A subcritical simulation is run to obtain water surface elevation using calibrated cross-sections. Simulated water surface elevation is then transferred to flood extent and depth. Simulated 100-year flood maps are shown in Figs. 6.9 to 6.12. The flood extent has increased from 11.23 km^2 to 13.66 km^2 (table 6.2) or 21.6% (Fig. 6.13). The annual increase rate is about 0.08km^2. It is always worthy to ask "based on the retrospective analysis, if current trend is maintained, how the flood extent will change in next 20 years?" To answer this question, a prediction of the discharge rate at each cross-section is made based on the trend determined from the 28 year of analysis. Using the predicted discharge rate, flood extent can be derived from the HEC-RAS

model and a GIS. Fig. 6.14 shows the projected flood extent of a 100-year event in year 2020. According to the analysis, current floodplain will expand about 20% in the next 20 years.

Table 6.2

Simulated flood extent and mean depth

Year	Area (sq. km)	Mean depth (ft)
1974	11.23	0.222
1984	11.90	0.235
1990	12.60	0.25
2002	13.66	0.28

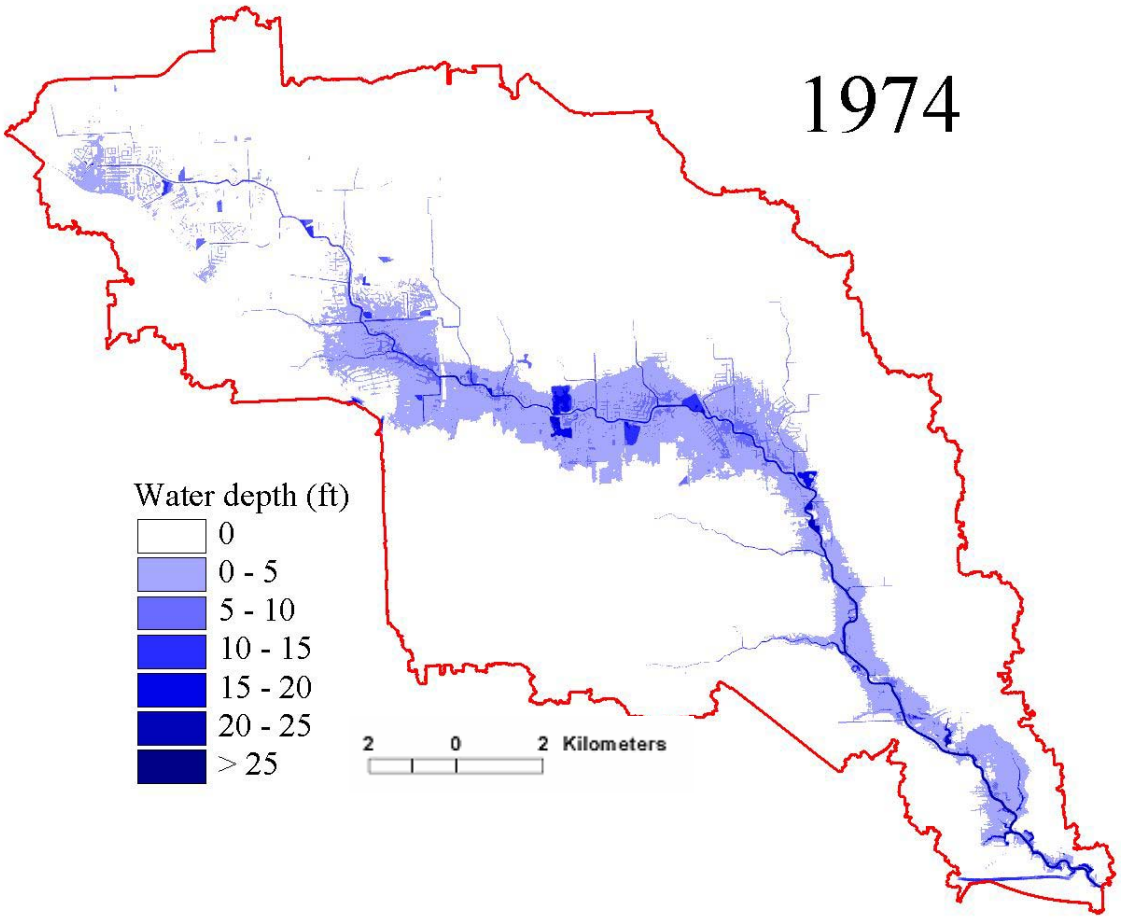

Fig. 6.9 Floodplain of 1974 scenario

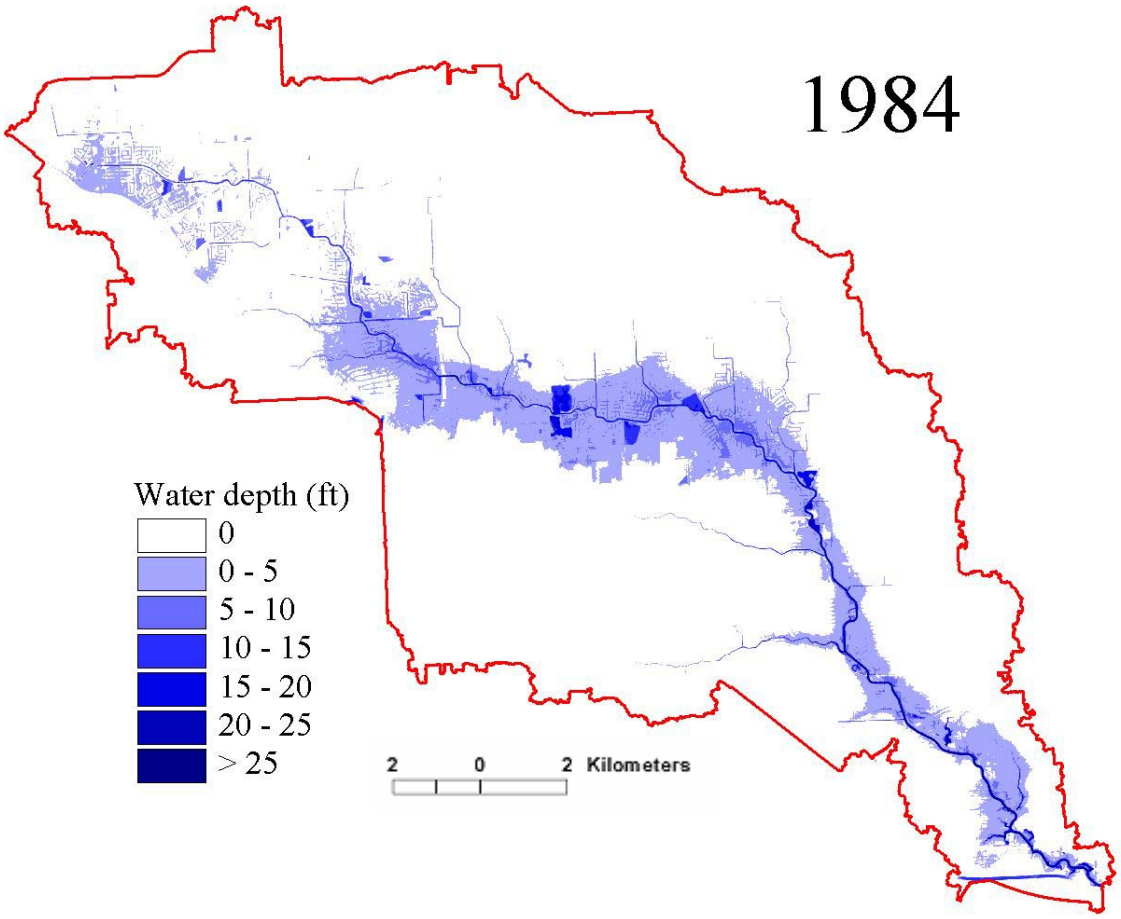

Fig. 6.10 Floodplain of 1984 scenario

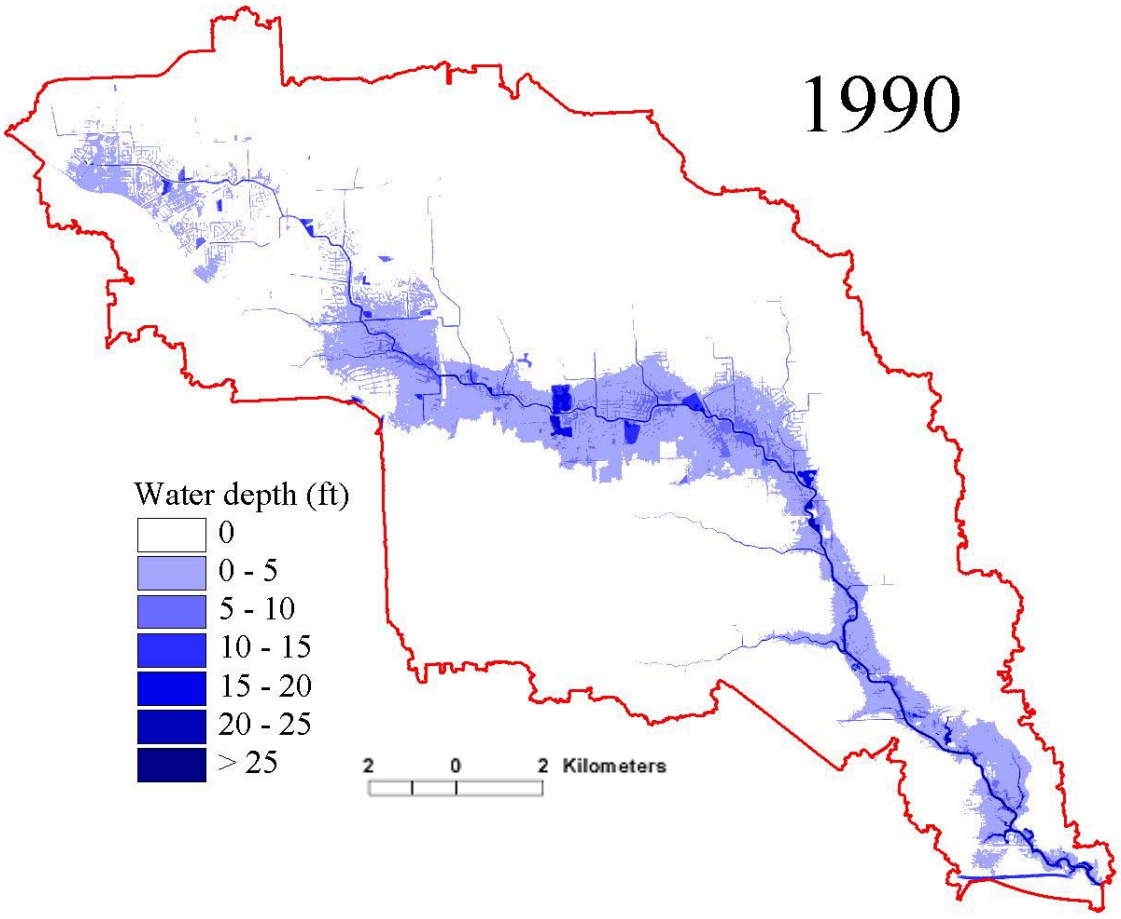

Fig. 6.11 Floodplain of 1990 scenario

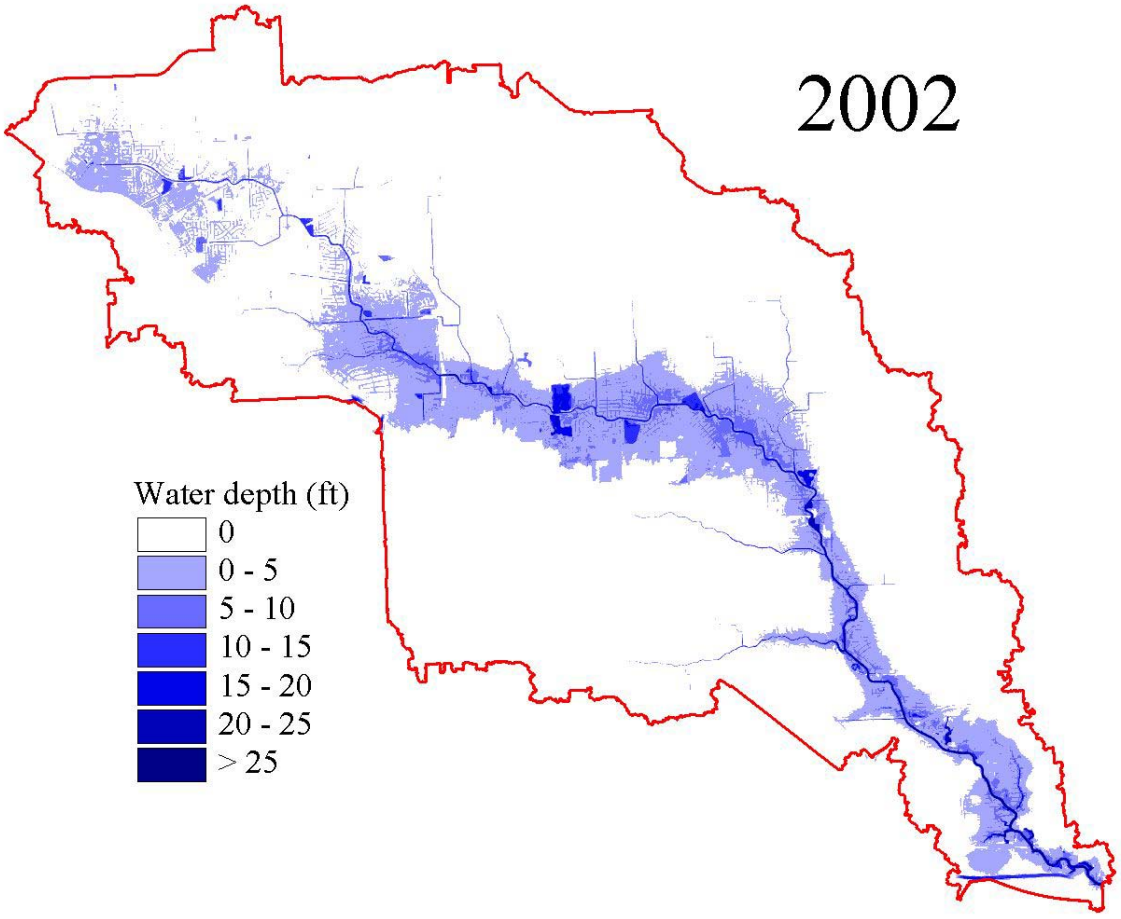

Fig. 6.12 Floodplain of 2002 scenario

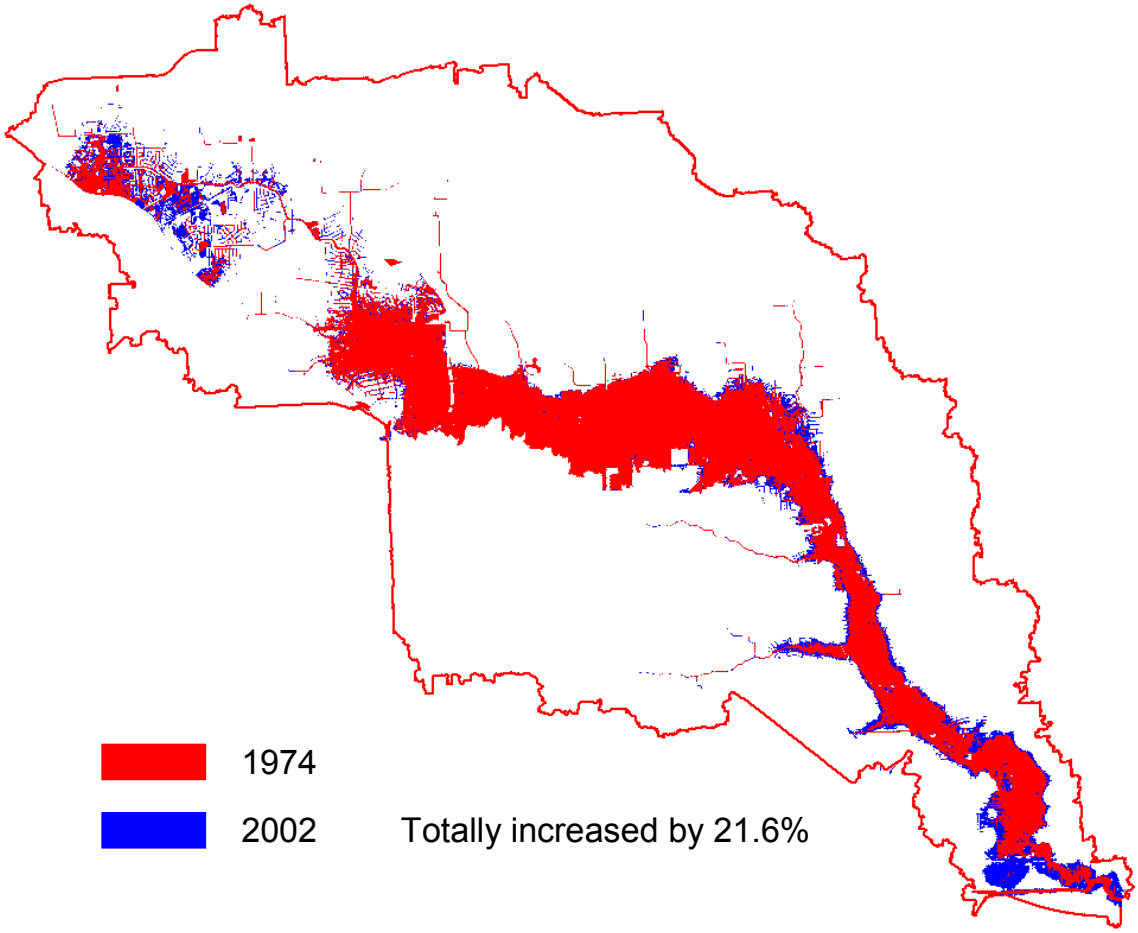

Fig. 6.13 Comparison of the floodplain of 1974 and 2002

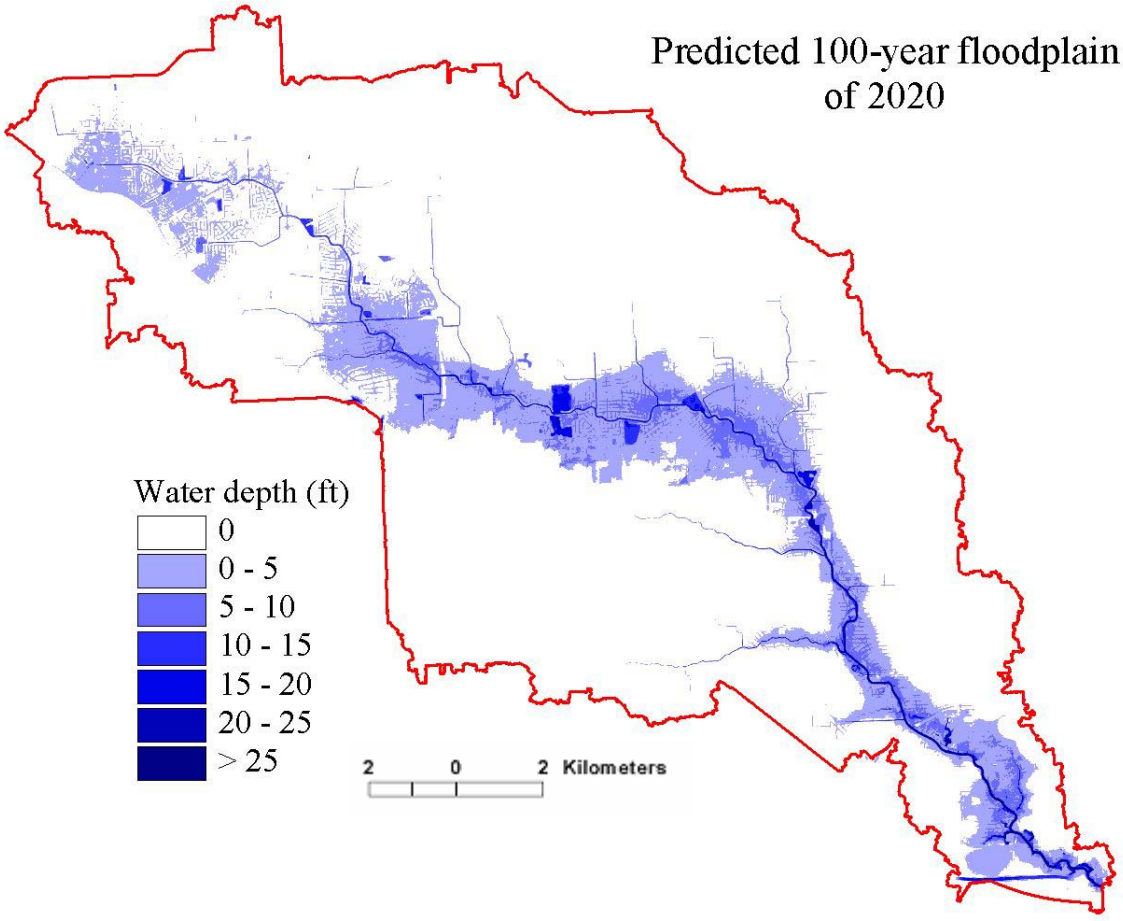

Fig. 6.14 Predicted 100-year floodplain of year 2020

6.2.7. Summary

The scenario analysis is an effective measure to help understanding the impact of undergoing development and environmental changes on the resultant flooding damages and to serve as references and guidelines for urban development planning and decision making. Scenarios are built to re-construct and quantify the distribution of the surface

imperviousness of pass three decades using Landsat satellite images. A set of Landsat images spanning from 1974 to 2002 provides pre-development land use and land cover information for the study area. Surface imperviousness which is one of most important indicator of urban growth and land cover change is quantified from a spectral mixture analysis. The major advantage of this method is that it does not require input of training datasets. This is very important for retrospective studies because it is relatively hard to find reference data for earlier ages. The sum-to-one constrain and non-negative constrain is posed to the least square estimates of endmember fractions. The percent of impervious surface within each pixel is calculated from the high reflectance object endmember and the low reflectance object endmembers. Since soil exposure is limited in the study area, soil component is masked and eliminated from the mixture model. The RMSE of subpixel imperviousness estimation is about 9.4%. The accuracy is consistent to the reported numbers in the literature. Using the same approach, surface imperviousness condition of year 1974, 1984, and 1990 is estimated. The result shows a roughly 1% percent increment of the percentage of impervious area. The total areal size of impervious surface has increased by 2.6 times from 1974 to 2002.

The impact of changes of imperviousness includes larger volume of surface water runoff and higher peak flow. The runoff volume has increased by 33.43% for a 100-year returning frequency rainfall from 1974 to 2002. The peak flow increases by 19.65% at the watershed outlet. Higher peak flow causes the floodplain to expand. The floodplain extent is 21.64% larger in 2002 than in 1974 due to urban growth. If current trend is continued, the floodplain will expand by another 20% in next 20 years.

6.3. Effects of flood control facilities

6.3.1. Introduction

The intensive utilization of land for residential, industrial, and commercial purposes is the evidence of urbanization. Being aware of the potential flooding threaten to the lives and properties, local governments, engineering departments, and planning agencies have employed joint efforts to flood damage relief and migration. Overall, there are several practical measures for floodwater reductions, including reducing the surface water runoff, increasing the flood water detention capability, slowing the in-channel flow, and increasing the channel carriage capability, etc. Reducing the surface runoff does not belong to any of the practical engineering approaches. However, constructions of permeable pavement and parking lots, wide filter or buffer strips of vegetation, and small detention pond or vegetated depressions to temporally hold and infiltrate water are efficient for reduction of surface water runoff (Green et al., 2000). This control option may be less effective when successive storms are too close while local soil infiltration and surface storage have become saturated. The second practice is to increase the storage of storm water facilities, such as building dams or constructing reservoirs. However, the success of a dam built depends on the prior analysis of hydrologic models. Through construction of upstream storage facilities, the flood is expected to be reduces both in the peak magnitude and the concentration speed. Although theoretically a dam would reduce the flood risks of the downstream areas, there were some criticizes that a dam failure makes the flood severer (Green et al., 2000). Due to the cost and complexity to operate a dam and other factors such as the stability, maintenance requirement, and cost

effectiveness, constructing flood water detention basins is more simple and effective. Basically, the detention basins function for two purposes; one is to attenuate the peak of the flows from upstream that drains into the basin directly through topography or by pipelines, the other is to allow the water to spill into the basin through the spillway when water level in the channel is above some designed level. The detained water will drain back to the channel gradually through orifices. The observed hydrograph right downstreamly to the detention basins will be a flat and elongated curve comparing to the original. Channelization projects could increase the water conveyance capacity and as a result, the risk of flood maybe reduced. The common operations include widening, deepening, straightening, and concretizing the channels. Given the same amount of discharge rate, the modified channel could have a lower water surface profile but with a shorter peak concentration time. The velocity in the channels is also increased which could be a potential menace for the downstream areas. The channelization of the tributary branches have to be planned carefully to avoid the chances that timing of the peak flow to be coincided. Furthermore, the engineering operations need to apply to the entire bayou systems consistently, especially for downstream channels. Otherwise, the upstream channelization would only transfer the flood risks to the downstream areas with higher flow velocities and shortened peak flow time.

Current literature mostly concentrates on the negative effects of the human-induced environmental changes, such as deforestation, intensive farming, and development of surfaces impermeable to water. However, the operations mentioned in the last paragraph clearly stated that through man efforts, the natural flood water could be deducted or

controlled, at least partially, by the management measures and engineering efforts. Albeit comparing to the natural forces, the engineering efforts to alter the earth surface are merely countable, they are effective to provide protection at the regional scale. To clarify this point, the case study of Tropical Storm Allison in the White Oak Bayou watershed was performed to simulate the effects of detention basins. The observed and simulated hydrograph at the watershed outlet location could reach a peak up to 900 cubic meters per second. The largest regional detention basin in the watershed could accommodate as much as 694216.19 cubit meter. This number is only equivalent to about 12-minute attenuation of the peak flow, which is even not detectable for a model with a 15-minute time step of simulation. However, the hydrograph immediate downstream to the detention basin shows a significant peak attenuation and hindrance. Once the information about the detention structures or other flood control projects is available, their effects could be evaluated and quantified through hydrological and hydraulic models. Significance of distinguishing the positive and negative human-induced effects on flood occurrences and magnitudes is evident. Firstly, it allows the model to be capable quantifying the effects that are significant enough to alter the surface water profile in the channels. Secondly, the scenario studies could become more specific, such as current or historical land use/cover circumstances without the flood control facilities. The third, for the design purposes, it is crucial to evaluate the capability of current design of flood control structures to function under circumstances of different storm event scenarios or urbanization scenarios.

6.3.2. Scenario analysis of detention basins

Harris County Flood Control District has planned and implemented number of projects to relief and migrate potential flood risks, including several regional flood water detention basins (Fig. 6.15). Five large regional flood water detention ponds were constructed mainly in the 1970s and 1980s, as well as at least four miles of channel modifications (HCFCD 2005). During the Tropical Storm Allison, all the detention basins were filled with flood water (HCFCD 2005). The initial design of these flood water detention ponds was based on the 100-year event with inflow and outflow pipes, orifices, and spillways meet the requirement specified in the manual (HCFCD 2005). Nevertheless, there were no quantitative studies carried on how much those flood control facilities were actually "controlling" the flood water in an extreme storm event such as TSA.

As discussed in chapter V, the hydrological model developed in this research implements the detention basin model as one of the hydrologic response units with the ability to receive floodwater from the adjacent channel spillway. These detention basins were conceptualized as level-pools with inflow from the spillway and outflows through orifices. These detention basins were cascaded one each other along the channel with some other upstream units routing into them. These detention basins can be turned off in the model to perform different scenario analysis. Turning off the detention basins is equivalent to letting the outflow equals to inflow when routing water through each detention basin in the model. Specific observing outlets were inserted downstream to these detention basins in the model to record the hydrograph simulated in the model to

detect the changes. These outlets were also chosen to be located on the cross-sections in the hydraulic model. The flood extent and depth map can be drawn so to visualize and quantify the changes owing to the detention basins. The scenario analysis can be performed on the existence or absence of the detention basins.

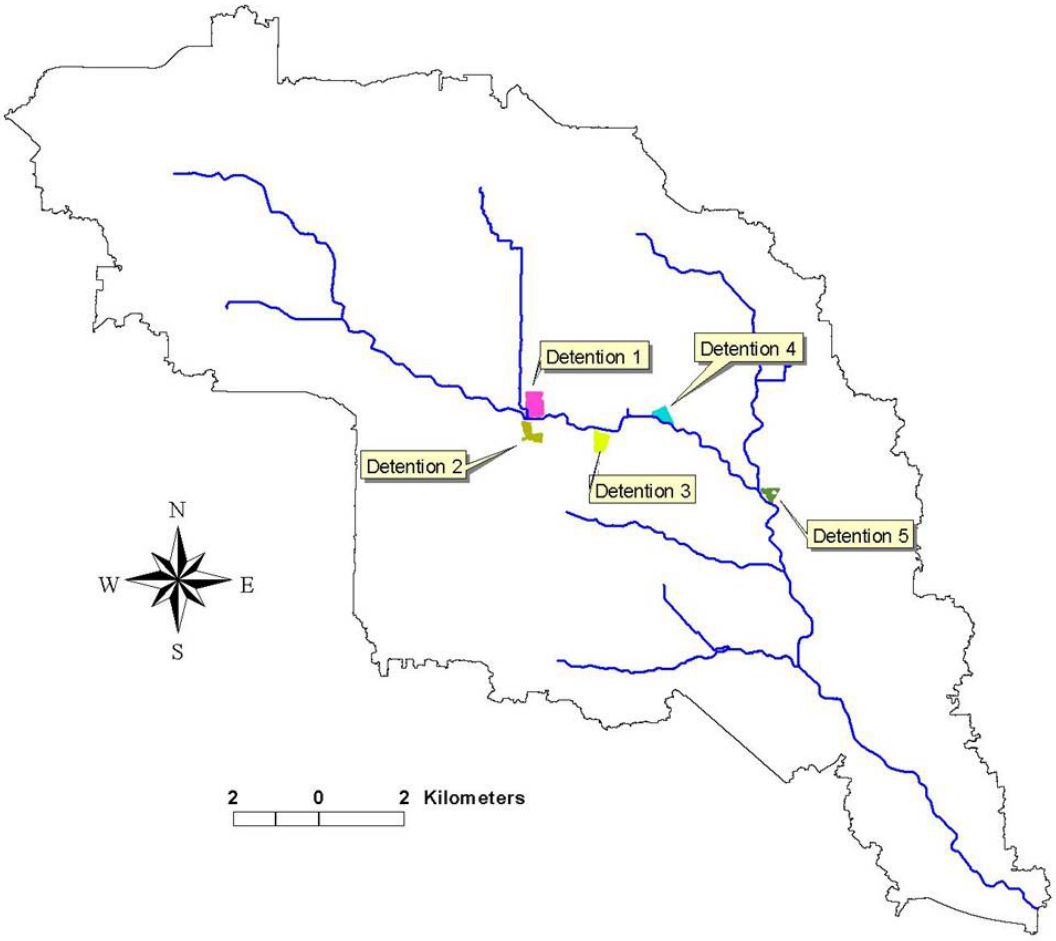

Fig. 6.15 Five large detention basins in the study area

6.3.3. Results and discussion

Hydrological model simulation provides discharge rates at the outlet and each location to be observed. Eight observers were inserted into the model as marked in Fig. 6.16. Table 6.3 shows the discharge rates for scenario with detention basins and without them in year 2002 and 1974. It can be seen that at locations 4, 5, 6, and 7, peak discharge rate has been significantly reduced and even lower than the predevelopment condition in 1974. These locations are protected by the two largest detention basins (basin 1 & 2). Hydraulic model simulation produces a floodplain map with detention basins, as shown in Fig. 6.17. The reduced flood extent due to the detention basin is 10.4%. The downstream locations are protected by the detention basins. As illustrated in Fig. 6.18, the flood extent has been significantly reduced after the floodwater detention basins are constructed. Fig. 6.19 presents additional information by comparing the flood water depth value of year 1974 flood to current scenario but with detention basins. As can be observed, the flood depth in current scenario is reduced to the same level of 1974's. It is significant for local government and flood control department because it provides the information about how well these designed flood control facilities would work during flooding. It is also the baseline information of further construction and projects.

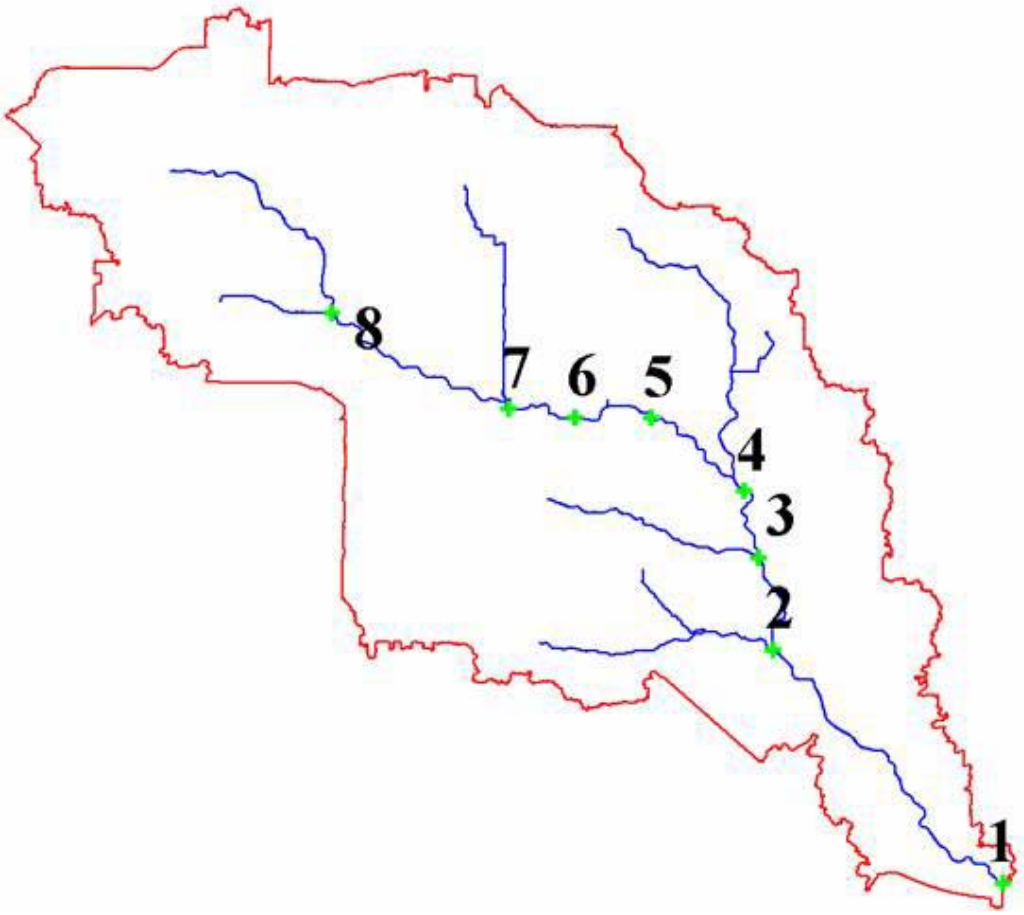

Fig. 6.16 Observation sites in the distributed model

Table 6.3

Discharge rates simulated by the model

Discharge (ft3/s) at Location	Scenario 2002	Scenario 2002 (Detention)	Scenario 1974
1	31964.66	30837.46	26773.85
2	30137.81	28293.29	24968.20
3	23660.78	21890.46	19777.39
4	20653.71	18289.75	17332.16
5	16289.75	13816.25	13911.66
6	15219.08	12770.32	13045.94
7	13968.20	11738.52	12219.08
8	9303.89	9293.29	8399.29

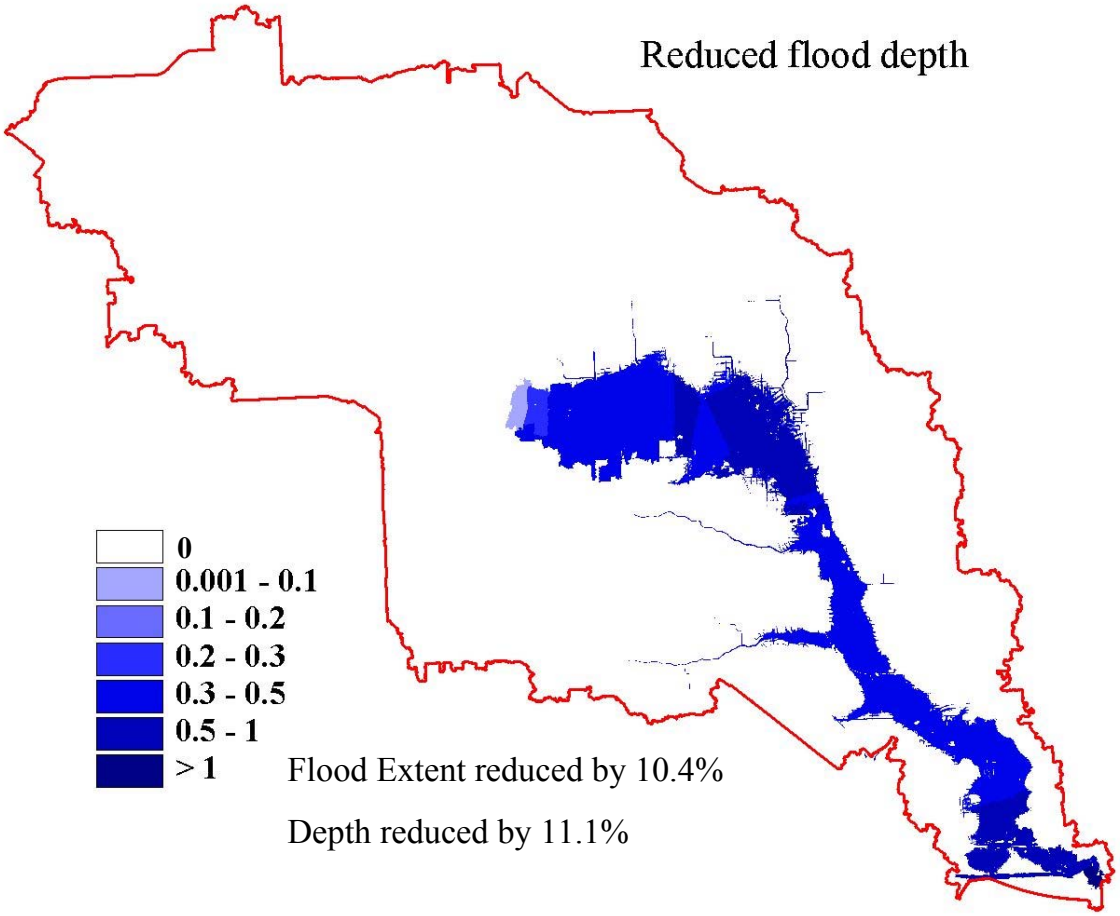

Fig. 6.17 Flood extent and depth differences with and without detention basins

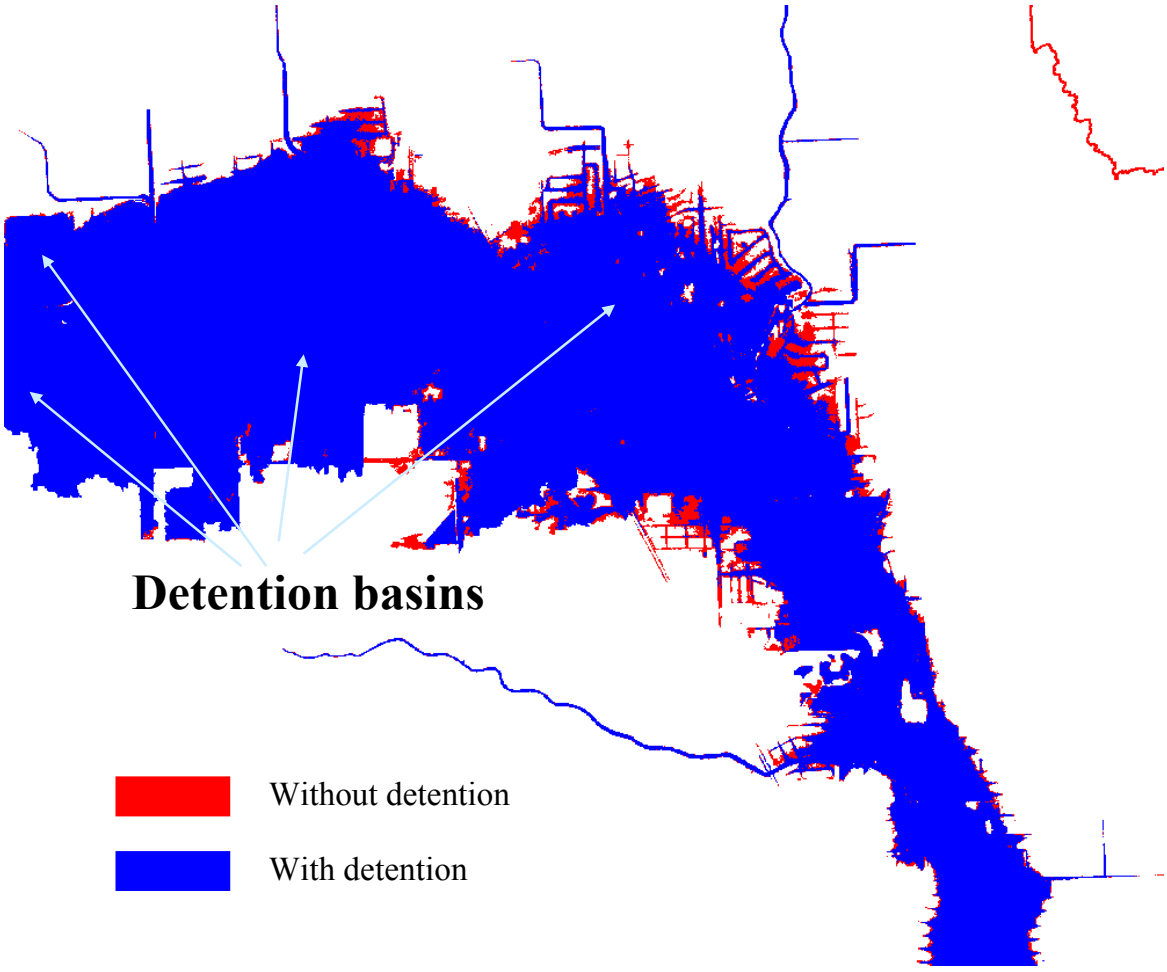

Fig. 6.18 Floodwater depth and extent difference with and without detention basins

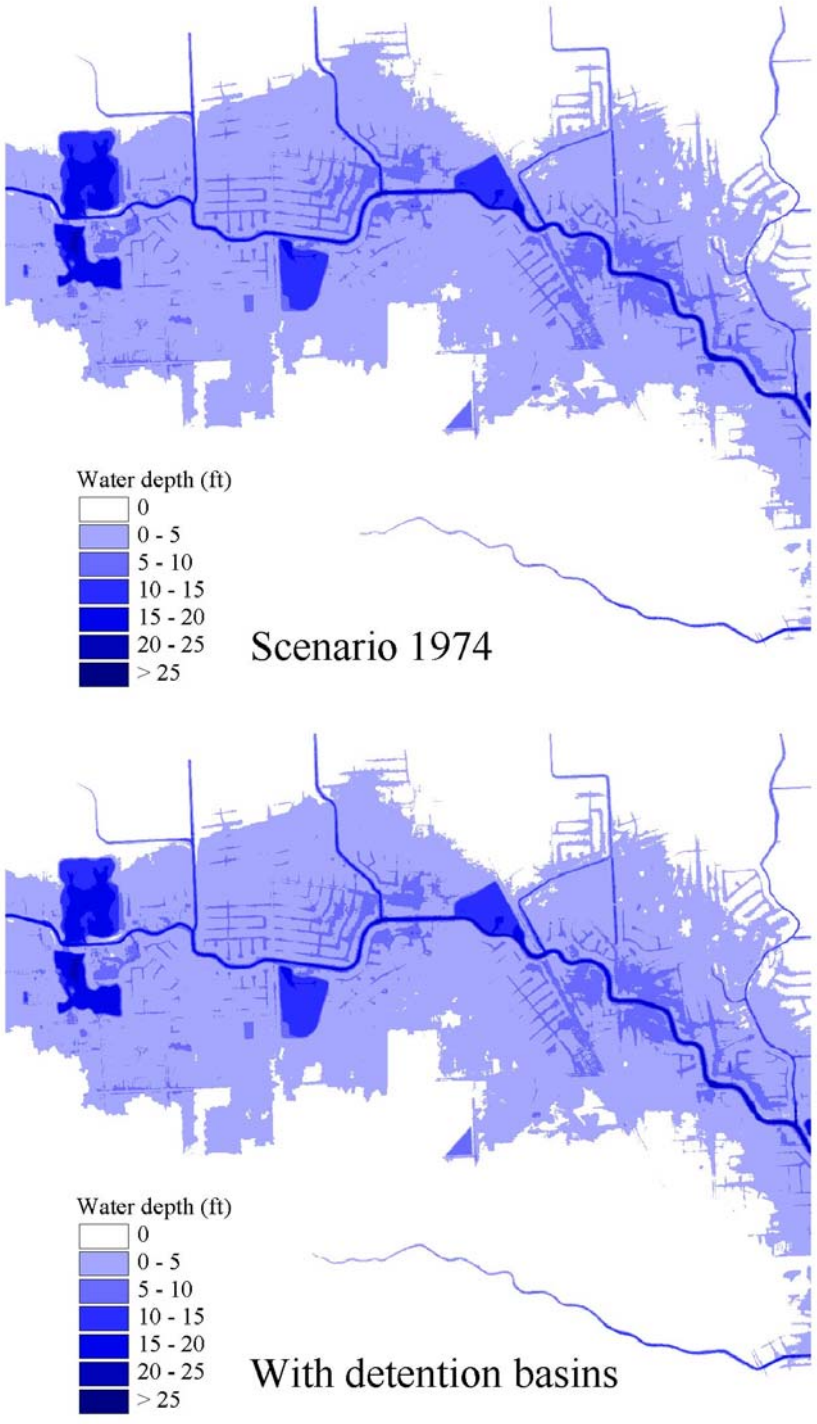

Fig. 6.19 Comparison of floodwater depth of the 1974 scenario to current urban sprawl with constructed detention basins

6.4. Impact of land subsidence

6.4.1. Introduction

Land subsidence is sinking of Earth's surface topography caused by over extracting of underground materials. In most cases, land subsidence is referred to the gradual change in a long term. Causes of land subsidence can attribute to oil and gas extraction, underground mining, overdrawing of groundwater, sinkholes, and thawing permafrost (National Research Council, 1991). The Houston-Galveston Bay area is possibly the most adversely affected area by land subsidence. During 1900 to 1995, the most significant land subsidence can be found in this area is up to 10 feet, and almost 3,200 $mile^2$ area had subsidence larger than 1 ft (USGS, 2002). The major influential factor of distribution of land subsidence is the groundwater pumpage and major oil fields (Coplin and Galloway, 1999). Before 1940s, water supply of this area was mostly supported by ground water. With the growing awareness of land subsidence and its associated problems, the Harris-Galveston Coastal Subsidence District was founded in 1975 to restrict groundwater use and avoid over-reliance of groundwater. The water supply is gradually converted to surface water supply.

In low-lying areas, land subsidence contributes to the increasing frequency and magnitude of flooding. Land subsidence has caused this area more prone to flooding from both riverine and coastal sources. Relative to sea level rise, chances and extent of sea water surge will be severer if coastal area experiences land subsidence up to 10 ft. The magnitude of human-induced land subsidence is significantly larger than sea level rise observed for past decade in this area. Land subsidence will also generate more

"sink" area by reducing local gradient or even reversing the direction of gradient. Most areas will adversely affected by land subsidence. The problem becomes severer if surface flow is reversed. Riverine flood water spill overbank will follow the reversed flow path and inundate those areas with deeper water and consequently cause more loss.

6.4.2. Land subsidence data source

People have developed various methods to monitor land subsidence. Traditionally, the monitoring is accomplished by spirit leveling method. This method can archive vertical resolution at about 0.1 to 1 millimeters and lines or network of control points can be established. Differential GPS has been used a lot nowadays to acquire ground control points. Therefore, it could be a substitute of spirit leveling method. However, both methods suffer intensive labor and money expenses. Recently, InSAR emerges as a powerful tool to measure earth surface displacement using radar. High resolution measurement of movement can be made by subtracting or "interfering" the phase component of two radar images at the same area but at different time (Galloway et al., 2000). The method provides unprecedented spatial details and high accuracy measurement of land subsidence. However, owning to relatively short term of availability of radar data, survey and bend mark data is still the only source for historical land subsidence.

USGS released the land subsidence map for Houston-Galveston area which traced back to 1900s. Fig. 6.20 shows the map of land subsidence developed by USGS. During last century, this area experienced severe land subsidence which can reach 10 ft for some locations. USGS also released the map showing significant land subsidence occurred

from 1970s (Fig. 6.21). As can be seen, the most significant land subsidence centered in the case study area which has the magnitude up to 5 ft.

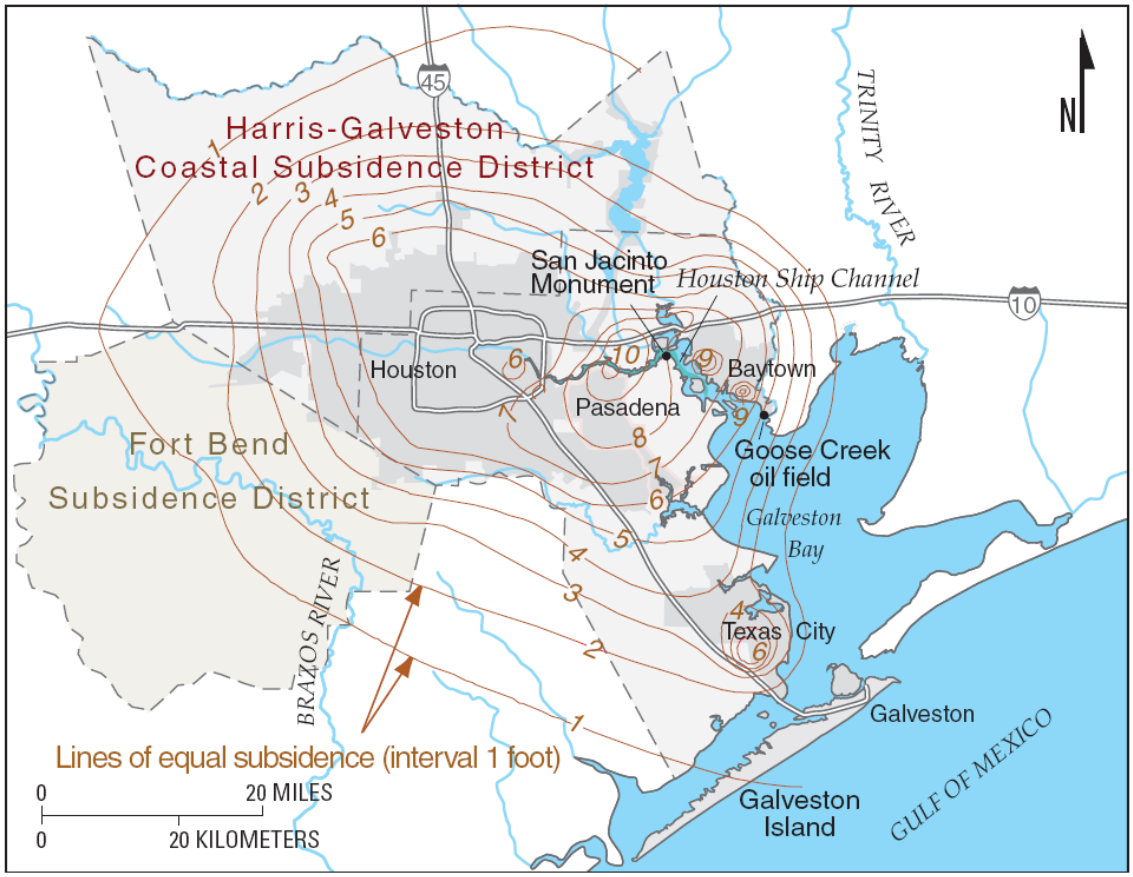

Fig. 6.20 Land subsidence map from 1906 to 1995 (USGS 2002)

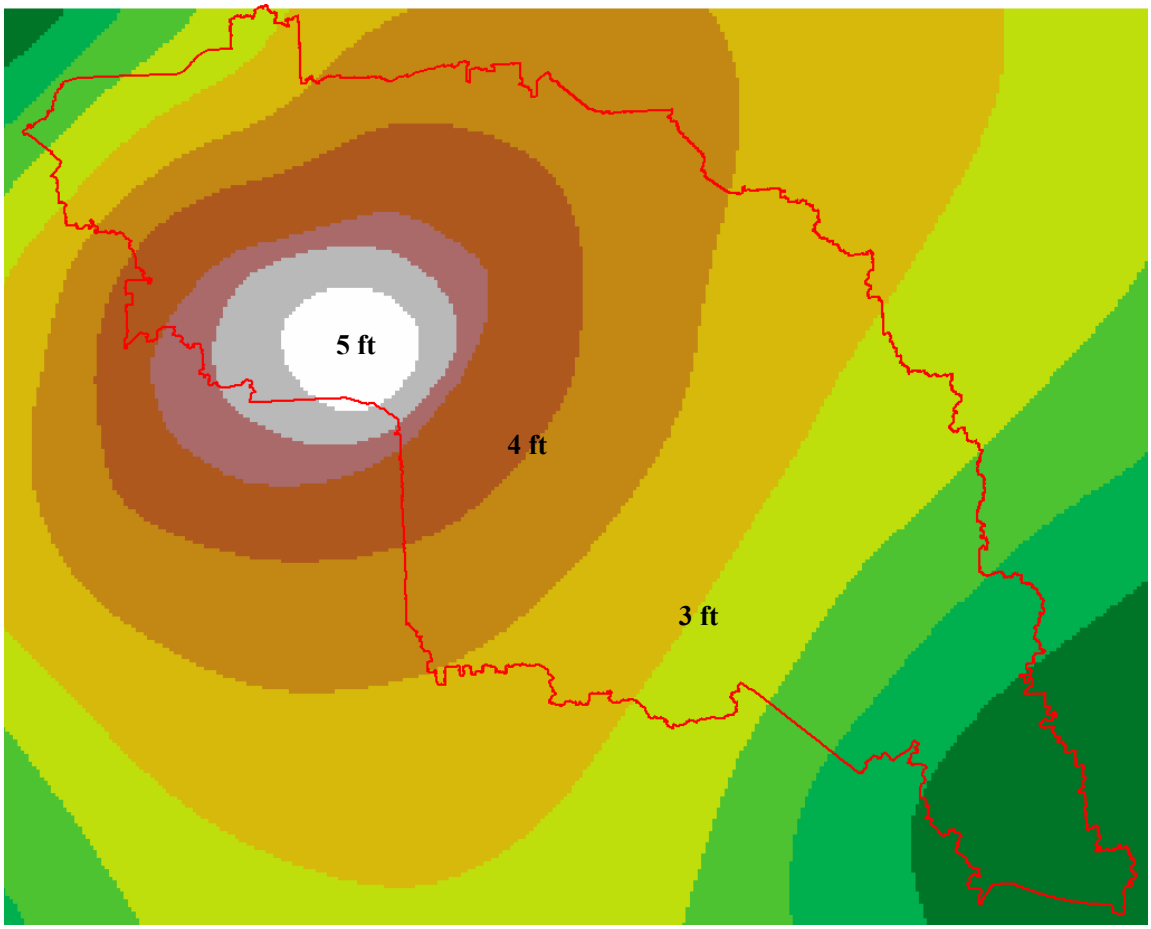

Fig. 6.21 Land subsidence during 1978 – 2000 in Harris County, TX (USGS 2002)

6.4.3. Results and discussion

To model the effect of land subsidence on the flood extent and magnitude, the map is overlaid with current elevation model acquired by LIDAR technology. Land subsidence map from Fig. 6.21 is digitized as contour lines and geo-referenced. The contour lines are then interpolated using Arc/Info TOPOGRID module (lower-left map of Fig. 6.21).

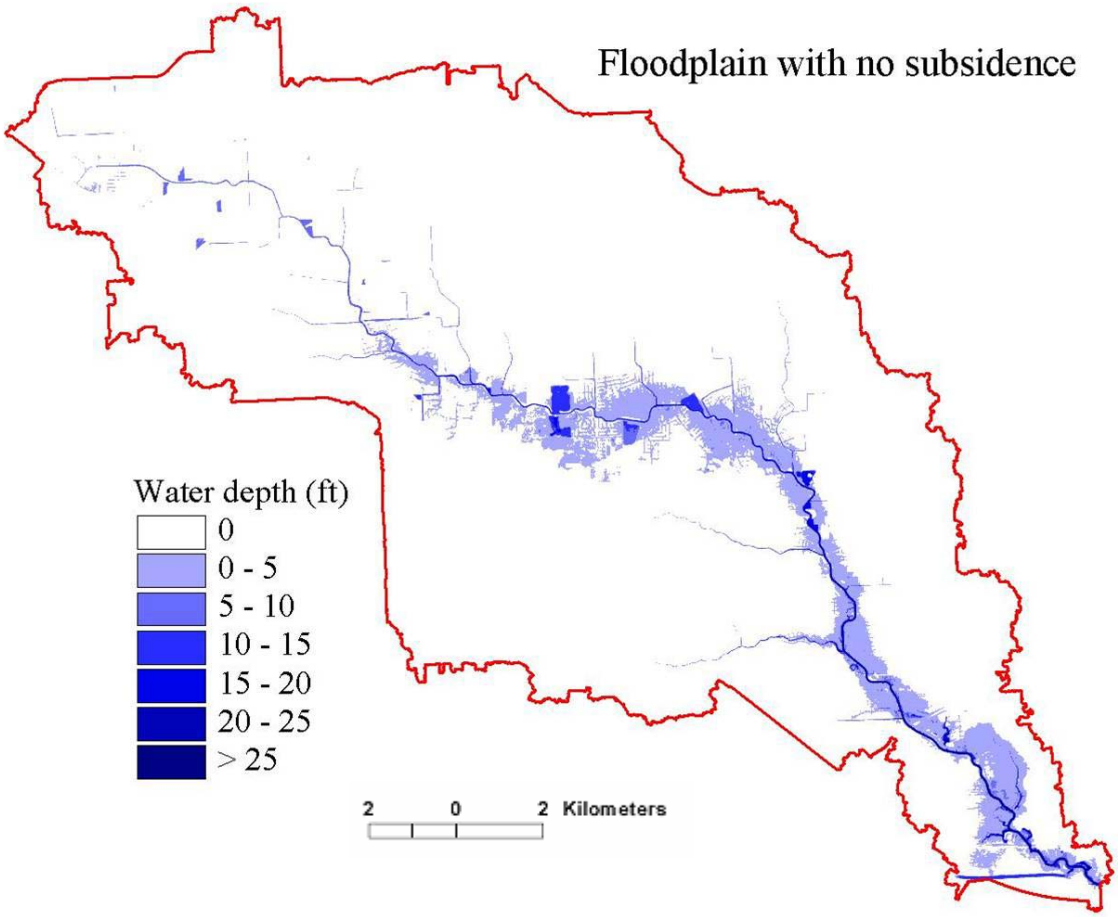

Fig. 6.22 Floodplain without land subsidence

The subsided among is removed from current elevation model by subtracting the interpolated subsidence map. The 100-year water surface elevation is also adjusted according to the local subsidence value. Then, a flood extent and depth map can be generated from the methods described previously. The map can be found in Fig. 6.22. The map illustrates the floodplain without subsidence or "pre-subsidence" condition. The extent and depth are significantly reduced by comparing it to current floodplain map. This indicates significant change in floodplain has taken place due to local and regional

land subsidence. This suggests that policies or planning must be done to ensure no further land subsidence would continue in this area because it is proved that riverine flood damage has been significantly enhanced owning to land subsidence.

6.5. Impact of changing precipitation trends

Global climate change has been one of the major environmental problems that people concern about in recent decades. The associated problems include sea level rise, extreme weather conditions, draughts and floods, etc. Greenhouse gases (water vapor, carbon dioxide, etc.) have been released at much higher rates than 200 years ago. The 9 warmest years in last century were within recent two decades. Higher air temperature may execrate water cycling speed and precipitation may occur in shorter but intense manner. Extreme weather conditions such as massive rainfall events may happen more frequently, which leads to more serious flooding.

According to climate models, Texas may have a slightly more annual precipitation in the future. However, summer precipitation may expect to increase about 30% (EPA, 1997). Fig. 6.23 shows the historical climate trend in the United States (Kunkel et al., 1995). From this figure, we can see that precipitation in Texas in last century has increased about 10% to 20%. Although no trend analysis of the frequency of extreme rainfall events or completed rainfall records can be found in the literature, it is reasonable to assume that the 100-year returning frequency event may also have an increase of magnitude at a rate from 10% to 20% in this area. Therefore, when mapping the floodplain, the change of the extent and flood water depth is expected. It is very important for planning and policy making, because if designed flood control facility is

using underestimated data, the structure may not work properly or even fail. Flood insurance map may also need to be updated according the potential climate change to avoid property loss.

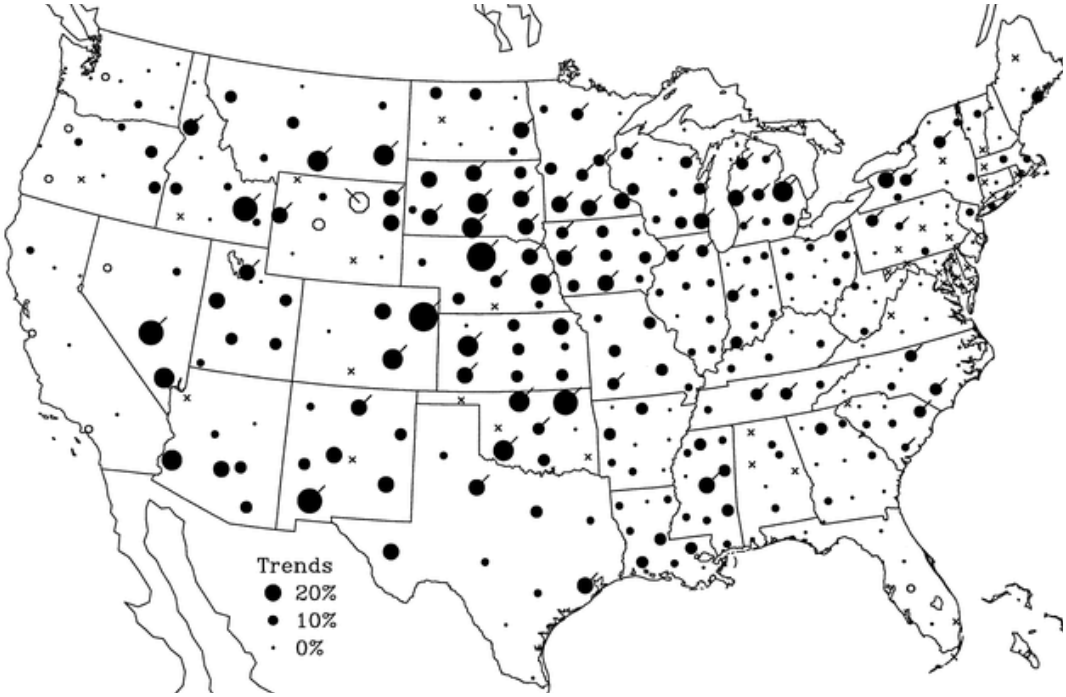

Fig. 6.23 Trends of US precipitation (Kunkel et al. 1999)

10% and 20% increase to the total amount rainfall is added and the distribution of rainfall intensity for the 24-hour period is interpolated. The rainfall data is then input to the rainfall component of the model. The resultant flood extent and depth map is shown in Fig. 6.24 and Fig. 6.25. The total flood extent will increase about 17.3% for the 10% scenario and 26.4% for the 20% scenario. The increment is almost same as the scenario of urban expansion discussed in last section. A comparison of floodplain maps is

displayed as Fig. 6.26. We can see the evasion of floodplain is mainly distributed in upstream area.

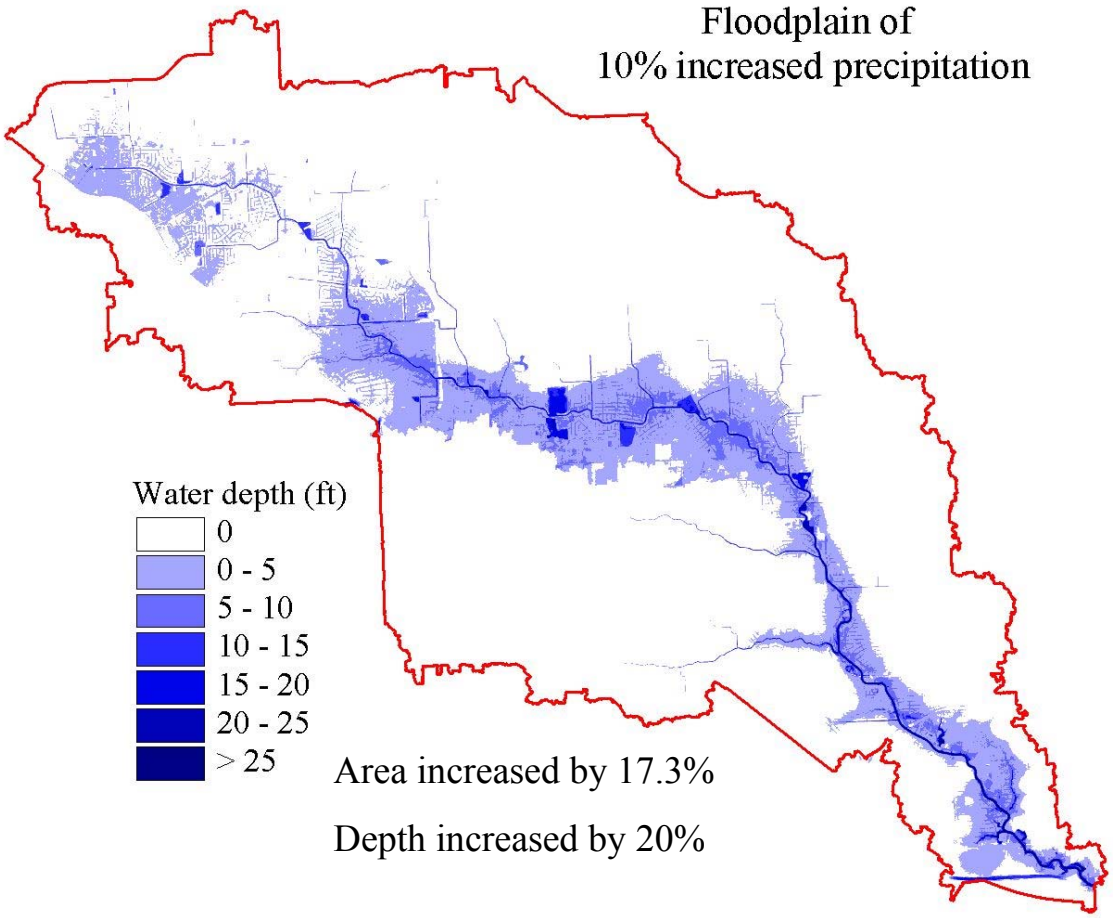

Fig. 6.24 Floodplain of the rainfall event with 10% increased precipitation

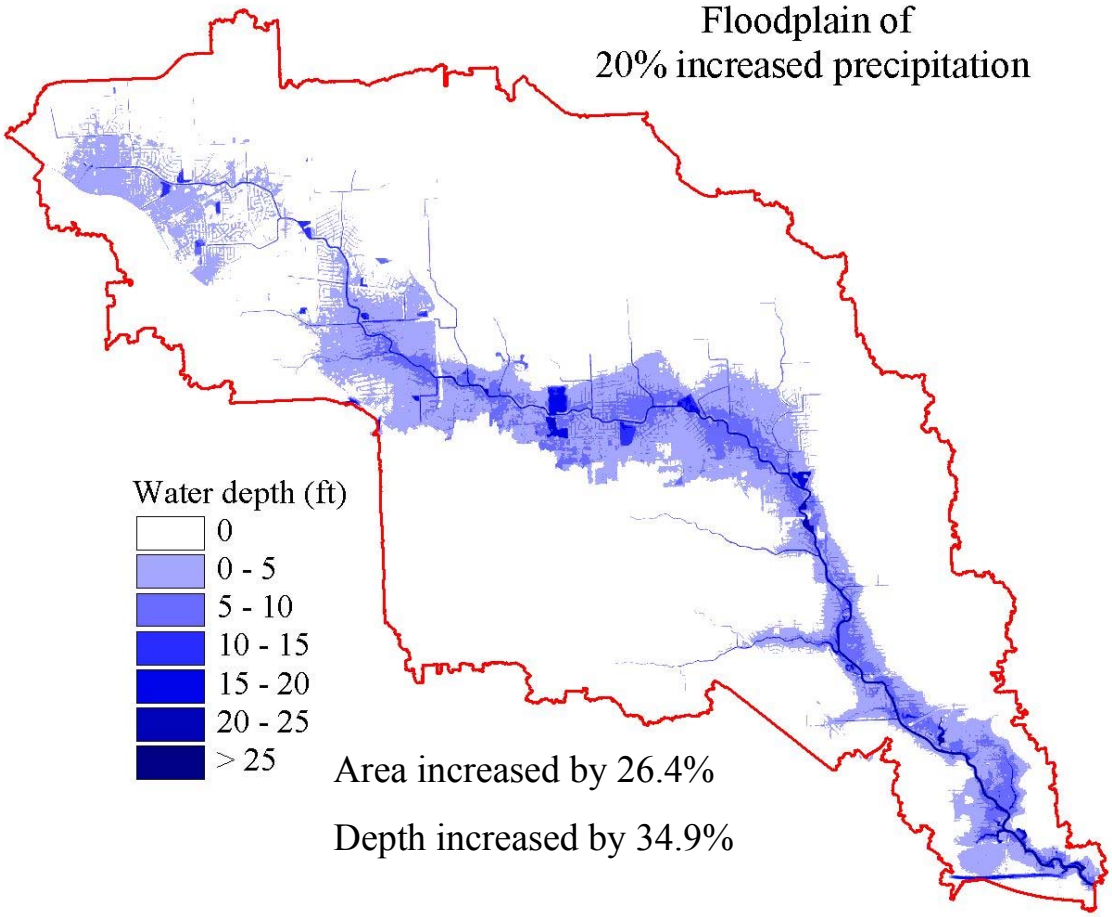

Fig. 6.25 Floodplain of the rainfall event with 20% increased precipitation

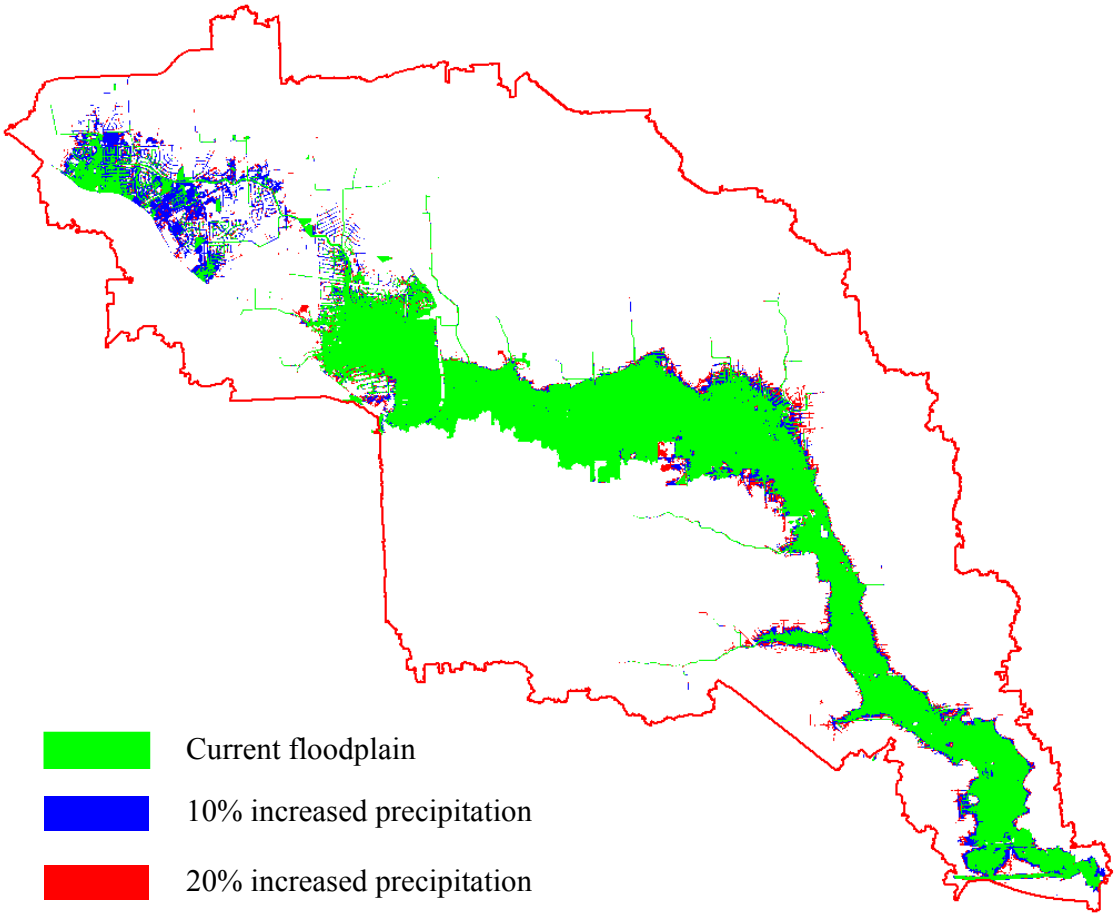

Fig. 6.26 Comparison of floodplain of the rainfall event with 10% (blue) and 20% (red) increased precipitation to current floodplain boundary

6.6. Summary and conclusions

Natural and human-induced environmental changes and the consequences of hydrologic responses and flooding are discussed in this chapter. Urban expansion of Houston metropolitan area can be quantified using the areal percentage of impervious surfaces. Landsat images are ideal source for this type of analysis because of its long term availability, moderate-to-high spatial resolution, and consistency in generations of

sensors. Subpixel level of surface imperviousness can be obtained through spectral unmixing analysis. This method is based on the conceptual Vegetation-Imperviousness-Soil (VIS) model. The advantage of this method is that no training data is required. It is ideal for retrospective analysis since acquisition of ground truth is not always possible for most applications. Furthermore, since endmembers are picked from each image, cross-platform calibration and extensive atmospheric correction are not necessary. The accuracy assessment using high resolution IKONOS image shows an RMSE of less than 0.1 with very high correlation coefficient. Urban imperviousness conditions spanning from 1974 to 2002 are estimated using the same routine. The results show an increment of 1% of total impervious surface each year during this 28-year time period. Owning to the urban growth, the peak flow of a 100-year event has increased about 19.62%. The floodplain extent has increased from 11.23 km^2 to 13.66 km^2.

Not only adverse effects of urban development are analyzed, the effect of construction of flood control facilities is also quantified analytically. To compensate higher flooding risks induced by urban growth, 5 large regional floodwater detention basins are constructed since 1970s. Using the LIDAR DEM, geometry and spatial properties of these detention basins are automatically extracted via a new approach. These detentions are incorporated into the hydrological analysis to quantify their effects on attenuating peak flows. The result shows that by constructing these detention basins, the intermediate downstream areas are efficiently protected. The depth and extent of flooding is reduced to the level of 1970 scenario (pre-development scenario).

Land subsidence is one of the most serious problems in the Houston-Galveston Bay area. It is reported to have as much as 10 ft land subsidence in some locations. Up to 5 ft land subsidence occurred in my study area during 1970s to 1990s. Land subsidence has significant effect on both sea tidal flooding and riverine flooding. The scenario that has no land subsidence is constructed and analyzed. A significantly reduced flooded extent and depth is observed from model simulation. This suggested that land subsidence has been one of the major factors that lead to more frequent and severer flooding. Planning and policies are very important to avoid further development of land subsidence. Regional climate change also suggests potential increase of flooding risks. According the literature, 10% to 20% more annual precipitation are expected in this area. By assuming higher frequency of extreme rainfall events, the analysis shows about 20% potential expansion of floodplain in the future. Since this magnitude is almost same as the scenario of urban growth, it is important to consider this change when performing flood insurance studies or planning.

CHAPTER VII

SUMMARY AND CONCLUSIONS

This study addresses conceptual and technical issues for incorporating multi-scale remote sensing data in hydrological/hydraulic modeling and investigates impacts of natural and human-induced environmental changes on hydrologic processes and flood hazards using the state-of-the-art GIS and remote sensing technologies. Issues of fusing multi-scale remote sensing data into the distributed hydrologic models and extracting quantitative information for hydrological objects from high resolution remote sensing data are tackled, and new modeling framework and algorithms have been proposed and implemented. By utilizing various remote sensing and GIS data sources, hydrological responses to natural and human-induced environmental changes are quantitatively evaluated.

Current hydrologic modeling frameworks have the difficulty in incorporating multi-scale remote sensing data, especially high-resolution remote sensing data like LIDAR DEMs. Neither raster-based distributed modeling framework nor lumped modeling structure is suitable for fusing multi-scale and high resolution data in hydrologic modeling. Lumped models tend to lose the spatial detail as it only partitions the watershed to be modeled into a few of large subbasins. Although raster-based distributed models enjoy the advantage of preserving the spatial details of input data and modeling results, they are computationally inefficient or not viable in the face of high resolution remote sensing input data. This research presents an object-oriented modeling framework for fusing multi-scale remote sensing data in hydrological modeling process.

In contrast to the constant scale and resolution of input data in the raster-based distributed modeling framework, the object-oriented modeling framework is based on spatial hydrologic units of variable size and shape, namely, variable scale and resolution. A segmentation algorithm has been developed in this research to generate the spatial hydrological units based on multi-scale input remote sensing data. The geometric and hydrologic properties of these spatial hydrologic units are quantified, and their topological relationships are modeled using the Region Adjacency Graph (RAG) in the upstream and downstream context. For each spatial hydrologic unit, rainfall loss is calculated using Green-Ampt infiltration model, and flow path response function of each spatial hydrologic unit is determined from the first and second momentum variables of the first-passage-time distribution. The object-oriented hydrologic modeling framework with variable spatial hydrologic units has the benefits of high computational efficiency, while keeping the essential details of spatial information. Therefore, it overcomes the drawbacks of the conventional lumped and distributed modeling frameworks. For the case study area, the object-oriented hydrologic modeling approach reduces the computation by over 1700 times compared with the fully distributed modeling approach, while the resultant hydrograph from the object-oriented approach is virtually the same as that from the fully distributed hydrologic modeling approach.

LIDAR technology has been recognized as a cost-effective means to acquire high accuracy ground elevation information. This research suggests that the 30 m USGS DEMs are not adequate to depict subtle local terrain variations, which are critical for hydrological and hydraulic modeling of low-lying coastal floodplains. Due to the coarse

resolution and vertical truncation errors of the USGS DEMs, the surface slopes of about half of my study area are inaccurately calculated to be zero, which has to be replaced using arbitrary small slope values (e.g. 0.005 percent rise). The arbitrary assignment of surface slope values for a large modeling area has introduced considerable uncertainty in hydrologic model. Sensitivity analysis of flow parameters suggests the level of uncertainty introduced by arbitrary assignments of surface slopes is commeasurable with that of the hydraulic radius and Manning's roughness coefficient. This research shows that high quality LiDAR DEMs can improve the reliability and accuracy of the calibrated flow parameters and hence enhance the hydrological modeling results. In the hydraulic modeling, the replacement of the USGS DEMs with high-resolution LiDAR DEMs has resulted in a precise determination of floodplain boundary and highly accurate estimates for flood depth and extent in simulation and scenario analyses.

This research also demonstrates that with high-resolution LiDAR DEMs subtle terrain features and micro hydrologic objects can be extracted and measured. An automated method has been developed for detecting and quantifying surface depressions and detention basins from LiDAR DEMs. The quantitative information about the location, shape, and storage capacity of detention basins has been derived. Based on this quantitative information, a four-stage mass balance level-pool model is used to calculate the mass-balance between the detention basins and river channels. Using this approach, the ability of detention basins to attenuate floodwater is quantitatively evaluated. The analysis results show that construction of regional detention basins in the watershed has reduced the flood risk to the pre-development level, largely offsetting the adverse effect

of the increased impervious surface due to the rapid urbanization. This analysis result offers further evidence that urban floodwater detention basins are a cost-effective and efficient measure for mitigating and controlling flood hazards in the low-lying coastal plains.

In most hydraulic modeling software packages such as HEC-RAS, Triangulated Irregular Network (TIN) method is commonly used to interpolate water surface elevations of all cross-sections along the river channels into a water surface elevation grid. The extent and depth of flood inundation are then determined by intersecting and differencing the water surface grid and the bare-earth DEM. Since the hydraulic connectivity is not taken into consideration, many isolated areas that have a surface elevation lower than the water elevation but are not hydraulically connected to the flood water source would be mistakenly labeled as parts of flood plains, especially those low elevation areas surrounded by flood defense structures. This research designs a new method for determining flood extent and depth based on a raster data structure. This method employs a breadth-first search algorithm to build a flow path from cross-sections and check the hydraulic connectivity for each grid. The flow distances from the upstream and downstream cross-sections and their water surface elevations are used to determine the flood depth for each grid cell. This method solves the problem of erroneous delineation of isolated low elevation areas as the flood plain and ensures the continuity and connectivity of the delineated floodplain to the flood water source-river channels, and therefore is superior to the conventional hydraulic modeling methods.

Based on the calibrated hydrological and hydraulic modeling system with multiple remote sensing data inputs, simulation and scenarios analyses have been conducted to evaluate the impacts of natural and human-induced environmental changes on hydrologic processes and flood hazards. Population growth and rapid expansion of urban built-up areas have resulted in profound changes to the Earth's land surface. The proliferation of asphalt and concrete materials creates extensive impervious surfaces. Large quantity of impervious surfaces decreases infiltration and increases storm-runoff rates and hence makes urban areas more vulnerable to flood damage. The hydrologic effect of urbanization is quantified though the quantity and temporal variation of impervious surface in the watershed. This research implemented a constrained linear spectral unmixing method, which is applied to time series satellite images for measuring surface imperviousness at subpixel level. Conceptually, the linear spectral unmixing method assumes that a single pixel's spectrum is a linear combination of a number of spectrally distinct endmembers (pure materials). Although some remote sensing software packages like ENVI has implemented the linear spectral unmixing method using an ordinary regression algorithm, the solution may not satisfy the conditions that the computed fractions (abundances) of endmembers are positive and their sum equals to 1, thus resulting in erroneous imperviousness estimates. This research introduces a constrained linear spectral unmixing method and enforces the computed fractions of endmembers to meet the positive and unity conditions, thus producing more reasonable and reliable estimates for surface imperviousness. The accuracy assessment shows that the imperviousness estimate for each pixel from the constrained linear spectral unmixing

method is accurate within a fraction of 0.1. Application of the constrained linear spectral unmixing method to time series of LANDSAT images spanning from 1974 to 2002 reveals that the impervious surface in the case study watershed has been increased from 10.1% to 38.4% during the past 28 years. Correspondingly, the peak flow for a 100-year event has increased by about 19.62%, and the floodplain extent has expanded by about 21.6%.

Despite the adverse effect of urbanization, some human activities like construction of flood control facilities have positive effects in reducing the flood risk and magnitude. Based on quantitative information derived from the high resolution LiDAR DEMs, the effect of regional floodwater detention basins on attenuating peak flows and flood magnitude has been investigated. The analysis result shows that these detention basins have effectively reduced the flood depth and extent and protected the downstream areas. The construction of these regional detention basins has greatly offset the adverse effect of increased impervious surface, making the depth and extent for a 100-year flood for the downstream areas to the level of 1970s land cover condition.

Land subsidence is one of the most serious environmental problems faced by many metropolitan areas. Houston-Galveston Bay area has experienced as much as 10 feet land subsidence in some locations during last century. Up to 5 feet land subsidence occurred in the case study area from 1970s to 1990s. Model simulation results show that land subsidence has been an important factor leading to more frequent and serious flood hazards

The published regional climate change studies have revealed an increasing trend in precipitation. In the past century, 10% to 20% precipitation increase has been observed for the case study area. If this trend continues in the future, the 100-year floodplain will expand by 17% ~ 26% in the next century.

The research findings from the simulation and scenario analyses are valuable for guiding smart urban growth and sustainable resource developments in Houston metropolitan area. Wise planning measures and land use and water resource policies need to be formulated for reducing the adverse effect of human activities on hydrological processes and further enhancing our capability in controlling and mitigating flood risk and damage. The floodplain boundary maps for different probabilistic flood events (10-, 50-, 100-year floods) show the flood risk and vulnerability of different locations, which should be used as a scientific basis for determining flood insurance rates and allocating house developments, infrastructures and economic activities. Detention basins have been assessed to be effective in flood control, and these flood control facilities should be

appropriately maintained and enhanced. The rapid increase in impervious surface induced by urbanization and substantial land subsidence induced by uncontrolled extraction of ground water, natural gas and oil have been two primary factors exacerbating the flood frequency and magnitude and corresponding economic damages. Smart urban growth measures are needed to ensure sufficient lawns, parks, open spaces, and urban forests, and avoid large continuous impervious surface during the continued urbanization process. Sustainable resource development policies should be addressed to guide the use and extraction of ground water and oil resources. The locations, density and extraction rates of water and oil wells should be carefully examined and controlled to avoid further land subsidence. Floodplain boundaries are dynamic and subject to changes of many environmental factors, including the precipitation. Timely updating of floodplain maps based on the best available information is necessary and important for planning and implementing flood control and management activities.

REFERENCES

Abbot, M.B., Bathurst, J.C., Cunge, J.A., O'Connell, P.E., Rasmussen, J., 1986. An introduction to the European Hydrological System, SHE. 2. Structure of a physically-based, distributed modelling system. Journal of Hydrology, 87, 61-77.

Andersen, J., Dybkjaer, G., Jensen, K.H., Refsgaard, J.C., Rasmussen, K., 2002. Use of remotely sensed precipitation and leaf area index in a distributed hydrological model. Journal of Hydrology, 264, 34-50.

Arnold, J.G., Srinivasan, R., Muttiah, R.S., William, J.R., 1998. Large area hydrologic modeling and assessment. Part I: Model development. Journal of American Water Resources Association, 34(1), 73-89.

Arnold, P., Bouvier, C., Cisneros, L., Dominguez, R., 2002. Influence of rainfall spatial variability on flood prediction. Journal of Hydrology, 260, 216-230.

Ball, G.H., Hall, D.J., 1965. A novel method of data analysis and pattern classification, Stanford Research Institute, Menlo Park, CA.

Ball, J.E., Luk, K.C., 1998. Modeling spatial variability of rainfall over a catchment. Journal of Hydrologic Engineering, 3(2), 122-130.

Band, L.E., 1986. Topographic partition of watershed with digital elevation models. Water Resources Research, 22, 15-24.

Band, L.E., 1999. Spatial hydrology and landforms. In: Longley, P.A., Goodchild, M.F., Maguire, D.J. and Rhind, D.W. (Editors), Geographical Information Systems. Principles and Technical Issues. John Wiley & Sons, New York, pp. 527-542.

Bates, P.D., Roo, A.P.J.D., 2000. A Simple raster-based model for flood inundation simulation. Journal of Hydrology, 236, 54-77.

Beasley, D.B., Huggins, L.F., 1978. ANSWERS:A hydrologic/water quality simulator for watershed research, 10th Conference on Winter Simulation. IEEE Computer Society Press, Miami Beach, FL, pp. 507-515.

Bedient, P.B., Hoblit, B.C., Gladwell, D.C., Vieux, B.E., 2000. NEXRAD radar for flood prediction in Houston. Journal of Hydrologic Engineering, 5(3), 269-277.

Bedient, P.B., Huber, W.C., 2002. Hydrology and Floodplain Analysis. Prentice-Hall, Inc., Upper Saddle River, NJ.

Bernard, L., Kruger, T., 2000. Integration of GIS and spatio-temporal simulation models: interoperable components for different simulation strategies. Transactions in GIS, 4(3), 197-216.

Beven, K., 2002. Towards an alternative blueprint for a physically based digitally simulated hydrologic response modelling system. Hydrological Processes, 16, 189-206.

Beven, K.J., Kirkby, M.J., 1979. A physically-based variable contributing area model of basin hydrology. Hydrological Sciences Bulletin, 24(1), 43-69.

Bjerklie, D.M., Dingman, S.L., Vorosmarty, C.J., Bolster, C.H., Congalton, R.G., 2003. Evaluating the potential for measuring river discharge from space. Journal of Hydrology, 278, 17-38.

Boardman, J.W., Kruse, F.A., Green, R.O., 1993. Mapping target signature via partial unmixing of AVIRIS data, Summaries of JPL Air-borne Earth Science Workshop, Pasadena, CA, pp. 11-14.

Bouwer, H., 1969. Infiltration of water into nonuniform soil. Journal of Irrigation and Drainage Engineering, 95, 451-462.

Braun, P., Molnar, T., Kleeberg, H.-B., 1997. The problem of scaling in grid-related hydrological process modelling. Hydrologic Processes, 11, 1219-1230.

Bultot, F., Bupriez, G.L., Gellens, D., 1990. Simulation of land use changes and impacts on the water balance - a case study for Belgium. Journal of Hydrology, 114, 327-348.

Burrough, P.A., 1986. Principles of Geographic Information Systems for Land Resources Assessment. Oxford University Press, New York.

Chang, C.-I., 2006. A fast iterative algorithm for implementation of pixel purity index. IEEE Transactions on Geoscience and Remote Sensing, 3(1), 63-67.

Chang, C.-I., Heinz, D.C., 2000. Constrained subpixel target detection for remotely sensed imagery. IEEE Transactions on Geoscience and Remote Sensing, 38(3), 1144-1159.

Chang, C.-I., Ren, H., Chang, C.-C., D'Amico, F., Jensen, J.O., 2004. Estimation of subpixel target size for remotely sensed imagery. IEEE Transactions on Geoscience and Remote Sensing, 42(6), 1309-1320.

Cheng, S.J., Wang, R.Y., 2002. An approach for evaluating the hydrological effects of urbanization and its application. Hydrological Processes, 16, 1403-1408.

Chirico, G.B., Grayson, R.B., Western, A.W., 2003. On the computation of the quasi-dynamic wetness index with multiple-flow-direction algorithms. Water Resources Research, 39, 1115-1122.

Chow, V.T., Maidment, D.R., Mays, L.W., 1988. Applied Hydrology. McGraw-Hill, New York.

Coon, W.F., 2003. Simulating land-use changes and stormwater-detention basins and evaluating their effect on peak streamflows and stream-water quality in Irondequoit Creek Basin, New York. Open-File Report 03-136, U. S. Geological Survey, Reston, VA.

Coon, W.F., Johnson, M.S., 2005. Effects of Land-Use Changes and Stormflow-Detention Basins on Flooding and Nonpoint-Source Pollution, in Irondequoit Creek Basin, Monroe and Ontario Counties, New York—Application of a Precipitation-Runoff Model. Scientific Investigations Report 2005-5070, U.S. Department of the Interior, U.S. Geological Survey, Reston, VA.

Coplin, L.S., Galloway, D.L., 1999. Houston-Galveston, Texas - Managing coastal subsidence, Land subsidence in the United States: U.S. Geological Survey Circular 1182, pp. 35-48.

Cormen, T.H., Leiserson, C.E., Rivest, R.L., 1996. Introduction to Algorithms. MIT Press, Cambridge, MA.

Council, N.R., 1991. Mitigating Losses from Land Subsidence in the United States. National Academy Press, Washington, DC.

Courant, R., Friedrichs, K., Lewy, H., 1956. On the Partial Difference Equations of Mathematical Physics. New York University, Institute of Mathematics, New York.

Crum, T., Alberty, R., 1993. The WSR-88D and the WSR-88D operational support facility. Bulletin of American Meteorology Society, 74, 1669-1687.

Dawdy, D.R., Bergmann, J.M., 1969. Effects of rainfall variability on streamflow simulation. Water Resources Research, 5, 958-966.

Dechter, R., Pearl, J., 1988. The optimality of A*. In: Kanal, L. and Kumar, V. (Editors), Search in Artificial Intelligence. Springer, New York, pp. 166-199.

DIAD, 2000. ALERT real-time weather monitoring and flood warning, pp. 23.

Doan, J.H., 2000. Hydrologic model of the Buffalo Bayou using GIS. In: Maidment, D. and Djokic, D. (Editors), Hydrologic and Hydraulic Modeling Support with Geographic Information Systems. ESRI Press, Redland CA, pp. 113-143.

Droogers, P., Kite, G., 2002. Remotely sensed data used for modelling at different hydrological scales. Hydrological Processes, 16, 1543-1556.

Elliot, A.H., 1998. Model for preliminary catchment-scale planning of urban stormwater quality controls. Journal of Environment Management, 52(3), 273-288.

Emerson, C.H., 2003. Evaluation of the additive effects of stormwater detention basins at the watershed scale. MS Thesis, Drexel University, Philadelphia, PA, 130 pp.

Emerson, C.H., Welty, C., Traver, R.G., 2005. Watershed-scale evaluation of a system of storm water detention basins. Journal of Hydrologic Engineering, 10(3), 237-242.

EPA (Environmental Protection Agency), 1997. Climate change and Texas. United States Environmental Protection Agency, EPA report 230-F-97-008qq.

FEMA (Federal Emergency Management Agency), 2003. Disaster Costs 1990-1999. FEMA's Online Library, URL: http://www.fema.gov/library/df_7.shtm, Accessed: April 2004.

Feng, C.-C., Sorokine, A., 2001. Incorporating hydrologic semantic information for interoperable GIS with hydrologic model, 9th ACM International Symposium on Advances in Geographic Information Systems. ACM Press, Atlanta, GA, pp. 59-63.

Freeze, R.A., Harlan, R.L., 1969. Blueprint for a physically-based digitally-simulated hydrologic response model. Journal of Hydrology, 9, 237-258.

Fulton, R.A., Breidenbach, J.P., Seo, D., Miller, D.A., 1998. The WSR-88D rainfall algorithm. Weather and Forecasting, 13, 377-395.

Galloway, D.L., Jones, D.R., Ingebritsen, S.E., 2000. Measuring land subsidence from space: US Geological Survey Fact Sheet 051-00.

Garbrecht, J., Martz, L.W., 2000. Digital elevation model issues in water resources modeling. In: Maidment, D. and Djokic, D. (Editors), Hydrologic and Hydraulic Modeling Support with Geographic Information Systems. ESRI Press, Redland CA, pp. 1-27.

Goldman, D.M., 1989. Loss rate representation in the HEC-1 watershed model. In: Morel-Seytoux, H.J. (Editor), Unsaturated Flow in Hydrologic Modeling Theory

and Practice. NATO-ASI Series. Kluwer Academic Publisher, Boston, MA, pp. 435-454.

Goodchild, M.F., 1992. Geographical data modeling. Computers & Geosciences, 18(4), 401-408.

Gordon, S.I., 1980. Utilizing Landsat imagery to monitor land-use change: A case study in Ohio. Remote Sensing of Environment, 9(3), 183-276.

Green, C.H., Parker, D.J., Tunstall, S.M., 2000. Assessment of Flood Control and Management Options, Flood Hazard Research Center, Middlesex University, Cape Town, South Africa.

Green, W.H., Ampt, C.A., 1911. Studies on soil physics, I. Flow of water and air through soils. Journal of Agricultural Sciences, 4, 1-24.

Guo, J.C.Y., 2004. Hydrology-based approach to storm water detention basin design using new routing schemes. Journal of Hydrologic Engineering, 9(4), 4333-4336.

Gyasi-agyei, Y., Willgoose, G., Troch, F.P.D., 1995. Effects of vertical resolution and map scale of digital elevation models on geomorphological parameters used in hydrology. Hydrological Processes, 9, 363-382.

Haddeland, I., Matheussen, B.V., Lettermaier, D.P., 2002. Influence of spatial resolution on simulated streamflow in a macroscale hydrologic model. Water Resources Research, 38(7), 1124-1134.

Hardy, R.J., Bates, P.D., Anderson, M.G., 1999. The importance of spatial resolution in hydraulic models for floodplain environments. Journal of Hydrology, 1999, 124-136.

Harrell, L.J., Ranjithan, S.R., 2003. Detention pond design and land use planning for watershed management. Journal of Water Resources Planning and Management, 129(2), 98-106.

HCFCD (Harris County Flood Control District), 2005. White Oak Bayou Watershed. Harris County Flood Control District. URL: http://www.hcfcd.org/P_whiteoakbayou.html. Accessed: August 2005.

HCFCD (Harris County Flood Control District), FEMA (Federal Emergency Management Agency), 2002. Tropical Storm Allison event analysis, Volume 1, Final Technical Report, Harris County Flood Control District, Federal Emergency Management Agency, LJA Engineering & Surveying, Inc. PBS&J, Houston, TX.

Hill, J., Megier, J., Mehl, W., 1995. Land degradation, soil erosion and desertification monitoring in Mediterranean ecosystems. Remote Sensing Reviews, 12, 107-130.

Hoblit, B.C., Liu, L., Curtis, D.C., 2002. Extreme rainfall estimation using radar for Tropical Storm Allison. URL: http://www.onerain.com/includes/pdf/whitepaper/Hoblit_EWRI_2002.pdf. Accessed: July 2006.

Hutchinson, M.F., 1988. Calculation of hydrologically sound digital elevation models, Third International Symposium on Spatial Data Handling, Sydney, Australia, pp. 117-133.

Hutchinson, M.F., 1989. A new procedure for gridding elevation and stream line data with automatic removal of spurious pits. Journal of Hydrology, 106, 211-232.

IEEE, 1990. IEEE Standard Computer Dictionary: A Compilation of IEEE Standard Computer Glossaries. Institute of Electrical and Electronics Engineers, New York.

Jenson, S.K., Domingue, J.O., 1988. Extracting topographic structure from digital elevation data for geographic information system analysis. Photogrammetric Engineering and Remote Sensing, 54(11), 1593-1600.

Ji, M.H., Jenson, J.R., 1999. Effectiveness of subpixel analysis in detecting and quantifying urban imperviousness from Landsat Thermatic Mapper Imagery. Geocarto International, 14(4), 31-39.

Julien, P.Y., Moglen, G.E., 1990. Similarity and length scale for spatially varied overland flow. Water Resources Research, 26(8), 1819-1832.

Julien, P.Y., Saghafian, B., Ogden, F.L., 1995. Raster-based hydrologic modeling of spatially varied surface runoff. Water Resources Bulletin, 31(3), 523-536.

Kang, I.S., Park, J.I., Singh, V.P., 1998. Effect of urbanization on runoff characterstics of the On-Cheon Stream watershed in Pusan, Korea. Hydrological Processes, 12, 351-363.

Karl, T.R., Knight, R.W., 1998. Secular trends of precipitation amount, frequency, and intensity in the United States. Bulletin of American Meteorology Society, 79, 231-241.

Karl, T.R., Knight, R.W., Easterling, D.R., Quayle, R.G., 1996. Indices of climate change for the United States. Bulletin of American Meteorology Society, 77(2), 279-292.

Kouwen, N., Soulis, E.D., Pietroniro, A., Donald, J., Harrington, R.A., 1993. Grouped response units for distributed hydrologic modeling. Water Resources Planning and Management, 119(3), 289-305.

Kunkel, K.E., Andsager, K., Easterling, D.R., 1999. Long-term trends in extreme precipitation events over the conterminous United States and Canada. Journal of Climate, 12, 2515-2527.

Kunkel, K.E., Changnon, S.A., Angel, J.R., 1994. Climatic aspects of the 1993 upper Mississippi River basin flood. Bulletin of American Meteorology Society, 75, 811-822.

Laba, M., Smith, S.D., Degloria, S.D., 1997. Landat-based land cover mapping in the lower Yuna River watershed in the Dominican Republic. International Journal of Remote Sensing, 18(14), 3011-3025.

Lakshmi, V., Susskind, J., 2001. Utilization of satellite data in land surface hydrology: sensitivity and assimilation. Hydrological Processes, 15, 877-892.

Lee, J.G., Heaney, J.P., 2003. Estimation of urban imperviousness and its impacts on storm water systems. Journal of Water Resources Planning and Management, 129(5), 419-426.

Li, R.M., Stevens, M.A., Simons, D.B., 1976. Solutions to Green-Ampt infiltration equations. Journal of Irrigation and Drainage Engineering, 102(IR2), 239-248.

Liang, C., Mackay, D.S., 2000. A general model of watershed extraction and representation using globally optimal flow paths and up-slope contributing areas. International Journal of Geographical Information Science, 14(4), 337-358.

Liu, Y.B., Gebremeskel, S., Smedt, F.D., Hoffmann, L., Pfister, L., 2003. A diffusive transport approach for flow routing in GIS-based flood modeling. Journal of Hydrology, 283, 91-106.

Mackay, D.S., Band, L.E., 1998. Extraction and representation of nested catchment areas from digital elevation models in lake-dominated topography. Water Resources Research, 34(4), 897-901.

Maidment, D.R., 1993. GIS and hydrologic modeling. In: Goodchild, M.F., Parks, B.O. and Steyaert, L.T. (Editors), Environmental Modeling with GIS. Oxford University Press, Oxford, pp. 147-167.

Mark, D.M., 1983. Automatic detection of drainage networks from digital elevation models. Cartographica, 21, 168-178.

Markham, B.L., Barker, J.L., 1987. Thematic Mapper bandpass solar exoatmospheric irradiances. International Journal of Remote Sensing, 8, 517-523.

Martz, L.W., Garbrecht, J., 1998. The treatment of flat areas and depressions in automated drainage analysis of raster digital elevation models. Hydrological Processes, 12, 843-855.

McCuen, R.H., 2004. Hydrologic Analysis and Design. Pearson Prentice Hall, Upper Saddle River, NJ.

McDonald, J.F., 1995. Houston remains unzoned. Land Economics, 7(1), 137-140.

Mimikou, M.A., Bastas, E.A., 1996. Flood forecasting based on radar rainfall measurements. Journal of Water Resources Planning and Management, 122(3), 151-156.

Moglen, G.E., Hartman, G.L., 2002. Resolution effects on hydrologic modeling parameters and peak discharge. Journal of Hydrologic Engineering, 6(6), 490-497.

Molnar, D.K., Julien, P.Y., 2000. Grid-size effects on surface runoff modeling. Journal of Hydrologic Engineering, 5(1), 8-6.

Molnar, P., Ramirez, J.A., 1998. Energy dissipation theories and optimal channel characteristics of river networks. Water Resources Research, 34(7), 1809-1818.

Moore, I.D., Grayson, R.B., Landson, A.R., 1991. Digital terrain modeling: a review of hydrologic, geomorphologic, and biological applications. Hydrologic Processes, 5, 3-30.

Moore, I.D., Turner, K., Wilson, J., Jenson, S., Band, L., 1993. GIS and land-surface-subsurface modeling. In: Goodchild, M., Parks, B. and Steyaert, L. (Editors), Environmental Modeling with GIS. Oxford University Press, Oxford, pp. 196-230.

Nauman, E.B., 1981. Residence time distribution in systems governed by the dispersion equations. Chemical Engineering Science, 36, 957-966.

Nearing, M.A., Liu, B.Y., Risse, L.M., Zhang, X., 1996. Curve number and Green-Ampt effective hydraulic conductivities. Water Resources Bulletin, 32, 125-136.

Ng, H.Y.F., Marsalek, J., 1989. Simulation of the effects of urbanization on basin streamflow. Water Resources Bulletin, 25(1), 117-124.

Noman, N.S., Nelson, E.J., Zundel, A.K., 2001. Review of automated floodplain delineation from digital terrain models. Journal of Water Resources Planning and Management, 127(6), 394 - 402.

NRCS (Natural Resources Conservation Service), 2006. NRCS Planning and Design Manual. URL: http://www.abe.msstate.edu/Tools/csd/p-dm/index.html. Accessed: June 2006.

NWS (National Weather Service), 2001. Tropic Storm Allison, heavy rains and floods, Texas and Louisiana June 2001, NOAA, NWS, Silver Spring, MD.

O'Callaghan, J.F., Mark, D.M., 1984. The extraction of drainage networks from digital elevation data. Computer Vision, Graphics and Image Processing, 28, 323-344.

Olivera, F., Koka, S., 2004. Hydrodynamic dispersive and advective processes in watershed responses. Journal of Hydrologic Engineering, 9(6), 534-543.

Olivera, F., Maidment, D., 1999. Geographic information system (GIS)-based spatially distributed model for runoff routing. Water Resources Research, 35(4), 1155-1164.

Perry, C.A., 2000. Significant floods in the United States during the 20th century - USGS measures a century of floods, USGS Fact Sheet 023-00, US Department of the Interior, US Geological Survey.

Peuquet, D.J., 1994. A conceptual framework and comparison of spatial data models. Cartographica, 66-113.

Pielke, R.A., Downton, M.W., 2000. Precipitation and damaging floods: trends in the United States 1932-1997. Journal of Climate, 13(20), 3625-3637.

Planchon, O., Darboux, F., 2001. A fast, simple and versatile algorithm to fill the depressions of digital elevation models. Catena, 46, 159-176.

Raza, A., Kainz, W., 1999. Cell tuple based spatio-temporal data model: an object oriented approach, Seventh ACM International Symposium on Advances in Geographic Information Systems. ACM Press, New York, NY, Kansas City, Missouri, pp. 20-25.

Ridd, M.K., 1995. Exploring a V-I-S (vegetation-impervious surface-soil) model for urban ecosystem analysis through remote sensing: comparative anatomy for cities. International Journal of Remote Sensing, 16, 2165-2185.

Schueler, T., 1999. The importance of imperviousness. Watershed Protection Techniques, 1(3), 100-111.

Soil Conservation Service (SCS), 1976. Soil Survey of Harris County, Texas, U. S., Department of Soil Conservation Service, Reston, VA.

Soil Conservation Service (SCS), 1986. Urban Hydrology for small watersheds. Technical Release 55 (TR55). U.S. Department of Agriculture, Conservation Engineering Division.

Sedgewich, R., 2002. Algorithms in C++: Part5 Graph Algorithms. Addison-Wesley, New York.

Singh, V.P., 1997. Effect of spatial and temporal variability in rainfall and watershed characteristics on streamflow hydrograph. Hydrologic Processes, 11, 1649-1669.

Singh, V.P., Woolhiser, D.A., 2002. Mathematical modeling of watershed hydrology. Journal of Hydrologic Engineering, 7(4), 270-292.

Smith, A.J., 2000. Subpixel estimates of impervious surface cover using Landsat TM imagery, Geography Department, University of Maryland, College Park.

Smith, J.A., Seo, D.J., Baeck, M.L., Hudlow, M.D., 1996. An intercomparison study of WSR-88D precipitation estimates. Water Resources Research, 32(7), 2035-2045.

Soille, P., 2002. Morphological Image Analysis, Principles and Applications. Springer-Verlag, Berlin.

Srinivasan, R., Engel, B.A., 1991. Effect of slope prediction methods on slope and erosion estimates. Applied Engineering in Agriculture, 7, 779-783.

Sui, D.Z., Maggio, R.C., 1998. FIRM maps are not so firm: uncertainties in FEMA's flood insurance rate map and how GIS can help., GIS/LIS'98, pp. 144-153.

Sui, D.Z., Maggio, R.C., 1999. Integrating GIS with Hydrological modeling: practices, problems, and prospects. Computers, Environmental and Urban Systems, 23, 33-51.

Tamminen, S., Laurinen, P., Roning, J., 1999. Comparing regression trees with neural networks in aerobic fitness approximation, International ICSC Symposium on Advances in Intelligent Data Analysis (AIDA'99), Rochester NY, pp. 414-419.

Tommervik, H., Hogda, K.A., Solheim, I., 2003. Monitoring vegetation changes in Pasvik (Norway) and Pechegna i n Kola Peninsula (Russia) using multitemporal Landsat MSS/TM data. Remote Sensing of Environment, 85(370-388).

Tsihrintzis, V.A., Hamid, R., 1997. Modeling and management of urban stormwater runoff quality: a review. Water Resources Management, 11, 137-164.

USACE (United States Army Corps of Engineers), 2000. Hydrologic Modeling System HEC-HMS, Technical Reference Manual, Davis, CA, pp. 157.

USACE (United States Army Corps of Engineers), 2002. HEC-GeoRAS, an extension for support of HEC-RAS using Arcview, User's Manual, Version 3.1. Hydrologic Engineering Center, Davis, CA, pp.154.

USGS (United States Geological Survey), 20002 Houston-Galveston Bay area, Texas from space - a new tool for mapping land subsidence, USGS Fact Sheet 110-02, US Department of the Interior, US Geological Survey.

Van Der Meer, F., De Jong, S.M., 2000. Improving the results of spectral unmixing of Landsat Thematic Mapper imagery by enhancing the orthogonality of end-members. International Journal of Remote Sensing, 21, 2781-2797.

Walker, J.P., Willgoose, G.R., 1999. On the effect of digital elevation model accuracy on hydrology and geomorphology. Water Resources Research, 35(7), 2259-2268.

Wang, L., Liu, H., 2006. Identification and filling of surface depressions in digital elevation models for hydrologic modeling. International Journal of Geographical Information Science, 20(2), 193-213.

Wang, Y.Q., Zhang, X., Lampa, W., 2000. Improvement of spatial accuracy in natural resources mapping using multisensor remote sensing and multisource spatial data, 4th International Symposium on Spatial Accuracy Assessment in Natural Resources and Environmental Sciences, Amsterdam, Netherlands, July, 2000, pp. 723-730.

Ward, D., Phinn, S.R., Murry, A.T., 2000. Monitoring growth in rapidly urbanized areas using remotely sensed data. Professional Geographer, 52(3), 371-386.

Wilson, J., Brandes, E., 1979. Radar measurement of rainfall: a summary. Bulletin of American Meteorology Society, 60, 1048-1058.

Wolock, D.M., Price, C.V., 1994. Effects of digital elevation model map scale and data resolution on a topography-based watershed model. Water Resources Research, 30(11), 3041-3052.

Worboy, M.F., 1994. Object-oriented approaches to geo-referenced information. International Journal of Geographic Information Systems, 8(4), 385-399.

Wu, C., Murray, A.T., 2003. Estimating impervious surface distribution by spectral mixture analysis. Remote Sensing of Environment, 84, 493-505.

Yang, L., Huang, C., Homer, C.G., Wylie, B.K., Coan2, M.J., 2003. An approach for mapping large-area impervious surface: synergistic use of Landsat-7 ETM+ and high spatial resolution imagery. Canadian Journal of Remote Sensing, 29(2), 230-240.

Yuan, M., 2001. Representing complex geographic phenomena in GIS. Cartography and Geographic Information Science, 28(2), 83-96.

Zhang, W.H., Montgomery, D.R., 1994. Digital elevation models grid size, landscape representation, and hydrologic simulation. Water Resources Research, 30(4), 1019-1028.

VITA

Name: Lei Wang

Address: Department of Geography, Texas A&M University, College Station, TX 77843

Email Address: wanglei@geog.tamu.edu

Education: Ph.D., Geography, Texas A&M University, College Station, 2006

M.S., Cartography and GIS, Institute of Remote Sensing Applications, Chinese Academy of Sciences, Beijing, China, 2000

B.S., Geography, Peking University, 1997

Experience: 2005 - 2006, Research Assistant
Knowledge Engineering Laboratory, Texas A&M University

2002, Research Assistant
Department of Geography, Texas A&M University

2000-2001, Teaching Assistant
Department of Geography, Texas A&M University